5-2018

Multi-scale modeling of particle-laden flows

Anand Samuel Jebakumar
Purdue University

MULTI-SCALE MODELING OF PARTICLE-LADEN FLOWS

A Dissertation

Submitted to the Faculty

of

Purdue University

by

Anand Samuel Jebakumar

In Partial Fulfillment of the

Requirements for the Degree

of

Doctor of Philosophy

May 2018

Purdue University

West Lafayette, Indiana

THE PURDUE UNIVERSITY GRADUATE SCHOOL
STATEMENT OF COMMITTEE APPROVAL

Dr. John Abraham, Co-Chair

Department of Mechanical Engineering

Dr. Steven T. Wereley, Co-Chair

Department of Mechanical Engineering

Dr. Alina Alexeenko

Department of Aeronautics and Astronautics

Dr. Jun Chen

Department of Mechanical Engineering

Approved by:

Dr. Jay P. Gore

Head of the Graduate Program

ACKNOWLEDGMENTS

I would like to express utmost gratitude to my advisor, Prof. John Abraham for his constant support and guidance. He has been very patient and understanding and has provided several critical suggestions on my research. Discussions with him were valuable and have taught me to look at complex things from a fundamental perspective. He has been a continuous source of support to my personal and professional development. Without his help, this dissertation would not have been possible.

I am grateful to Prof. Alina Alexeenko, Prof. Jun Chen and Prof. Steven Wereley for agreeing to serve on my committee and for their helpful comments and suggestions. Thanks to Prof. Vinicio Magi for many fruitful discussions about numerical aspects of fluid flow simulations. I would like to thank Prof. Kannan Premnath for helpful insights into the lattice-Boltzmann method. Thanks to Prof. Graham Nathan and Dr. Timothy Lau for bringing preferential particle motion in pipe flows to notice.

Thanks to Ross Fellowship for providing financial support during this work and to Burton Morgan Fellowship for providing resources for professional development. Thanks to iTAP, XSEDE and eRSA for providing computational resources for this work. Thanks to the School of Mechanical Engineering for providing funding in the form of a teaching assistantship.

Thanks to fellow students in the group, Muhsin Ameen, May Yen, Zhiyan Wang and Jiacheng Zhang for their friendship and lively conversations. Thanks to Lenan Zhang for his eagerness and enthusiasm with the lattice-Boltzmann method.

Thanks to my parents, Jebakumar Jeevanandam and Sheela Jebakumar, for their love, support, encouragement and prayers during the course of this work. Finally, thanks to God Almighty for wisdom, strength, good health and the ability to finish this work.

TABLE OF CONTENTS

Page

Page

LIST OF TABLES

LIST OF FIGURES

Figure Page

Figure Page

SYMBOLS

$C_{\epsilon 3}$	An empirical constant that appears in the ϵ equation in the modeling of vortex stretching
$C_{\epsilon 4}$	An empirical constant that appears in the ϵ equation in the modeling of turbulence modulation
C_d	Drag coefficient
C_s	Smagorisnky constant
C_{12}	Change of f due to two-particle collision
D	Pipe diameter
D/Dt	Total derivative or material derivative
$\boldsymbol{F}$	External forces acting on molecules
$\boldsymbol{F_p}$	Drag force (vector) on a particle
F_x	Body force per unit volume
$H_s(x)$	Hermite polynomial of order 's'
$K(t,\tau)$	A kernel to weigh past history of relative acceleration
Kn	Knudsen number
L	Length scale
Ma	Mach number
P	Pressure
R	Ideal gas constant
Re	Reynolds number
Re_p	Reynolds number based on the particle diameter
Re_τ	Reynolds number based on the friction velocity
$S_{\epsilon 3}$	Source term in the ϵ equation to account for vortex stretching in round jets
$S_{\epsilon 4}$	Source term in the ϵ equation due to turbulence modulation

S_{ij}	Strain rate tensor
S_k	Source term in the k equation due to turbulence modulation
St	Stokes number
T	Temperature
U	Fluid velocity scale
U_b	Bulk fluid velocity
$U_{c,e}$	Centerline velocity of the jet at its exit
W_α	Weighting factor for $\boldsymbol{c_\alpha}$
$\boldsymbol{c}$	Molecular velocity scale
$\boldsymbol{c_\alpha}$	Discrete velocity vector
c_s	Speed of sound
d_p	Particle diameter
$\boldsymbol{dxdc}$	Phase space
f	Single particle distribution function
f^{eq}	Maxwellian equilibrium distribution function
f_α	Discretized distribution function
f_α^{eq}	Discretized equilibrium distribution function
g	Acceleration due to gravity
k	Turbulent kinetic energy
l_v	Viscous length scale
m_f	Mass of fluid
m_p	Particle mass
$\boldsymbol{u}$	Fluid velocity vector
u_τ	Friction velocity
$\boldsymbol{u'}$	Fluctuating fluid velocity vector
u^+	Velocity normalized by the friction velocity
$\boldsymbol{v_p}$	Particle velocity vector
$\boldsymbol{x_p}$	Particle position vector

y^+	y-coordinate (usually refers to distance from the wall) normalized by the viscous length scale
Δ	Filter width in LES
Θ	Particle concentration
Θ_b	Bulk particle concentration
Φ_m	Mass loading ratio
Φ_v	Volume fraction of particles
γ	Ratio of specific heat at constant pressure over specific heat at constant volume
δ	One half of the channel height
δ_{ab}	Kronecker delta function
δ_t	Lattice time step
δ_x	Lattice spacing
ϵ	Rate of dissipation of turbulent kinetic energy
η	Kolmogorov length scale
λ	Characteristic time over which f relaxes to f^{eq}
μ	Dynamic viscosity
ν	Kinematic viscosity
ν_{SGS}	Eddy viscosity due to subgrid stresses
ν_t	Eddy viscosity
ρ_f	Fluid density
ρ_p	Particle density
σ	Standard deviation
τ	Relaxation parameter
τ_e	Large eddy turn-over time scale
τ_f	Flow response time
τ_k	Kolmogorov time scale
τ_p	Particle response time
τ_w	Wall shear stress

$\phi(Re)$	Correction factor to the Stokes rag law at high Re
χ	Non-dimensional measure of vortex stretching
ω	Specific turbulence dissipation rate (in $k-\omega$ model)
ω_{ij}	Vorticity tensor (skew-symmetric)
$\boldsymbol{\nabla_x}$	Gradient in physical space
$\boldsymbol{\nabla_c}$	Gradient in velocity space

ABBREVIATIONS

ADM	Approximate Deconvolution Method
BBO	Basset-Boussinseq-Oseen
BGK	Bhatnagar-Gross-Krook
CFD	Computational Fluid Dynamics
DNS	Direct Numerical Simulation
GPU	Graphics Processing Unit
LBE	Lattice Boltzmann Equation
LBM	Lattice Boltzmann Method
LDA	Laser Doppler Anemometry
LES	Large Eddy Simulation
LGA	Lattice Gas Automata
MPI	Message Passing Intergace
MRT	Multiple Relaxation Time
PDE	Partial Differential Equation
PDF	Probability Density Function
PIV	Particle Image Velocimetry
PP-DNS	Point Particle - Direct Numerical Simulation
PR-DNS	Particle Resolved - Direct Numerical Simulation
RANS	Reynolds Averaged Navier Stokes
RMS	Root Mean Square
SGS	Sub-Grid Scale
SRT	Single Relaxation Time
SST	Shear Stress Transport
TKE	Turbulent Kinetic Energy

ABSTRACT

Jebakumar, Anand Samuel PhD, Purdue University, May 2018. Multi-Scale Modeling of Particle-Laden Flows. Major Professor: John Abraham, School of Mechanical Engineering.

Particle-laden flow occur in a wide range of engineering applications such as combustors, gasifiers, fluidized beds and pollution control systems. Particle-flow interactions are complex, especially in turbulent and confined flows. A proper understanding of these interactions is critical in designing devices with better performance characteristics. In this work, particle-laden flows in channels are numerically investigated with the lattice-Boltzmann method (LBM). A three-dimensional parallelized lattice-Boltzmann method code is developed to carry out these studies. The code resolves the particle surface and the boundary layer surrounding it to gain fundamental insights into particle-flow interactions. The lattice-Boltzmann method is assessed for its accuracy in solving several standard single-phase and multi-phase, laminar and turbulent flows. Direct numerical simulations (DNS) of particle-laden channel flows are then performed.

When the particle diameter is smaller than the Kolmogorov length scale, direct numerical simulations (DNS) with the point-particle approximation show that the Stokes number, St, mass loading of particles, i.e. ratio of mass of dispersed to carried phase, and particle diameter, are important parameters that determine the distribution of the particles across the channel cross-section and the impact of the particles on the flow field. When the St is infinitesimally small, the particles are uniformly distributed across the cross-section of the channel. As St is increased, the particle concentration near the wall increases. At even higher St, the particle concentration near the wall decreases, but it increases at the center of the channel. These changes in concentration are attributed to turbophoresis which causes preferential movement

of the particles. The impact of the turbophoretic force is affected by St and particle diameter. The parameters that influence the mean flow field of the carrier phase is primarily the mass loading.

To further improve the understanding of the physics of the flow, particle-resolved direct numerical simulations (PR-DNS) are carried out. Particle motion in a laminar channel flow is initially studied. The trajectory of a single particle is examined. It is shown that the mean equilibrium position of the particle in the channel depends on the St. Particles with low St reach an equilibrium position that lies between the wall and the center of the channel (Segre-Silberberg effect) while those with high St begin to oscillate about the center of the channel as they are transported by the fluid. The particle location and motion are determined by the interplay of three forces acting on the particle in the wall normal direction: the Saffman lift, Magnus lift and wall repulsion. Saffman lift and Magnus lift act to move the particle towards the wall while wall-repulsion opposes this motion.

Direct numerical simulations of turbulent flow past stationary particles in a channel are then carried out. These simulations provide information about particle-flow interactions when the particle is near the wall and at the center. Multiple particles fixed in a cross-sectional plane are also considered. The position of the particles in the channel, the particle size, the Reynolds number and the number of particles are varied. The details of the flow field are analyzed to provide insight into the factors that control the distance of influence of the fixed particle on the flow field. With a single particle case, the effect of the particle is felt for about 20 diameters downstream. When multiple particles are present, interaction between the vortices shed by the particles lengthens the distance to about 40 diameters downstream. The results suggest that in a particle-laden flow, if particles are separated by an average distance greater than 40 diameters, particle-fluid-particle interactions can be neglected. At shorter distances, these interactions become important.

Next particle-resolved direct numerical simulations (PR-DNS) in a turbulent channel flow are carried out to study the particle motion when the particle diameter is

larger than the Kolmogorov length scale. It is shown that in a turbulent channel flow, the dominant forces are the Saffman lift and the turbophoresis. When the particle is larger than the Kolmogorov length scale, turbophoresis can act in a local sense whereby the more intense exchange of momentum of eddies on the side of the particle with higher turbulent kinetic energy relative to the opposite side move the particle toward the lower turbulent kinetic energy region or in a global sense whereby even when the particles do not directly feel the effect of eddies, particles tend to diffuse down gradients of turbulent kinetic energy. The simulations show that particles with relatively lower St move preferentially toward the wall while those with higher St exhibit a relatively uniform concentration. This is consistent with the conclusion from the point-particle simulations. As particle size is increased, the St at which uniform distribution is reached increases. The likely reason is that the effect of local turbophoresis and Saffman lift increases for larger particles and these forces tend to concentrate particles near the wall. Higher St, i.e. higher inertia, is needed to overcome these forces.

1. INTRODUCTION

1.1 Background

Particle-laden flows are common in many applications of engineering interest like engines, combustors and gasifiers. In these devices, the flow is confined and turbulent in nature and as a result particle-wall and particle-turbulence interactions are important. These interactions are complex and not fully understood. While direct numerical simulations of the flows can provide physical insight and improve understanding, the wide range of length and time scales of the flow makes it impractical to do a fully-resolved simulation for engineering applications with current computational resources. This necessitates the use of models to account for the complex interactions. In order to develop such models, however, a firm understanding of particle-wall and particle-turbulence interactions is required. Experimental investigations themselves are not adequate to clarify the physics on account of the wide separation of scales. Numerical simulations play an essential role.

Particle-laden flows exhibit a variety of interesting features that become important in the presence of turbulence. Turbulent dispersion and turbulence modulation are two such phenomena that are relevant to many devices. Turbulence modulation refers to the attenuation/augmentation of turbulence by the particles. Such modulation can significantly alter the behavior of these flows. Dispersion of particles by turbulence is another aspect of interest in several applications. It has been shown through measurements that even in homogeneous isotropic turbulence, the particle concentration is not uniform [1]. Understanding the dispersion of particles is critical in designing engineering systems.

For instance, in a pulverized coal combustor, finely ground coal particles are carried by air in a pipe and are injected into the burner. Improper mixing of these

particles and/or wall deposition can negatively affect the combustion efficiency and might increase the pollutants in the exhaust gases. Particle-laden flows are also encountered in several pharmaceutical applications and effects such as clustering and wall deposition can significantly influence the outcome of pharmaceutical processes. The clustering effects can also be an advantage in some devices. For example, in a fly ash collection system, the flow can be adjusted so that the particles aggregate thereby making it easier to remove them from the flue gases.

Another application of interest is a solar thermochemical reactor. A solar reactor is a device that uses solar energy to aid the gasification of carbonaceous feedstock. The use of solar energy increases the conversion efficiency of the gasification process. One such design of a reactor, the vortex flow solar reactor of Z'Graggen *et al.* [2] is shown in Fig. 1.1. In this particular design, the feedstock is ground into small particles and is injected with steam. The particles are injected tangentially to form a vortex thereby maximizing its residence time inside the reactor. Solar radiation is incident on an optical window through which the particles are heated up. It is critical in this process to prevent the deposition of particles on the optical window as that would reduce the efficiency of the system considerably. Moreover, effects such as clustering/agglomeration and wall-deposition would decrease the effective surface area available for reaction with the steam. Numerical simulations can be employed to identify these undesirable effects and prevent them. Models that faithfully capture these effects are thus essential to these computations. This work aims at developing models that addresses issues such as these.

Motivated by the need to improve the understanding of particle-laden flows where particle-distribution is important, direct numerical simulations of particle-laden flows are carried out in this work. In the limit when the particle size is smaller than the Kolmogorov length scale, point-particle simulations are carried out. When the particle size is larger than the Kolmogorov length scale, particle-resolved simulations are carried out.

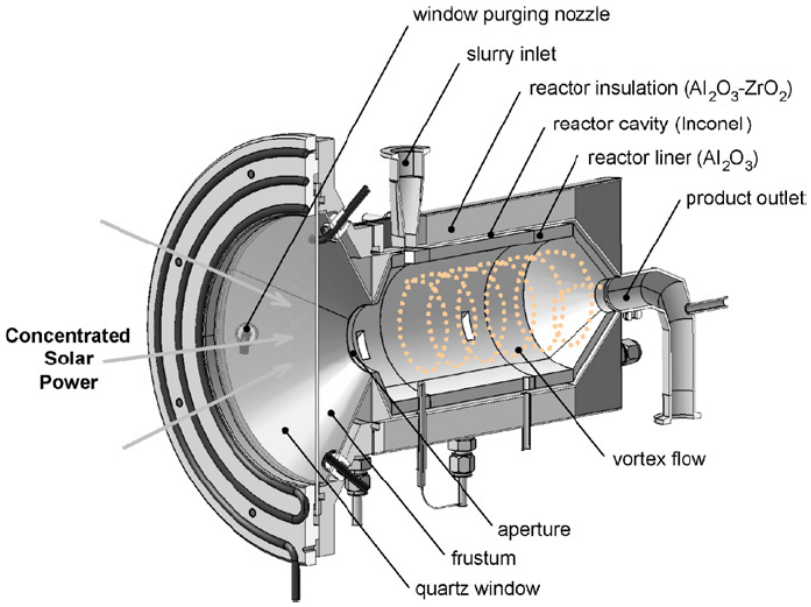

Figure 1.1: The vortex flow solar reactor of Z'Graggen *et al.* [2].

1.2 Objectives

The specific objectives of this work are the following:

1. Develop a highly parallelized numerical code to perform direct numerical simulations of particle-laden flows.

2. Conduct numerical simulations in laminar particle-laden flows to understand the mechanism responsible for particle transport.

3. Conduct numerical simulations in turbulent particle-laden flows to understand the mechanism responsible for particle transport.

4. Improve the understanding of two-way coupling between the carrier and dispersed phases.

1.3 Outline of Thesis

In Chapter 2, prior works on particle-laden flows are reviewed. After an introduction of various parameters involved in describing particle-laden flows, analytical studies on particle-laden flows are reviewed. This is then followed by a review of several experimental works. The current limitations in measurement techniques of particulate flows are discussed. After this, various computational approaches that are commonly in use to simulate particle-laden flows are reviewed. Modeling aspects that account for various particle-turbulence and particle-wall interactions are then presented. The chapter concludes with a summary that establishes the motivation for the present work.

The lattice-Boltzmann method is employed in this work for carrying out the Particle Resolved - Direct Numerical Simulations (PR-DNS). The general framework for the lattice Boltzmann method (LBM) is presented in Chapter 3. The derivation of the lattice Boltzmann equation (LBE) from the continuous Boltzmann equation and the derivation of Navier-Stokes equations from the LBE are described. Then, the

implementation of boundary conditions in the LBM framework is discussed. This is followed by a description of the implementation of the particle motion in the LBM framework. Computational cost and parallel scalability are important considerations in a DNS solver. This chapter concludes with information about the scaling characteristics of the LBM.

A series of tests are carried out to assess the accuracy of the code. The results of these tests are presented in Chapter 4. Comparisons are done with problems for which analytical solutions are available: the Taylor-Green vortex, the Couette flow and a channel flow. In addition, a lid-driven cavity problem is solved and results are compared with results available in literature. A 3D flow is also simulated for a channel flow with periodic boundaries in the stream-wise direction. The multiphase implementation of LBM is then assessed. Comparisons of the LBM predictions with results from literature are reported for two problems: a particle sedimenting in a channel under the action of gravity and a neutrally buoyant particle in a channel flow. A spherical particle sedimenting in a three dimensional duct is also compared with experimental and other numerical results. The code is then assessed for its accuracy in predicting single phase turbulent flows. Direct Numerical Simulations (DNS) are carried out using the LBM for a turbulent channel flow. Comparisons of various statistical quantities such as the mean velocity, turbulence intensity, Reynolds shear stress, fluctuating pressure and vorticity with standard DNS data from literature are presented.

The LBM is then used to simulate particles smaller than Kolmogorov length scale by treating them as point particles. These results are presented in Chapter 5. Two-way coupling and particle-particle collisions are implemented within the LBM framework. Results are presented for both the effect of turbulence on particle motion and the effect of particles on mean velocity and turbulent intensities.

Chapter 6 presents results for a single particle moving in a laminar channel flow at various St. They aid in explaining the particle-wall and particle-flow interactions

that are important in such flows. The mechanism of particle migration is explained in terms of various forces acting on the particle in the wall-normal direction.

Results for the effect of stationary particles on turbulence in a channel flow is presented in Chapter 7. The effect of particle size, Reynolds number, position of particles within the channel and the number of particles are investigated. The region of influence of the particles on the turbulent flow field is presented.

In Chapter 8, results are presented for particles in a turbulent channel flow at different St. The effect of turbophoresis and Saffman lift in the context of a turbulent flow is explained in this chapter. The influence of these forces on the particle motion at various St is studied.

Chapter 9 concludes with a summary of the thesis and the contributions of this project followed by a discussion of possible future work. The future work includes development of adaptive meshes, large-eddy simulation (LES) and Reynolds averaged Navier-Stokes (RANS) model development for particle dispersion and effects of non-spherical and polydisperse particles.

2. LITERATURE REVIEW

2.1 Introduction

In this chapter, a review of prior studies on particle-laden flows is discussed. Several relevant parameters that are used in the characterization of particle-laden flows are listed in Section 2.2. In Section 2.3, various kinds of particle-turbulence interactions are presented and discussed. Then in Section 2.4, analytical studies on particulate flows are reviewed. Experimental works done on particle-laden flows are presented in Section 2.5 while Section 2.6 explains different computational approaches to particle-laden flows. In Section 2.7, various Direct Numerical Simulation (DNS) studies on particle-laden flows are presented. Works on RANS modeling of particle-laden flows are presented in Section 2.8 while LES modeling of particulate flows are in Section 2.9. Finally in Section 2.10, a summary of the gaps in existing understanding of particle-turbulence interactions are presented to motivate the present work.

2.2 Relevant Parameters

The important non-dimensional parameters that are used in the characterization of particle-laden flows are presented in this section. The volume fraction of the dispersed phase, Φ_v is defined as:

$$\Phi_v = \frac{\delta V_p}{\delta V}, \tag{2.1}$$

where δV_p is the volume occupied by the particles in a suspension of volume δV. (The averaging volume is chosen large enough so that Φ_v is independent of the size of the

volume). The mass loading ratio, Φ_m is defined as the ratio of particle mass, m_p, to the fluid mass, m_f, in a given volume, i.e.

$$\Phi_m = \frac{m_p}{m_f}. \tag{2.2}$$

This can be related to Φ_v through the density ratio of the particle to the fluid as follows:

$$\Phi_m = \frac{\rho_p}{\rho_f}\left(\frac{\Phi_v}{1-\Phi_v}\right), \tag{2.3}$$

where ρ_p and ρ_f are the density of the particle and fluid, respectively. The Reynolds number, Re, is defined as the ratio of the inertial forces to the viscous forces, i.e.

$$Re = \frac{\rho_f U L}{\mu}, \tag{2.4}$$

where U is a velocity scale, L is a length scale and μ is the viscosity of the fluid. Depending on the length scale and the velocity scale chosen, there can be different Re. A Re based on the length scale of the particle is known as the particle Reynolds numbers, Re_p, and is given by

$$Re_p = \frac{\rho_f U d_p}{\mu}, \tag{2.5}$$

where d_p is the diameter of the particle. In turbulent flows, another Re is defined based on the friction velocity u_τ and the viscous length scale l_v as follows:

$$Re_\tau = \frac{\rho_f u_\tau l_v}{\mu}. \tag{2.6}$$

The Stokes number, St, is another important parameter in describing particle-fluid interaction. It is defined as the ratio of particle response time τ_p to the flow response time τ_f, i.e.

$$St = \frac{\tau_p}{\tau_f}. \tag{2.7}$$

The particle time constant is generally used as a measure of the response time of the particle. The particle time constant is defined here as the time taken by a particle

released in a quiescent fluid to slow down to 36% $(1/e)$ of its initial velocity. For a spherical particle at low Re_p, the particle time constant is given by,

$$\tau_p = \frac{(2\rho_p + \rho_f)d_p^2}{36\mu}. \tag{2.8}$$

If the particle density is much higher than the fluid density, then Eq. (2.8) reduces to

$$\tau_p = \frac{\rho_p d_p^2}{18\mu}. \tag{2.9}$$

The flow response time can be obtained as

$$\tau_f = \frac{L}{U}, \tag{2.10}$$

where L represents a length scale and U a velocity scale. For instance, in the case of a channel flow, L can be taken as the channel height and U as the maximum mean velocity. Another time scale that can be defined in the case of a turbulent flow is the Kolmogorov time scale, τ_k, which denotes the time scale of the smallest eddy beyond which viscous effects dominate. τ_k is given by

$$\tau_k = \left(\frac{\nu}{\epsilon}\right)^{1/2}, \tag{2.11}$$

where ν represents the kinematic viscosity of the fluid and ϵ the average rate of dissipation of turbulent kinetic energy. A particle with a low St follows the fluid element, while one with a high St is not affected significantly by the flow. Particles with St of the order unity exhibit interesting behavior and often form clusters.

2.3 Particle-Fluid Interactions

Particle-laden flows are complex on account of the non-linear interactions between the dispersed and carrier phase. In most industrial applications where particle-laden flows are present, the flow field is turbulent. Predicting single phase turbulent flows,

in itself is not trivial and has several aspects that are not completely understood. The addition of a dispersed phase to this problem makes it even more challenging. Two important features of this class of flow that are of relevance to various industrial devices are particle dispersion and turbulence modulation. Both these effects are discussed in detail below.

2.3.1 Particle Dispersion

Particle dispersion refers to the transport of particles by the turbulent flow. Instinctively, one would expect particles in a turbulent flow to be distributed uniformly on account of enhanced mixing due to turbulence. This, however, is not the case in most flows. Particles in a turbulent flow often tend to form clusters. Even in an homogeneous isotropic turbulent flow, the particle concentration is highly non-uniform. Figure 2.1 shows the laser image of particles in an homogeneous isotropic turbulence with no mean flow [3]. It can be seen that the particles are densely concentrated in certain areas while the concentration is sparse in other areas. This is referred to as preferential accumulation and has been studied by several researchers in the past [3–6]. Some of the key findings of these studies are as follows:

- Particles that are heavier than the fluid tend to aggregate in regions of high strain rate and avoid regions of intense vorticity.
- Particles that are lighter than the fluid tend to aggregate in vortical regions.

An important effect of turbulence on particle motion is the "crossing trajectories" effect. Yudine [7] observed that heavy particles falling in a turbulent flow field under the effect of gravity moves from one eddy to another due to inertia. This can happen even in the absence of gravity if the response time of the particle is large such that it moves out of the eddy. Thus if a particle is captured in an eddy there are two things that might happen: If the St is small, the particle follows the fluid element and behaves as a tracer particle. If the St is large and/or if there is a potential field

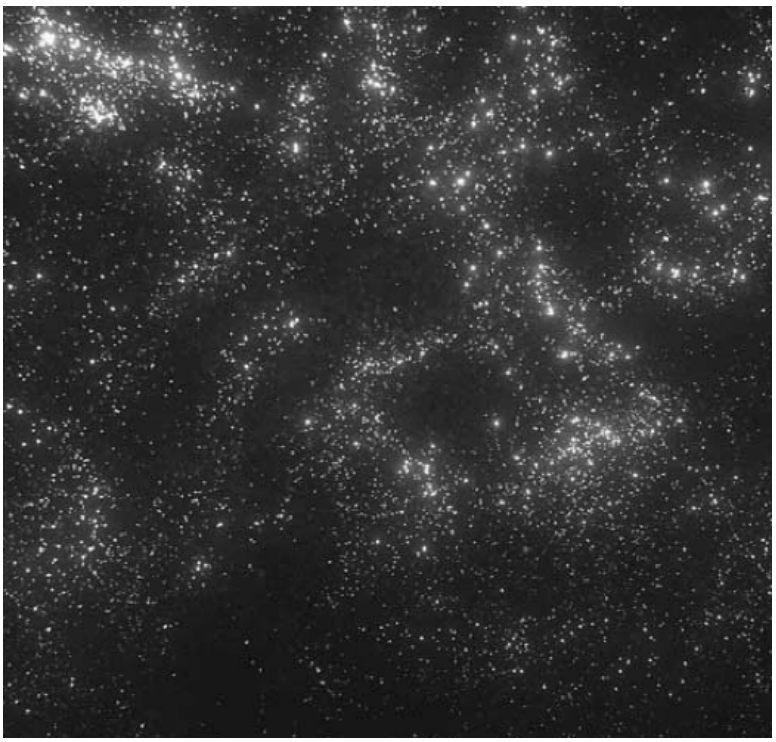

Figure 2.1: Experimental image of particles in homogeneous isotropic turbulence at St = 0.57 (Adapted from [3]).

(gravity for instance), then the particle crosses an eddy and moves to another. This is referred to as the "crossing trajectories" effect. This effect has been studied by many researchers in the past [8,9]. The influence of this effect on preferential concentration has been explained by Eaton and Fessler [10].

Another example of preferential migration/aggregation is shown in a recent experimental study of Lau and Nathan [11]. The main objective of their study was to examine the effect of St on the structure of a turbulent particle-laden jet. In order to do this, particles were introduced into a turbulent pipe flow and were transported by the flow. The length of the pipe was sufficiently long to achieve a fully developed flow. They noticed that the particle concentration at the exit of the pipe was not uniform. The particles migrated toward or away from the axis depending on their St. Figure 2.2 shows the concentration profile of particles normalized by the bulk concentration at the exit of a turbulent pipe flow. At a low St of 0.3, the particle concentration near the wall is about 2.5 times the bulk concentration. For a St of 11.2, the particle concentration is high near the axis of the pipe. Particles with a St of 1.4 are distributed almost uniformly. Thus, as the St increases from 0.3 to 11.2, the radial concentration profile changes from a 'U-shape' to a '$\wedge$-shape'. Thus turbulence might not necessarily cause uniform mixing of the dispersed phase and can sometimes inhibit effective mixing, but the reasons are not well understood.

Understanding this phenomena is important in several applications. For example, when fuel particles are delivered to a combustor, these particles are carried by a stream of air through a pipe. It is, of course, desirable to avoid deposition of particles on the walls of the pipe as this can affect the particle flow rates and distribution. The uniformity of the particle distribution in the pipe and at the exit of the pipe is an important consideration in the design of the delivery system and possibly in the performance of the combustor. Some applications require effects such as wall-deposition. For example, in a pollutant control system, small particulate matter can be isolated and removed if it deposits on the wall.

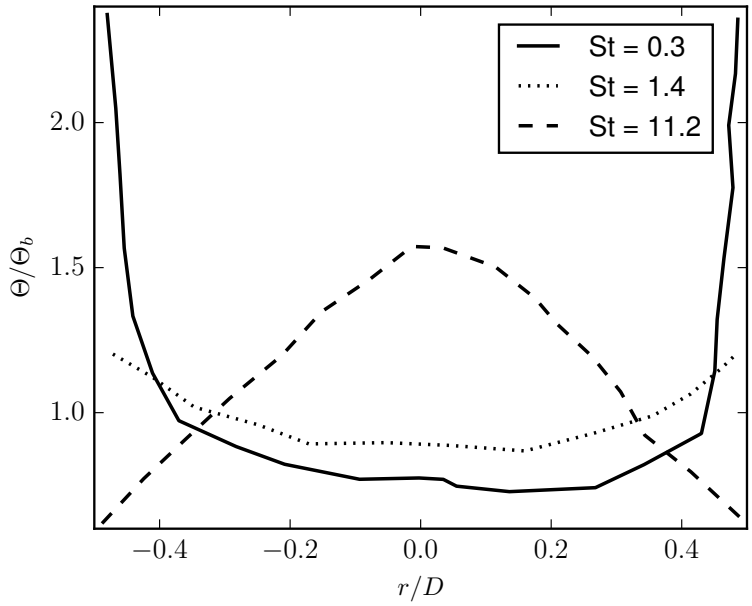

Figure 2.2: Concentration profile of particles at the exit of a turbulent pipe flow (Adapted from Lau and Nathan [11]).

2.3.2 Turbulence Modulation

Another interesting aspect of particle-laden flows is turbulence modulation. At low particle mass loading ratios (Φ_m), the turbulent flow field of the carrier phase is similar to its single phase counterpart. However, as Φ_m increases, the dispersed phase begins to affect the turbulence in the carrier phase. This is referred to as turbulence modulation.

Elghobashi [12] classified particle-laden flows into three regimes based on the volume fraction of the dispersed phase, Φ_v. Figure 2.3 shows these regimes as a function of the volume fraction of the dispersed phase (Φ_v). For low values of Φ_v, there exists a one-way coupling regime where the particles are affected by the flow field, but not vice versa. As Φ_v increases, two-way coupling becomes important i.e. the flow field and the particles influence each other. For even higher values of Φ_v, the inter-particle interactions also become important. In this regime, the two phases interact with the other and with itself, i.e. four-way coupling exists. The ratio of the particle characteristic time to the flow time, the Stokes number (St), is also a controlling parameter; it is depicted on the ordinate in Fig. 2.3. In the two-way coupling regime, particles can either enhance production or dissipation of turbulent kinetic energy depending on the value of St. This regime is of particular interest in the current study.

There are several mechanisms that contribute to turbulence modulation in a dilute suspension [1]:

- Enhanced dissipation or production of turbulent kinetic energy due to the particles.
- Transfer of kinetic energy from the particles to the fluid and vice versa.
- Vortex shedding behind the particles.

Understanding of turbulence modulation is still limited. This is because in order to study the physics, the dissipation of turbulent kinetic energy near the surface of the particle has to be measured. This, however, is challenging with our current

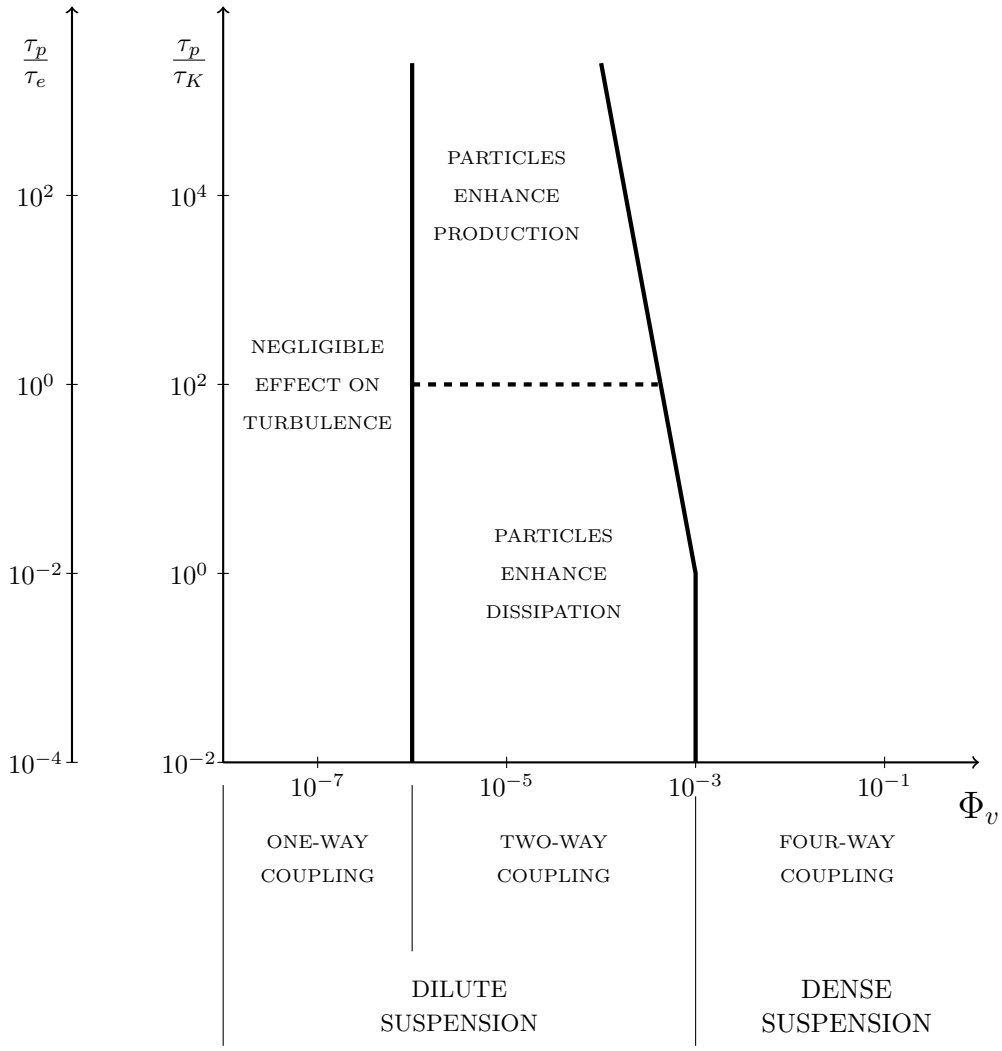

Figure 2.3: Regimes of particle-turbulence interactions (Adapted from Elghobashi [12]).

measurement techniques. In the case of numerical simulations, the particle itself has to be resolved to ensure that the dissipation is properly captured. This is computationally expensive and very few works have attempted to carry out particle-resolved Direct Numerical Simulations (DNS) of turbulent flows. This limited understanding has contributed to the paucity in models to account for turbulence modulation.

2.4 Analytical Studies on Particulate Flows

Stokes [13] was the first to study the force on a particle in creeping flow. He derived an analytical expression for the force acting on a fixed sphere in a uniform flow at Re approaching zero which is given as:

$$\mathbf{F_p} = 3\pi\mu d\mathbf{u}. \tag{2.12}$$

In later works, Basset [14], Boussinesq [15] and Oseen [16] independently examined the motion of a sphere in a quiescent incompressible fluid. Recent studies have extended these results to include cases such as particle motion in a compressible fluid [17]. Bretherton [18] showed through an analytical study that a particle in a Stokes flow does not migrate across streamlines in a shear flow. Saffman [19] investigated the effects of inertia using perturbation analysis and found that a particle in a linear unbounded shear flow experiences a lateral force. Hence, lateral migration arises due to an inertial force at non-zero Re. This force is generally referred to as Saffman lift and denotes the force acting on a particle on account of the velocity gradient across it in a direction perpendicular to the flow when the particle leads or lags the flow. The Saffman lift force tends to push a particle that leads the fluid into a region with lower velocity and vice versa. McLaughlin [20] analyzed the inertial lift acting on a particle in a wall-bounded linear shear flow. While analytical studies provide useful insight into the fluid dynamics involved, their scope is limited to low Re.

2.5 Experimental Works on Particle-Laden Flows

2.5.1 Measurement Techniques

Experimental research in multi-phase flows has focused on measuring the mean and root mean square velocity of the carrier phase as well as the particle velocity and concentration. Photographic techniques have been used in the past [21–25] to determine the particle velocity and concentration. Later works [26–30] have adopted laser-Doppler anemometer (LDA) techniques to study turbulent multi-phase flows. This technique involves measuring the velocity of small particles (also known as tracer particles) that are introduced into the fluid. These particles have very low St and hence are assumed to portray a faithful representation of the flow dynamics. Larger particles (the dispersed phase) produce a stronger signal thus making it easy to distinguish the dispersed phase from the tracer particles.

Particle-image velocimetry (PIV) is being increasingly used in several recent works [11, 31]. The fluid is seeded with tracer particles as in LDA. However, PIV produces two-dimensional (or three-dimensional) velocity fields while LDA measures the fluid velocity at a point. The measurement of carrier phase velocity near the surface of the dispersed phase is still a challenge. Measurement of dissipation of turbulent kinetic energy is critical to understand the physics behind turbulence modulation. This, however, is difficult owing to the need to know the spatial derivatives of all velocity components. This problem can be overcome by employing very high spatial resolution PIV measurements.

2.5.2 Interesting Findings

Segré and Silberberg [21–23] used an optical system to study the motion of neutrally buoyant spherical particles in a Poiseuille flow. They observed that a particle released close to the axis is displaced radially outward while one released close to the wall moves inwards. They report a build up of concentration at about two-thirds of

the radius of the pipe. This was the first observation of preferential migration of particles in a carrier phase. This effect has been confirmed by several researchers in later works [24, 25, 32, 33] and is referred to as the Segré-Silberberg effect. This indicates that even in the case of a laminar flow, particles exhibit a tendency to migrate to an equilibrium position. This position could possibly depend on several parameters including the particle-fluid density ratio, the particle Reynolds number Re_p, the ratio of particle diameter to the pipe diameter and the St, among others.

Rogers and Eaton [27] used LDA to study the effect of particles in a flat plate boundary layer. The St of the particles considered in the study was between 1 and 10 and the mass loading, Φ_m, was 0.2. They report that particles with St of the order unity tends to suppress the fluid turbulence significantly. They also state that particles appear to take energy from all fluid scales equally. Kulick *et al.* [28] have reported measurements of particle-laden turbulent channel flow. They observe that the attenuation of turbulence due to the particles increase with St and Φ_m. Further, they report that the turbulence attenuation is stronger in the transverse direction than the streamwise direction. Sato *et al.* [29] studied particle-laden turbulent wall jets using the LDA. They report that particles of St close to unity are concentrated near the wall where the shear is largest, while those with higher St are distributed nearly uniformly.

Suzuki *et al.* [34] have reported measurements of particle-laden turbulent flow using the Particle Tracking Velocimetry. They found that particles augment the streamwise turbulent intensity significantly near the center of the channel while it is unchanged at $y^+ < 20$. They also observed that the particles are densely distributed near the low speed streaks. Tanak and Eaton [31] carried out sub-Kolmogorov resolution PIV measurements of particlulate flow in forced isotropic turbulence. They found that the turbulent kinetic energy was attenuated by 25 % because of the particles. However, the change in dissipation is relatively small.

2.6 Computational Studies on Particle-Laden Flows

Computational studies of particle-laden flows can be divided into two categories: simulations where all the relevant length (and time) scales are resolved (DNS) and those where the effect of particles are taken into account through models (RANS and LES). While DNS studies yield insight into the physics behind complex particle-turbulence interaction, they cannot be used to study engineering systems owing to the prohibitively high computational cost. Computational work is thus often two-fold: DNS studies of canonical flows are carried out to improve our understanding of the basic mechanisms; this understanding is used to develop models that can capture these effects with a desired level of accuracy.

2.7 Direct Numerical Simulation of Particle-Laden Flows

DNS studies of particle-laden flows can be broadly classified into two methods:

1. Point Particle - Direct Numerical Simulation (PP-DNS).
2. Particle Resolved - Direct Numerical Simulation (PR-DNS).

2.7.1 Point Particle DNS

In this method, the particle is assumed to be a point and the interphase coupling is achieved through drag force relations. There is an implicit assumption that the particle is smaller than the smallest length scale of the flow, i.e. the Kolmogorov length scale.

Squires and Eaton [5] have reported DNS studies of particulate flows in forced isotropic turbulence using the point particle approach. They have carried out computations of cases with three different particle time constants (normalized by the large eddy turnover time): 0.075, 0.150 and 0.520. They report that particle inertia causes a bias in the trajectory toward regions of low vorticity and high strain

rate. This preferential concentration is most pronounced for the case where the non-dimensional time constant (i.e. St) is 0.15. In another work [35], they show that the turbulent kinetic energy increased at higher wave numbers (smaller length scales) and decreased at smaller wave numbers. They also report that the turbulence modulation is different for each case of St. This is because in the case of the intermediate St, the preferential concentration is more pronounced. These studies suggest that an appropriate model for turbulence modulation would have some dependence on the St.

Ferrante and Elghobashi [36] have carried out DNS of isotropic turbulence laden with particles using the point particle approach. They have performed cases with three different St (based on the Kolmogorov time scale): a) micro particles where $St << 1$, b) critical particles for which $St \approx 1$ and c) large particles where $St > 1$. The mass loading is unity and the volume loading is 10^{-3}. Their findings are as follows: Micro particles act as tracers and remain in their initial surrounding vortices. Large particles cross over and enter new eddies. Critical particles are ejected from the core of the vortices to the periphery. After this, they do not move over to new eddies but accumulate in convergence regions.

2.7.2 Particle Resolved DNS

Particle-resolved simulations involve the numerical resolving the particle as a moving boundary by enforcing the no-slip boundary condition on its surface. These kind of simulations are computationally very expensive. They often involve a limited number of particles, far less than what one would encounter practically. One of the earliest particle-resolved studies is that of Feng *et al.* [37,38] who performed two-dimensional numerical simulations of circular "particles" settling in a channel with no mean flow, transported in a Couette flow and in a Poiseuille flow. All flow cases considered were in the laminar regime. For a particle in a channel flow, they were able to observe the Segré-Silberberg effect. They identified Saffman lift (corrected to account for the

velocity profile curvature of an undisturbed Poiseuille flow), Magnus lift, and wall repulsion to be the dominant forces that cause the particle migration. They have reported the dependence of the particle migration trajectories on parameters such as the Re_p , the ratio of channel height to the particle diameter (H/d ratio) and the density ratio of the particle to the fluid. Mortazavi and Tryggvason [39] performed similar simulations with deformable drops in a channel flow. They observed that at high Re, the drops began to oscillate about the center of the channel. Zeng *et al.* [40] performed numerical simulations of a spherical particle in a wall-bounded flow and studied the dependence of the lift-coefficient on the Re based on a particle length scale . Nourbakhsh *et al.* [41] have done 3D simulations of drops in a Poiseuille flow and have studied the effect of capillary number (Ca), the Re and the volume fraction on the drop migration.

Burton and Eaton [42] have carried out particle-resolved DNS studies of a fixed particle in a decaying homogeneous isotropic turbulence. The particle diameter is approximately twice the Kolmogorov length scale of the unladen turbulence. They report a significant attenuation of the turbulent kinetic energy within one diameter of the particle surface. Outside 5 diameters, the turbulence modification is negligible. Bagchi and Balachander [43] have carried out DNS simulations of a particle in a frozen isotropic turbulence to study the prediction of the drag force on a particle by integrating the pressure and shear stress on its surface. They found that the standard drag correlation based on the mean relative velocity results in a reasonably accurate prediction of the mean drag obtained from the DNS. However, the accuracy of prediction of the instantaneous drag decreases with increasing particle size. In a later work [44], they study the effect of turbulence on the wake of an isolated particle. They observe that at particle Re less than 210, the effect of free stream turbulence is to introduce wake oscillations. At higher Re, the turbulence promotes early onset of vortex shedding.

One of the main advantages of the particle-resolved method is that the force acting on the particle is computed directly from the viscous stresses acting on the particle

and no model is used. Moreover, as the flow field around every particle is resolved, the dissipation of kinetic energy at the surface is resolved and need not be modeled [45].

2.7.3 Approaches in Particle-Resolved DNS

Since this work involves particl- resolved DNS (PR-DNS), various techniques that are commonly employed for PR-DNS are discussed. The general strategy in any PR-DNS computation involves the following [45]:

- Solve for fluid flow by imposing no-slip and no penetration boundary condition at the particle surface.
- Compute the hydrodynamic forces acting on the particle.
- Update the position and velocity of the particle due to the hydrodynamic forces as well as other forces such as ones due to inter-particle collision.

It can be seen that PR-DNS eliminates the need for any force equation/drag model for the particle. Since the flow field around the particle is resolved, effects such as dissipation of turbulent kinetic energy, k, at the particle surface and augmentation of k due to vortex shedding behind the particle are resolved.

There are different techniques to carry out a PR-DNS. These approaches can be broadly divided into two classes:

- Those that use a body fitted mesh to represent the surface of the particle.
- Methods where a regular Cartesian grid is used to solve for the flow and the particle surface is tracked separately.

The first approach has been used in several works [37,38,42–44,46,47]. One of the main drawbacks of using a body-fitted mesh is that the solution domain has to be re-meshed after the particle moves and the solution on the older grid has to be cast on the newer grid through interpolation. This is no longer necessary when Cartesian

grids are used and the particle surface is tracked separately. Examples of works where the second approach is adopted includes Ref. [48–50].

Figure 2.4 shows the particle representation by a body fitted mesh. This mesh is taken at some time instant during the simulation. Now as the particles move in the domain, they would occupy/cover certain fluid cells. Similarly, areas that were occupied by the particle in prior time steps might become fluid cells. Thus a new mesh should be generated for this current particle position. The hydrodynamic variables in the new cells are obtained from the old cells through interpolation. Fig. 2.5 shows the particle representation on a Cartesian grid. In this method, since the grid is fixed, no remeshing/interpolation is needed. Each grid point has a flag variable that tracks if the node is a solid or fluid node. There are special rules to treat newly appeared/disappeared fluid nodes.

In this work, we have used a relatively new computational approach, called the Lattice Boltzmann Method (LBM), to carry out the particle-resolved DNS computations. The LBM involves solution of the Boltzmann equation with discrete velocity directions. The local and explicit nature of the collision operator makes the code highly parallelizable. The particle implementation is relatively easy compared with traditional methods. The LBM has been used for particle-laden flows in the past [51–54]. In recent works, the LBM has been used in PR-DNS as well [55, 56]. The details of the method as well as its implementation is done in Chapter 3.

2.8 RANS Computations of Particle-Laden Flows

While DNS studies provide valuable insight into the particle dynamics in a turbulent flow, they cannot be used in the prediction of flows of engineering interest owing to the high Re and the number of particles in such systems, which renders the computations impractical with current resources. Thus modeling of some sort is required. A common approach used in the prediction of turbulent flows for practical purposes is to solve the Reynolds Averaged Navier Stokes (RANS) equations. The

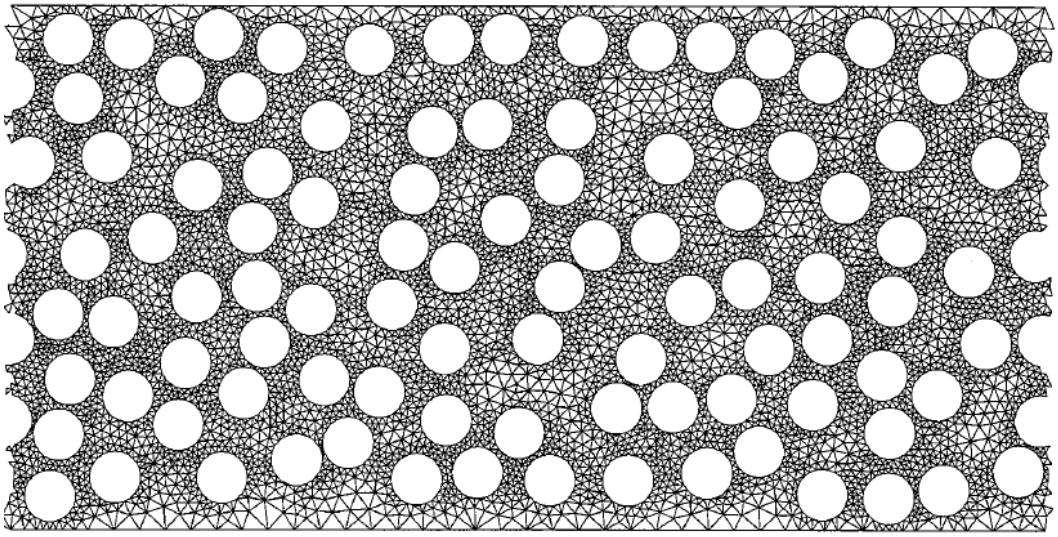

Figure 2.4: Body-fitted mesh for a two-dimensional channel with circular particles (Adapted from [57]).

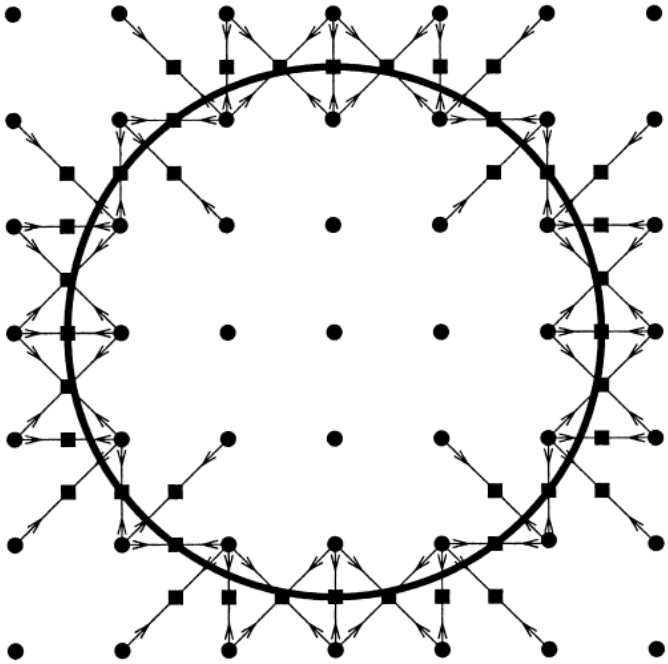

Figure 2.5: A circular particle in a fixed Cartesian grid (Adapted from [58]).

RANS equations are obtained by averaging the Navier-Stokes equations to obtain the mean flow properties. Since only the mean quantities are of interest for most engineering applications, the RANS equations should give enough information about the flow. However, the process of averaging yields terms that are dependent on the fluctuating quantities. These are similar to the viscous stresses and are called Reynolds stress.

The effect of the Reynolds stress needs to be modeled to solve the RANS equations. This is done by employing the Boussinesq assumption which approximates the Reynolds stress to an eddy viscosity times the strain rate tensor. The eddy viscosity, ν_t, is modeled from a turbulent length scale, l, and velocity scale q,

$$\nu_t = Cql. \tag{2.13}$$

This, in fact, is done by drawing an analogy between the eddy viscosity which is a measure of diffusion of momentum due to random turbulent eddies and the molecular viscosity which represents diffusion of momentum due to random molecular collisions. The eddy viscosity is also referred to as turbulent diffusivity and represents the enhanced diffusive properties of the flow due to turbulent mixing.

Different RANS models find the eddy viscosity through various methods. In algebraic models such as the mixing length model, the eddy viscosity is found from an algebraic relation between the velocity gradient and a mixing length specified a priori. More often, the models involve the solution of one or more partial differential equations (PDEs). The Spalart-Allmaras model involves a PDE for the eddy viscosity. This is referred to as a one-equation model. Two equation models (where two additional PDEs are solved to get the eddy viscosity) are more commonly used in practice. Some of the two equation models are: $k-\epsilon$, $k-\omega$ and SST $k-\omega$ among others. These two equations are used to get a velocity scale and length scale of the turbulent flow from which the eddy viscosity is computed. Other models such as the Reynolds stress model have a PDE for each of the Reynolds stress component. In

all these methods, the additional PDEs have terms that remain unclosed. These are often modeled using various assumptions (e.g. gradient diffusion hypothesis).

In the context of particle-laden flow, the addition of particles affects the turbulent diffusivity. As discussed earlier in the section, particles can either augment or attenuate turbulence. This effect has to be modeled. Further, to include the effect of turbulent dispersion, we need models to get a random velocity component. In this section, RANS models for particle-laden flows that are currently in use are discussed and their ability to predict flows of interest is examined.

There are different approaches to model particle-laden flows. Each approach has certain limited range of applicability depending on parameters such as the St, the relative size of the particle with respect to a length scale of the flow (for instance, the Kolmogorov length scale) among others. There are several reviews [1, 59–62] that discuss various approaches commonly employed in numerical simulations of multiphase flows. These methods can be divided into two broad sections:

1. Eulerian-Eulerian approach.

2. Eulerian-Lagrangian approach.

2.8.1 Eulerian-Eulerian Approach

The Eulerian-Eulerian approach was first formulated for numerical computations by Spalding [63, 64]. In the Eulerian-Eulerian approach (also known as two-fluid approach), the dispersed and the carrier phase are assumed to be inter-penetrating fluid. The particulate phase are obtained by volume averaging over the computational cell. The averaging volume should be large enough so that the properties do not depend on the size of the averaging volume. Further, the averaged properties should have continuous spatial derivatives. This places a restraint on the minimum resolvable length scale. Conservation equations for mass and momentum are developed for the volume averaged particle properties. The interphase coupling is taken care of through source and/or sink terms in these equations.

If the particle size is smaller than the Kolmogorov length scale, η, the particles can be treated as point sources. However, if the particles are comparable to or larger than η, the contribution of particles to the dynamics of the turbulent flow should be included.

In two-fluid approach, transport equations for the dispersed phase should be developed and corresponding transport properties should be defined. Elghobashi and Abou-Arab [65] used volume average equations to derive equations of mass and momentum transfer. They have also proposed constitutive equations based on gradient transport assumption. These equations have been used extensively in several works that adopt two-fluid approach. The transport properties for the particle phase are usually based on experimental works or empirical relations. In a later work, Rizk and Elghobashi [66] incorporated a semi-empirical correlation proposed by Picart *et al.* [67] to account for crossing trajectory effect.

If two-fluid models are used to compute wall-bounded flows, then the specification of the boundary condition for the dispersed phase at the wall poses a problem. For the dispersed phase continuity equation, if the wall absorbs the particles, then the bulk particle density at the wall cannot be specified as zero. If the particles collide with the wall elastically, then the normal gradient of the bulk particle density can be set to zero. Similarly in the particle momentum equation, the tangential velocity of the particles at the wall cannot be set to zero. Chung *et al.* [68] set the gradient of the particle velocity to be equal to the velocity gradient of the fluid at the wall. Ding *et al.* [69] introduced a slip velocity for the particles analogous to rarefied flows. Another approach is to use probability density function to describe the particle velocity and position and develop equations for its evolution.

2.8.2 Eulerian-Lagrangian Approach

The Eulerian-Lagrangian approach was proposed by Crowe *et al.* [70]. In this approach, the carrier phase is solved by Eulerian equations while the dispersed phase

is tracked by a Lagrangian approach. The particle is assumed to be smaller than the relevant fluid scale and is treated as a point (it does not occupy any volume). Equations of motion are solved to track the position, velocity and energy of the particles. The interphase-coupling is often achieved by employing semi-empirical relations.

Practical systems often have a large number of particles the tracking of which are beyond current computer capability. In order to resolve this issue, Lagrangian models identify a parcel of particles as a single computational particle with the same properties as the physical particles. There are two issues that merit discussion with regards to modeling of particle-laden flows: particle dispersion and turbulence modulation.

Particle Dispersion: In the Lagrangian approach, the force acting on the particle is used to obtain the velocity and position of the particle. The Basset-Boussinesq-Oseen (BBO) equation gives the unsteady force acting on the particle at low Re. Maxey and Riley [71] have derived the BBO equation from first principles for spherical particles at low Re. At higher Re, a correction is included in the drag force term and the equation is thus represented as (Ref. [1])

$$\begin{aligned}\mathbf{F_p} = 3\pi\mu d(\mathbf{u}-\mathbf{v_p})\phi(Re) + m_f\frac{D\mathbf{u}}{Dt} + \frac{m_f}{2}\left(\frac{D\mathbf{u}}{Dt} - \frac{d\mathbf{v_p}}{dt}\right) \\ +\frac{3}{2}d^2\sqrt{\pi\rho_f\mu}\int_{-\infty}^{t} K(t,\tau)\frac{d(\mathbf{u}-\mathbf{v_p})}{dt}d\tau + (m_p - mf)g,\end{aligned} \tag{2.14}$$

where m_p and m_f denote the mass of the particle and the mass of the displaced fluid, $\mathbf{u}$ and $\mathbf{v_p}$ represent the fluid and particle velocity, $K(t,\tau)$ is a kernel that weighs the past history of relative acceleration and g is the acceleration due to gravity. The terms on the right hand side are as follows: the unsteady drag, the pressure gradient, the virtual mass, the Basset force and gravity. The function $\phi(Re)$ represents a correction for the drag law at high Re and is given by Schiller and Nauman (See Ref. [72]) as:

$$\phi(Re) = 1 + 0.15Re^{0.687}. \tag{2.15}$$

When the particle to fluid density ratio is high ($\rho_p/\rho_f \sim 10^3$), the virtual mass force and the Basset force become negligible. This force is used to update the velocity of the particle as:

$$\mathbf{F_p} = m_f \frac{d\mathbf{v_p}}{dt}. \tag{2.16}$$

Based on this velocity, the trajectory of the particle is computed as follows:

$$\mathbf{v_p} = m_f \frac{d\mathbf{x_p}}{dt}. \tag{2.17}$$

Solving the RANS equations gives the mean velocity. To account for the dispersion of the particles due to the turbulent eddies, a model is required. The model should be able to capture effects such as preferential concentration and "crossing trajectories".

Several models have been proposed to account for the effect of turbulent fluctuations on the particle motion. Yuu *et al.* [73] assumed that the particle would remain in an eddy until the eddy lifetime after which it would encounter another eddy. The fluid velocity used in the particle's equation of motion was taken to be the sum of the mean velocity (from RANS) and a fluctuating component chosen from a Gaussian distribution with zero mean and standard deviation σ given by:

$$\sigma = (2k/\epsilon)^{2/3}, \tag{2.18}$$

where k and ϵ are the turbulent kinetic energy and dissipation rate, respectively. This method assumes that the turbulence is locally isotropic. Dukowicz [74], in his method, displaces the particle by a random distance in each time step. The distance is selected from a Gaussian pdf that corresponds to a particle dispersion coefficient. These effects however are not capable of predicting the "crossing trajectories" effect.

Gosman and Ioannides [75] proposed a stochastic model similar to that of Yuu *et al.* [73]. However, the particle can move outside an eddy before the eddy decays. This is done by by using the fluctuating velocity from the Gaussian pdf until the particle crosses the eddy (size of the integral length scale) or until the turnover time of the

eddy after which a new component is chosen. This model captures the "crossing trajectories" effect. Owing to its simplicity and robustness, this is commonly used in many commercial codes [64].

Turbulence Modulation: Another effect that needs to be modeled is turbulence modulation. In order to include turbulence modulation in the computations, an extra source term needs to be included in the k and ϵ equations. The source term in the k equation can be related to the drag force on the particle, $\mathbf{F_p}$, and the fluctuating component of the gas phase velocity $\mathbf{u}'$. The source term for inclusion of turbulence modulation in the k equation is given by the following expression [76]:

$$S_k = \sum \mathbf{F_p} \cdot \mathbf{u}'. \tag{2.19}$$

The summation is done over all the particles in the computational cell. The source term in the ϵ equation is given by [76]

$$S_{\epsilon 4} = C_{\epsilon 4} S_k \frac{\epsilon}{k}, \tag{2.20}$$

where $C_{\epsilon 4}$ is an empirical constant. Inclusion of turbulence modulation introduces an empirical constant $C_{\epsilon 4}$ that needs to be determined. The dependence of the solution as well as the effects of this model are important considerations. The accuracy of the models employed has an impact on the results.

2.9 Large Eddy Simulation of Particle-Laden Flows

Large Eddy Simulation (LES) refers to a computational technique where all the large energy containing eddies are resolved. The effect of the small eddies is accounted for by a Subgrid Scale (SGS) model. The governing equations are obtained by filtering the Navier-Stokes equations. The filtered equations have subgrid stresses which denote the effect of the smaller length scales. This is analogous to the Reynolds stresses encountered in Reynolds Averaged Navier Stokes equations. The subgrid stresses are

related to the strain rate tensor through the eddy viscosity (Boussinesq approximation). The eddy viscosity itself should be modeled and is important in the context of an LES computation. The eddy viscosity is usually calculated by the Smagorinsky model as,

$$\nu_{SGS} = (C_s\Delta)^2|\sqrt{2S_{ij}S_{ij}}|, \tag{2.21}$$

where Δ is the filter width (a measure of the grid size), S_{ij} is the strain rate tensor and C_s is the Smagorinsky constant with value between 0.1 and 0.2. In LES of particle-laden flows, if the particle is smaller than the grid size, then the point particle approach can be adopted. The particles are solved in a Lagrangian framework. The force acting on the particle is found from the Basset-Boussinesq-Oseen equation and is used to update the velocity and position of the particle. The momentum change of the particle appears as a sink term in the momentum equation for the fluid, thus accounting for the interphase coupling.

Wang and Squires [77] have carried out LES studies of particle-laden turbulent channel flow. They report that the LES is able to capture effects such as preferential concentration and increased particle fluctuations in the streamwise direction reasonably well. Yamamoto *et al.* [78] have done LES simulations of turbulent gas-particle flow in a vertical channel flow. They have considered the effect of interparticle collisions in their work. The shape and scale of particle concentrations are in good agreement with the measurements. The computed turbulence attenuation by particles agrees well with the experimental data for low St but begins to deviate for high St.

Apte *et al.* [79] have performed LES of particle-laden swirling flow in a coaxial-jet combustor and have compared their results to measurements of Sommerfeld and Qiu [80]. They report that the LES results are significantly more accurate than the RANS predictions of the same problem [81]. Moin and Apte [82] have extended this work to do a multiscale, multiphysics turbulent reacting flow simulation in a real gas-turbine combustor to assess the predictive capabilities of the solver.

In the above works, there are two important issues that are not considered:

1. Modification of unresolved (subgrid) turbulence by the particle motion

2. Effect of the unresolved turbulent scales on the particle dynamics

Kuerten and Vreman [83] use an inverse filtering model to account for the subgrid effects in the particle motion. This method is referred to as the Approximate Deconvolution Method (ADM). They show that with this model, the turbophoresis effect is better resolved in LES computations and results agree well with DNS data. Shotorban and Mashayek [84] have proposed a stochastic model for the particle motion in the LES of a turbulent flow. They have carried out cases of particle-laden isotropic turbulence. They conclude that for particles with small time constants, they achieved good agreements with the DNS results. They report that for particles with large time constants, the model needs to be adjusted. Bini and Jones [85] have introduced the concept of LES filtered probability density function (PDF) approach to provide a probabilistic description of two-phase flows in the context of LES. Models for closing the unknown terms in the transport equation for the joint filtered PDF for the dispersed phase have been proposed in their work. A subgrid dispersion model that accounts for the effects of the unresolved turbulent eddies on the particle is used. They have used this method to study a particle-laden mixing layer and have compared their results with the measurements of Lazaro and Lasheras [86–88]. They report that a good agreement is achieved between the LES and experimental results if the subgrid dispersion model is chosen such that is has a functional dependence on the particle response time.

Cernick *et al.* [89] have compared the SGS models of Fukagata *et al.* [90] (ADM), Shotorban and Mashayek [84] and Berrouk *et al.* [91] for a particle-laden decaying homogeneous turbulence. They report that the ADM models improve results but is capable of recovering only a portion of the SGS turbulent kinetic energy. The stochastic methods recover sufficient SGS energy, but show a large range of results depending on the St and the filter size. In general, the stochastic models perform well at low St, but are not able to predict preferential concentration.

Fox [92] presents a comprehensive review of various LES models that exists for multiphase flows. From the above discussions, it is quite clear that there are still modifications to be made in the SGS models. This requires information from fully resolved DNS computations to see what the SGS models are missing in their current closure approximations and determine how best to improve them.

2.10 Summary and Contribution of this Work

Wall-bounded particle-laden flows have several interesting features. While considerable data is available from prior studies, there are several unanswered questions such as the mechanisms driving particle-wall interaction and particle-turbulence interaction. As discussed earlier, the observation of Lau and Nathan [11] raises a question: *What causes the migration of particles toward the wall in the case of lower St* ($<< 1$) *and toward the axis for higher St* ($>> 1$) *and uniform distribution at intermediate St* (~ 1)*?* This work aims to answer this by carrying out Direct Numerical Simulations (DNS). From the literature review, it can be seen that most DNS studies have adopted the point particle approach. While this enables the simulation of a large number of particles, it is dependent on the semi-empirical drag force relations that are used. Furthermore, the particles are implicitly assumed to be smaller than the Kolmogorov length scale. In this study, the particles will be fully resolved and the hydrodynamic force acting on the particle will be computed directly without any models. In order to carry out the DNS studies, the lattice Boltzmann method (LBM) is adopted.

3. FORMULATION OF THE LATTICE-BOLTZMANN METHOD

3.1 Introduction

In order to carry out the particle-resolved Direct Numerical Simulations (DNS), the Lattice-Boltzmann Method (LBM) will be used. The LBM solves the Lattice Boltzmann Equation (LBE) which can be considered similar to a finite difference discretization of the Boltzmann equation. Historically, the method developed from Lattice Gas Automata (LGA) where fluid particles move along lattices and collide with each other. There are specified collision rules according to which the particle velocity changes after collision. These rules are chosen so that the macroscopic physics is reproduced correctly. In this chapter, a basic introduction to the LBM is presented and its connection to the Boltzmann equation as well as to the Navier-Stokes equation is shown.

The basic concept of the LBM is introduced in Section 3.2. A rigorous derivation of the LBM from the continuous Boltzmann equation is presented in Section 3.3. The LBM reproduces the Navier-Stokes equation in the continuum limit. The derivation of the Navier-Stokes equation from the LBM is given in Section 3.4. In Section 3.5, the numerical aspects of the LBM are discussed. The common techniques to handle boundary conditions are presented in Section 3.6. The implementation of a moving particle in the LBM framework is described in Section 3.7. In Section 3.8, relevant works that have used the LBM to study particle-laden flow are reviewed and the contribution of this work is presented.

3.2 The Lattice-Boltzmann Method

The Lattice-Boltzmann Method (LBM) is a relatively new computational technique for simulating fluid flow. It is based on the following idea: The dynamics of physical processes at larger length and time scales are a result of the collective behavior of molecular interactions (free flight of molecules and collision); however, the macroscopic details are insensitive to the underlying microscopic details [93]. The LBM was developed as an alternative method to LGA to overcome certain drawbacks associated with it. The LGA was introduced by Frisch *et al.* [94] and Wolfram [95] to simulate fluid behavior as described by the Navier-Stokes equations (NSE).

In LGA, individual particles move on a lattice from one node to another. When two or more particles arrive at the same lattice node, they collide with each other. The outcome of the collision is determined by a set of rules. The lattices are identified by the following naming convention: DdQq where 'd' specifies the dimension of the lattice and 'q' specifies the number of discrete velocities. For instance, a D2Q9 lattice has two spatial dimensions and 9 discrete velocity directions. Lattices must be built in such a way that the Navier-Stokes equations can be recovered by a multi-scale expansion. This places two constraints on the lattice: *i)* The lattice should be symmetric *ii)* It should have more than four velocity directions in addition to a possible zero velocity vector [94]. Figure 3.1 shows a D3Q19 lattice that is commonly employed in the LBM.

At a lattice node, a particle can either be present or absent and hence they can be represented by Boolean numbers (0s and 1s). This eliminates the issue of rounding error that is a big issue especially in turbulence simulations. However, the results from LGA simulations show large variations and complicated averaging schemes should be used to interpret the results. Another problem is that the maximum number of particles that can be simulated is less than the total number of lattice nodes available. This leads to a large computational time and necessitates the use of a large grid. Moreover, the LGA lacks Galilean invariance.

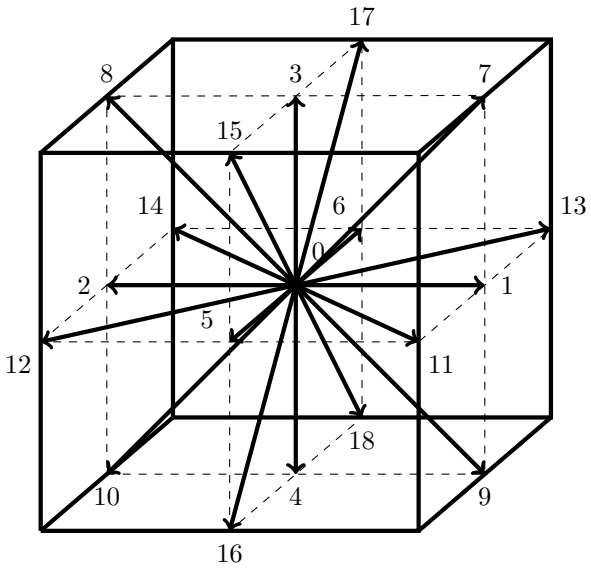

Figure 3.1: Lattices for LBM and LGA.

The LBM was introduced by McNamara and Zanetti [96] to overcome these drawbacks of the LGA. The LBM, instead of using particles, uses single particle distribution function that stream from one lattice node to another. The distribution functions are based on the Maxwell-Botlzmann statistics. A number of modifications have been proposed for the collision operator. Higuera and Jiménez [97] linearized the collision operator by assuming that the actual distribution is close to the Maxwellian equilibrium distribution. Higuera *et al.* [98] proposed a collision operator that is linearly stable. A single relaxation time model, also known as the Bhatnagar-Gross-Krook (BGK) model [99], was proposed by Chen *et al.* [100] and Qian *et al.* [101]. The LBM can thus be viewed as an extension of the LGA where the particle distribution functions stream and collide according to a collision operator.

Alternatively, the LBM can be connected to the Boltzmann equation. He and Luo [102,103] showed that the LBE can be derived from the Boltzmann equation when the continuous velocity space is simplified into a discrete velocity space. This enabled the application of many ideas pertinent to the Boltzmann equation to the LBE. There has been significant development in the LBM and it has found applications in a wide range of flows. Refs [104–109] can be consulted for a detailed review of the development and applications of the LBM.

3.3 From the Boltzmann Equation to the LBE

The Boltzmann equation describes the evolution of a single particle distribution function which is defined as the probability of finding a molecule/atom (referred to as particles hereafter in this section) between $\boldsymbol{x}$ and $\boldsymbol{x} + \boldsymbol{dx}$ with velocity between $\boldsymbol{c}$ and $\boldsymbol{c} + \boldsymbol{dc}$ per unit volume per unit velocity cubed. In other words, the number of particles, dN, that are between $\boldsymbol{x}$ and $\boldsymbol{x} + \boldsymbol{dx}$ with velocity between $\boldsymbol{c}$ and $\boldsymbol{c} + \boldsymbol{dc}$ can be expressed in terms of the distribution function as follows:

$$dN = nf(\boldsymbol{x}, \boldsymbol{c})\boldsymbol{dx}\boldsymbol{dc}, \tag{3.1}$$

where n is the number of particles per unit volume (the number density) at $\boldsymbol{x}$. The 6 dimensional volume element $\boldsymbol{dxdc}$ is known as phase space. The distribution function is a function of time and its evolution as given by the Boltzmann equation is

$$\frac{Df}{Dt} = \frac{\partial f}{\partial t} + \boldsymbol{c} \cdot \boldsymbol{\nabla}_{\boldsymbol{x}} f + \boldsymbol{F} \cdot \boldsymbol{\nabla}_{\boldsymbol{c}} f = C_{12}, \tag{3.2}$$

where $\boldsymbol{F}$ represents external forces, $\boldsymbol{\nabla}_{\boldsymbol{x}}$ and $\boldsymbol{\nabla}_{\boldsymbol{c}}$ represent the gradient in the physical and velocity space, respectively, and C_{12} represents the effect of two particle collisions. It is assumed that the gas is dilute and hence only two particle collisions are important. In the absence of external forces, the Boltzmann equation reduces to

$$\frac{\partial f}{\partial t} + \boldsymbol{c} \cdot \boldsymbol{\nabla}_{\boldsymbol{x}} f = C_{12}. \tag{3.3}$$

The collision operator that Boltzmann proposed is a integral operator making the equation a complex integro-differential equation which is difficult to solve for practical cases. If the actual distribution is close to the Maxwellian equilibrium distribution f^{eq}, then the collision operator can be expressed by the Bhatnagar-Gross-Krook (BGK) operator which is given as

$$C_{12} = -\frac{1}{\lambda}(f - f^{eq}), \tag{3.4}$$

where λ is a characteristic time over which the distribution function relaxes to its equilibrium state. Thus Eq. (3.3) becomes

$$\frac{\partial f}{\partial t} + \boldsymbol{c} \cdot \boldsymbol{\nabla}_{\boldsymbol{x}} f = -\frac{1}{\lambda}(f - f^{eq}). \tag{3.5}$$

The Maxwellian equilibrium distribution function is given by

$$f^{eq} = \frac{\rho}{(2\pi RT)^{D/2}} exp\left[\frac{-(\boldsymbol{c} - \boldsymbol{u})^2}{2RT}\right], \tag{3.6}$$

where R is the ideal gas constant, D is the number of spatial dimensions and ρ, $\boldsymbol{u}$ and T are the density, bulk velocity and temperature, respectively. For an isothermal

fluid, the density and the velocity can be obtained as zeorth-order and first-order moments of the distribution functions, respectively, i.e.

$$\rho = m \int f \boldsymbol{dc} = m \int f^{eq} \boldsymbol{dc}, \tag{3.7}$$

$$\rho \boldsymbol{u} = m \int f \boldsymbol{c} \boldsymbol{dc} = m \int f^{eq} \boldsymbol{c} \boldsymbol{dc}, \tag{3.8}$$

where m is the mass of the particle (a molecule/atom). Since m is just a constant in cases with a single fluid, it is dropped so that a form of a non-dimensional ρ and $\boldsymbol{u}$ can be obtained as

$$\rho = \int f \boldsymbol{dc} = \int f^{eq} \boldsymbol{dc}, \tag{3.9}$$

$$\rho \boldsymbol{u} = \int f \boldsymbol{c} \boldsymbol{dc} = \int f^{eq} \boldsymbol{c} \boldsymbol{dc}. \tag{3.10}$$

3.3.1 Time discretization

Equation (3.5) can be integrated over a time step δ_t to obtain

$$f(\boldsymbol{x} + \boldsymbol{c}\delta_t, \boldsymbol{c}, t + \delta_t) = \frac{1}{\lambda} e^{-\delta_t/\lambda} \int_0^{\delta_t} e^{t'/\lambda} f^{eq}(\boldsymbol{x} + \boldsymbol{c}t', \boldsymbol{c}, t + t') dt' + e^{-\delta_t/\lambda} f(\boldsymbol{x}, \boldsymbol{c}, t). \tag{3.11}$$

Assuming δ_t is small and f^{eq} is smooth locally, a linear approximation can be made as

$$f^{eq}(\boldsymbol{x} + \boldsymbol{c}t', \boldsymbol{c}, t + t') = \left(1 - \frac{t'}{\delta_t}\right) f^{eq}(\boldsymbol{x}, \boldsymbol{c}, t) + \frac{t'}{\delta_t} f^{eq}(\boldsymbol{x} + \boldsymbol{c}\delta_t, \boldsymbol{c}, t + \delta_t) + O(\delta_t^2), \tag{3.12}$$

where $0 \leq t' \leq \delta_t$. Now consider the first term on the right hand side of Eq. (3.11). $f^{eq}(\boldsymbol{x} + \boldsymbol{c}t', \boldsymbol{c}, t + t')$ can be replaced by the expression in Eq. (3.12) after neglecting terms of order $O(\delta_t^2)$ and higher. Thus the integral in Eq. (3.11) simplifies as follows:

$$\begin{aligned}\int_0^{\delta_t} e^{t'/\lambda} f^{eq}(\boldsymbol{x} + \boldsymbol{c}t', \boldsymbol{c}, t + t')dt' = \int_0^{\delta_t} e^{t'/\lambda} \left(1 - \frac{t'}{\delta_t}\right) f^{eq}(\boldsymbol{x}, \boldsymbol{c}, t)dt' + \\ \int_0^{\delta_t} e^{t'/\lambda} \frac{t'}{\delta_t} f^{eq}(\boldsymbol{x} + \boldsymbol{c}\delta_t, \boldsymbol{c}, t + \delta_t)dt'.\end{aligned} \tag{3.13}$$

Since $f^{eq}(\boldsymbol{x}, \boldsymbol{c}, t)$ and $f^{eq}(\boldsymbol{x} + \boldsymbol{c}\delta_t, \boldsymbol{c}, t + \delta_t)$ have no functional dependence on t' they can be moved outside the integral. Thus Eq. (3.13) reduces to

$$\begin{aligned}\int_0^{\delta_t} e^{t'/\lambda} f^{eq}(\boldsymbol{x} + \boldsymbol{c}t', \boldsymbol{c}, t + t')dt' = f^{eq}(\boldsymbol{x}, \boldsymbol{c}, t) \int_0^{\delta_t} \left(e^{t'/\lambda} - e^{t'/\lambda} \frac{t'}{\delta_t}\right) dt' + \\ f^{eq}(\boldsymbol{x} + \boldsymbol{c}\delta_t, \boldsymbol{c}, t + \delta_t) \int_0^{\delta_t} e^{t'/\lambda} \frac{t'}{\delta_t} dt',\end{aligned} \tag{3.14}$$

which can be further simplified as:

$$\begin{aligned}\int_0^{\delta_t} e^{t'/\lambda} f^{eq}(\boldsymbol{x} + \boldsymbol{c}t', \boldsymbol{c}, t + t')dt' = f^{eq}(\boldsymbol{x}, \boldsymbol{c}, t) \int_0^{\delta_t} e^{t'/\lambda} dt' + \\ \frac{1}{\delta_t} \left[f^{eq}(\boldsymbol{x} + \boldsymbol{c}\delta_t, \boldsymbol{c}, t + \delta_t) - f^{eq}(\boldsymbol{x}, \boldsymbol{c}, t)\right] \int_0^{\delta_t} t' e^{t'/\lambda} dt'.\end{aligned} \tag{3.15}$$

Now

$$\int_0^{\delta_t} e^{t'/\lambda} dt' = \lambda e^{\delta_t/\lambda} \left(1 - e^{-\delta_t/\lambda}\right), \tag{3.16}$$

and

$$\int_0^{\delta_t} t' e^{t'/\lambda} dt' = \lambda e^{\delta_t/\lambda} \delta_t \left[1 + \frac{\lambda}{\delta_t} \left(1 - e^{-\delta_t/\lambda}\right)\right]. \tag{3.17}$$

A Taylor expansion of $e^{-\delta_t/\lambda}$ gives

$$e^{-\delta_t/\lambda} = 1 - \frac{\delta_t}{\lambda} + O(\delta_t^2). \tag{3.18}$$

Neglecting order $O(\delta_t^2)$ and higher and substituting into Eq. (3.16), we get

$$\int_0^{\delta_t} e^{t'/\lambda} dt' = \lambda e^{\delta_t/\lambda} \left[1 - \left(1 - \frac{\delta_t}{\lambda}\right)\right], \tag{3.19}$$

$$\int_0^{\delta_t} e^{t'/\lambda} dt' = \delta_t e^{\delta_t/\lambda}. \tag{3.20}$$

On similar substitution of $e^{-\delta_t}/\lambda$ into Eq. (3.17), we get

$$\int_0^{\delta_t} t' e^{t'/\lambda} dt' = \lambda e^{\delta_t/\lambda} \delta_t \left[1 + \frac{\lambda}{\delta_t}\left(1 - \left(1 - \frac{\delta_t}{\lambda}\right)\right)\right]. \tag{3.21}$$

All the terms in the right hand side cancel out yielding

$$\int_0^{\delta_t} t' e^{t'/\lambda} dt' = 0. \tag{3.22}$$

Substituting Eqs. (3.20) and (3.22) into Eq. (3.15), we get

$$\int_0^{\delta_t} e^{t'/\lambda} f^{eq}(\boldsymbol{x} + \boldsymbol{c}t', \boldsymbol{c}, t + t') dt' = f^{eq}(\boldsymbol{x}, \boldsymbol{c}, t) \delta_t e^{\delta_t/\lambda}. \tag{3.23}$$

Substituting Eq. (3.23) into Eq. (3.11)

$$f(\boldsymbol{x} + \boldsymbol{c}\delta_t, \boldsymbol{c}, t + \delta_t) = \frac{\delta_t}{\lambda} f^{eq}(\boldsymbol{x}, \boldsymbol{c}, t) + e^{-\delta_t/\lambda} f(\boldsymbol{x}, \boldsymbol{c}, t). \tag{3.24}$$

Substitute the Taylor expansion of $e^{-\delta_t/\lambda}$ (Eq. (3.18) to get

$$f(\boldsymbol{x} + \boldsymbol{c}\delta_t, \boldsymbol{c}, t + \delta_t) = \frac{\delta_t}{\lambda} f^{eq}(\boldsymbol{x}, \boldsymbol{c}, t) + \left(1 - \frac{\delta_t}{\lambda}\right) f(\boldsymbol{x}, \boldsymbol{c}, t), \tag{3.25}$$

which can be simplified as

$$f(\boldsymbol{x} + \boldsymbol{c}\delta_t, \boldsymbol{c}, t + \delta_t) - f(\boldsymbol{x}, \boldsymbol{c}, t) = -\frac{\delta_t}{\lambda} \left[f(\boldsymbol{x}, \boldsymbol{c}, t) - f^{eq}(\boldsymbol{x}, \boldsymbol{c}, t)\right], \tag{3.26}$$

or

$$f(\boldsymbol{x}+\boldsymbol{c}\delta_t,\boldsymbol{c},t+\delta_t)-f(\boldsymbol{x},\boldsymbol{c},t)=-\frac{1}{\tau}\left[f(\boldsymbol{x},\boldsymbol{c},t)-f^{eq}(\boldsymbol{x},\boldsymbol{c},t)\right], \tag{3.27}$$

where $\tau=\dfrac{\lambda}{\delta_t}$ is the non-dimensional relaxation time. Equation (3.27) is the time discrete version of the Boltzmann equation and is first order accurate in time. $f^{eq}(\boldsymbol{x},\boldsymbol{c},t)$ is shown as an explicit function of time, but this dependence comes from its dependence on the hydrodynamic variables ρ and $\boldsymbol{u}$. Moreover, Eq. (3.27) has an infinite number of velocity directions. In order to simplify the problem, it should be discretized over a finite set of velocity directions.

3.3.2 Velocity Space Discretization

The velocity space should now be discretized to enable us to evaluate moments of the distribution function. For a discrete velocity space, the moments can be evaluated by quadratures, i.e.

$$\int \psi(\boldsymbol{c})f(\boldsymbol{x},\boldsymbol{c},t)\boldsymbol{dc}=\sum_{\alpha}W_\alpha\psi(\boldsymbol{c})f(\boldsymbol{x},\boldsymbol{c_\alpha},t), \tag{3.28}$$

where $\psi(\boldsymbol{c})$ is a polynomial of $\boldsymbol{c}$, W_α is the weighting factor for the discrete velocity $\boldsymbol{c_\alpha}$. Thus the hydrodynamic moments can be calculated as

$$\rho=\sum_{\alpha}f_\alpha=\sum_{\alpha}f_\alpha^{eq}, \tag{3.29}$$

$$\rho\boldsymbol{u}=\sum_{\alpha}\boldsymbol{c_\alpha}f_\alpha=\sum_{\alpha}\boldsymbol{c_\alpha}f_\alpha^{eq}, \tag{3.30}$$

where

$$f_\alpha\equiv f_\alpha(\boldsymbol{x},t)\equiv W_\alpha f(\boldsymbol{x},\boldsymbol{c_\alpha},t), \tag{3.31}$$

$$f_\alpha^{eq}\equiv f_\alpha^{eq}(\boldsymbol{x},t)\equiv W_\alpha f^{eq}(\boldsymbol{x},\boldsymbol{c_\alpha},t). \tag{3.32}$$

There are two factors that should be taken into consideration in the discretization of the velocity space:

- Discretization of the velocity space should be coupled to the physical space so that a lattice structure is obtained.
- The quadrature of the velocity space should retain the symmetry of the stress tensor as required by the Navier-Stokes equations.

In order to arrive at a discrete velocity space, the Maxwellian equilibrium distribution function, Eq. (3.6), is expanded by a Taylor series in $\boldsymbol{u}$.

$$f^{eq} = \frac{\rho}{(2\pi RT)^{D/2}} exp\left[\frac{-(\boldsymbol{c}-\boldsymbol{u})^2}{2RT}\right], \tag{3.33}$$

$$f^{eq} = \frac{\rho}{(2\pi RT)^{D/2}} exp\left[\frac{-\boldsymbol{c}^2 + 2(\boldsymbol{c}\cdot\boldsymbol{u}) - \boldsymbol{u}^2}{2RT}\right], \tag{3.34}$$

$$f^{eq} = \frac{\rho}{(2\pi RT)^{D/2}} exp\left(\frac{-\boldsymbol{c}^2}{2RT}\right) exp\left[\frac{(\boldsymbol{c}\cdot\boldsymbol{u})}{RT} - \frac{\boldsymbol{u}^2}{2RT}\right]. \tag{3.35}$$

Recalling that the Taylor expansion of e^x is given by

$$e^x = 1 + \frac{x^1}{1!} + \frac{x^2}{2!} + O(x^3), \tag{3.36}$$

Eq. (3.35) reduces to

$$f^{eq} = \frac{\rho}{(2\pi RT)^{D/2}} exp\left(\frac{-\boldsymbol{c}^2}{2RT}\right)\left[1 + \frac{(\boldsymbol{c}\cdot\boldsymbol{u})}{RT} - \frac{\boldsymbol{u}^2}{2RT} + \frac{(\boldsymbol{c}\cdot\boldsymbol{u})^2}{2(RT)^2}\right] + O\left(\left[\frac{\boldsymbol{c}\cdot\boldsymbol{u}}{RT}\right]^3\right). \tag{3.37}$$

In order for this expansion to be valid, the term $\left[\frac{\boldsymbol{c}\cdot\boldsymbol{u}}{RT}\right]$ should be small. The particle speed c is of the order of the speed of sound c_s which is given as

$$c_s = C\sqrt{RT}, \tag{3.38}$$

where C is a constant and is equal to the square root of the specific heat ratio γ. The value of C is close to 1 and is taken to be 1 in the LBM framework. Thus

$$c_s = \sqrt{RT}. \tag{3.39}$$

Thus the magnitude of $\boldsymbol{u}$ should be small compared to the speed of sound, i.e. the Mach number should be low. This is referred to as the low-Mach number approximation. The next step is to derive an expression for the discretized equilibrium function f_α^{eq} with known weights that would yield the hydrodynamic variables. Recall that the evaluation of moments using f^{eq} involve an integral of the form

$$I = \int \psi(\boldsymbol{c}) f^{eq}(\boldsymbol{x}, \boldsymbol{c}, t) \boldsymbol{dc}. \tag{3.40}$$

Neglecting higher order terms in Eq. (3.37) and substituting it in Eq. (3.40), we get

$$I = \frac{\rho}{(2\pi RT)^{D/2}} \int \psi(\boldsymbol{c}) exp\left(\frac{-\boldsymbol{c}^2}{2RT}\right)\left[1 + \frac{(\boldsymbol{c}\cdot\boldsymbol{u})}{RT} - \frac{\boldsymbol{u}^2}{2RT} + \frac{(\boldsymbol{c}\cdot\boldsymbol{u})^2}{2(RT)^2}\right]\boldsymbol{dc}. \tag{3.41}$$

The integral on the right hand side is over a vector element $\boldsymbol{dc}$. For a two-dimensional case, this requires a double integration. Let us employ a Cartesian coordinate system where $\psi(\boldsymbol{c})$ can be represented as

$$\psi_{m,n}(\boldsymbol{c}) = c_x^m c_y^n, \tag{3.42}$$

where c_x and c_y are the Cartesian components of the particle velocity $\boldsymbol{c}$. If u_x and u_y are the components of the macroscopic velocity $\boldsymbol{u}$, then f^{eq} can be expressed as

$$\begin{aligned} f^{eq} = \frac{\rho}{(2\pi RT)^{D/2}} exp\left(\frac{-(c_x^2 + c_y^2)}{2RT}\right) \times \\ \left[1 + \frac{(c_x u_x + c_y u_y)}{RT} - \frac{(u_x^2 + u_y^2)}{2RT} + \frac{(c_x u_x + c_y u_y)^2}{2(RT)^2}\right]. \end{aligned} \tag{3.43}$$

Thus

$$\psi_{m,n}(\boldsymbol{c})f^{eq} = \frac{\rho}{(2\pi RT)^{D/2}} exp\left(\frac{-(c_x^2+c_y^2)}{2RT}\right)\times \left[\begin{array}{l} c_x^m c_y^n + \frac{(c_x^{m+1}c_y^n u_x + c_x^m c_y^{n+1}u_y)}{RT} - \\ \frac{(u_x^2+u_y^2)c_x^m c_y^n}{2RT} + \\ \frac{(c_x^{m+2}c_y^n u_x^2 + 2c_x^{m+1}c_y^{n+1}u_x u_y + c_x^m c_y^{n+2}u_y^2)}{2(RT)^2} \end{array}\right] \tag{3.44}$$

With $\boldsymbol{dc} = dc_x dc_y$, Eq. (3.41) can be written as

$$I = \int_{-\infty}^{\infty}\int_{-\infty}^{\infty} \frac{\rho}{(2\pi RT)} exp\left(\frac{-(c_x^2+c_y^2)}{2RT}\right)\times \left[\begin{array}{l} c_x^m c_y^n\left(1-\frac{\boldsymbol{u}^2}{2RT}\right) + \frac{(c_x^{m+1}c_y^n u_x + c_x^m c_y^{n+1}u_y)}{RT} + \\ \frac{(c_x^{m+2}c_y^n u_x^2 + 2c_x^{m+1}c_y^{n+1}u_x u_y + c_x^m c_y^{n+2}u_y^2)}{2(RT)^2} \end{array}\right] dc_x dc_y. \tag{3.45}$$

Let

$$\alpha = \frac{c}{\sqrt{2RT}}, \tag{3.46}$$

$$d\alpha = \frac{dc}{\sqrt{2RT}}, \tag{3.47}$$

$$I_s = \int_{-\infty}^{\infty} e^{-\alpha^2}\alpha^s d\alpha. \tag{3.48}$$

Thus Eq. (3.45) can be expressed as

$$I = \frac{\rho}{\pi}\left(\sqrt{2RT}\right)^{m+n} \times \left[\begin{array}{l} I_m I_n\left(1-\frac{\boldsymbol{u}^2}{2RT}\right) + \frac{2(I_{m+1}I_n u_x + I_m I_{n+1}u_y)}{\sqrt{2RT}} + \\ \frac{(I_{m+2}I_n u_x^2 + 2I_{m+1}I_{n+1}u_x u_y + I_m I_{n+2}u_y^2)}{RT} \end{array}\right] \tag{3.49}$$

The evaluation of this integral requires the evaluation of the integral I_s. To do this so that the hydrodynamic variables are recovered exactly, He and Luo [102, 103] have suggested to use the 3^{rd} order Gauss-Hermite quadrature formula. Thus,

$$I_s = \sum_{k=1}^{3} w_k \alpha_k^s. \tag{3.50}$$

The Gauss-Hermite quadrature weighting coefficients w_k corresponding to the abscissa α_k needs to be determined. This is given by the roots of the third order Hermite polynomial. The Hermite polynomial of order 's', $H_s(x)$, is given as

$$H_s(x) = (-1)^s e^{x^2} \frac{d^s}{dx^s} e^{-x^2}, s = 0, 1, 2, .. \tag{3.51}$$

Thus the third order Hermite Polynomial is

$$H_3(x) = -e^{x^2} \frac{d^3}{dx^3} e^{-x^2}. \tag{3.52}$$

The quadrature abscissas are given as the roots of the equation $H_3(\alpha) = 0$, i.e.,

$$\alpha(2\alpha^2 - 3) = 0, \tag{3.53}$$

which gives,

$$\alpha_1 = -\sqrt{\frac{3}{2}},\ \alpha_2 = 0,\ \alpha_3 = +\sqrt{\frac{3}{2}}. \tag{3.54}$$

The corresponding weights are given as [110],

$$w_k = \frac{2^{s+1} s! \sqrt{\pi}}{[H_{s+1}(\alpha_k)]^2}, \tag{3.55}$$

which gives

$$w_1 = \frac{1}{6}\sqrt{\pi},\ w_2 = \frac{2}{3}\sqrt{\pi},\ w_3 = \frac{1}{6}\sqrt{\pi}. \tag{3.56}$$

Now

$$I_m I_n = \left[\sum_{i=1}^{3} w_i \alpha_i^m\right]\left[\sum_{j=1}^{3} w_j \alpha_j^n\right] = \sum_{i,j=1}^{3} w_i w_j \alpha_i^m \alpha_j^n. \tag{3.57}$$

We know

$$\alpha_i^m \alpha_j^n = \frac{c_i^m c_j^n}{(\sqrt{2RT})^{m+n}}. \tag{3.58}$$

Define $\psi_{m,n}(\boldsymbol{\alpha}_{ij})$ as follows

$$\psi_{m,n}(\boldsymbol{\alpha}_{ij}) = \alpha_i^m \alpha_j^n. \tag{3.59}$$

Then,

$$\psi_{m,n}(\boldsymbol{\alpha}_{ij}) = \frac{\psi_{m,n}(\boldsymbol{c}_{ij})}{(\sqrt{2RT})^{m+n}}, \tag{3.60}$$

where $\psi_{m,n}(\boldsymbol{c}_{ij}) = c_i^m c_j^n$. Thus $I_m I_n$ can be expressed as

$$I_m I_n = \sum_{i,j=1}^{3} w_i w_j \frac{\psi_{m,n}(\boldsymbol{c}_{ij})}{(\sqrt{2RT})^{m+n}}. \tag{3.61}$$

The integral I in Eq. (3.49) simplifies to

$$\begin{aligned} I = &\sum_{i,j=1}^{3} \psi_{m,n}(\boldsymbol{c}_{ij}) \times \\ &\left(\frac{w_i w_j}{\pi}\rho\left[1 - \frac{\boldsymbol{u}^2}{2RT} + \frac{(c_i u_x + c_j u_y)}{RT} + \frac{(c_i u_x)^2 + 2c_i u_x c_j u_y + (c_j u_y)^2}{2(RT)^2}\right]\right), \end{aligned} \tag{3.62}$$

which can be simplified as

$$\begin{aligned} I = &\sum_{i,j=1}^{3} \psi_{m,n}(\boldsymbol{c}_{ij}) \times \\ &\left(\frac{w_i w_j}{\pi}\rho\left[1 - \frac{\boldsymbol{u}^2}{2RT} + \frac{(c_i u_x + c_j u_y)}{RT} + \frac{(c_i u_x + c_j u_y)^2}{2(RT)^2}\right]\right), \end{aligned} \tag{3.63}$$

finally yielding

$$I = \sum_{i,j=1}^{3} \psi_{m,n}(\boldsymbol{c}_{ij}) \left(\frac{w_i w_j}{\pi}\rho\left[1 + \frac{\boldsymbol{c}_{ij}\cdot\boldsymbol{u}}{RT} + \frac{(\boldsymbol{c}_{ij}\cdot\boldsymbol{u})^2}{2(RT)^2} - \frac{\boldsymbol{u}^2}{2RT}\right]\right), \tag{3.64}$$

where c_i and c_j (or alternatively c_x and c_y) are the Cartesian components of $\boldsymbol{c_{ij}}$. Comparing Eq. (3.41) with Eq. (3.64) and recognizing that the integral in the former equation is replaced by the Gauss-Hermite quadrature in the latter, we can arrive at an expression for the discretized equilibrium distribution function, f_{ij}^{eq} as,

$$f_{ij}^{eq} = \frac{w_i w_j}{\pi}\rho\left[1 + \frac{\boldsymbol{c}_{ij}\cdot\boldsymbol{u}}{RT} + \frac{(\boldsymbol{c}_{ij}\cdot\boldsymbol{u})^2}{2(RT)^2} - \frac{\boldsymbol{u}^2}{2RT}\right]. \tag{3.65}$$

A D2Q9 lattice that is commonly employed in two-dimensional LBM computations is shown in Fig. 3.2. This includes one velocity that corresponds to particles at rest. This is actually obtained from $\boldsymbol{c_{ij}}$ whose Cartesian components are abscissas of the Gauss-Hermite quadrature employed in the evaluation of moments of the distribution function ($\alpha_2 = 0$). Set $c^2 = 3RT$, so that the lattice can be represented as follows:

$$\boldsymbol{c}_\beta = \boldsymbol{c}_{ij} = \begin{cases} (0,0) & \beta = 0 \\ c(cos\theta_\beta, sin\theta_\beta) & \beta = 1,2,3,4 \\ \sqrt{2}c(cos\theta_\beta, sin\theta_\beta) & \beta = 5,6,7,8. \end{cases} \tag{3.66}$$

The discrete form of the equilibrium distribution function can now be written as

$$f_\beta^{eq} = f_{ij}^{eq} = w_\beta\,\rho\left[1 + \frac{3}{c^2}\boldsymbol{c}_{ij}\cdot\boldsymbol{u} + \frac{9}{2c^4}(\boldsymbol{c}_{ij}\cdot\boldsymbol{u})^2 - \frac{3}{2c^2}\boldsymbol{u}^2\right], \tag{3.67}$$

where w_β is given as

$$w_\beta = \frac{w_i w_j}{\pi}, \tag{3.68}$$

$$w_\beta = \begin{cases} 4/9 & \beta = 0 \\ 1/9 & \beta = 1,2,3,4 \\ 1/36 & \beta = 5,6,7,8. \end{cases} \tag{3.69}$$

Thus, the time discrete version of the Boltzmann equation given by Eq. (3.27)

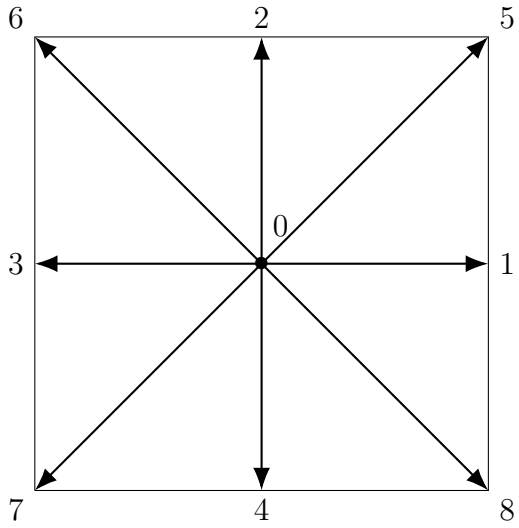

Figure 3.2: A D2Q9 lattice.

simplifies to

$$f_\beta(\boldsymbol{x} + \boldsymbol{c}_\beta \delta_t, t + \delta_t) - f_\beta(\boldsymbol{x}, t) = -\frac{1}{\tau}\left[f_\beta(\boldsymbol{x}, t) - f_\beta^{eq}(\boldsymbol{x}, t)\right]. \tag{3.70}$$

This equation is referred to as the Lattice Boltzmann Equation (LBE).

3.4 From the LBE to the Navier-Stokes Equations

The macroscopic behavior of the fluid as represented by the Navier-Stokes equations is obtained from the LBE by the Chapman-Enskog multi-scale expansion technique. This is an asymptotic expansion method to derive macroscopic equations from Boltzmann-type kinetic equations also yielding transport coefficients in terms of macroscopic parameters. In this section, a two-dimensional D2Q9 lattice is considered and the Chapman-Enskog expansion is done to recover the Navier-Stokes equations.

The Cartesian components of the particle velocities for a two-dimensional lattice with 8 velocity vectors and a null vector (D2Q9) are given by

$$\begin{aligned} e_{0,1} &= [0,0], \\ e_{1,i} &= c\left[cos\left(\frac{i-1}{2}\pi\right), sin\left(\frac{i-1}{2}\pi\right)\right],\ i=1,2,3,4, \\ e_{2,i} &= c\left[cos\left(\frac{i-1}{2}\pi+\frac{\pi}{4}\right), sin\left(\frac{i-1}{2}\pi+\frac{\pi}{4}\right)\right],\ i=1,2,3,4, \end{aligned} \tag{3.71}$$

where $c = \delta_x/\delta_t$. Here, δ_x is the lattice spacing and δ_t is the time taken for the particles to move from one lattice node to an adjacent node. In this derivation, we need the properties of the following tensor:

$$\sum_i (e_{\sigma i\alpha} e_{\sigma i\beta}). \tag{3.72}$$

Here σ corresponds to the type of the particle based on its speed and hence we have $\sigma \in \{0,1,2\}$. i represents the direction of the particle velocity for a given speed and hence $i \in \{1,2,3,4\}$. The Greek symbols $\alpha, \beta, ..$ represent the components pf the Cartesian coordinate. On account of the symmetry of the lattice, the tensors of odd orders are zero.

$$\sum_i e_{\sigma i\alpha} = 0, \tag{3.73}$$

$$\sum_i e_{\sigma i\alpha} e_{\sigma i\beta} e_{\sigma i\gamma} = 0, \tag{3.74}$$

$$\sum_i e_{\sigma i\alpha} e_{\sigma i\beta} e_{\sigma i\gamma} e_{\sigma i\theta} e_{\sigma i\eta} = 0. \tag{3.75}$$

Tensors of second and fourth order are given below following Wolf-Gladrow [111]:

$$\sum_i e_{\sigma i\alpha} e_{\sigma i\beta} = 2c^2 e_\sigma^2 \delta_{\alpha\beta}, \tag{3.76}$$

where

$$e_\sigma = \begin{cases} 1 & \sigma = 1, \\ \sqrt{2} & \sigma = 2, \end{cases} \tag{3.77}$$

and $\delta_{\alpha\beta}$ is the Kronecker delta function defined as

$$\delta_{\alpha\beta} = \begin{cases} 1 & \alpha = \beta, \\ 0 & \alpha \neq \beta. \end{cases} \tag{3.78}$$

Similarly

$$\sum_i e_{\sigma i\alpha} e_{\sigma i\beta} e_{\sigma i\gamma} e_{\sigma i\theta} = \begin{cases} 2c^4 \delta_{\alpha\beta\gamma\theta} & \sigma = 1, \\ 4c^4 \Delta_{\alpha\beta\gamma\theta} - 8c^4 \delta_{\alpha\beta\gamma\theta} & \sigma = 2, \end{cases} \tag{3.79}$$

where

$$\delta_{\alpha\beta\gamma\theta} = \begin{cases} 1 & \alpha = \beta = \gamma = \theta, \\ 0 & otherwise, \end{cases} \tag{3.80}$$

and

$$\Delta_{\alpha\beta\gamma\theta} = \delta_{\alpha\beta}\delta_{\gamma\theta} + \delta_{\alpha\gamma}\delta_{\beta\theta} + \delta_{\alpha\theta}\delta_{\beta\gamma}. \tag{3.81}$$

It should be noted that $\delta_{\alpha\beta}$ and $\Delta_{\alpha\beta\gamma\theta}$ are isotropic while $\delta_{\alpha\beta\gamma\theta}$ is anisotropic.

Let us now consider the LBE

$$f_\beta(\boldsymbol{x} + \boldsymbol{c}_\beta \delta_t, t + \delta_t) - f_\beta(\boldsymbol{x}, t) = -\frac{1}{\tau}\left[f_\beta(\boldsymbol{x}, t) - f_\beta^{eq}(\boldsymbol{x}, t)\right]. \tag{3.82}$$

The fluid density and velocity is then defined as the zeroth and first moment of the distribution function, respectively,

$$\rho = \sum_\sigma \sum_i f_{\sigma i}(\boldsymbol{x}, t), \tag{3.83}$$

$$\rho \boldsymbol{u} = \sum_\sigma \sum_i f_{\sigma i}(\boldsymbol{x}, t) \boldsymbol{e}_{\sigma i}. \tag{3.84}$$

Let us represent the discretized equilibrium distribution function, $f_{\sigma i}^{eq}$ as follows

$$f_{\sigma i}^{eq}(\boldsymbol{x},t) = f_{\sigma i}^{0}(\boldsymbol{x},t). \tag{3.85}$$

Now lets expand the unknown equilibrium distribution function until the quadratic terms in the macroscopic velocity,

$$f_{\sigma i}^{0}(\boldsymbol{x},t) = A_\sigma + B_\sigma(\boldsymbol{e}_{\sigma i}\cdot\boldsymbol{u}) + C_\sigma(\boldsymbol{e}_{\sigma i}\cdot\boldsymbol{u})^2 + D_\sigma\boldsymbol{u}^2. \tag{3.86}$$

Since we neglect the higher order terms, the validity of the results are applicable to only weakly incompressible flows. The constants $A_\sigma, B_\sigma, C_\sigma$ and D_σ are assumed to depend only on the density and are independent of the macroscopic velocity $\boldsymbol{u}$. Since $\boldsymbol{u}_{0i} = \boldsymbol{u}_{01} = \boldsymbol{0}$, we have $B_0 = 0$ and $C_0 = 0$. Hence,

$$f_{0i}^{0}(\boldsymbol{x},t) = A_0 + D_0\boldsymbol{u}^2, \tag{3.87}$$

$$f_{1i}^{0}(\boldsymbol{x},t) = A_1 + B_1(\boldsymbol{e}_{1i}\cdot\boldsymbol{u}) + C_1(\boldsymbol{e}_{1i}\cdot\boldsymbol{u})^2 + D_1\boldsymbol{u}^2, \tag{3.88}$$

$$f_{2i}^{0}(\boldsymbol{x},t) = A_2 + B_2(\boldsymbol{e}_{2i}\cdot\boldsymbol{u}) + C_2(\boldsymbol{e}_{2i}\cdot\boldsymbol{u})^2 + D_2\boldsymbol{u}^2. \tag{3.89}$$

Alternatively, in tensor form, this is expressed as

$$f_{\sigma i}^{0} = A_\sigma + B_\sigma e_{\sigma i\alpha}u_\alpha + C_\sigma e_{\sigma i\alpha}e_{\sigma i\beta}u_\alpha u_\beta + D_\sigma u^2. \tag{3.90}$$

Since collision conserves mass and momentum, and the relaxation to the equilibrium distribution takes place by collisions, we can write

$$\sum_\sigma\sum_i f_{\sigma i}(\boldsymbol{x},t) = \sum_\sigma\sum_i f_{\sigma i}^{0}(\boldsymbol{x},t) = \rho(\boldsymbol{x},t), \tag{3.91}$$

$$\sum_\sigma\sum_i f_{\sigma i}(\boldsymbol{x},t)\boldsymbol{e}_{\sigma i} = \sum_\sigma\sum_i f_{\sigma i}^{0}(\boldsymbol{x},t)\boldsymbol{e}_{\sigma i} = \rho(\boldsymbol{x},t)\boldsymbol{u}(\boldsymbol{x},t). \tag{3.92}$$

Substituting for the equilibrium distribution function in Eq. (3.91), we get

$$\sum_{\sigma}\sum_{i} f^0_{\sigma i}(\boldsymbol{x},t) = \sum_{\sigma}\sum_{i}\left(A_\sigma + B_\sigma e_{\sigma i\alpha}u_\alpha + C_\sigma e_{\sigma i\alpha}e_{\sigma i\beta}u_\alpha u_\beta + D_\sigma u^2\right),$$
$$= \sum_{\sigma} A_\sigma \sum_{i} 1 + u_\alpha \sum_{\sigma} B_\sigma \sum_{i} e_{\sigma i\alpha} + u_\alpha u_\beta \sum_{\sigma} C_\sigma \sum_{i} e_{\sigma i\alpha}e_{\sigma i\beta} + u^2 \sum_{\sigma} D_\sigma \sum_{i} 1.$$

Second term has a tensor of odd order which vanishes. For $\sigma = 0$, $\sum_i 1 = 1$ and for $\sigma = 1$ and $\sigma = 2$, $\sum_i 1 = 4$. The third term can be simplified using Eq. (3.76). Thus

$$\sum_{\sigma}\sum_{i} f^0_{\sigma i}(\boldsymbol{x},t) = A_0 + 4A_1 + 4A_2 + u_\alpha u_\beta\left(2c^2C_1\delta_{\alpha\beta} + 4c^2C_2\delta_{\alpha\beta}\right) + u^2\left(D_0 + 4D_1 + 4D_2\right). \tag{3.93}$$

Since $u_\beta\delta_{\alpha\beta} = u_\alpha$, we have

$$\sum_{\sigma}\sum_{i} f^0_{\sigma i}(\boldsymbol{x},t) = A_0 + 4A_1 + 4A_2 + u_\alpha u_\alpha\left(2c^2C_1 + 4c^2C_2\right) + u^2\left(D_0 + 4D_1 + 4D_2\right), \tag{3.94}$$

$$\sum_{\sigma}\sum_{i} f^0_{\sigma i}(\boldsymbol{x},t) = A_0 + 4A_1 + 4A_2 + u^2\left(2c^2C_1 + 4c^2C_2 + D_0 + 4D_1 + 4D_2\right). \tag{3.95}$$

From Eq. (3.91), we have

$$A_0 + 4A_1 + 4A_2 + u^2\left(2c^2C_1 + 4c^2C_2 + D_0 + 4D_1 + 4D_2\right) = \rho. \tag{3.96}$$

Since both the density and the coefficients C_σ and D_σ do not depend on the velocity, the coefficient of u^2 should be zero. Thus we have the following equations:

$$A_0 + 4A_1 + 4A_2 = \rho, \tag{3.97}$$

$$2c^2C_1 + 4c^2C_2 + D_0 + 4D_1 + 4D_2 = 0. \tag{3.98}$$

Substituting for the equilibrium distribution function in Eq. (3.91) and with additional simplification, the equation becomes,

$$\sum_{\sigma}\sum_{i} f^{0}_{\sigma i} e_{\sigma i\alpha} = \sum_{\sigma}\sum_{i} \left(A_{\sigma} e_{\sigma i\alpha} + B_{\sigma} e_{\sigma i\alpha} e_{\sigma i\beta} u_{\beta} + C_{\sigma} e_{\sigma i\alpha} e_{\sigma i\beta} e_{\sigma i\gamma} u_{\beta} u_{\gamma} + D_{\sigma} u^{2} e_{\sigma i\alpha} \right),$$

$$\rho u_{\alpha} = \sum_{\sigma} A_{\sigma} \sum_{i} e_{\sigma i\alpha} + u_{\beta} \sum_{\sigma} B_{\sigma} \sum_{i} e_{\sigma i\alpha} e_{\sigma i\beta} +$$

$$u_{\beta} u_{\gamma} \sum_{\sigma} C_{\sigma} \sum_{i} e_{\sigma i\alpha} e_{\sigma i\beta} e_{\sigma i\gamma} + u^{2} \sum_{\sigma} D_{\sigma} \sum_{i} e_{\sigma i\alpha}.$$

Since all odd tensors vanish under summation, we have only B_{σ} terms which can be simplified using Eq. (3.76) to obtain

$$\rho u_{\alpha} = u_{\beta} \left(2c^{2} B_{1} \delta_{\alpha\beta} + 4c^{2} B_{2} \delta_{\alpha\beta} \right).$$

This finally simplifies to

$$2c^{2} B_{1} + 4c^{2} B_{2} = \rho. \tag{3.99}$$

Now we will show through a Chapman-Enskog expansion that in the continuum limit, the Navier-Stokes equations can be recovered from the LBE. Let us introduce a small parameter, ϵ, that compares orders of quantities upon the application of the asymptotic expansion. This would be similar to a Knudsen number, Kn, which is defined as the ratio of molecular mean free path to a macroscopic length scale. In the context of the LBE, the advection time can be taken as the small parameter:

$$\epsilon = \delta_{t}. \tag{3.100}$$

According to the observation by Maxwell, which was further refined by Chapman and Enskog, a macroscopic definition of a fluid comes by piecing together local equilibria defined by values of local hydrodynamic variables which are varying slowly in space

and time, thus implying continuum equations as consistency conditions. Thus the distribution function can be expanded in terms of the small parameter, ϵ, as

$$f_{\sigma i} = \sum_{n=1}^{\infty} \epsilon^n f_{\sigma i}^{(n)} = f_{\sigma i}^0 + \epsilon^1 f_{\sigma i}^1 + \epsilon^2 f_{\sigma i}^2 + ... \tag{3.101}$$

The unknown higher order quantities such as $f_{\sigma i}^1$ will be determined from the analysis. The hydrodynamic variables are then defined as consistency conditions,

$$\sum_{\sigma} \sum_{i} f_{\sigma i}^0 \begin{pmatrix} 1 \\ \boldsymbol{e}_{\sigma i} \end{pmatrix} = \begin{pmatrix} \rho \\ \rho \boldsymbol{u} \end{pmatrix}, \tag{3.102}$$

$$\sum_{\sigma} \sum_{i} f_{\sigma i}^n \begin{pmatrix} 1 \\ \boldsymbol{e}_{\sigma i} \end{pmatrix} = \begin{pmatrix} 0 \\ 0 \end{pmatrix}, n > 0. \tag{3.103}$$

Only the zeroth order distribution function, i.e., the equilibrium distribution function contributes to the conserved quantities. These quantities are collision invariant. The distribution function relaxes to the equilibrium through collisions. Hence the zeroth and first moment of the higher order distribution functions are zero.

Now $f_{\sigma i}(\boldsymbol{x}+\boldsymbol{e}_{\sigma i}\epsilon, t+\epsilon)$ can be expanded using a Taylor series expansion as follows,

$$f_{\sigma i}(\boldsymbol{x} + \boldsymbol{e}_{\sigma i}\epsilon, t + \epsilon) = f_{\sigma i}(\boldsymbol{x}, t) + \frac{\epsilon^1}{1!} D_t^1 f_{\sigma i}(\boldsymbol{x}, t) + \frac{\epsilon^2}{2!} D_t^2 f_{\sigma i}(\boldsymbol{x}, t) + O(\epsilon^3), \tag{3.104}$$

where $D_t \equiv \partial_t + \boldsymbol{e}_{\sigma i} \cdot \boldsymbol{\nabla}$ is the total derivative. Equation (3.104) can be written as

$$f_{\sigma i}(\boldsymbol{x} + \boldsymbol{e}_{\sigma i}\epsilon, t + \epsilon) - f_{\sigma i}(\boldsymbol{x}, t) = \epsilon D_t f_{\sigma i}(\boldsymbol{x}, t) + \frac{\epsilon^2}{2} D_t^2 f_{\sigma i}(\boldsymbol{x}, t) + O(\epsilon^3). \tag{3.105}$$

Neglecting higher order terms and substituting this into the LBE (Eq. (3.70)), we get

$$\epsilon D_t f_{\sigma i}(\boldsymbol{x}, t) + \frac{\epsilon^2}{2} D_t^2 f_{\sigma i}(\boldsymbol{x}, t) = -\frac{1}{\tau}[f_{\sigma i}(\boldsymbol{x}, t) - f_{\sigma i}^0(\boldsymbol{x}, t)]. \tag{3.106}$$

To compute variations of $f_{\sigma i}$ at different time scales, following the multiscale procedure of Frisch *et al.* [112, 113], two time scales t_0 and t_1 are introduced in this analysis

$$t_0 = t, \tag{3.107}$$

$$t_1 = \epsilon t. \tag{3.108}$$

Here, the variable t_0 is a slower time scale representing a process on the macroscopic level such as diffusion; t_1 is a faster time scale representing perturbations in mass density or sound waves and bulk motion or convection. Thus

$$t = t(t_0, t_1). \tag{3.109}$$

Hence the partial derivative operator $\dfrac{\partial}{\partial t}$ can be written as

$$\frac{\partial}{\partial t} = \frac{\partial t_0}{\partial t}\frac{\partial}{\partial t_0} + \frac{\partial t_1}{\partial t}\frac{\partial}{\partial t_1}, \tag{3.110}$$

which can be further simplified as

$$\partial_t = \partial_{t_0} + \epsilon\partial_{t_1}. \tag{3.111}$$

Thus the total derivative can be expressed as

$$D_t = \partial_{t_0} + \epsilon\partial_{t_1} + \boldsymbol{e}_{\sigma i}\cdot\boldsymbol{\nabla}. \tag{3.112}$$

Substituting Eq. (3.101) in Eq. (3.106) and neglecting terms of order $O(\epsilon^3)$ and higher, we get

$$\epsilon D_t(f^0_{\sigma i} + \epsilon f^1_{\sigma i}) + \frac{\epsilon^2}{2}D_t^2(f^0_{\sigma i}) = -\frac{1}{\tau}\left[f^0_{\sigma i} + \epsilon f^1_{\sigma i} + \epsilon^2 f^2_{\sigma i} - f^0_{\sigma i}\right]. \tag{3.113}$$

Expanding this with Eq. (3.112), we get

$$\epsilon(\partial_{t_0} + \epsilon\partial_{t_1} + \boldsymbol{e}_{\sigma i} \cdot \boldsymbol{\nabla})(f^0_{\sigma i} + \epsilon f^1_{\sigma i}) + \frac{\epsilon^2}{2}(\partial_{t_0} + \epsilon\partial_{t_1} + \boldsymbol{e}_{\sigma i} \cdot \boldsymbol{\nabla})^2(f^0_{\sigma i}) = -\frac{1}{\tau}\left[f^0_{\sigma i} + \epsilon f^1_{\sigma i} + \epsilon^2 f^2_{\sigma i} - f^0_{\sigma i}\right]. \tag{3.114}$$

Expanding and neglecting terms of order $O(\epsilon^3)$ and higher,

$$\epsilon(\partial_{t_0} + \boldsymbol{e}_{\sigma i} \cdot \boldsymbol{\nabla})f^0_{\sigma i} + \epsilon^2\left[(\partial_{t_0} + \boldsymbol{e}_{\sigma i} \cdot \boldsymbol{\nabla})f^1_{\sigma i} + \partial_{t_1} f^0_{\sigma i}\right] + \frac{\epsilon^2}{2}(\partial_{t_0} + \boldsymbol{e}_{\sigma i} \cdot \boldsymbol{\nabla})^2(f^0_{\sigma i}) = -\frac{1}{\tau}\left[\epsilon f^1_{\sigma i} + \epsilon^2 f^2_{\sigma i}\right]. \tag{3.115}$$

Let us now consider the behavior of the distribution function at scales t_0 and t_1. Comparing different order of ϵ in Eq. (3.115) we get equations for successive approximations to the distribution functions. Equating order $O(\epsilon)$ terms, we get

$$O(\epsilon) \,:\, (\partial_{t_0} + \boldsymbol{e}_{\sigma i} \cdot \boldsymbol{\nabla})f^0_{\sigma i} = -\frac{1}{\tau} f^1_{\sigma i}. \tag{3.116}$$

The equation to order $O(\epsilon^2)$ is

$$O(\epsilon^2) \,:\, (\partial_{t_0} + \boldsymbol{e}_{\sigma i} \cdot \boldsymbol{\nabla})f^1_{\sigma i} + \partial_{t_1} f^0_{\sigma i} + \frac{1}{2}(\partial_{t_0} + \boldsymbol{e}_{\sigma i} \cdot \boldsymbol{\nabla})^2(f^0_{\sigma i}) = -\frac{1}{\tau} f^2_{\sigma i}. \tag{3.117}$$

Multiplying Eq. (3.116) by the operator $\frac{1}{2}(\partial_{t_0} + \boldsymbol{e}_{\sigma i} \cdot \boldsymbol{\nabla})$, we get

$$\frac{1}{2}(\partial_{t_0} + \boldsymbol{e}_{\sigma i} \cdot \boldsymbol{\nabla})^2 f^0_{\sigma i} = -\frac{1}{2\tau}(\partial_{t_0} + \boldsymbol{e}_{\sigma i} \cdot \boldsymbol{\nabla})f^1_{\sigma i}. \tag{3.118}$$

Substituting Eq. (3.118) in Eq. (3.117), we get

$$(\partial_{t_0} + \boldsymbol{e}_{\sigma i} \cdot \boldsymbol{\nabla})f^1_{\sigma i} + \partial_{t_1} f^0_{\sigma i} - \frac{1}{2\tau}(\partial_{t_0} + \boldsymbol{e}_{\sigma i} \cdot \boldsymbol{\nabla})f^1_{\sigma i} = -\frac{1}{\tau} f^2_{\sigma i}, \tag{3.119}$$

$$\partial_{t_1} f^0_{\sigma i} + \left[1 - \frac{1}{2\tau}\right](\partial_{t_0} + \boldsymbol{e}_{\sigma i} \cdot \boldsymbol{\nabla})f^1_{\sigma i} = -\frac{1}{\tau} f^2_{\sigma i}. \tag{3.120}$$

To derive continuity equations for mass and momentum to first order in ϵ, zeroth and first order moments of Eq. (3.116) is taken. The zeroth-order moment gives

$$\sum_{\sigma}\sum_{i}(\partial_{t_0} + \boldsymbol{e}_{\sigma i}\cdot\boldsymbol{\nabla})f^0_{\sigma i} = \sum_{\sigma}\sum_{i} -\frac{1}{\tau}f^1_{\sigma i}. \tag{3.121}$$

Recalling that the zeroth-moment of any higher order term of the distribution function is zero, we get

$$\sum_{\sigma}\sum_{i}\partial_{t_0}f^0_{\sigma i} + \sum_{\sigma}\sum_{i}\boldsymbol{e}_{\sigma i}\cdot\boldsymbol{\nabla}f^0_{\sigma i} = 0. \tag{3.122}$$

Since the summation operator is linear, we have

$$\partial_{t_0}\sum_{\sigma}\sum_{i}f^0_{\sigma i} + \sum_{\sigma}\sum_{i}\boldsymbol{e}_{\sigma i}\cdot\boldsymbol{\nabla}f^0_{\sigma i} = 0, \tag{3.123}$$

which yields

$$\partial_{t_0}\rho + \sum_{\sigma}\sum_{i}\boldsymbol{e}_{\sigma i}\cdot\boldsymbol{\nabla}f^0_{\sigma i} = 0. \tag{3.124}$$

Now $\boldsymbol{e}_{\sigma i}\cdot\boldsymbol{\nabla}f^0_{\sigma i}$ can be expressed as

$$\boldsymbol{e}_{\sigma i}\cdot\boldsymbol{\nabla}f^0_{\sigma i} = \boldsymbol{\nabla}\cdot\boldsymbol{e}_{\sigma i}f^0_{\sigma i}. \tag{3.125}$$

Thus Eq. (3.124) becomes

$$\partial_{t_0}\rho + \sum_{\sigma}\sum_{i}\boldsymbol{\nabla}\cdot\boldsymbol{e}_{\sigma i}f^0_{\sigma i} = 0, \tag{3.126}$$

$$\partial_{t_0}\rho + \boldsymbol{\nabla}\cdot\sum_{\sigma}\sum_{i}\boldsymbol{e}_{\sigma i}f^0_{\sigma i} = 0, \tag{3.127}$$

$$\partial_{t_0}\rho + \boldsymbol{\nabla}\cdot(\rho\boldsymbol{u}) = 0, \tag{3.128}$$

which is the first-order continuity equation. Now taking the first-order moment of Eq. (3.116), we get

$$\sum_{\sigma}\sum_{i}\boldsymbol{e}_{\sigma i}(\partial_{t_0}+\boldsymbol{e}_{\sigma i}\cdot\boldsymbol{\nabla})f^0_{\sigma i}=\sum_{\sigma}\sum_{i}-\frac{1}{\tau}\boldsymbol{e}_{\sigma i}f^1_{\sigma i}. \tag{3.129}$$

Since the first moment of any higher-order distribution function is zero, we get

$$\sum_{\sigma}\sum_{i}\boldsymbol{e}_{\sigma i}\partial_{t_0}f^0_{\sigma i}+\sum_{\sigma}\sum_{i}\boldsymbol{e}_{\sigma i}\boldsymbol{e}_{\sigma i}\cdot\boldsymbol{\nabla}f^0_{\sigma i}=0. \tag{3.130}$$

As in the previous derivation,

$$\partial_{t_0}\sum_{\sigma}\sum_{i}\boldsymbol{e}_{\sigma i}f^0_{\sigma i}+\boldsymbol{\nabla}\cdot\sum_{\sigma}\sum_{i}\boldsymbol{e}_{\sigma i}\boldsymbol{e}_{\sigma i}f^0_{\sigma i}=0, \tag{3.131}$$

which yields

$$\partial_{t_0}(\rho\boldsymbol{u})+\boldsymbol{\nabla}\cdot\boldsymbol{\Pi}^0=0, \tag{3.132}$$

where

$$\boldsymbol{\Pi}^0=\sum_{\sigma}\sum_{i}\boldsymbol{e}_{\sigma i}\boldsymbol{e}_{\sigma i}f^0_{\sigma i}, \tag{3.133}$$

is the first-order momentum flux tensor. Similarly taking the zeroth-order moment of Eq. (3.120) gives the second order equation for ρ as

$$\partial_{t_1}\rho=0. \tag{3.134}$$

The first moment of Eq. (3.120) gives the second order equation for $\rho\boldsymbol{u}$ as

$$\partial_{t_1}(\rho\boldsymbol{u})+\boldsymbol{\nabla}\cdot\left(\varphi\boldsymbol{\Pi}^1\right)=0, \tag{3.135}$$

where

$$\boldsymbol{\Pi}^1=\sum_{\sigma}\sum_{i}\boldsymbol{e}_{\sigma i}\boldsymbol{e}_{\sigma i}f^1_{\sigma i}, \tag{3.136}$$

is the second moment of the first order distribution function $f^1_{\sigma i}$ and represents the second-order momentum flux tensor. Moreover, the term φ is given by

$$\varphi = \left[1 - \frac{1}{2\tau}\right]. \tag{3.137}$$

The next step is to simplify the momentum flux tensors. Firstly, consider $\mathbf{\Phi}^0$. Expressing in tensor form with free indices α and β as the coordinates, we have

$$\Pi^0_{\alpha\beta} = \sum_{\sigma}\sum_{i} e_{\sigma i\alpha} e_{\sigma i\beta} f^0_{\sigma i}. \tag{3.138}$$

Substituting for the equilibrium distribution function from Eq. (3.86) in the tensor form, we have

$$\Pi^0_{\alpha\beta} = \sum_{\sigma}\sum_{i} e_{\sigma i\alpha} e_{\sigma i\beta} \left[A_\sigma + B_\sigma(e_{\sigma i\gamma} u_\gamma) + C_\sigma(e_{\sigma i\gamma} e_{\sigma i\theta} u_\gamma u_\theta) + D_\sigma u^2\right]. \tag{3.139}$$

Now, Eq. (3.139) can be expressed as

$$\begin{aligned}\Pi^0_{\alpha\beta} = &\sum_{\sigma}\sum_{i} A_\sigma e_{\sigma i\alpha} e_{\sigma i\beta} + \sum_{\sigma}\sum_{i} B_\sigma e_{\sigma i\alpha} e_{\sigma i\beta} e_{\sigma i\gamma} u_\gamma + \\ &\sum_{\sigma}\sum_{i} C_\sigma e_{\sigma i\alpha} e_{\sigma i\beta} e_{\sigma i\gamma} e_{\sigma i\theta} u_\gamma u_\theta + \sum_{\sigma}\sum_{i} D_\sigma e_{\sigma i\alpha} e_{\sigma i\beta} u^2.\end{aligned} \tag{3.140}$$

Using the tensor properties in Eqs. (3.76-3.81) and Eqs. (3.73-3.75), we can simplify further as

$$\begin{aligned}\Pi^0_{\alpha\beta} = 2c^2\delta_{\alpha\beta}\left[(A_1 + D_1u^2) + 2(A_2 + D_2u^2)\right] + \\ 2c^4 u_\gamma u_\theta \left[C_1\delta_{\alpha\beta\gamma\theta} + C_2\left(2\Delta_{\alpha\beta\gamma\theta} - 4\delta_{\alpha\beta\gamma\theta}\right)\right].\end{aligned} \tag{3.141}$$

Performing the following tensor manipulation,

$$\begin{aligned} u_\gamma u_\theta \Delta_{\alpha\beta\gamma\theta} &= u_\gamma u_\theta(\delta_{\alpha\beta}\delta_{\gamma\theta} + \delta_{\alpha\gamma}\delta_{\beta\theta} + \delta_{\alpha\theta}\delta_{\beta\gamma}), \\ &= u^2\delta_{\alpha\beta} + 2u_\alpha u_\beta, \end{aligned} \tag{3.142}$$

we get,

$$\begin{aligned}\Pi^0_{\alpha\beta} =& 2c^2\delta_{\alpha\beta}\left[(A_1 + D_1u^2) + 2(A_2 + D_2u^2)\right] + \\ & 2c^4\left[C_1u_\gamma u_\theta\delta_{\alpha\beta\gamma\theta} + 2C_2\left(u^2\delta_{\alpha\beta} + 2u_\alpha u_\beta\right) - 4C_1u_\gamma u_\theta\delta_{\alpha\beta\gamma\theta}\right].\end{aligned} \tag{3.143}$$

Separating terms of $\delta_{\alpha\beta}$ and $\delta_{\alpha\beta\gamma\theta}$, we have

$$\begin{aligned}\Pi^0_{\alpha\beta} = &\left[2c^2(A_1 + 2A_2) + 2u^2c^2(D_1 + 2D_2 + 2c^2C_2)\right]\delta_{\alpha\beta} + \\ & 8C_2c^4u_\alpha u_\beta + 2\left(C_1 - 4C_2\right)c^4u_\gamma u_\theta\delta_{\alpha\beta\gamma\theta}.\end{aligned} \tag{3.144}$$

By comparing this equation with the momentum equation (continuum case), we can say that the coefficient of $\delta_{\alpha\beta}$ represents pressure. However, there is a velocity dependence in this term. To remove this, set the coefficient of u^2 to zero,

$$D_1 + 2D_2 + 2c^2C_2 = 0. \tag{3.145}$$

The value of the momentum flux tensor thus obtained depends on the frame of reference due to the anisotropic term $\delta_{\alpha\beta\gamma\theta}$. Galilean invariance can be achieved set its coefficient to zero, i.e.

$$C_1 - 4C_2 = 0. \tag{3.146}$$

Thus the momentum flux tensor can be simplified as

$$\Pi^0_{\alpha\beta} = 2c^2\delta_{\alpha\beta}\left(A_1 + 2A_2\right) + 8C_2c^4u_\alpha u_\beta. \tag{3.147}$$

Assuming

$$8C_2c^4 = \rho, \tag{3.148}$$

and

$$2c^2\left(A_1 + 2A_2\right) = c_s^2\rho, \tag{3.149}$$

where c_s which will be determined in terms of unknown parameters later, we have

$$\Pi^0_{\alpha\beta} = c_s^2 \rho \delta_{\alpha\beta} + \rho u_\alpha u_\beta. \tag{3.150}$$

Substituting Eq. (3.150) in Eq. (3.132), we get

$$\partial_{t_0}(\rho \boldsymbol{u}) + \boldsymbol{\nabla} \cdot (\rho \boldsymbol{u}\boldsymbol{u}) = -\boldsymbol{\nabla}(c_s^2 \rho). \tag{3.151}$$

Equation (3.128) along with Eq. (3.151) constitute the Euler equations which are derived from the first-order expansion of the LBE.

Now let us simplify $\boldsymbol{\Pi}^1$. In order to do this, we need to express $f^1_{\sigma i}$ in terms of the equilibrium distribution function $f^0_{\sigma i}$. From Eq. (3.116), we get

$$f^1_{\sigma i} = \tau \left[\partial_{t_0} f^0_{\sigma i} + \boldsymbol{e}_{\sigma i} \cdot \boldsymbol{\nabla} f^0_{\sigma i} \right]. \tag{3.152}$$

Substituting this expression for $f^1_{\sigma i}$ in Eq. (3.136), we get

$$\boldsymbol{\Pi}^1 = \sum_\sigma \sum_i \boldsymbol{e}_{\sigma i} \boldsymbol{e}_{\sigma i} \tau \left[\partial_{t_0} f^0_{\sigma i} + \boldsymbol{e}_{\sigma i} \cdot \boldsymbol{\nabla} f^0_{\sigma i} \right]. \tag{3.153}$$

This can be represented in tensor form as

$$\Pi^1_{\alpha\beta} = \sum_\sigma \sum_i e_{\sigma i\alpha} e_{\sigma i\beta} \tau \left[\partial_{t_0} f^0_{\sigma i} + e_{\sigma i\lambda} \partial_\lambda f^0_{\sigma i} \right], \tag{3.154}$$

$$\Pi^1_{\alpha\beta} = \tau \partial_{t_0} \sum_\sigma \sum_i e_{\sigma i\alpha} e_{\sigma i\beta} f^0_{\sigma i} + \tau \partial_\lambda \sum_\sigma \sum_i e_{\sigma i\alpha} e_{\sigma i\beta} e_{\sigma i\lambda} f^0_{\sigma i}. \tag{3.155}$$

Substituting Eq. (3.86) in the tensor form in Eq. (3.155), we have

$$\begin{aligned} \Pi^1_{\alpha\beta} =& \tau \partial_{t_0} \Pi^0_{\alpha\beta} + \\ & \tau \partial_\lambda \sum_\sigma \sum_i e_{\sigma i\alpha} e_{\sigma i\beta} e_{\sigma i\lambda} \left[A_\sigma + B_\sigma (e_{\sigma i\gamma} u_\gamma) + C_\sigma (e_{\sigma i\gamma} e_{\sigma i\theta} u_\gamma u_\theta) + D_\sigma u^2 \right]. \end{aligned} \tag{3.156}$$

Substituting Eq. (3.150) in Eq. (3.156) and using the tensor properties in Eqs. (3.76-3.81) and Eqs. (3.73-3.75), we get

$$\Pi^1_{\alpha\beta} = \tau\partial_{t_0}\left(c_s^2\rho\delta_{\alpha\beta} + \rho u_\alpha u_\beta\right) + \tau\partial_\lambda \sum_\sigma \sum_i B_\sigma e_{\sigma i\alpha} e_{\sigma i\beta} e_{\sigma i\lambda} e_{\sigma i\gamma} u_\gamma, \tag{3.157}$$

$$\Pi^1_{\alpha\beta} = \tau\partial_{t_0}\left(c_s^2\rho\delta_{\alpha\beta} + \rho u_\alpha u_\beta\right) + \tau\partial_\lambda\left[B_1 u_\gamma(2c^4\delta_{\alpha\beta\lambda\gamma}) + B_2 u_\gamma(4c^4\Delta_{\alpha\beta\lambda\gamma} - 8c^4\delta_{\alpha\beta\lambda\gamma})\right]. \tag{3.158}$$

Using tensor properties, we have

$$\begin{aligned} \partial_\lambda\left[B_2 u_\gamma \Delta_{\alpha\beta\lambda\gamma}\right] &= \partial_\lambda\left[B_2 u_\gamma\left(\delta_{\alpha\beta}\delta_{\lambda\gamma} + \delta_{\alpha\lambda}\delta_{\beta\gamma} + \delta_{\alpha\gamma}\delta_{\beta\lambda}\right)\right], \\ &= \partial_\lambda(B_2 u_\lambda\delta_{\alpha\beta}) + \partial_\alpha(B_2 u_\beta) + \partial_\beta(B_2 u_\alpha). \end{aligned} \tag{3.159}$$

From the first order continuity equation (Eq. (3.128), we have

$$\partial_{t_0}\rho = -\boldsymbol{\nabla}\cdot(\rho\boldsymbol{u}). \tag{3.160}$$

Thus we have

$$\partial_{t_0}(c_s^2\rho) = c_s^2\partial_{t_0}\rho = -c_s^2\boldsymbol{\nabla}\cdot(\rho\boldsymbol{u}). \tag{3.161}$$

Equation (3.158) thus becomes

$$\Pi^1_{\alpha\beta} = \tau\left\{\begin{array}{l} -c_s^2\partial_\gamma(\rho u_\gamma)\delta_{\alpha\beta} + \partial_{t_0}(\rho u_\alpha u_\beta) + \\ 2c^4\partial_\lambda\left[(B_1 - 4B_2)u_\gamma\right]\delta_{\alpha\beta\lambda\gamma} + \\ 4c^4\left[\partial_\lambda(B_2 u_\lambda)\delta_{\alpha\beta} + \partial_\alpha(B_2 u_\beta) + \partial_\beta(B_2 u_\alpha)\right]. \end{array}\right\} \tag{3.162}$$

To avoid anisotropy, set the coefficient of $\delta_{\alpha\beta\lambda\gamma}$ to zero,

$$B_1 - 4B_2 = 0. \tag{3.163}$$

Using Eq. (3.99) and Eq. (3.162), B_1 and B_2 can be determined,

$$B_1 = \frac{\rho}{3c^2}, \tag{3.164}$$

$$B_2 = \frac{\rho}{12c^2}. \tag{3.165}$$

Thus $\Pi^1_{\alpha\beta}$ becomes

$$\Pi^1_{\alpha\beta} = \tau \left\{ \begin{array}{l} -c_s^2 \partial_\gamma(\rho u_\gamma)\delta_{\alpha\beta} + \partial_{t_0}(\rho u_\alpha u_\beta) + \\ \frac{1}{3}c^2 \left[\partial_\lambda(\rho u_\lambda)\delta_{\alpha\beta} + \partial_\alpha(\rho u_\beta) + \partial_\beta(\rho u_\alpha)\right]. \end{array} \right\} \tag{3.166}$$

The Euler equations (Eqs. (3.128) and (3.151)) can be written in tensor form as

$$\partial_{t_0}\rho + \partial_\lambda(\rho u_\lambda) = 0. \tag{3.167}$$

$$\partial_{t_0}(\rho u_\lambda) + \partial_\gamma(\rho u_\gamma u_\lambda) = -\partial_\lambda(c_s^2\rho). \tag{3.168}$$

Now the time derivative term $\partial_{t_0}(\rho u_\alpha u_\beta)$ can be simplified using Eqs. (3.167) and (3.168) as follows:

$$\begin{aligned}
&\partial_{t_0}(\rho u_\alpha u_\beta) \\
&\quad = \partial_{t_0}\left[(\rho u_\alpha)u_\beta\right], \\
&\quad = u_\beta \partial_{t_0}(\rho u_\alpha) + \rho u_\alpha \partial_{t_0} u_\beta, \\
&\quad = u_\beta\left[-\partial_\gamma(\rho u_\gamma u_\alpha) - \partial_\alpha(c_s^2\rho)\right] + u_\alpha\left[\partial_{t_0}(\rho u_\beta) - u_\beta\partial_{t_0}\rho\right], \\
&\quad = -u_\beta\partial_\gamma(\rho u_\gamma u_\alpha) - u_\beta\partial_\alpha(c_s^2\rho) + u_\alpha\left[-\partial_\gamma(\rho u_\gamma u_\beta) - \partial_\beta(c_s^2\rho)\right] + u_\alpha u_\beta\partial_\lambda(\rho u_\lambda), \\
&\quad = -u_\beta\partial_\gamma(\rho u_\gamma u_\alpha) - u_\beta\partial_\alpha(c_s^2\rho) - u_\alpha u_\beta\partial_\gamma(\rho u_\gamma) - \rho u_\alpha u_\gamma\partial_\gamma u_\beta - u_\alpha\partial_\beta(c_s^2\rho) + \\
&\qquad u_\alpha u_\beta\partial_\lambda(\rho u_\lambda).
\end{aligned}$$

Since the third and sixth term are same (repeated indices being dummy indices), they cancel out to yield

$$\partial_{t_0}(\rho u_\alpha u_\beta) = -u_\beta \partial_\gamma(\rho u_\gamma u_\alpha) - u_\beta \partial_\alpha(c_s^2 \rho) - \rho u_\alpha u_\gamma \partial_\gamma u_\beta - u_\alpha \partial_\beta(c_s^2 \rho). \tag{3.169}$$

Substituting Eq. (3.169) into Eq. (3.166), we get

$$\Pi^1_{\alpha\beta} = \tau \left\{ \begin{array}{l} -c_s^2 \partial_\gamma(\rho u_\gamma)\delta_{\alpha\beta} - u_\beta \partial_\gamma(\rho u_\gamma u_\alpha) - u_\beta \partial_\alpha(c_s^2 \rho) - \rho u_\alpha u_\gamma \partial_\gamma u_\beta - \\ u_\alpha \partial_\beta(c_s^2 \rho)) + \dfrac{1}{3} c^2 \left[\partial_\lambda(\rho u_\lambda)\delta_{\alpha\beta} + \partial_\alpha(\rho u_\beta) + \partial_\beta(\rho u_\alpha)\right]. \end{array} \right\} \tag{3.170}$$

The second and fourth terms are of the order $O(u^3)$. Neglecting these terms and simplifying, we obtain

$$\Pi^1_{\alpha\beta} = \tau \left\{ \left(\frac{c^2}{3} - c_s^2 \right) \partial_\gamma(\rho u_\gamma)\delta_{\alpha\beta} - u_\beta \partial_\alpha(c_s^2 \rho) - u_\alpha \partial_\beta(c_s^2 \rho) + \frac{c^2}{3} \left[\partial_\alpha(\rho u_\beta) + \partial_\beta(\rho u_\alpha)\right] \right\}. \tag{3.171}$$

Until now, we have not defined the speed of sound c_s in terms of other parameters. If we set

$$\frac{c^2}{3} - c_s^2 = 0, \tag{3.172}$$

Eq. (3.171) is considerably simplified. This yields

$$c_s = \frac{1}{\sqrt{3}} c, \tag{3.173}$$

which provides an expression for the speed of sound within the LBE framework. Thus $\Pi^1_{\alpha\beta}$ becomes

$$\Pi^1_{\alpha\beta} = \tau c_s^2 \left\{ -u_\beta \partial_\alpha \rho - u_\alpha \partial_\beta \rho + \partial_\alpha(\rho u_\beta) + \partial_\beta(\rho u_\alpha) \right\}, \tag{3.174}$$

$$\Pi^1_{\alpha\beta} = \tau c_s^2 \left\{ -u_\beta \partial_\alpha \rho - u_\alpha \partial_\beta \rho + u_\beta \partial_\alpha \rho + \rho \partial u_\beta + u_\alpha \partial_\beta \rho + \rho \partial_\beta u_\alpha \right\}, \tag{3.175}$$

$$\Pi^1_{\alpha\beta} = \tau c_s^2 \rho \left(\partial_\alpha u_\beta + \partial_\beta u_\alpha \right). \tag{3.176}$$

Let us combine the equations of first and second order to get the macroscopic equations. Consider Eq. (3.128) + $\epsilon\times$ Eq. (3.134) gives

$$\partial_{t_0}\rho + \epsilon\partial_{t_1}\rho + \boldsymbol{\nabla}\cdot(\rho\boldsymbol{u}) = 0. \tag{3.177}$$

Using Eq. (3.111), we can write

$$\partial_t\rho + \boldsymbol{\nabla}\cdot(\rho\boldsymbol{u}) = 0. \tag{3.178}$$

This is the continuity equation. Next consider Eq. (3.132) + $\epsilon\times$ Eq. (3.135)

$$\partial_{t_0}(\rho\boldsymbol{u}) + \epsilon\partial_{t_1}(\rho\boldsymbol{u}) + \boldsymbol{\nabla}\cdot\left(\boldsymbol{\Pi}^0 + \varphi\epsilon\boldsymbol{\Pi}^1\right) = 0, \tag{3.179}$$

which becomes

$$\partial_t(\rho\boldsymbol{u}) + \boldsymbol{\nabla}\cdot\left(\boldsymbol{\Pi}^0 + \varphi\epsilon\boldsymbol{\Pi}^1\right) = 0. \tag{3.180}$$

In tensor form

$$\partial_t(\rho u_\alpha) + \partial_\beta\left(\Pi^0_{\alpha\beta} + \varphi\epsilon\Pi^1_{\alpha\beta}\right) = 0. \tag{3.181}$$

Substituting Eq. (3.150) and 3.176 into Eq. (3.181), we get

$$\partial_t(\rho u_\alpha) + \partial_\beta\left(c_s^2\rho\delta_{\alpha\beta} + \rho u_\alpha u_\beta\right) + \partial_\beta\left[\varphi\epsilon\tau c_s^2\rho\left(\partial_\alpha u_\beta + \partial_\beta u_\alpha\right)\right] = 0. \tag{3.182}$$

Substituting Eq. (3.137) into Eq. (3.182), we get

$$\partial_t(\rho u_\alpha) + \partial_\beta\left(\rho u_\alpha u_\beta\right) = -\partial_\alpha(c_s^2\rho) + \partial_\beta\left(\tau\left[1 - \frac{1}{2\tau}\right]c_s^2\epsilon\left[\partial_\alpha u_\beta + \partial_\beta u_\alpha\right]\right). \tag{3.183}$$

Replacing ϵ by δ_t

$$\partial_t(\rho u_\alpha) + \partial_\beta\left(\rho u_\alpha u_\beta\right) = -\partial_\alpha(c_s^2\rho) + \partial_\beta\left(\left[\tau - \frac{1}{2}\right]c_s^2\delta_t\left[\partial_\alpha u_\beta + \partial_\beta u_\alpha\right]\right). \tag{3.184}$$

Define the strain rate tensor $S_{\alpha\beta}$ as

$$S_{\alpha\beta} = \frac{1}{2}\left(\partial_\alpha u_\beta + \partial_\beta u_\alpha\right). \tag{3.185}$$

Substituting Eq. (3.185) into Eq. (3.184) to get

$$\partial_t(\rho u_\alpha) + \partial_\beta\left(\rho u_\alpha u_\beta\right) = -\partial_\alpha(c_s^2\rho) + \partial_\beta\left(2\left[\tau - \frac{1}{2}\right]c_s^2\delta_t S_{\alpha\beta}\right). \tag{3.186}$$

The coefficient appearing before the strain rate term is analogous to viscosity. Thus the viscosity in the LBE framework is represented as

$$\nu = \left[\tau - \frac{1}{2}\right]c_s^2\delta_t. \tag{3.187}$$

The term $-\frac{1}{2}c_s^2\delta_t$ is an artifact arising from the discreteness of the lattice. If the velocity space were continuous as in the Boltzmann equation, this term would vanish and we would get the viscosity (momentum transport coefficient) in terms of a molecular velocity scale (average molecular speed) and a length scale (mean free path) or time scale (time between molecular collisions). Further, in Eq. (3.186), the pressure is given as

$$p = c_s^2\rho. \tag{3.188}$$

We can see that the pressure is related to the density through an equation that is similar to the ideal gas equation. The second order momentum flux tensor can thus be represented as

$$\Pi^1_{\alpha\beta} = 2\tau c_s^2\rho S_{\alpha\beta}. \tag{3.189}$$

From Eq. (3.136), we can write

$$\sum_\sigma\sum_i e_{\sigma i\alpha}e_{\sigma i\beta}f^1_{\sigma i} = 2\tau c_s^2\rho S_{\alpha\beta}. \tag{3.190}$$

For a first order expansion,

$$f_{\sigma i}^{1} = \frac{1}{\delta_t}\left(f_{\sigma i} - f_{\sigma i}^{0}\right). \tag{3.191}$$

Thus Eq. (3.190) becomes

$$\sum_{\sigma}\sum_{i} e_{\sigma i\alpha} e_{\sigma i\beta} \frac{1}{\delta_t}\left(f_{\sigma i} - f_{\sigma i}^{0}\right) = 2\tau c_s^2 \rho S_{\alpha\beta}. \tag{3.192}$$

Thus the strain rate tensor can be evaluated directly from the distribution function as

$$S_{\alpha\beta} = \frac{1}{2\tau c_s^2 \rho \delta_t} \sum_{\sigma}\sum_{i} e_{\sigma i\alpha} e_{\sigma i\beta}\left(f_{\sigma i} - f_{\sigma i}^{0}\right). \tag{3.193}$$

Finally, the momentum equation becomes

$$\partial_t(\rho u_\alpha) + \partial_\beta\left(\rho u_\alpha u_\beta\right) = -\partial_\alpha(p) + \partial_\beta\left(2\nu S_{\alpha\beta}\right). \tag{3.194}$$

Thus the long term behavior of the LBE corresponds to that described by equations which are similar to the Navier-Stokes equations.

Now, we determine the rest of the coefficients to complete the expression for the equilibrium distribution function. From Eq. (3.148) we have

$$C_2 = \frac{\rho}{8c^4}. \tag{3.195}$$

From Eq. (3.146),

$$C_1 = \frac{\rho}{2c^4}. \tag{3.196}$$

For A_σ, we have two equations (Eq. (3.97) and Eq. (3.149)) but three unknowns. Fixing one free variable to be that used in common LBE models [114]

$$A_0 = \frac{4}{9}\rho. \tag{3.197}$$

Thus the other two coefficients are found as

$$A_0 = \frac{1}{9}\rho, \tag{3.198}$$

$$A_0 = \frac{1}{36}\rho. \tag{3.199}$$

Similarly for D_σ, there are two equations (Eq. (3.98) and Eq. (3.145)) while three unknowns. Since all coefficients determined so far for $\sigma = 2$ are one fourth of that for $\sigma = 1$ impose

$$D_1 = 4D_2. \tag{3.200}$$

This yields

$$D_0 = -\frac{2}{3c^2}\rho, \tag{3.201}$$

$$D_0 = -\frac{1}{6c^2}\rho, \tag{3.202}$$

$$D_0 = -\frac{1}{24c^2}\rho. \tag{3.203}$$

Thus the primary consideration in determining these coefficients is that the resulting equilibrium distribution function obeys conservation laws and symmetry constraints. These considerations however do not yield a unique set of coefficients allowing some coefficients to be chosen freely.

Thus the equilibrium distribution function can be written as

$$f_{01}^0 = \frac{4}{9}\rho\left[1 - \frac{3}{2c^2}u^2\right], \tag{3.204}$$

$$f_{1i}^0 = \frac{1}{9}\rho\left[1 + \frac{3}{c^2}(\boldsymbol{e}_{1i}\cdot\boldsymbol{u}) + \frac{9}{2c^4}(\boldsymbol{e}_{1i}\cdot\boldsymbol{u})^2 - \frac{3}{2c^2}u^2\right], \tag{3.205}$$

$$f_{2i}^0 = \frac{1}{36}\rho\left[1 + \frac{3}{c^2}(\boldsymbol{e}_{2i}\cdot\boldsymbol{u}) + \frac{9}{2c^4}(\boldsymbol{e}_{2i}\cdot\boldsymbol{u})^2 - \frac{3}{2c^2}u^2\right]. \tag{3.206}$$

This equation is identical to Eq. (3.67) which is the equilibrium distribution derived from a Taylor series expansion of the Maxwellian distribution function for a discrete velocity space.

3.5 Numerical Aspects

As we have discussed, the LBE is a discretized version of the Boltzmann equation with finite velocities. The solution of the LBE involves two operations, viz. streaming and collision. Streaming represents the free flight of molecules from one lattice node to the other during which they do not collide with other molecules. Collision represents the interaction of molecules with each other once they arrive at a lattice node. Collisions in the LBM are commonly represented by the BGK model in which the distribution function relaxes to its equilibrium value through collisions over a characteristic time. The equilibrium distribution is selected so that it recovers the Navier-Stokes equations in the continuum and low-Mach number limit. The lattice is selected so that it preserves the symmetry of the stress tensor in the Navier-Stokes equations. The LBE is given as

$$f_\alpha(\boldsymbol{x} + \boldsymbol{c}_\alpha \delta_t, t + \delta_t) - f_\alpha(\boldsymbol{x}, t) = -\frac{1}{\tau}\left[f_\alpha(\boldsymbol{x}, t) - f_\alpha^{eq}(\boldsymbol{x}, t)\right], \tag{3.207}$$

which is solved in two steps:

$$\bar{f}_\alpha(\boldsymbol{x}, t) = f_\alpha(\boldsymbol{x}, t) - \frac{1}{\tau}\left[f_\alpha(\boldsymbol{x}, t) - f_\alpha^{eq}(\boldsymbol{x}, t)\right], \tag{3.208}$$

$$f_\alpha(\boldsymbol{x} + \boldsymbol{c}_\alpha \delta_t, t + \delta_t) = \bar{f}_\alpha(\boldsymbol{x}, t). \tag{3.209}$$

The first step represents collision where the distribution function relaxes to its equilibrium value in time $\tau\delta_t$ where τ is referred to as the relaxation parameter. In the second step, the distribution function streams to a neighboring node with velocity $\boldsymbol{e}_\alpha$ in time δ_t. Now, the density and velocity can be found as

$$\rho(\boldsymbol{x}, t) = \sum_\alpha f_\alpha(\boldsymbol{x}, t), \tag{3.210}$$

$$\rho(\boldsymbol{x}, t)\boldsymbol{u}(\boldsymbol{x}, t) = \sum_\alpha \boldsymbol{c}_\alpha f_\alpha(\boldsymbol{x}, t). \tag{3.211}$$

The pressure is found by an equation of state

$$p = c_s^2 \rho, \tag{3.212}$$

where c_s represents the speed of sound in the LBM framework. The kinematic viscosity of the fluid is related to the relaxation time and lattice parameters as

$$\nu = c_s^2 \left(\tau - \frac{1}{2} \right) \delta_t. \tag{3.213}$$

An important consideration in the selection of the lattice parameters is the Mach number, Ma which is given as

$$Ma = \frac{u}{c_s^2} = \frac{u \delta_t}{\sqrt{3} \delta_x}. \tag{3.214}$$

Since the Taylor expansion of the Mach number that is used in the LBM is valid only for low Ma, the Ma should be less than 0.3 (weakly compressible flow). The relaxation parameter τ should be greater than 0.5 to avoid negative viscosities. Moreover, values of τ that are too close to 0.5 can cause instabilities. The multiple relaxation time (MRT) implementation [115, 116] of the LBM can, be employed to address this challenge. This becomes important in turbulent flow simulations. It is a common practice to set δ_x and δ_t to unity since only non-dimensional results are reported.

3.6 Boundary Conditions

One of the main differences between conventional CFD techniques (i.e. solving the Navier-Stokes equations) and the LBM is the implementation of the boundary condition. In the LBM, the boundary conditions for the distribution function are generally unknown. While periodic boundary conditions are trivial to implement, others such as a no-slip wall and stress free boundaries are more involved. Some basic boundary conditions that are used in this work are reviewed in this section.

3.6.1 Bounce-Back Boundary Condition

This was proposed by Wolfram [95] and Lavallée [117] in the context of the LGA. This has been used in the LBM as well. Consider the D2Q9 lattice shown in Fig. 3.2. If the wall is at the bottom surface (along the line containing the points at the end of direction 4, 7 and 8). While streaming from the center (node marked as 0), the distribution functions that move in the direction 4, 7 and 8 strike the wall. However, the distribution functions in the direction 2, 5 and 6 are unknown since there is no fluid node from which they can be streamed. In order to obtain these distribution functions, those that strike the wall are assumed to bounce back so that it reaches the node from which it originated with the same speed but pointing in the opposite direction. Thus for this case, we have

$$f_2(x, y) = f_4(x, y), \tag{3.215}$$

$$f_5(x, y) = f_7(x, y), \tag{3.216}$$

$$f_6(x, y) = f_8(x, y). \tag{3.217}$$

While this boundary condition is easy to implement, several works [118–120] have shown that this boundary condition is first order accurate while the accuracy of the LBM is second order. Thus bounce-back boundary condition reduces the accuracy of the LBM.

3.6.2 Half-Way Bounce-Back Boundary Condition

Ziegler [119] noticed that if the wall was assumed to be placed half way between the last fluid node and the first solid node, then the boundary condition so achieved was second order accurate. He *et al.* [121] have confirmed through an analytical study that this method does give second order accuracy. This is referred to as the half way bounce back boundary condition and is used in this study to represent stationary no slip walls.

3.6.3 Extrapolation Method

This method was proposed by Chen *et al.* [122] and is based on simple extrapolation. This method can be used to simulate a variety of boundary conditions such as: specified velocity, density and open/stress free boundary conditions. In this method, the value of the unknown distribution function is calculated from those at the boundary and the first interior node through extrapolation. For instance, in Fig. 3.2, if the surface on the left (along the line containing the points at the end of direction 3, 6 and 7) is a boundary and the center (node marked as 0) is referred to as (i, j), then the unknown distribution function before streaming is obtained as

$$f_1(i-1, j) = 2f_1(i, j) - f_1(i+1, j). \tag{3.218}$$

The values of density or velocity are set prior to calculating the equilibrium distribution function. This method is simple to implement and is used to represent inlet/outlet boundary conditions in this current work.

3.6.4 Momentum Augmented Half-Way Bounce-Back Method

While the half way bounce-back method can be used to represent stationary no-slip walls, it cannot be used as such for moving walls. Ladd [51, 52] proposed a correction to account for the motion of the wall. An additional term is added to the distribution function as follows:

$$f_\alpha(\boldsymbol{x}, t) = f_{\alpha'}(\boldsymbol{x}, t) + \frac{2w_\alpha}{c_s^2}\rho(\boldsymbol{x}, t)(\boldsymbol{e}_\alpha \cdot \boldsymbol{u}(\boldsymbol{x}, t)), \tag{3.219}$$

where α' is the direction that streams into the wall and α is the direction that streams from the wall. It should be noted that the extra term does not conserve mass when the motion of the wall is not strictly tangential to the flow direction.

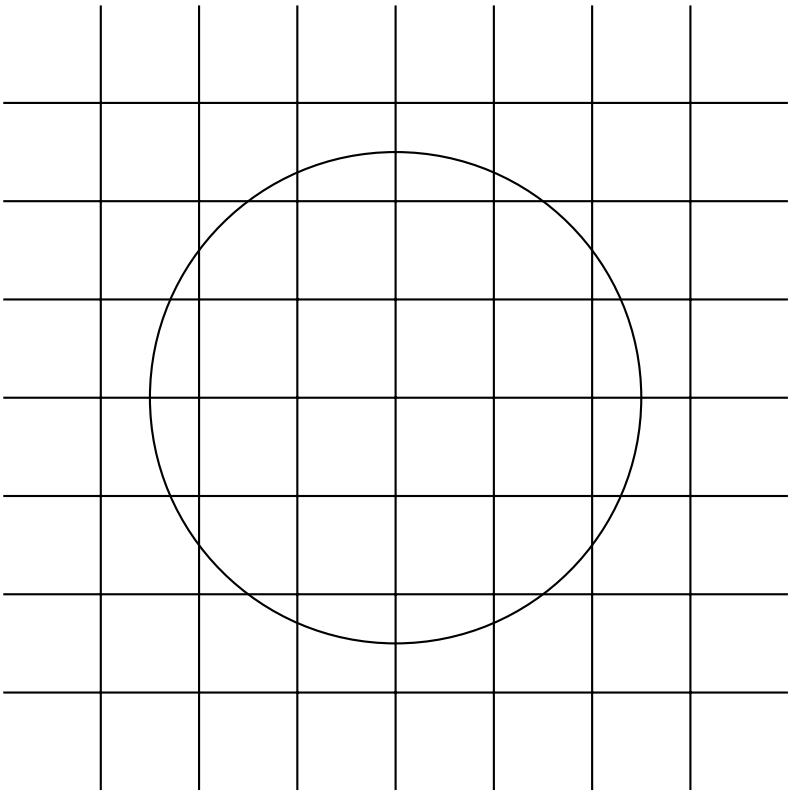

Figure 3.3: A particle in a D2Q9 lattice.

3.6.5 Bounce-Back for Curved Boundaries

The simulation of particles is done by representing them as a solid boundary that moves in the fluid. However, the boundaries are not straight and hence the wall would not be located at a distance that is half way between two lattice nodes. Figure 8.2 shows a circular (2D) particle in a D2Q9 lattice. It is seen that the particle boundary cuts the lattice links at random position which is not necessarily the midpoint.

Bouzidi *et al.* [123] as well as Lallemand and Luo [124] have proposed a technique to account for curved boundaries. Consider the one-dimensional situation in Fig. 8.3. Fluid node at $\boldsymbol{r}_j$ is the last node near the wall while $\boldsymbol{r}_s$ is the first node in the solid region. The intersection of the wall and the boundary link is represented as $\boldsymbol{r}_w$. The distance of the wall from the last fluid node is given as $q\delta_x = |\boldsymbol{r}_j - \boldsymbol{r}_w|$. If $q = 1/2$, the wall is located midway between the last fluid node and the first solid node and a

half way bounce-back can be applied (Fig. 8.3a). However, if $q < 1/2$, the particle would reach position $\boldsymbol{r}_i$ between $\boldsymbol{r}_j$ and $\boldsymbol{r}_{j'}$ (Fig. 8.3b). Similarly, if $q > 1/2$, the particle would reach position $\boldsymbol{r}_i$ between $\boldsymbol{r}_j$ and $\boldsymbol{r}_{j'}$ (Fig. 8.3c).

The following procedure is adopted to preserve the boundary representation of the particle:

1. For $q < 1/2$ (Fig. 8.3b), the distribution function at $\boldsymbol{r}_i$ is computed from the post collision distribution functions at $\boldsymbol{r}_{j''}$,$\boldsymbol{r}_{j'}$ and $\boldsymbol{r}_j$ through interpolation. This distribution function is then streamed so that it arrives at $\boldsymbol{r}_j$.

2. For $q > 1/2$ (Fig. 8.3c), the distribution function at $\boldsymbol{r}_j$ is streamed to $\boldsymbol{r}_i$. Then the post streaming distribution functions at $\boldsymbol{r}_{j''}$,$\boldsymbol{r}_{j'}$ and $\boldsymbol{r}_i$ is used to evaluate the distribution function at $\boldsymbol{r}_j$.

One can use either a linear or a quadratic interpolation. Let f^c denote the post collision distribution function (i.e. after collision but before streaming). Direction '1' represents streaming into the wall and '3' represents streaming from the wall in this case. Using a linear interpolation, for $q < 1/2$, we get

$$f_1^c(\boldsymbol{r}_i, t) = 2q f_1^c(\boldsymbol{r}_j, t) + (1 - 2q) f_1^c(\boldsymbol{r}_{j'}, t), \tag{3.220}$$

$$f_3(\boldsymbol{r}_j, t + \delta_t) = f_1^c(\boldsymbol{r}_i, t). \tag{3.221}$$

For $q > 1/2$, we have,

$$f_3(\boldsymbol{r}_j, t + \delta_t) = \frac{1}{2q} f_3(\boldsymbol{r}_i, t + \delta_t) + \frac{(2q - 1)}{2q} f_3(\boldsymbol{r}_{j'}, t + \delta_t). \tag{3.222}$$

In the case of quadratic interpolation, for $q < 1/2$, we have

$$f_1^c(\boldsymbol{r}_i, t) = q(2q + 1) f_1^c(\boldsymbol{r}_j, t) + (1 + 2q)(1 - 2q) f_1^c(\boldsymbol{r}_{j'}, t) - q(1 - 2q) f_1^c(\boldsymbol{r}_{j''}, t), \tag{3.223}$$

$$f_3(\boldsymbol{r}_j, t + \delta_t) = f_1^c(\boldsymbol{r}_i, t). \tag{3.224}$$

For $q > 1/2$, we have

$$f_3(\boldsymbol{r}_j, t+\delta_t) = \frac{1}{q(2q+1)} f_3(\boldsymbol{r}_i, t+\delta_t) + \frac{(2q-1)}{2q} f_3(\boldsymbol{r}_{j'}, t+\delta_t) + \frac{(1-2q)}{(1+2q)} f_3(\boldsymbol{r}_{j''}, t+\delta_t). \tag{3.225}$$

In the case of a moving boundary, an extra term needs to be added to account for the motion of the walls. For a linear interpolation, this is given as

$$\delta f_3(\boldsymbol{r}_j, t+\delta_t) = \frac{2w_1}{c_s^2}\rho(\boldsymbol{r}_j, t)(\boldsymbol{e}_1 \cdot \boldsymbol{u}(\boldsymbol{r}_j, t), \qquad q < 1/2, \tag{3.226}$$

$$\delta f_3(\boldsymbol{r}_j, t+\delta_t) = \frac{w_1}{qc_s^2}\rho(\boldsymbol{r}_j, t)(\boldsymbol{e}_1 \cdot \boldsymbol{u}(\boldsymbol{r}_j, t), \qquad q > 1/2. \tag{3.227}$$

When quadratic interpolation is used, we have

$$\delta f_3(\boldsymbol{r}_j, t+\delta_t) = \frac{2w_1}{c_s^2}\rho(\boldsymbol{r}_j, t)(\boldsymbol{e}_1 \cdot \boldsymbol{u}(\boldsymbol{r}_j, t), \qquad q < 1/2, \tag{3.228}$$

$$\delta f_3(\boldsymbol{r}_j, t+\delta_t) = \frac{2w_1}{q(2q+1)c_s^2}\rho(\boldsymbol{r}_j, t)(\boldsymbol{e}_1 \cdot \boldsymbol{u}(\boldsymbol{r}_j, t), \qquad q > 1/2. \tag{3.229}$$

Both these expressions simplify to yield the same value when $q = 1/2$ which corresponds to the standard half way bounce-back scheme. Since the scheme uses only interpolations, it has good stability properties.

3.7 Particle Motion Implementation

Ladd [51, 52] pioneered simulations of particulate flows using the LBM. In his work, he considers the particle to be a solid wall that moves with some velocity. The boundary conditions for the moving particle is implemented by the momentum augmented half way bounce-back scheme that has been explained in Section 4.6.4. As noted earlier, this boundary condition does not conserve mass and hence he allowed for some mass influx to the particle. This constrains the density of the particle to be higher than that of the fluid.

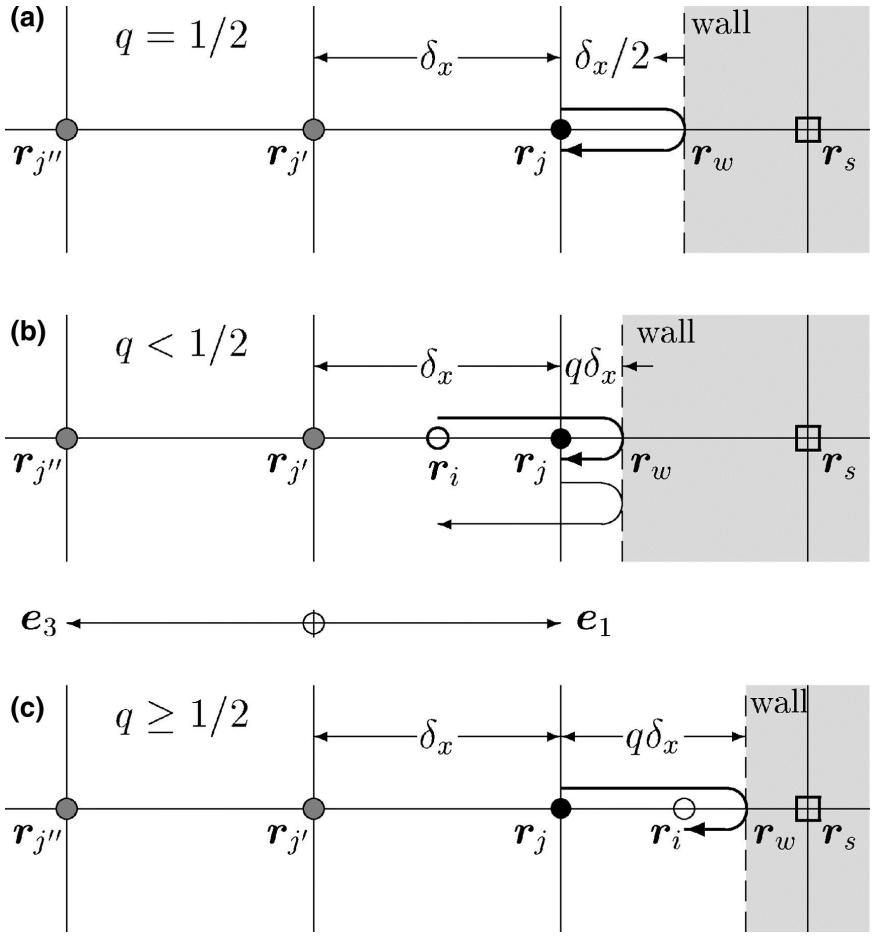

Figure 3.4: Boundary condition for a curved wall (Adapted from Ref. [124]).

Aidun *et al.* [53] proposed an improvement to this method that enables the simulation of particles with solid to fluid density ratio less than 1. His method treats the particle as a solid boundary and does not allow the fluid to enter the particle. This method is used in this current work and is described below:

As the particle moves in the computational domain, some of the fluid nodes would be uncovered while some may be covered. In such cases, the density of the newly appeared fluid node is obtained as the average density of all the neighboring fluid nodes. The velocity of the uncovered node is equal to the sum of the velocity of the particle and the angular velocity times the position vector joining the lattice node and the particle center. From this velocity and density, the equilibrium distribution functions are calculated and are assigned as the distribution functions of this node. This newly created fluid node gains some momentum. The particle momentum should therefore decrease by the same amount to ensure momentum conservation. Similarly, when a particle covers a fluid node, it gains the momentum of the fluid node at that instant. The local fluid mass is not conserved due to the nodes that appear and disappear. However, it has been reported in the work of Aidun *et al.* [53] that the effect of this numerical inconsistency is insignificant and is less than the numerical noise in the computations. The total average mass in the macroscopic level is conserved.

The next step is to compute the drag force acting on the particle. This is done by the momentum exchange method as was done in the work of Mei *et al.* [125]. In this method, the momentum transferred by the fluid molecules to the solid particle as it bounces back from the surface of the particle is summed up to get the total momentum transferred to the particle in a time step. This method eliminates the need to calculate the drag force from derivatives as is done in conventional CFD methods. The forces due to a particle covering and uncovering a fluid node are added to the force found by the momentum exchange method and is used to update the velocity and position of the particle.

This technique gives rise to fluctuations in the force acting on the particle as it moves across the lattice nodes. Figures 3.5 and 3.6 show the instantaneous and

averaged force acting on the particle in both the direction parallel to the wall and normal to it during one of the computations in this work. It is seen that there is a high frequency fluctuation (black line) that arises due to the particle covering and uncovering fluid nodes. The red line shows the time average of this force over a time span t_p, where t_p represents the time taken by the fluid to traverse a distance equal to the radius of the particle (r_p/U). The particle motion however, depends on the averaged force and is not influenced significantly by these high frequency fluctuations. The torque acting on the particle is found out similarly and is used to update the angular velocity of the particle. It should be noted that the particle rotation would not change its orientation but would change the fluid velocity at its boundary.

3.8 Prior Works on Particle-Laden Flows using the LBM

In this section, prior computational works that have used the LBM to study particle-laden flows are presented. Areas that have not been addressed in the current literature are discussed.

Ladd [51, 52] was the first to carry out a particle-laden flow simulation using the LBM. Ladd performed simulations in the creeping flow regime as well as for low Reynolds number (Re) flows. Aidun *et al.* [53] have done simulations on particles, whose density is close to that of the fluid. Qi *et al.* [54, 126–128] have also carried out LBM simulations of various flows with circular, elliptical and rectangular particles as well as three-dimensional cylindrical particles. A detailed study has been done in these works comparing their results with several finite-element solutions of the Navier-Stokes equations. It is shown in these works that the LBM is able to capture important effects such as the Segré-Silberberg effect as well as the Drafting, Kissing and Tumbling phenomena.

While earlier studies have focused more on laminar flows, recent works have reported particulate flows in turbulent conditions. Gao *et al.* [55] have studied the effect of particles on decaying isotropic turbulence. They found that at a given vol-

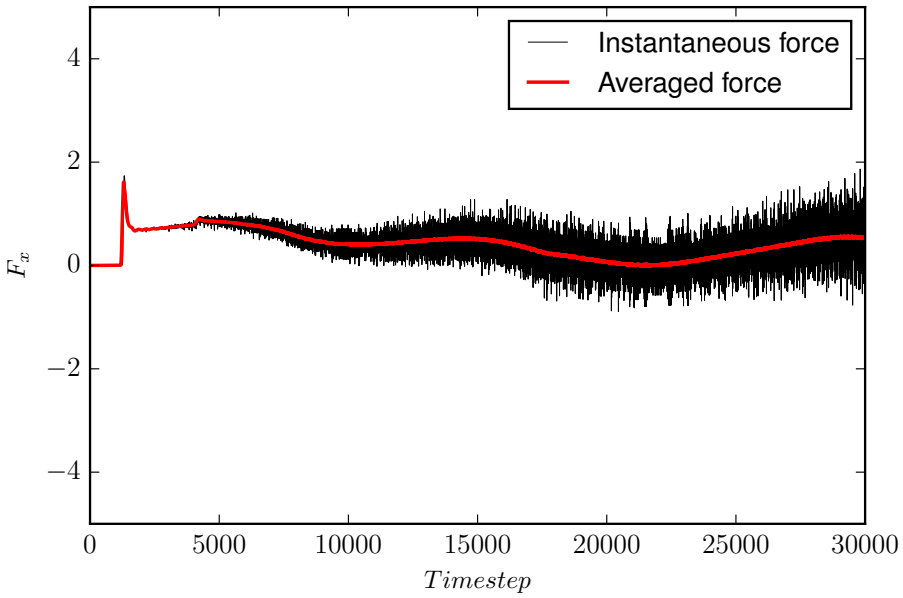

Figure 3.5: Hydrodynamic forces acting on the particle in the direction parallel to the wall.

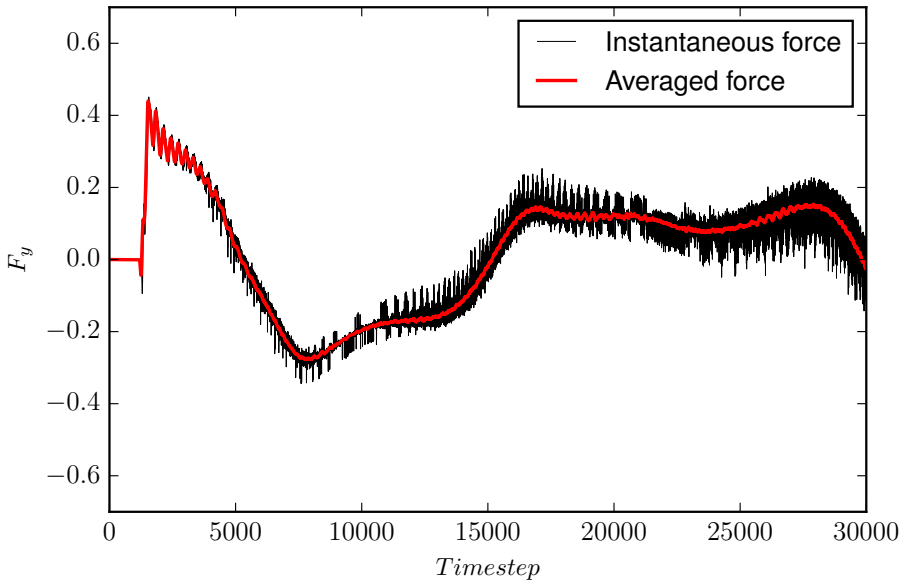

Figure 3.6: Hydrodynamic forces acting on the particle in the direction normal to the wall.

ume fraction, the dynamics of the particle-laden flow depends on the effective particle surface area and the Stokes number, St. The presence of particles enhances dissipation at small scales while reducing kinetic energy at large scales. Wang *et al.* [56] have used the LBM to study particulate flow in forced turbulence. They find that the particle-laden turbulence is much more dissipative due to the boundary layer near the particle surface. Wang *et al.* [129] have reported LBM simulations of particles in a turbulent channel flow. They have studied the turbulence modulation effect as well as the concentration of particles across the channel. They found that particles enhance the turbulence intensity in the near wall region while suppressing it near the center. While the particle concentration is complicated, they report a dynamic equilibrium resembling the Segré-Siblerberg effect.

The number of works that report particle-laden turbulent flow using the LBM is few. Moreover, these studies do not report particle-wall interactions and particle-turbulence interactions. Particle behavior depends on several parameters such as the Reynolds number, the Stokes number, the size of the particle relative to the channel and the density ratio. The migration of particles as well as the mechanism behind this migration has not been analyzed in sufficient detail. Effects such as Saffman lift and turbophoresis have not been studied in detail in the context of particulate flows in channels and jets. This current work aims to address these issues. A fundamental understanding of the physics behind particle-wall and particle-turbulence interactions is essential to develop models that can represent particle-laden flows.

3.9 Scalability

One of the main requirements of any DNS solver is parallel scalability. DNS computations are extremely costly due to the large number of grid points and time steps. Ideally, a DNS solver should scale linearly with the number of processors. Figure 3.7 shows the scaling results of Clausen *et al.* [130] for a single phase LBM code on upto 65,536 cores. It can be seen that even for this extremely large number

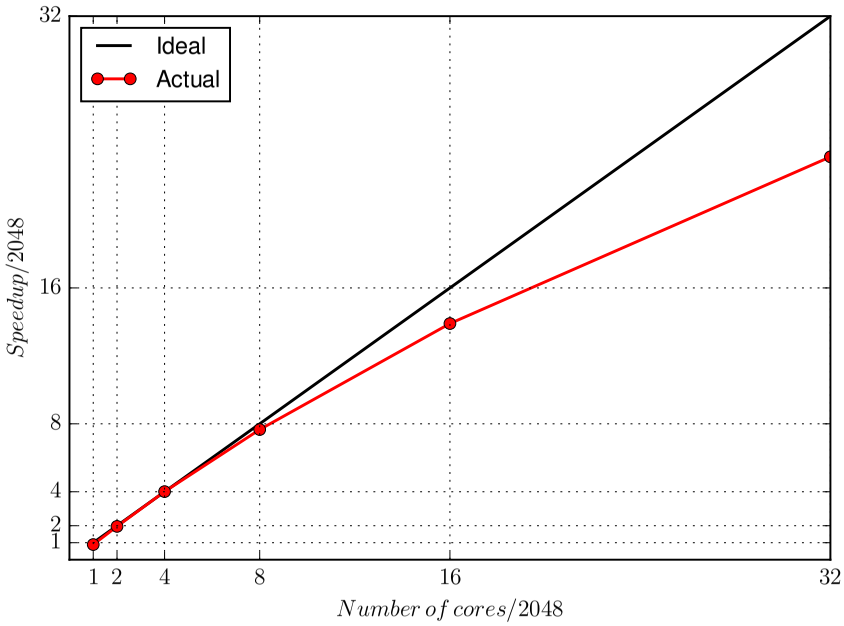

Figure 3.7: Scaling for a single phase LBM code on BlueGene/P installation at Argonne National Lab (Adapted from [130]).

of cores, the code reaches over 75% of its ideal speedup. Further, the inclusion of a dispersed phase is relatively simple in the LBM framework. These aspects make the LBM a natural choice for this work.

4. EVALUATION OF THE LBM CODE

4.1 Introduction

The Lattice Boltzmann Method (LBM) simulates fluid flow as described by the Navier-Stokes equations. The LBM has been evaluated for several standard test cases by many researchers [131, 132]. Since the code to simulate particle-laden flows has been developed independently as a part of this work, it is assessed for its accuracy by comparing simulated results for a series of flows ranging from simple laminar cases to three dimensional turbulent flow conditions.

This chapter is organized as follows: In Section 4.2, the LBM is employed to study a decaying Taylor Vortex. Sections 4.3 and 4.4 present results for the case of a plane channel flow and a transient Couette flow. The results for these flows are compared with analytical solutions. In Section 4.5, the computed results of a lid-driven cavity are compared with the numerical results based on Navier-Stokes equations. In Section 4.6, the motion of a circular particle (2D) under various conditions is computed and compared with results available from the literature. In Section 4.7, a three dimensional channel flow problem is solved using the LBM and its results are compared with analytical solutions. In Section 4.8, the sedimentation of a sphere in a duct is compared with experimental data available. In Section 4.9, a turbulent channel flow problem is computed. All length and time scales are resolved in this study. The statistics are compared with the DNS results of Lee and Moser [133] that was obtained using a pseudo-spectral code solving the Navier-Stokes equations. The summary of the chapter is presented in Section 4.10. In the remainder of this chapter, unless otherwise specified, the results are presented in lattice units, i.e., the velocities are scaled by the particle speed c, and the distance by the lattice spacing δ_x.

4.2 Decaying Taylor Vortex

Here, we consider a decaying Taylor Vortex in a square domain of side 2π that is periodic in both directions. This problem has no inflow/outflow or wall boundaries making it an ideal starting point to solve using the LBM. The initial conditions are given as

$$u(x, y, 0) = -u_0 cos(k_1 x) sin(k_2 y) \tag{4.1}$$

$$v(x, y, 0) = u_0 (k_1/k_2) sin(k_1 x) cos(k_2 y) \tag{4.2}$$

where u_0 is a characteristic velocity scale and k_1 and k_2 are integers. Figures 4.1 and 4.2 show the velocity contour plots of the initial field. This velocity field will decay due to viscous dissipation if no external energy is supplied. The transient solution for this problem is given by Taylor [134] as

$$u(x, y, t) = -u_0 exp[-\nu t(k_1^2 + k_2^2)] cos(k_1 x) sin(k_2 y) \tag{4.3}$$

$$v(x, y, t) = u_0 (k_1/k_2) exp[-\nu t(k_1^2 + k_2^2)] sin(k_1 x) cos(k_2 y) \tag{4.4}$$

ν being the viscosity of the fluid. An initial Reynolds number, Re can be defined based on the characteristic velocity u_0 and length of the domain 2π. The Re in this particular case is 20. The domain is represented by having 61x61 lattice nodes across the domain.

In order to assess the accuracy of the computed solution, we compare the velocity at the midsection of the domain with the analytical solution. Figure 4.3 shows the u velocity normalized by u_0 along $x = \pi$ as a function of y. The curve represents the solution computed by the LBM and the points denote the analytical solution. It can be seen that the LBM results agree well with the analytical solution. Similarly, Fig. 4.4 shows the v velocity normalized by u_0 along $y = \pi$ as a function of x. Again, it can be seen that the LBM results are in good agreement with the analytical results.

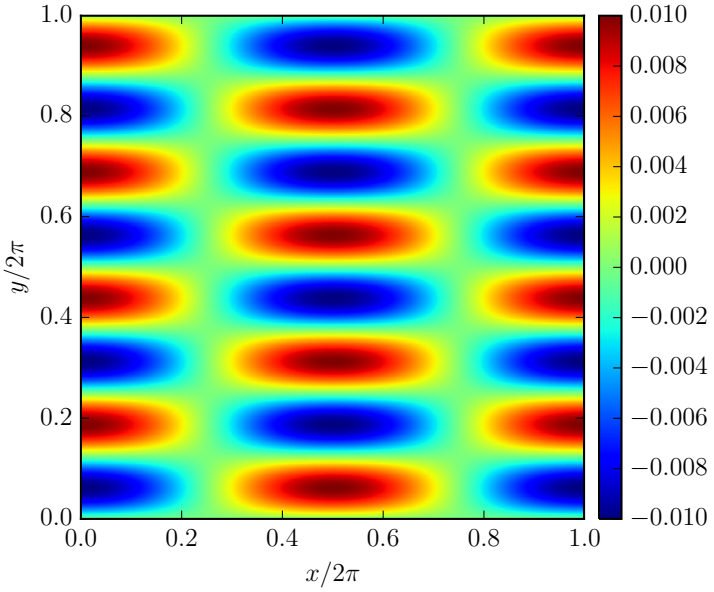

Figure 4.1: Contour plot showing the initial u velocity.

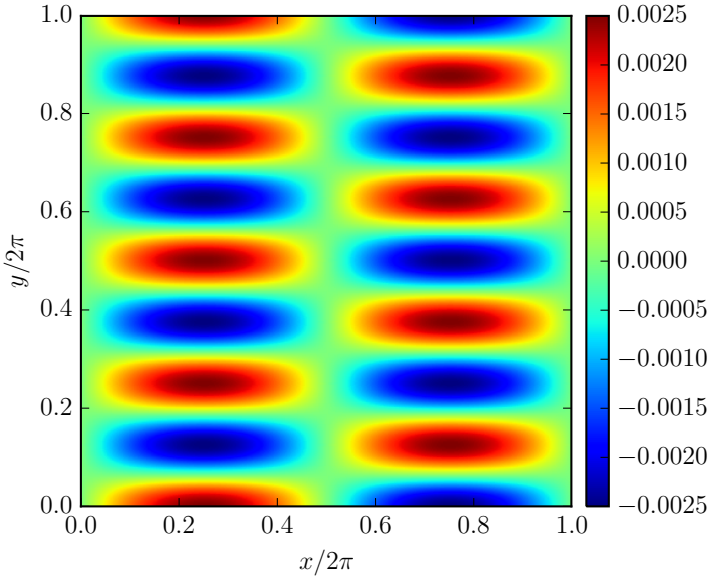

Figure 4.2: Contour plot showing the initial v velocity.

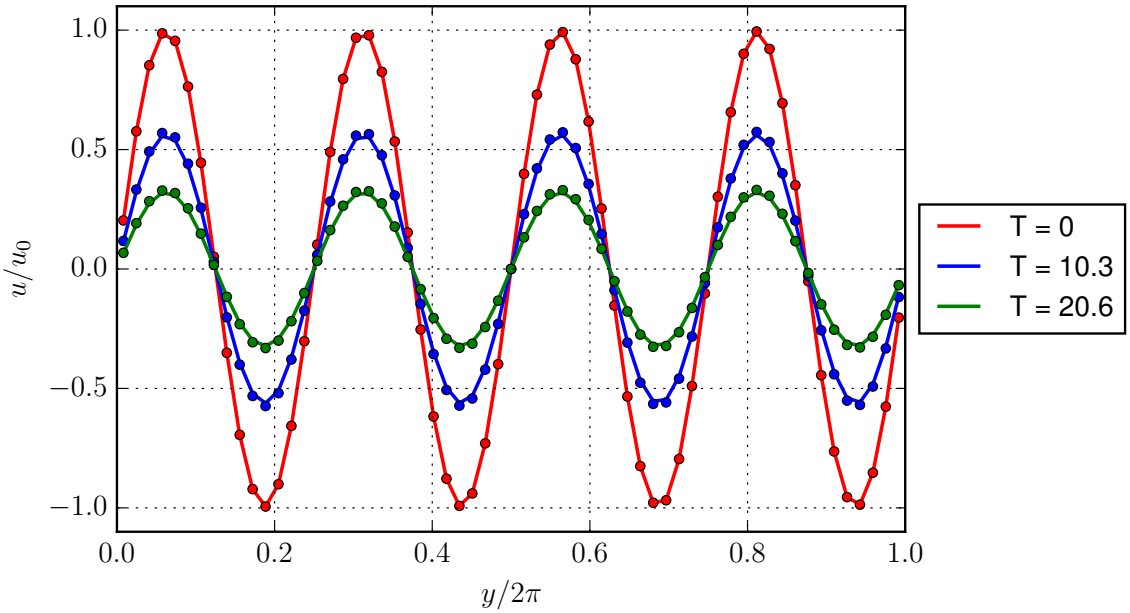

Figure 4.3: u velocity at the midsection ($x = \pi$) as a function of y.

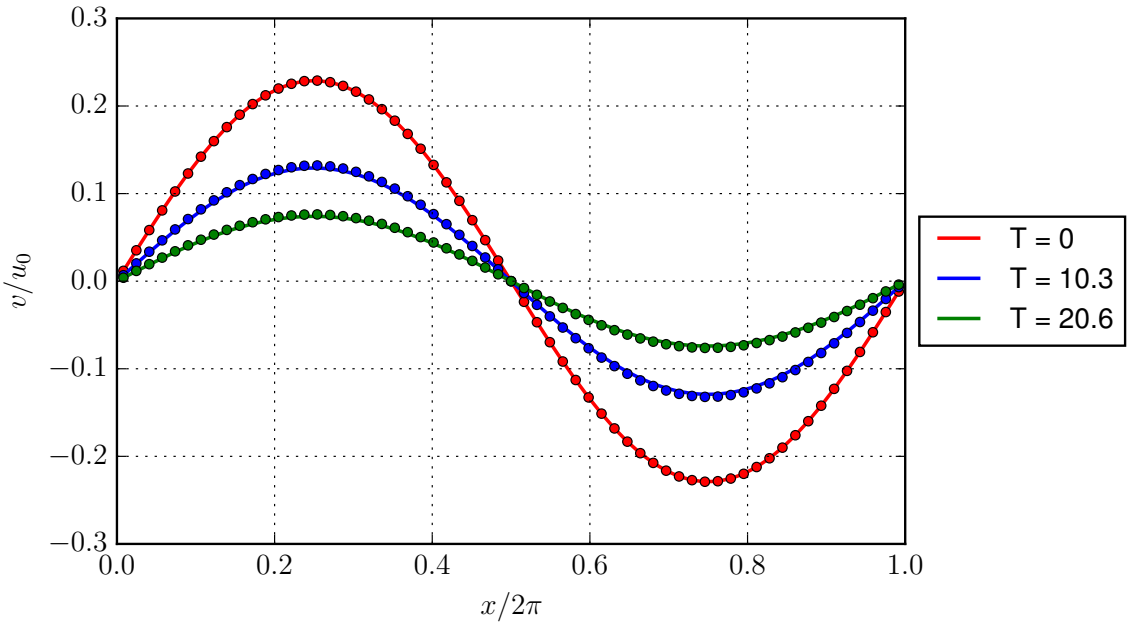

Figure 4.4: v velocity at the midsection ($y = \pi$) as a function of x.

4.3 Plane Channel Flow

Now, we consider a problem with wall boundary conditions. The plane channel flow refers to a flow that is bounded by walls on the top and bottom. The flow is driven by maintaining a constant pressure gradient between the inlet and the outlet. As discussed in Chapter 4, in the LBM, the pressure is related to the density by an equation of state. So varying the pressure implies varying density. However, the LBM allows only weak variations of density. In order to overcome this, we use a body force acting on the flow that overcomes the viscous drag at the walls and drives the flow. The body force per unit volume, F_x, that should be applied to bring about the same effect as the pressure gradient is given as

$$F_x = \frac{\partial p}{\partial x}. \tag{4.5}$$

The inlet and outlet surfaces are specified as periodic boundaries since there is no gradient in the X-direction except the pressure gradient that is now represented by a body force. Initially, the flow accelerates until the drag at the walls is balanced by the body force. The steady flow has only u velocity component which is a function of the distance from the wall y. The analytical velocity profile can be obtained by solving the Navier-Stokes equations and is given as

$$u(y) = \frac{H^2}{2\mu}\left(\frac{\partial p}{\partial x}\right)\left[\left(\frac{y}{H}\right)^2 - \left(\frac{y}{H}\right)\right], \tag{4.6}$$

where H is the height of the channel and μ is the dynamic viscosity of the fluid.

The Reynolds number Re considered in this study is 72. The flow domain is resolved by having 40 points across the channel height. We have only 3 points in the X-direction because the boundaries are periodic. In this case, the lattice spacing δ_x and time step δ_t are taken to be 1, yielding the particle speed as 1. Thus all the parameters viz., the distance, time etc., are reported in terms of the lattice spacing and time step as mentioned earlier. In this case, $H = 40$ and the relaxation parameter

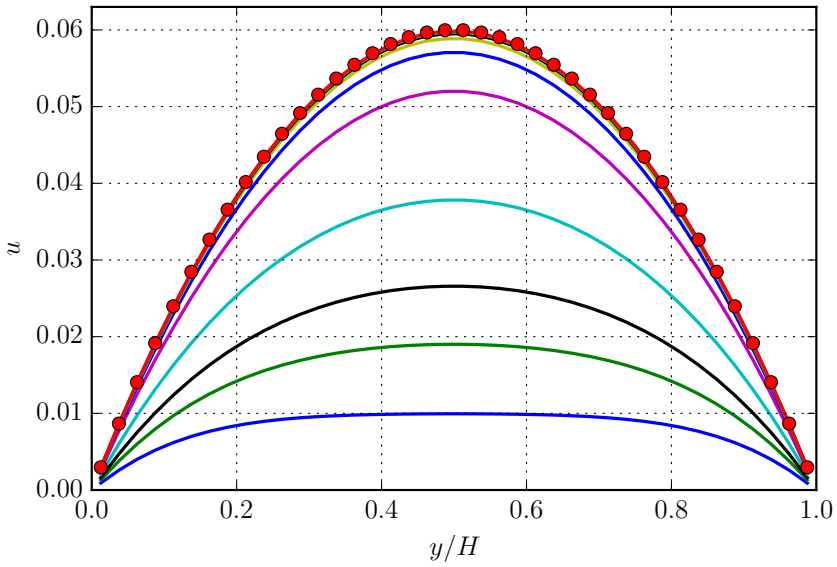

Figure 4.5: u velocity as a function of y.

is 0.6. For these parameters, the maximum velocity is 0.06. Figure 4.5 shows the temporal development of the velocity profile. The dots are the analytical solution. We can see that there is a good agreement between the LBM solution and the analytical result.

In order to assess the order of accuracy of the LBM, we repeat this computation for different grid sizes and compare the root mean square value (RMS) of the error once the solution becomes steady. Figure 4.6 shows the RMS of the error plotted against $1/N^2$, where N is the number of points that is used to resolve the length of the channel. In the LBM framework, the viscosity is dependent on the lattice spacing and hence the viscosity of the fluid is different in each case. However, the Reynolds number is kept constant and hence a comparison can be made between the error and the lattice spacing. It can be seen that the error varies linearly when plotted against $1/N^2$. This suggests that the LBM produces results that are second order accurate in space.

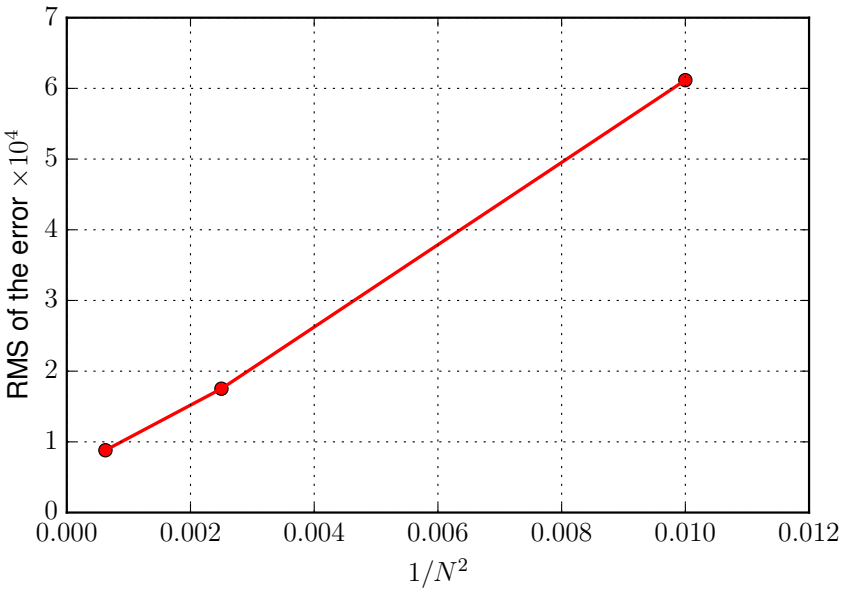

Figure 4.6: RMS error of the u velocity plotted against $1/N^2$.

4.4 Transient Couette Flow

Next, we consider the transient evolution of velocity profile in a Couette flow. This problem involves flow between two walls. The upper wall is fixed while the lower wall moves with a constant velocity U_w. A Reynolds number (Re) can be defined on the basis of the distance between the walls, H and U_w as

$$Re = \frac{U_w H}{\nu} \tag{4.7}$$

where ν is the viscosity of the fluid. The Re considered in this study is 120. The flow filed is resolved by having 40 points across between the two walls. Since the edges perpendicular to the wall are periodic, only 3 lattice nodes is used in that direction. The boundary condition for the moving wall is implemented by the momentum augmented half way bounce-back method that was explained in Section 4.6.4.

The analytical solution for this problem is given as

$$u(y,t) = U_w \left(1 - \frac{y}{H}\right) - \frac{2U_w}{\pi} \sum_{k=1}^{\infty} \frac{1}{k} sin\left(\frac{k\pi}{H} y\right) e^{-\frac{k^2\pi^2}{H^2}\nu t} \tag{4.8}$$

Figure 4.7 shows the computed (lines) and analytical (dots) velocity profiles at different time instants. The non-dimensional time, T is obtained as

$$T = \frac{tU_w}{H} \tag{4.9}$$

where t is the actual time. It can be seen from the figure that the LBM solution agrees very well with the analytical results.

4.5 Lid-Driven Cavity Flow

Until now, the bounded flow problems that we considered had features that were one-dimensional. Let us now consider a flow that has two-dimensional features. The

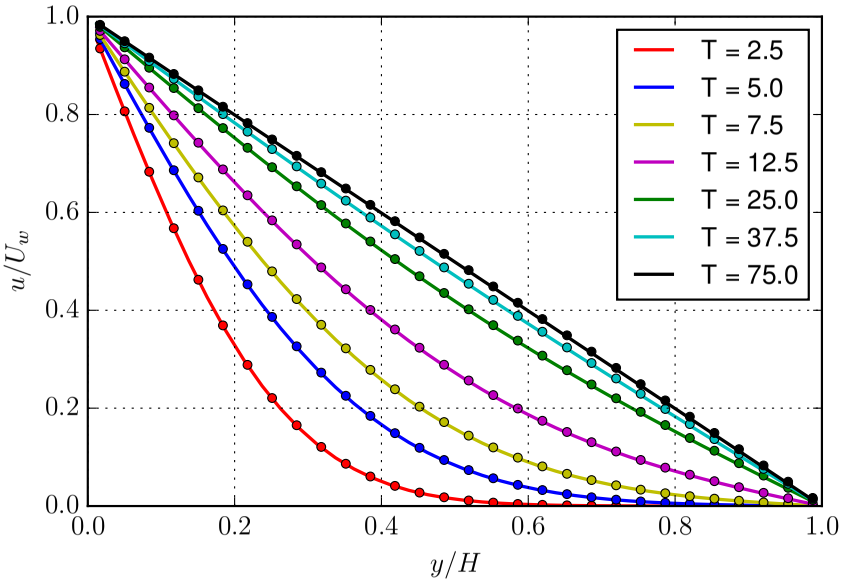

Figure 4.7: Temporal evolution of the velocity field in a transient Couette flow.

flow considered here is a lid-driven cavity. This consists of a square cavity of length L, which is bounded by stationary walls on the sides and the bottom. The fluid is set in motion by a lid on the top that moves with velocity U_l. This problem is a standard test case that is used to benchmark CFD codes. Ghia *et al.* [135] have studied this problem in detail using a vorticity-stream formulation of the Navier-Stokes equation. The data from their work will be used to compare the accuracy of the LBM results. A Reynolds number (Re) can be defined based on U_l and L as

$$Re = \frac{U_l L}{\nu} \tag{4.10}$$

where ν is the viscosity of the fluid. Three different Re are considered in this study: 100, 400 and 1000. A grid of 201 x 201 lattice points is used to resolve the flow field in all the cases. Half way bounce-back is used for the stationary walls and momentum augmented half way bounce-back is used for the moving wall. The computations are carried out until steady conditions are reached. Figure 4.8 shows the u velocity at the center of the cavity ($x = L/2$) as a function of y. The velocity is non-dimensionalized by U_l and the position by L. Similarly, Fig. 4.9 shows the v velocity at the center of the cavity ($y = L/2$) as a function of x. The velocity profiles have a strong dependence on Re. The lines represent the LBM results and the dots represent the results of Ghia *et al.* The results obtained are in good agreement with those of Ghia *et al.*. Figures 4.10 and 4.11 show the u and v contour plots of the case for $Re = 400$. Important features such as the primary vortex is captured properly with the LBM.

4.6 2D Particle-Laden Flow

Now, we look at the case of a single two-dimensional circular particle that can move in the flow field. In all our cases, the particle is resolved completely and no model is used to represent the particle-fluid coupling. Rather this is done at a fundamental level by computing the momentum change of the molecules as they bounce from the surface of the particle. The implementation of the particle motion has been

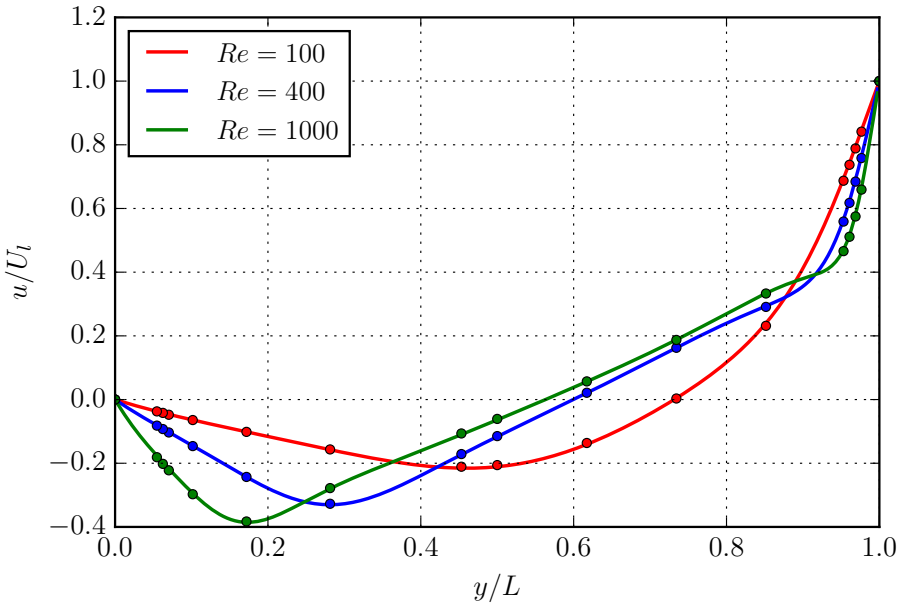

Figure 4.8: U velocity as a function of y at the midsection of the cavity ($x = L/2$).

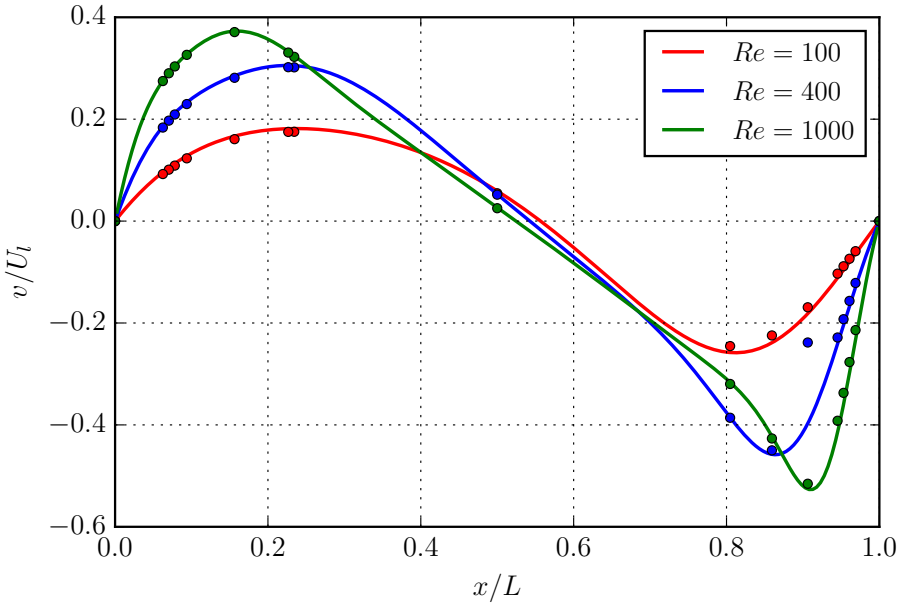

Figure 4.9: V velocity as a function of x at the midsection of the cavity ($y = L/2$).

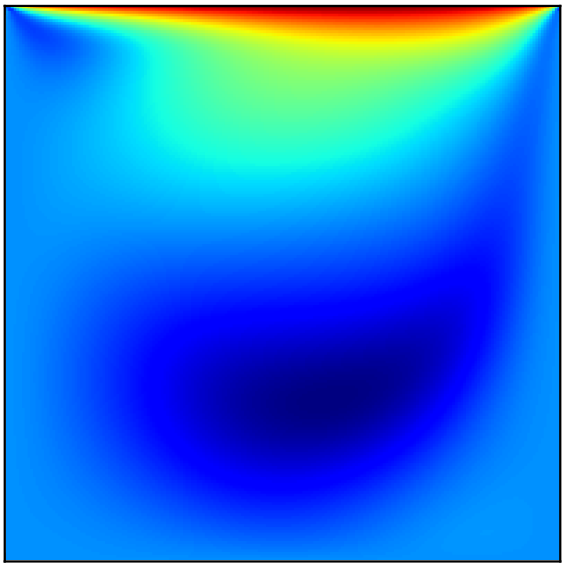

Figure 4.10: Contour plot showing the initial u velocity.

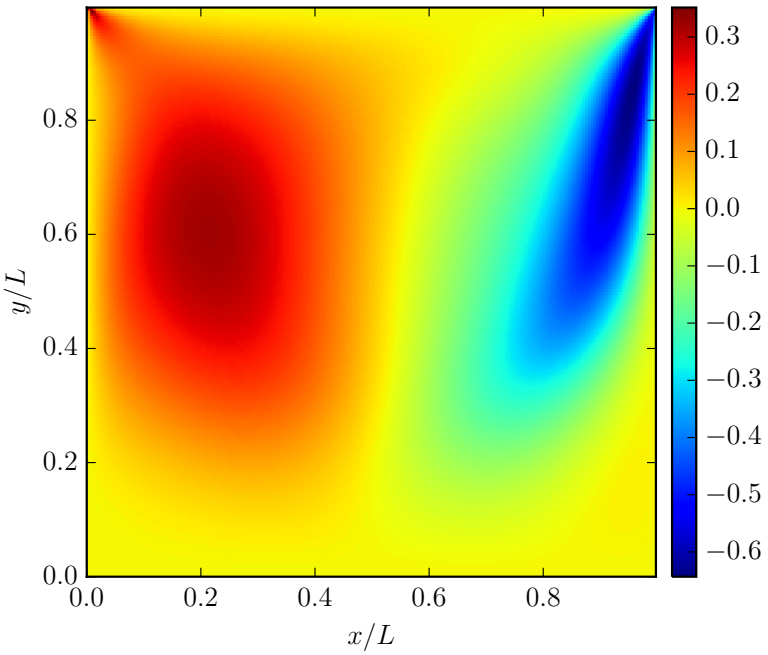

Figure 4.11: Contour plot showing the initial v velocity.

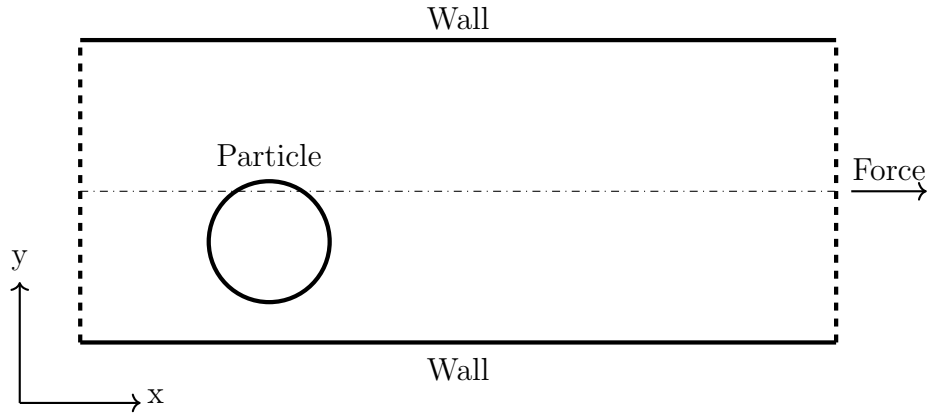

Figure 4.12: Schematic of setup for study of sedimentation of a particle.

explained in Section 4.7. We now compare our simulation results with those of Feng *et al.* [37, 38] for the case of a particle settling in a channel under the action of an imposed force (gravity), i.e. sedimentation, and a particle in a channel flow. The simulations of Feng *et al.* are two-dimensional with the fluid motion computed by solving the Navier-Stokes equation with a finite element solver.

4.6.1 Sedimentation

In this simulation, a particle is allowed to sediment between two walls under the action of an imposed force. The force acts in a direction parallel to the wall. As the particle settles, it will accelerate until it acquires a terminal velocity. A Reynolds (Re) number is defined based on the particle diameter d_p and its terminal velocity v_p as

$$Re = \frac{\rho v_p d_p}{\mu} \tag{4.11}$$

where ρ is the density of the fluid and μ is the viscosity of the fluid. A schematic of this setup is shown in Fig. 4.12. The particle is released from different y locations during different simulations.

Based on the value of the Re, Feng *et al.* [37] observed five distinct regimes of particle migration trajectories as listed in Table 4.1. At low Re, the centerline of the

Table 4.1: Particle migration regimes for a particle settling in a channel under gravity [37].

Regime	Description	Approx. Re number range
A	Steady equilibrium with monotonic approach	0.1∼2
B	Steady equilibrium with transient overshoot	3∼20
C	Weak oscillatory motion	20∼60
D	Strong oscillatory motion	60∼300
E	Irregular oscillatory motion	>300

channel would be the equilibrium position for the particle. When the Re increases, the top down symmetry of the flow around the particle begins to vanish due to periodic vortex shedding. This causes the particle to oscillate. A detailed explanation of this particle migration is given in Ref. [37].

The first set of simulations we carried out with the LBM was to assess the method for the sedimentation problem. The particle is allowed to settle under the influence of a force which acts in a direction parallel to the walls. The H/d (channel width to particle diameter) ratio is the same as that used by Feng *et al.* [37]. The inlet and the outlet are specified as periodic boundary conditions. A qualitative comparison of results obtained from the LBM with that of Feng *et al.* [37] is presented in Fig. 4.13. The Re is based on the particle terminal velocity as mentioned earlier. Hence, it is not known a priori. This makes it difficult to perform a simulation where our Re matches exactly with that of Feng *et al.* [37]. In our computations, we have performed simulations where the Re lies in a range where the particle behavior is similar to that observed by Feng *et al.* [37] and compared with their results. Hence, only a qualitative comparison can be made between the two figures. For this reason, the results are not plotted on the same graph.

It can be seen that for the regimes shown above, the LBM trends are in good agreement with that of Feng *et al.* Consider Figs. 4.13a and 4.13b. These figures show

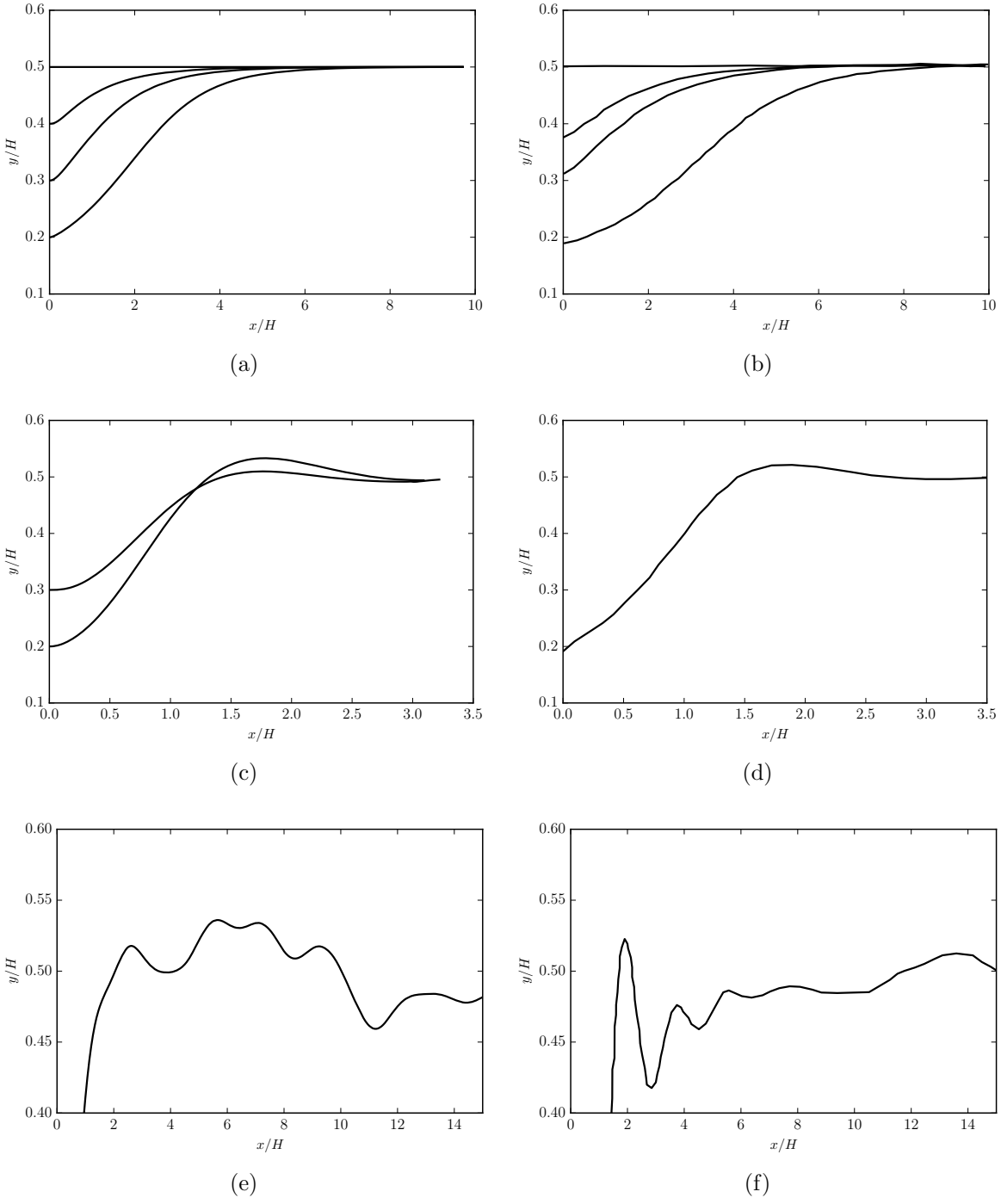

Figure 4.13: Particle migration trajectories for sedimentation: (a) Regime A LBM (Re = 1.224); (b) Regime A Feng *et al.* [37] (Re = 0.522); (c) Regime B LBM (Re = 10.8); (d) Regime B Feng *et al.* [37] (Re = 3.23); (e) Regime C LBM (Re = 48.15); (f) Regime C Feng *et al.* [37] (Re = 27.6).

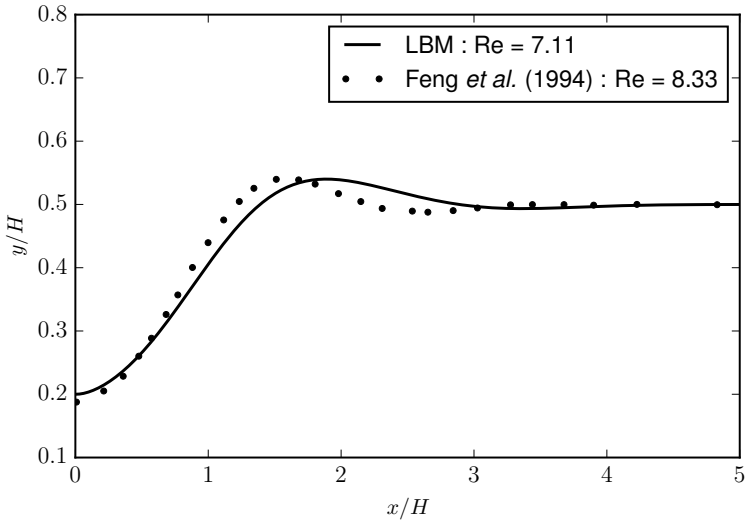

Figure 4.14: Quantitative comparison of particle migration trajectories at Regime B.

results for low Re when the particle migrates to the centerline of the channel as its equilibrium location. The LBM predicts this migration. There are some quantitative differences. For example, when the initial location is about y/H of 0.2, the particle reaches the axis at x/H of 7 in the LBM whereas the results of Feng *et al.* [37] show the equilibrium being reached at about 9. The difference is likely on account of the difference in Re between our simulations and that of Feng *et al.* [37]. We have computed one case where the Re is reasonably close to that of Feng *et al.* [37]. Figure 4.14 shows a quantitative comparison for this particular case. It can be seen that there is good agreement between the current work and that of Feng *et al.* [37]. Regimes D and E are difficult to simulate using the Single Relaxation Time (SRT) collision operator of the LBM. To achieve the high Re required to simulated these regimes, the relaxation parameter (τ) in the BGK collision operator has to be close to 0.5 which would make the computations unstable. The multiple relaxation time (MRT) implementation [115, 116] of the LBM can, however, be employed to address this challenge and will be used later in this work.

4.6.2 Neutrally Buoyant Particle in a Channel Flow

In the next set of simulations, we consider the motion of a neutrally buoyant particle in a channel flow. A Reynolds number Re_p based on the particle radius r and height of the channel H is defined as follows

$$Re_p = \frac{U_{max} r^2}{\nu H} \tag{4.12}$$

where U_{max} is the maximum velocity of the fluid, and ν is the viscosity of the fluid.

For this set of simulations, Feng *et al.* [38] observed the Segré-Silberberg effect where the particle migrates to a position between the centerline and the wall irrespective of the position from which it is released. Figure 4.15 shows a comparison between the particle trajectory obtained in this work and that of Feng *et al.* [38] at a Re_p of 0.875. For this Re_p, Feng *et al.* [38] have reported only the trajectory for the particle released from the centerline. There is a good agreement between the result of Feng *et al.* [38] and our results. From the LBM computations, it can be seen that when the particle is released from the center, it takes a longer time to come to its equilibrium position than when it is released at other locations. The equilibrium position also seems to be at some distance midway between the wall and the centerline. These trends are in agreement with the results of Feng *et al.* [38] for a Re_p of 0.625 (not shown here).

4.7 Three Dimensional Channel Flow

Next, we look at a three dimensional problem. The flow scenario considered here is that of a channel flow. The flow is driven by a constant pressure gradient. As done in the case of a two-dimensional channel flow, the pressure gradient is represented by means of a body force. The top and bottom surfaces are walls while the other surfaces are periodic. The fully-developed profile corresponds to a parabolic profile that varies depending on the position of the point under consideration with respect to

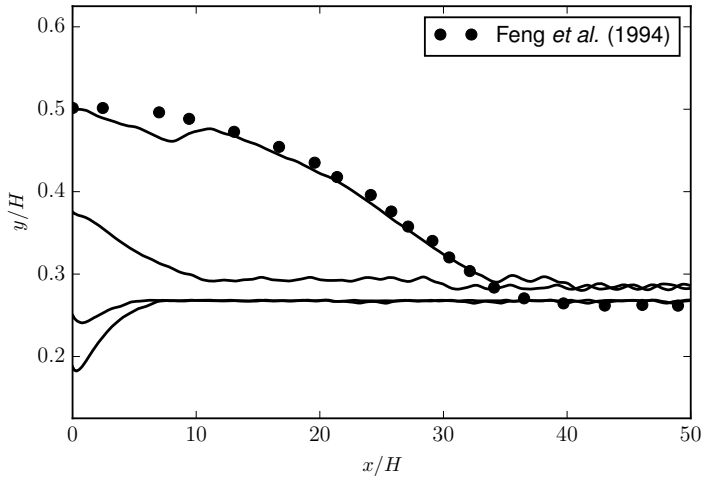

Figure 4.15: Comparison of the particle migration trajectories for a neutrally buoyant particle in a channel flow at $Re_p = 0.875$.

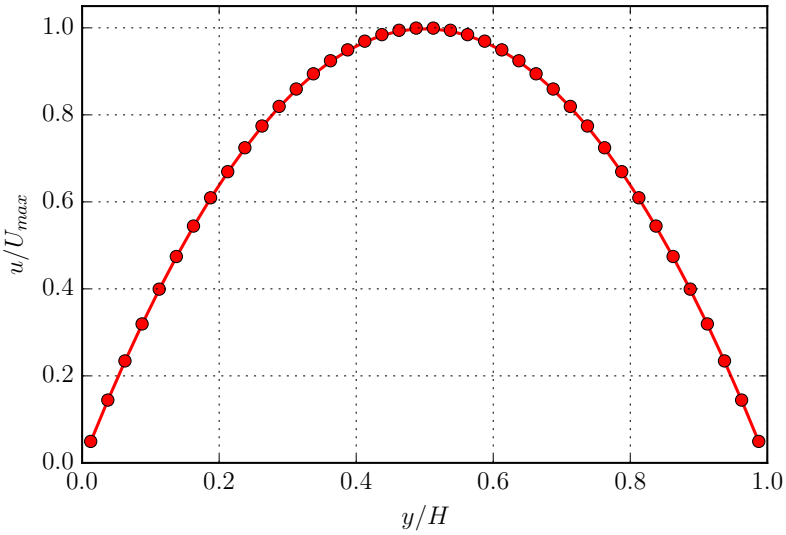

Figure 4.16: Steady state velocity profile in a channel flow.

the walls. The analytical velocity profile is given in Eqn. 4.6. A D3Q19 lattice is used in this simulation. The 3D code is parallelized using the Message Passing Interface (MPI). A 1D domain decomposition is used for this particular work. The simulation is carried out at a Reynolds number of 72. 40 lattice nodes are used to resolve the flow in the wall normal direction. Since the other directions are periodic, we have 16 and 3 lattice nodes in those directions. Figure 4.16 shows the non-dimensional velocity profile as a function of the non-dimensional distance from the wall. The lines represent the LBM results and the dots the analytical solution. It can be seen that there is good agreement between the LBM and the analytical results.

4.8 Sedimentation of a Sphere in a Duct

In order to check the particle motion implementation in the 3D code, we simulate a case of a sphere sedimenting in a duct. Experimental results are available for this problem from the work of Miyamura *et al.* [136] and computational results (from LBM) are available from the work of Aidun *et al.* [53]. In this problem, a sphere of diameter d is released from the center of a square duct of size L. In the creeping

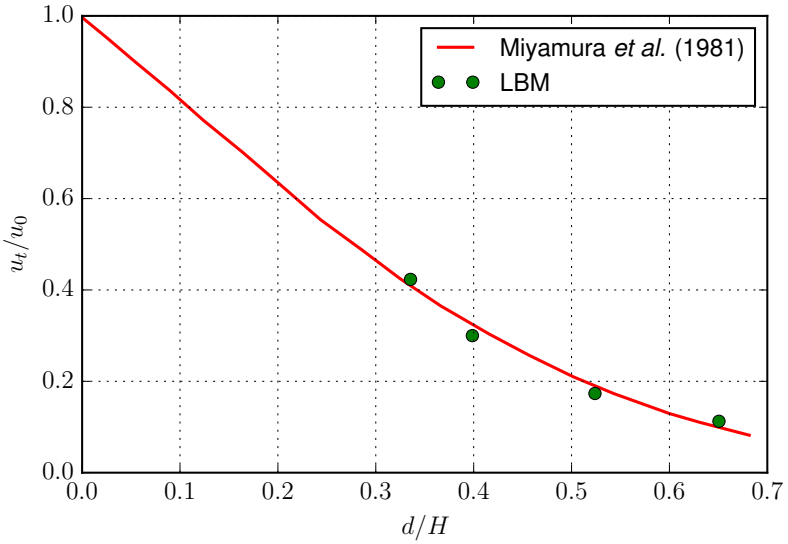

Figure 4.17: Terminal velocity of the particle for different d/L ratios.

regime, when the particle is not bounded by any flow, its terminal velocity u_0 can be obtained from Stokes drag as

$$u_0 = \frac{1}{18}\frac{(\rho_p - \rho_f)}{\mu} g d^2 \tag{4.13}$$

where ρ_p and ρ_f are the density of the particle and fluid respectively, μ is the dynamic viscosity of the fluid and g is the acceleration due to gravity. The presence of the walls however reduce the terminal velocity of the particle. The reduction factor, u_t/u_0 is plotted against d/L in Fig. 4.17. Two different cases are tried out: one with the half way bounce-back boundary condition for the particle and another with a second order accurate bounce-back boundary condition for the particle. The flow is resolved by having 512 nodes across the length of the duct and 32 x 32 nodes across its cross section. The terminal velocities predicted by our LBM code are in reasonably good agreement with the experimental results as well as the LBM results of Aidun *et al.* [53].

4.9 Turbulent Channel Flow

Until now, all the cases that we have examined are laminar flows. Now, we will consider a turbulent flow problem. Numerous studies have reported the statistics of a fully-developed turbulent channel flow. Kim *et al.* [137] in a seminal work employed the Direct Numerical Simulations (DNS) to study the turbulent channel flow. Subsequently, this work has been used as a benchmark to test DNS codes. In a recent work, Lee and Moser [133] have reported DNS simulations of a turbulent channel flow for up to a Re_τ of 5200. The detailed statistics of these simulations is available at the website: http://turbulence.ices.utexas.edu/ and will be used to test our DNS code.

We consider a turbulent channel flow with friction Reynolds number $Re_\tau \approx 180$. Re_τ is defined as

$$Re_\tau = \frac{u_\tau \delta}{\nu}, \tag{4.14}$$

where u_τ is the friction velocity, δ is half the channel height and ν is the viscosity of the fluid. The friction velocity, u_τ is obtained as

$$u_\tau = \sqrt{\frac{\tau_w}{\rho}}, \tag{4.15}$$

where τ_w is the wall shear stress and ρ is the density of the fluid. The setup is similar to that of a laminar channel flow. The upper and lower surfaces are walls while the other surfaces are periodic. In order to achieve the low viscosities needed for these relatively high Re simulations, the relaxation parameter has to be close to 0.5. The creates instabilities when the SRT collision operator is used. In order to circumvent this issue, the Multiple Relaxation Time (MRT) collision operator is used. Details about the lattice weights as well as the transformation matrix for the D3Q19 lattice can be found in the Appendix. The LBM has been used in past works to do a DNS of a turbulent channel flow [138, 139]. Our work will follow a similar path. Similar to the convention adopted in the laminar channel flow, the flow is along the X-axis,

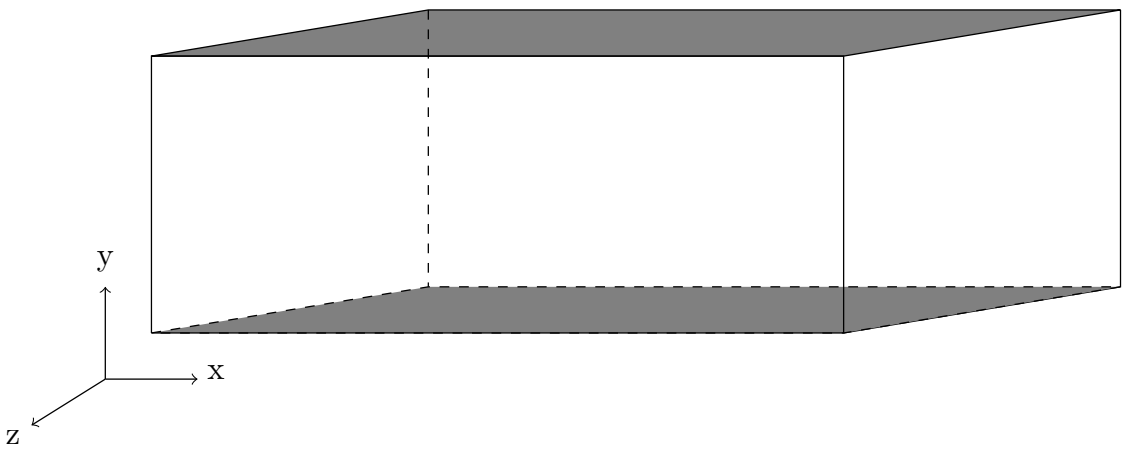

Figure 4.18: Schematic showing the setup for the DNS of a turbulent channel flow.

walls are normal to the Y-axis and the Z-direction is periodic. A schematic of the flow setup is shown in Fig. 4.18.

4.9.1 Numerical Parameters

In Direct Numerical Simulations (DNS) of a turbulent flow, all relevant flow scales are resolved. The Kolmogorov length scale, η_k refers to the scale where the inertial and viscous effects are in balance. At length scales smaller than η_k, viscous effects dominate. The grid used in DNS studies should be at least of the order of η_k so that most of the energy containing eddies are captured. Further, in the case of wall-bounded turbulent flows, there is another length scale l_v, referred to as the viscous length scale where the effect of the wall is felt. The viscous length scale can be determined from u_τ and ν as

$$l_v = \frac{\nu}{u_\tau}. \tag{4.16}$$

Usually, l_v is smaller than η_k. The grid employed in a DNS study should thus be of the order of l_v to capture the near wall effects correctly. All the length scales reported in this section are normalized by l_v and are indicated with a superscript $'+'$. Thus,

$$y^+ = \frac{y}{l_v}. \tag{4.17}$$

In our simulation, we first fix the Re_τ as 180. The grid used in our simulation is such that the first grid point is at a distance of $y^+ = 1.25$. Since the walls are represented by the half-way bounce-back scheme, we have grid spacing normalized by the viscous length scale as $\delta_x^+ = 2.5$. If we take the grid spacing to be $\delta_x = 1.0$, then the viscous length scale is $l_v = \dfrac{1}{\delta_x^+} = 0.4$. The next step is to find u_τ. In our simulation, we the fix time step $\delta_t = 1$ which yields the speed of the fluid particle to be 1. In order to satisfy the low Mach number constraint, the maximum velocity should be about 0.15. Fixing maximum velocity as 0.1, and assuming that $u_{max} \approx 20u_\tau$ for this Re_τ, we get $u_\tau = 5 \times 10^{-3}$. From Eq. (4.17), we can get the kinematic viscosity as $\nu = 2 \times 10^{-3}$. The relaxation parameter is related to the viscosity as

$$\nu = (\tau - 0.5)c_s^2\delta_t. \tag{4.18}$$

The relaxation parameter is found from this equation to be 0.506. Now, from Eq. (4.14), we find δ to be 72, which yields the channel height to be 144. The length and depth of the channel are 6δ and 3δ respectively. This ensures that the two point correlation vanishes at half the length of the domain. Thus the grid size is $432 \times 144 \times 216$ in the x, y and z directions respectively.

Since we know u_τ, we can find the shear stress at the wall from Eq. (4.15). Taking the fluid density to be 1.0, we get $\tau_w = 2.5 \times 10^{-5}$. A momentum balance on the entire domain would yield that at statistically steady conditions, the shear stress at

the walls is balanced by the pressure gradient times the channel height. In LBM, we represent the pressure gradient as a body force. Thus we have

$$F_x = \frac{dp}{dx} = \frac{2\tau_w}{H}. \tag{4.19}$$

This yields the body force as 3.4722×10^{-7}. We now have all the parameters that are required for this study.

4.9.2 Initial Conditions

In order to generate turbulence, a proper choice of initial condition is critical. In this work, the initial mean velocity is specified according to the $1/7^{th}$ power law as

$$u(y) = \left(1 - \frac{y}{\delta}\right)^{1/7} U_{max}, \tag{4.20}$$

where $U_{max} = 0.1$ as discussed previously. The coordinate system at the center of the channel so that y varies from $-\delta$ to $+\delta$. Now, a perturbation is superimposed on this mean field to generate turbulence. This perturbation is such that it excites the first few Fourier modes of the turbulence field via nonlinear interactions. This ensures that the turbulence is sustained. In this work, we have specified initial conditions as done in the work of Premnath *et al.* [139]. The initial perturbations are:

$$u_0' = \epsilon L_1 sin\left(\frac{2\pi y}{L_2}\right)\left[cos\left(\frac{2\pi x}{L_1}\right) sin\left(\frac{2\pi z}{L_3}\right) + \frac{1}{2}cos\left(\frac{4\pi x}{L_1}\right) sin\left(\frac{2\pi z}{L_3}\right) + \frac{1}{2}cos\left(\frac{2\pi x}{L_1}\right) sin\left(\frac{4\pi z}{L_3}\right)\right], \tag{4.21}$$

$$v_0' = -\epsilon L_2\left[1 + cos\left(\frac{2\pi y}{L_2}\right)\right]\left[sin\left(\frac{2\pi x}{L_1}\right) sin\left(\frac{2\pi z}{L_3}\right) + sin\left(\frac{4\pi x}{L_1}\right) sin\left(\frac{2\pi z}{L_3}\right) + sin\left(\frac{2\pi x}{L_1}\right) sin\left(\frac{4\pi z}{L_3}\right)\right], \tag{4.22}$$

$$w_0' = -\epsilon L_3 sin\left(\frac{2\pi y}{L_2}\right)\left[\frac{1}{2}sin\left(\frac{2\pi x}{L_1}\right)cos\left(\frac{2\pi z}{L_3}\right) + \frac{1}{2}sin\left(\frac{4\pi x}{L_1}\right)cos\left(\frac{2\pi z}{L_3}\right) + \frac{1}{4}sin\left(\frac{2\pi x}{L_1}\right)cos\left(\frac{4\pi z}{L_3}\right)\right], \tag{4.23}$$

where L_1, L_2 and L_3 are the lengths of the domain in X, Y and Z directions respectively and ϵ is the strength of the perturbation. No perturbations are applied to the density field.

4.9.3 Results and Discussion

Mean Profiles: The computations are carried out until the turbulence is fully-developed and the statistics are steady. To ensure this, we determine a time scale t_f which represents the time taken by a fluid element moving with the friction velocity to completely move out of the domain. Thus we have,

$$t_f = \frac{L_1}{u_\tau}. \tag{4.24}$$

For the current case, $t_f \approx 1 \times 10^5$. After $1t_f$ the mean profiles are obtained. In order to get the mean profiles, averaging is done in the streamwise and spanwise direction as well as in time. Temporal averaging was done for another $1t_f$ to get results independent of the sample size. Figure 4.19 shows the comparison between the mean velocity obtained using the LBM in this work with that obtained using a pseudo-spectral solver of the Navier-Stokes by Lee and Moser [133]. Both the velocity and the distance are scaled by wall units. It can be seen that for $y^+ < 25$ the two profiles agree closely with each other. This shows that the resolution employed near the wall is adequate to capture the relevant physics. At $y^+ > 25$, the LBM solution agrees reasonably well with the difference being less than 5%.

For wall-bounded turbulent flows, it is a well established fact that there is a viscous region where the u^+ varies linearly with y^+. This extends to about $y^+ \approx 10$. This is followed by a region where the u^+ varies logarithmically with y^+. This region is referred to as the log-law region and extends from $y^+ \approx 30$. Figure. 4.20 shows the

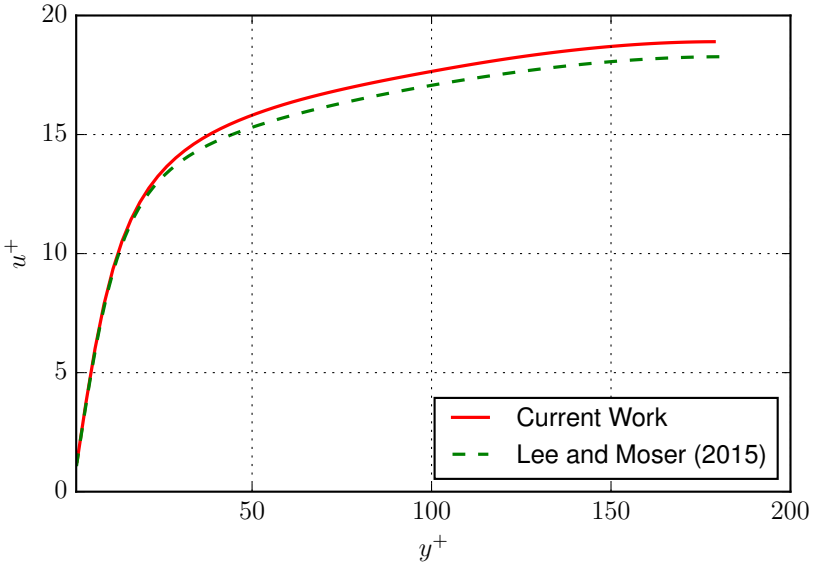

Figure 4.19: Mean velocity profile normalized by the friction velocity in a fully-developed turbulent channel flow.

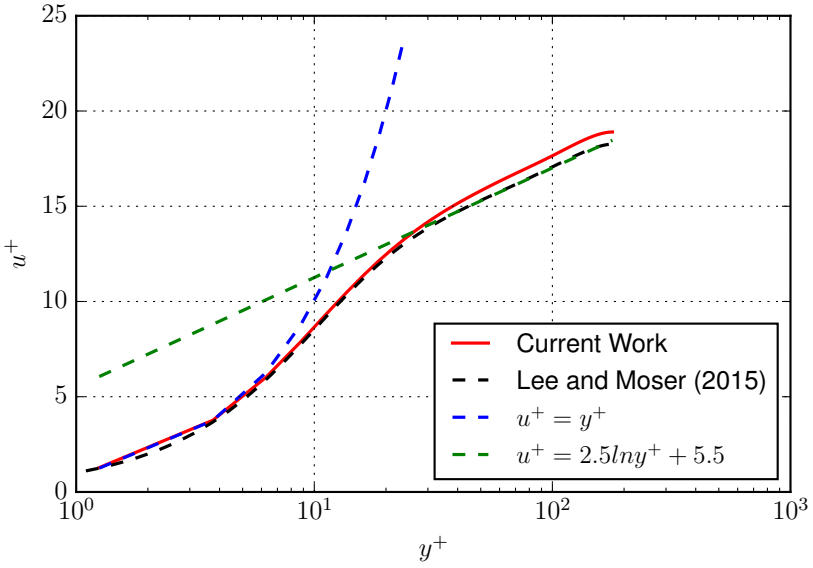

Figure 4.20: Semi-log plot of the mean velocity profile normalized by the friction velocity in a fully-developed turbulent channel flow.

mean velocity profile plotted on a semi-log scale. The linear and log curves are also shown. We can see that the LBM predicts both the linear and the log-law region. For $y^+ < 8$ there exists a linear region and for $y^+ > 25$, there is a logarithmic variation. Next we compare the intensities of the fluctuating quantities.

Root Mean Square of the Fluctuations: In order to ensure that our computational method captures the physics of turbulent flows correctly, it is important to compare the statistics of the fluctuating quantities as well. In this section, we compare the fluctuating intensities of the three components of velocities and vorticity as well as the pressure. In order to obtain these, the averaging time has to be longer than that for the mean profiles. In our current work, we average for about $\sim 3.5t_f$ in addition to the spatial averaging.

Figure 4.21 shows the intensity of the streamwise velocity component normalized by the friction velocity. It can be seen that this reaches a peak of about $2.75u_\tau$ at a y^+ of about 15. This is because the production of turbulent kinetic energy peaks at this region. As we move toward the wall, the intensities vanish because of the no-slip condition. This gives rise to a steep gradient in the region close to the wall. As we move toward the center, the intensities decrease since production of turbulent kinetic energy decreases. The LBM results capture these effects. Moreover, they are in reasonable agreement with the results of Lee and Moser [133], agreeing within 5%. Figures 4.22 and 4.23 show the intensity of the wall-normal and spanwise velocity fluctuations respectively. As was the case with the streamwise velocity fluctuations, the peak occurs at a region close to the wall. Comparison with the results of Lee and Moser reveals good agreement, agreeing within 5%.

Next, we compare the Reynolds stress, i.e. $< u'v' >$. Figure 4.24 shows the negative of Reynolds stress plotted against the distance from the wall. The Reynolds stress is zero at the wall, is maximum at about y^+ of 30 and then becomes zero at the center-line of the channel. The LBM results agree within 2% of the results of Lee and Moser [133].

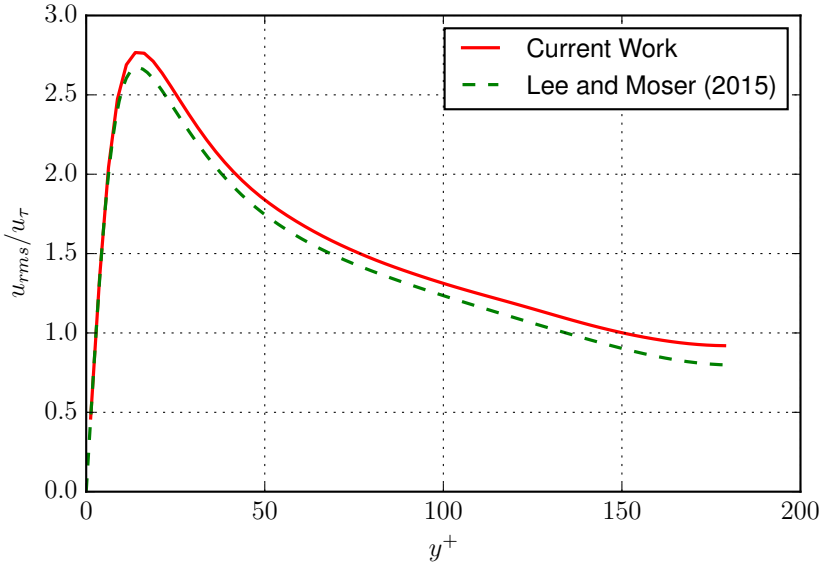

Figure 4.21: Root mean square (RMS) of the streamwise velocity fluctuations normalized by the friction velocity in a fully-developed turbulent channel flow.

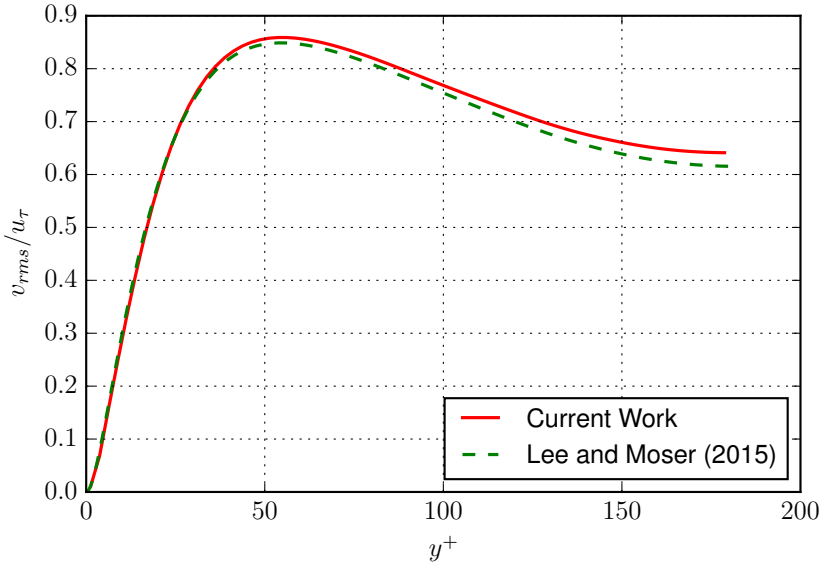

Figure 4.22: Root mean square (RMS) of the wall-normal velocity fluctuations normalized by the friction velocity in a fully-developed turbulent channel flow.

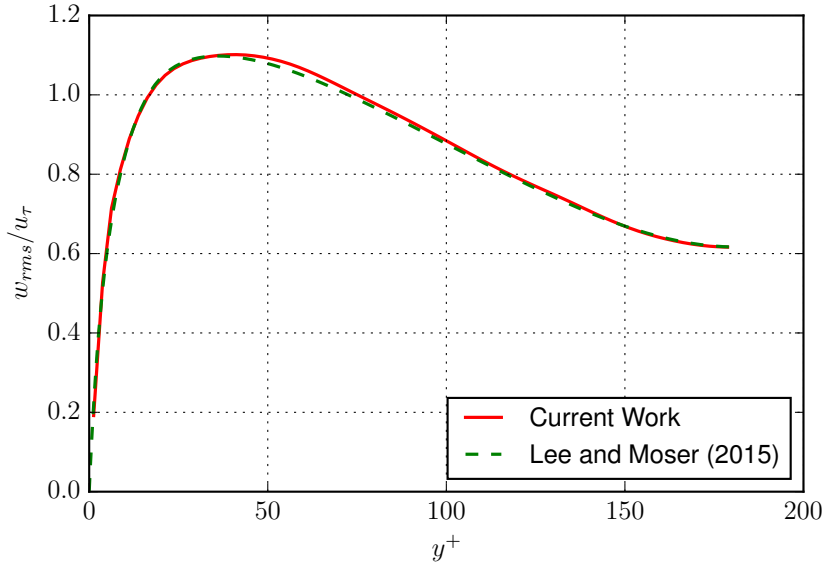

Figure 4.23: Root mean square (RMS) of the spanwise velocity fluctuations normalized by the friction velocity in a fully-developed turbulent channel flow.

Figure 4.24: Reynolds shear stress normalized by the friction velocity in a fully-developed turbulent channel flow.

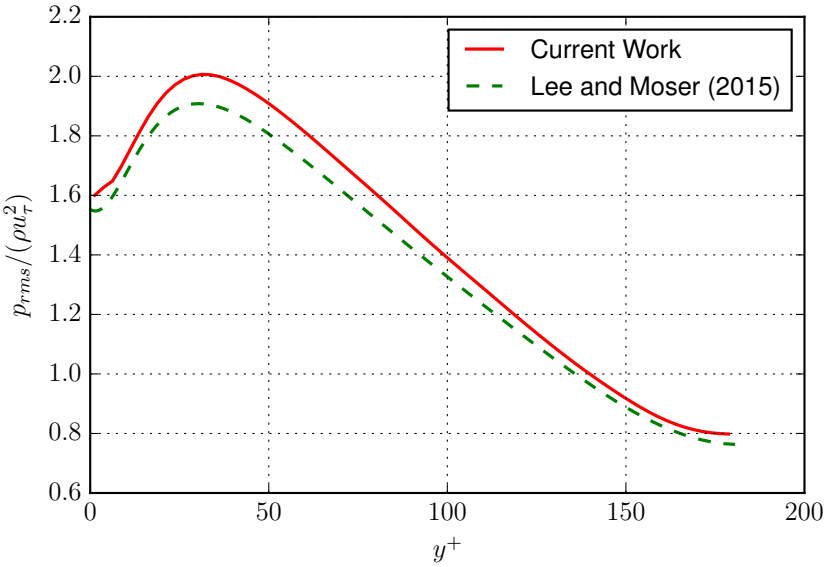

Figure 4.25: Root mean square (RMS) of the pressure fluctuations normalized by the friction velocity in a fully-developed turbulent channel flow.

We also compare the fluctuating RMS of the pressure. Figure 4.25 shows the comparison of the pressure normalized by the wall scaling parameter as a function of the distance from the wall. The pressure fluctuations start at a non-zero value at the wall. It increases initially, is maximum at about y^+ of 30 and then decreases. The results agree with those of Lee and Moser [133] within 10%. The differences are likely because the LBM allows for weak compressibility effects in the flow whereas the results of Lee and Moser are obtained using an incompressible Navier-Stokes code.

Now, we compare the variations in the fluctuations in the vorticity as we move from the wall to the center. Figures 4.26, 4.27 and 4.28 show the fluctuating vorticity in the streamwise, wall-normal and spanwise directions normalized by the wall scaling parameters. Near the wall, the vorticity components are significantly different from each other. This is due to the inhomogeneity and anisotropy of turbulence near the wall. At distances away from the wall, all the components of vorticity are similar. The LBM results are in good agreement with that of Lee and Moser [133], agreeing within 5%.

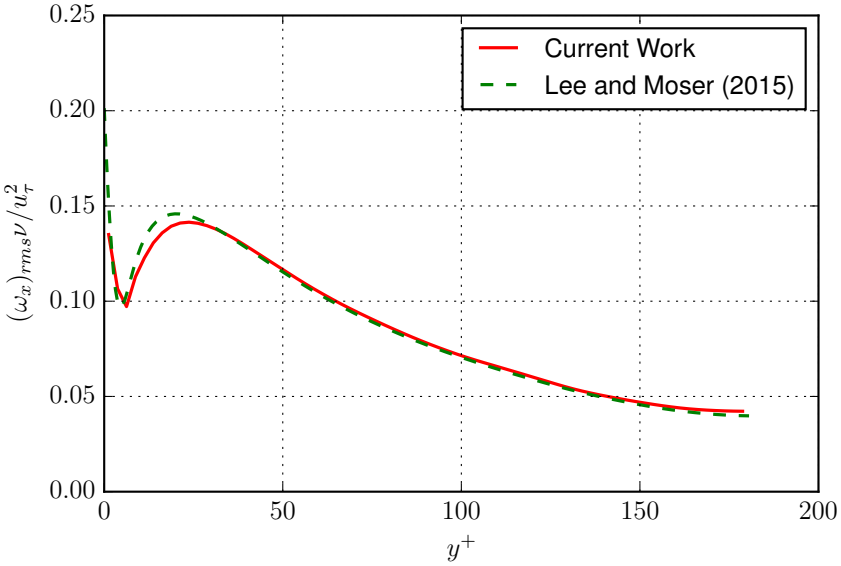

Figure 4.26: Root mean square (RMS) of the streamwise vorticity fluctuations normalized by the wall scaling parameters in a fully-developed turbulent channel flow.

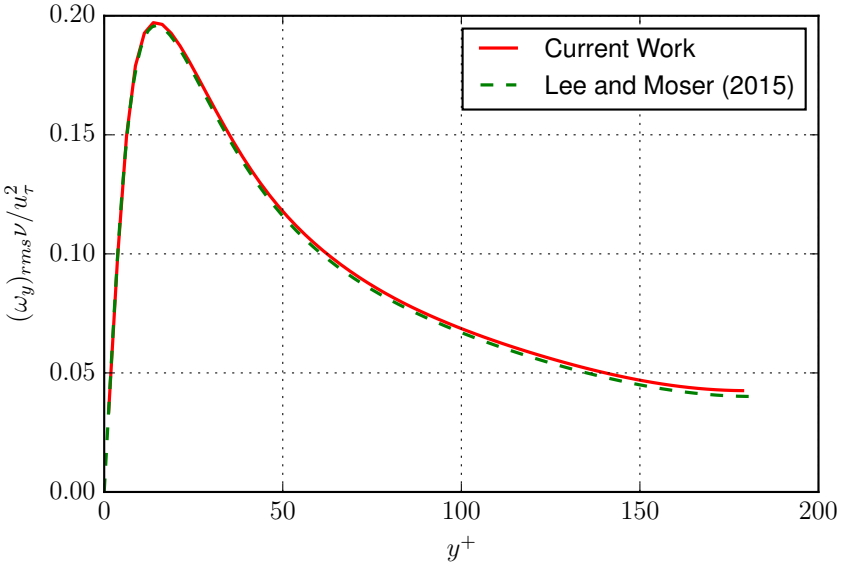

Figure 4.27: Root mean square (RMS) of the wall-normal vorticity fluctuations normalized by the wall scaling parameters in a fully-developed turbulent channel flow.

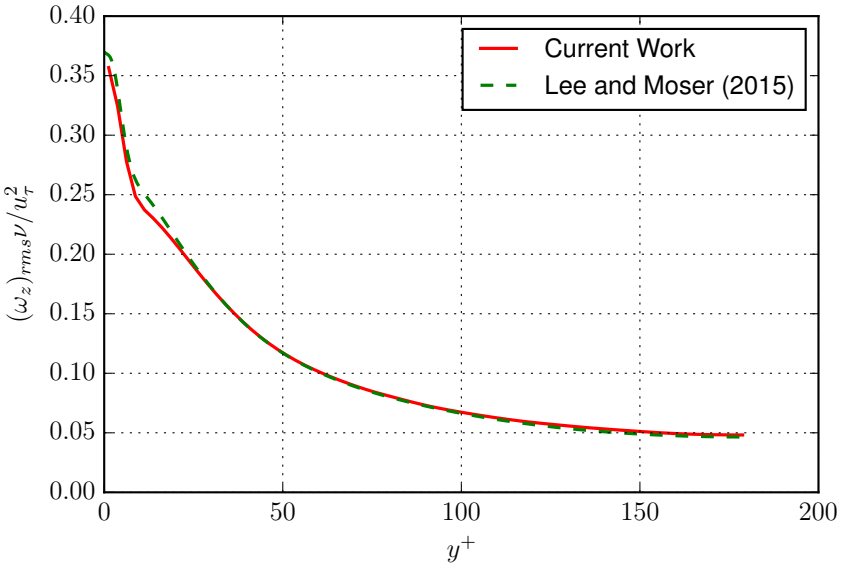

Figure 4.28: Root mean square (RMS) of the spanwise vorticity fluctuations normalized by the wall scaling parameters in a fully-developed turbulent channel flow.

Figures 4.29, 4.30 and 4.31 show the instantaneous streamwise, wall-normal and spanwise velocity contours at the mid-section of the channel ($z = 0$). Several turbulent structures are seen to be present throughout the domain. Streaks of fluid that rise from the wall at an angle of about 45^o are seen. This corresponds to the direction of the most extensional strain. There is enhanced mixing of the fluid as seen from Fig. 4.29 where, in most regions of the channel, the velocity is of the same order. Likewise Figs. 4.32, 4.33 and 4.34 show the instantaneous streamwise, wall-normal and spanwise velocity contours at the mid-section of the channel ($z = 0$). Similar trends as in the earlier figures can be observed here as well.

4.10 Summary

In this Chapter, we evaluated the LBM code developed in this study. We tested our code to study the following laminar flow problems: a decaying Taylor vortex, a channel flow (2D and 3D), transient Couette flow and a lid-driven cavity. We achieved good agreements (difference $< 5\%$) with analytical solutions (when available) and with measurements and other computations in cases where an analytical solution was not available. Then we studied the particle motion implementation in the code. The code predicted the Segré-Silberberg effect. The equilibrium position as well as the particle trajectory obtained with our code are in good agreement with prior data in the literature. Sedimentation of a sphere in a duct is simulated using this code to assess the accuracy of 3D computations. Good agreements are obtained with existing measurements and computations. Since our objective is to perform direct numerical simulations (DNS) of particle-laden flows, we assess the code to check if it predicts the turbulent features of a single phase flow. The flow under consideration is a fully-developed turbulent channel flow. Extensive results are available in the literature that report various statistical quantities. In particular, we compare the mean velocity, the fluctuating velocity, vorticity and pressure. We find that there is good agreement between the existing results and that from our code and the difference is less than

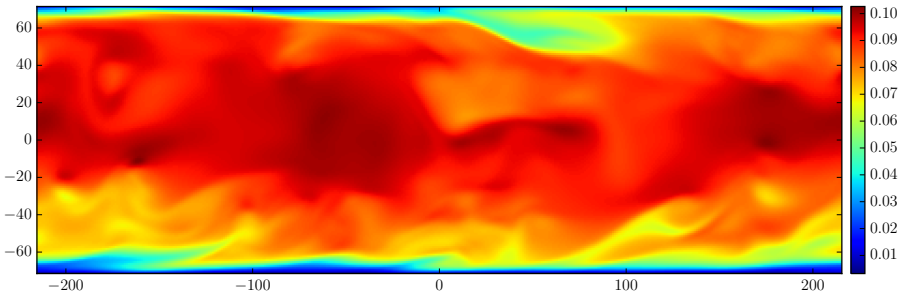

Figure 4.29: Contour plot of the instantaneous streamwise velocity in a fully-developed turbulent flow.

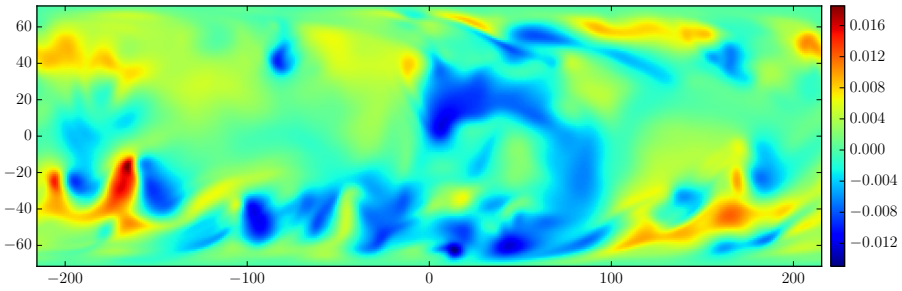

Figure 4.30: Contour plot of the instantaneous wall-normal velocity in a fully-developed turbulent flow.

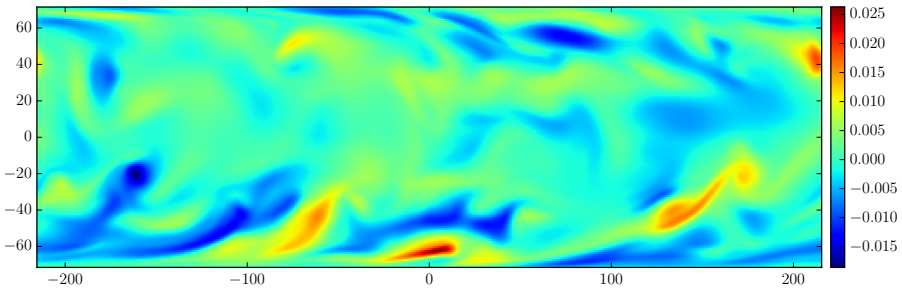

Figure 4.31: Contour plot of the instantaneous spanwise velocity in a fully-developed turbulent flow.

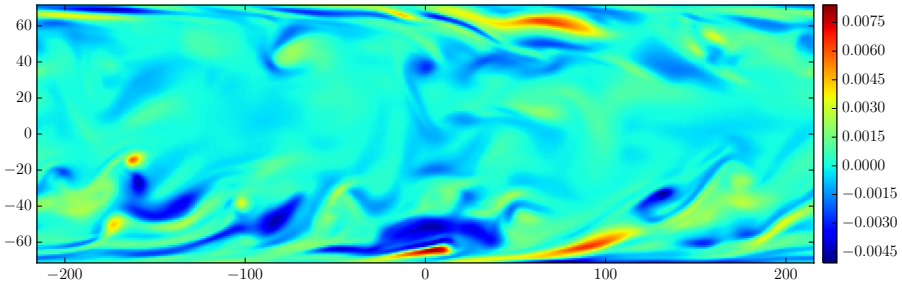

Figure 4.32: Contour plot of the instantaneous streamwise vorticity in a fully-developed turbulent flow.

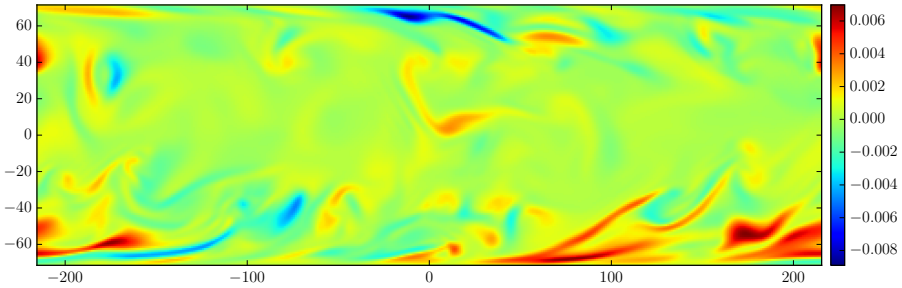

Figure 4.33: Contour plot of the instantaneous wall-normal vorticity in a fully-developed turbulent flow.

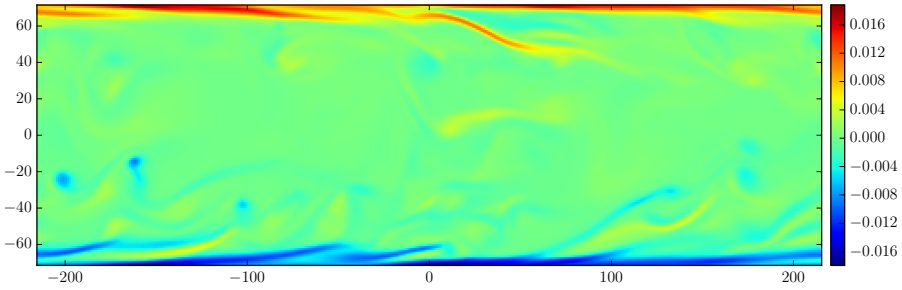

Figure 4.34: Contour plot of the instantaneous spanwise vorticity in a fully-developed turbulent flow.

5% in all cases except for fluctuating pressure where the difference is less than 10%. This is possibly due to the weak compressibility effects that are allowed in the LBM. Now we proceed to report some results of particle-laden flows that were carried out with this code.

5. POINT-PARTICLE SIMULATIONS OF PARTICLE TRANSPORT IN A TURBULENT CHANNEL FLOW

5.1 Introduction

In this chapter, the lattice-Boltzmann method (LBM) is employed to carry out direct numerical simulations of particles approximated as point-particles in the limit of $d_p < \eta_k$. Parts of this work has been submitted for publication in *International Journal for Numerical Methods in Fluids.*

As discussed in Chapter 2, the Stokes number St is an important parameter in particle-laden flows. The St is defined as the ratio of particle response time to the flow time scale, i.e.

$$St = \frac{\tau_p}{\tau_f}. \tag{5.1}$$

The particle time constant is generally used as a measure of the response time of the particle. If the particle density is much higher than the fluid density, the particle time constant, τ_p is given as, [140]

$$\tau_p = \frac{\rho_p d_p^2}{18\mu}. \tag{5.2}$$

The flow response time can be obtained as

$$\tau_f = \frac{L}{U}, \tag{5.3}$$

where L represents a length scale and U a velocity scale. For instance, in the case of a channel flow, L can be taken as the channel height and U as the maximum mean velocity. For turbulent flow in a channel of height, H, St can be written as,

$$St = \frac{\rho_p d_p^2 U}{18\mu H}. \tag{5.4}$$

Confined particle-laden flows have been studied by several researchers in the past. Segre and Silberberg [22, 23] studied the lateral migration of neutrally buoyant particles in a laminar pipe flow. They found that particles move to an equilibrium position in the pipe that is mid-way between the wall and the axis of the pipe. This effect is referred to as Segre-Silberberg effect. Feng et al. [37, 38] did numerical simulations of two-dimensional cylindrical particles in a laminar channel flow. They were able to recover the Segre-Silberberg effect. They identified that this effect is caused by the balance of three forces acting on the particle: Saffman lift [19], Magnus lift [141] and wall repulsion [142, 143].

Lau and Nathan [11] have studied the transport of particles in a turbulent pipe flow. They noticed that the radial particle concentration at the exit of the pipe was not uniform. The particles migrated toward or away from the axis depending on their St. This has been discussed in detail in Chapter 2. Figure 5.1 shows the concentration profile of particles, Θ, normalized by the bulk concentration, Θ_b at the exit of a turbulent pipe flow. At a low St of 0.3, the particle concentration near the wall is about 2.5 times the bulk concentration. For a St of 11.2, the particle concentration is high near the axis of the pipe. Particles with a St of 1.4 are distributed almost uniformly. Thus, as the St increases from 0.3 to 11.2, the radial concentration profile changes from a 'U-shape' to a '$\wedge$-shape'. The reason for this preferential migration is not well understood.

Shao et al. [144] numerically studied the effect of particles on turbulent intensities in a channel flow. They found that particle sedimentation on the walls can increase turbulent intensity from vortex shedding. If sedimentation effect is negligible, parti-

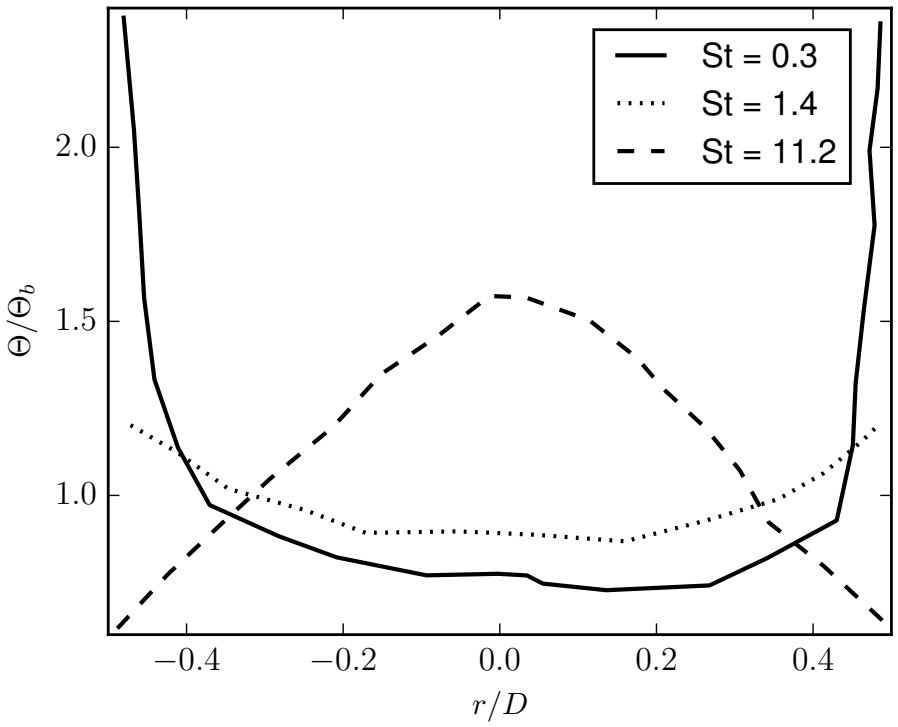

Figure 5.1: Concentration profile of particles at the exit of a turbulent pipe flow (Adapted from Lau and Nathan [11]).

cles decrease streamwise fluctuations of large scale vortices. Kidanemariam et al. [145] carried out simulations of particles in open channel flow. They found that particles lag the fluid velocity and tend to reside in low-speed streaks.

Li et al. [146] numerically studied the effect of particle motion on the carrier phase. They found that particle feedback causes the turbulence to become more anisotropic as mass loading is increased. Kulick et al. [28] experimentally investigated turbulence modulation by particles in a channel flow. They found that turbulence was attenuated by the addition of particles. The degree of attenuation increased with Stokes number, mass loading and distance from the wall. Attenuation is stronger in the transverse direction than in the streamwise direction.

While there are several studies focusing on turbulence modulation by particles, there are no numerical studies of particle transport in wall-bounded flows that clarify the mechanism responsible for the transport toward the wall or away from it. In this chapter, the lattice-Boltzmann method (LBM) is employed to carry out direct numerical simulations of particles approximated as point-particles in the limit of $d_p < \eta_k$. The next section discusses the computational method. This is followed by presentation of the results and their discussion from the point-particle direct numerical simulations (PP-DNS). The chapter ends with summary and conclusions.

5.2 The Computational Method

The lattice-Boltzmann method (LBM) is employed for our computations. Chapter 3 describes the LBM in detail and Chapter 4 presents results for several standard benchmark cases using the LBM. The implementation of point-particles in the LBM framework is described below.

The physical particles are treated in a Lagrangian framework. Since the particle size is smaller than the Kolmogorov length scale, i.e., $d_p < \eta_k$, the point-particle

approximation is employed in this work. The drag force, $\boldsymbol{F_d}$, acting on each particle is found out through a drag model and is given as

$$\boldsymbol{F_d} = \frac{1}{2}\rho_f |\boldsymbol{u_f} - \boldsymbol{u_p}|(\boldsymbol{u_f} - \boldsymbol{u_p}) C_d A, \tag{5.5}$$

where ρ_f is the fluid density, $\boldsymbol{u_p}$ is the particle velocity, $\boldsymbol{u_f}$ is the fluid velocity at the location of the particle, C_d is the drag coefficient and A is the cross-sectional area. Since the particles are spherical, the cross-sectional area, A, is given as,

$$A = \frac{\pi}{4} d_p^2, \tag{5.6}$$

where d_p is the particle diameter. Now, the location of the particle may not always coincide with the lattice point where fluid velocities are solved for. In order to obtain the velocity, a tri-linear interpolation using the neighboring eight points is employed [147]. The drag coefficient, C_d, for a particle in Stokes flow is given by

$$C_d = \frac{24}{Re}, \tag{5.7}$$

where Re is the Reynolds number based on the particle size and the relative velocity magnitude. Re is defined as

$$Re = \frac{|\boldsymbol{u_f} - \boldsymbol{u_p}| d_p}{\nu}. \tag{5.8}$$

5 A high-Reynolds number correction is incorporated into this expression to determine drag force acting on particles in turbulent flows. This modified drag coefficient is [76]

$$C_d = \frac{24}{Re}\left(1 + 0.15 Re^{0.687}\right). \tag{5.9}$$

To account for particle feedback on the fluid, the drag force is applied as an external body force to the lattice-Boltzmann equations with a reversed sign. This force is added to the source term in the lattice-Boltzmann equation.

Particle-particle collisions are modeled as elastic collisions following the approach of Li and McLaughlin [146]. If the particle computations are carried out serially, computational time for collision detection scales as $O(N^2)$, where N is the number of particles considered. In order to minimize this, the particle computations have been parallelized. The particles in each processor are stored as objects of a doubly linked-list in the corresponding processor. In the first step, particles are checked for collision with other particles in the same processor. In the next step, particles are checked for collision with other particles in the neighboring 26 processors since a three-dimensional domain decomposition is employed in this work. If a particle moves out of the processor limits, its information is transferred to the neighboring processor into which it moves and its information in the old processor is deleted. With the current implementation, computational time scales as $O(N^2/P)$, where P is the number of processors. This also ensures the load is reasonably balanced among all processors.

A turbulent channel flow with friction Reynolds number $Re_\tau \approx 180$ is simulated. Re_τ is defined as

$$Re_\tau = \frac{u_\tau \delta}{\nu}, \tag{5.10}$$

where u_τ is the friction velocity, δ is half the channel height and ν is the kinematic viscosity of the fluid. The friction velocity, u_τ, is obtained as

$$u_\tau = \sqrt{\frac{\tau_w}{\rho}}, \tag{5.11}$$

where τ_w is the wall shear stress and ρ is the density of the fluid. In order to achieve the low viscosities needed for these relatively high Re simulations, the relaxation parameter has to be close to 0.5. This would generate instabilities if a single relaxation time (SRT) collision operator is used. In order to circumvent this issue, the multiple relaxation time (MRT) collision operator is employed as discussed earlier. Details about the lattice weights as well as the transformation matrix for the D3Q19 lattice can be found in Appendix A. The LBM has been used in past works to carry out

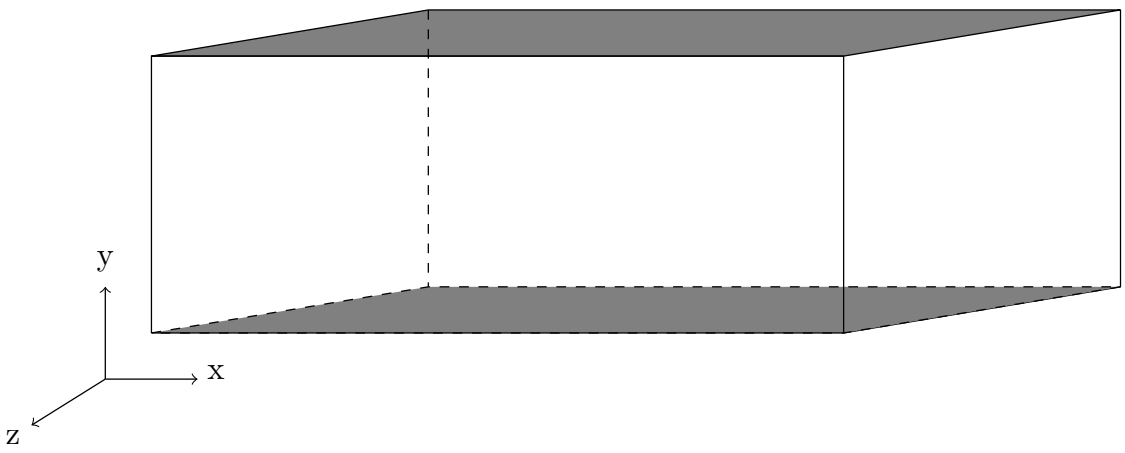

Figure 5.2: Schematic showing the setup for the DNS of a turbulent channel flow.

DNS of a turbulent channel flow [138, 139]. The flow is along the X-axis, walls are normal to the Y-axis and the Z-direction is periodic. A schematic of the flow setup is shown in Fig. 5.2.

The computations are carried out until the turbulence is fully-developed and the statistics are steady. In order to get the mean profiles, averaging is done in the streamwise and spanwise direction as well as in time.

5.3 Results and Discussion

The results and discussion below will consider the impact of particles on the mean flow and turbulent kinetic energy in the channel and also the effect of St on particle distribution across the cross section of the channel. The particle concentration profiles are obtained by separating the domain into slices in the Y-direction (i.e. normal to the walls) and then counting the number of particles in each slice. This is then normalized by the number of particles that should be in the slice if the particles are uniformly distributed. Thus each symbol represents a non-dimensional concentration of particles in that slice. Since the slices are discrete and averaging is done over a finite duration, the non-dimensional concentration shows some fluctuations. These

Table 5.1: Parameters employed for the PP-DNS simulations.

Case	St	ρ_p/ρ_f	d_p/η_k	m_p/m_f
1	0.001	1	0.2	9.31×10^{-6}
2	0.5	450	0.2	4.12×10^{-3}
3	2	1800	0.2	1.67×10^{-2}
4	10	9000	0.2	8.38×10^{-2}
5	40	36000	0.2	3.35×10^{-1}
6	100	90000	0.2	8.37×10^{-1}
7	0.5	112.5	0.4	8.38×10^{-3}
8	100	22500	0.4	1.676

fluctuations would decrease if we increase the number of particles or average over a long time. A curve is fit through the points to show the trends more clearly. Table 5.1 lists the conditions studied in this work. Notice from Table 5.1 that the particle diameter is smaller than the Kolmogorov length scale, i.e. $d_p/\eta_k < 1$, for all cases considered. Ten thousand particles are employed in the domain for the simulations. The Reynolds number based on the friction velocity, Re_τ, is 180. This corresponds to a bulk Reynolds number of about 6500.

It is expected that as the $St \rightarrow 0$, i.e. the tracer particle limit, the particles which are initially distributed uniformly in the domain will remain so. Figures 5.3a-5.3c show the normalized mean velocity, the turbulent kinetic energy (TKE), and particle number per unit volume, respectively, in a cross section of the channel. As expected, the results for the mean velocity and TKE show negligible difference from the single-phase flow results because the mass loading is only 9.31×10^{-6}. Figure 5.3c which shows the normalized particle concentration in a transverse cross-section of the channel shows a fairly uniform concentration.

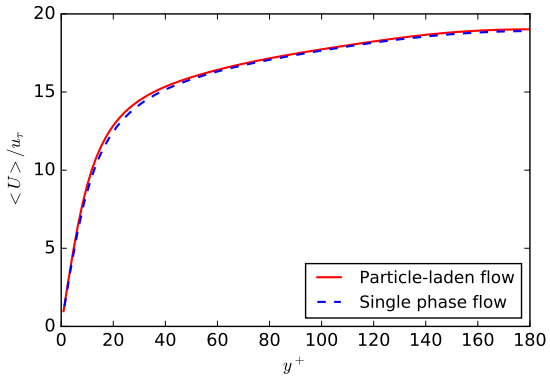

(a)

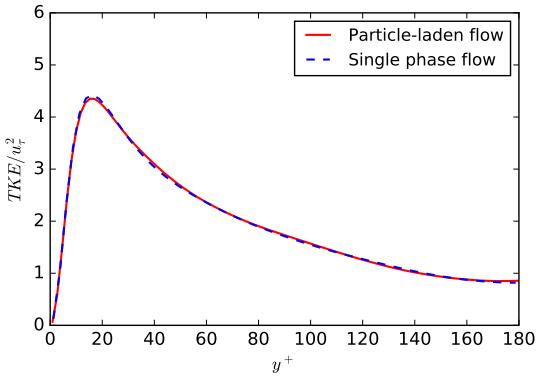

(b)

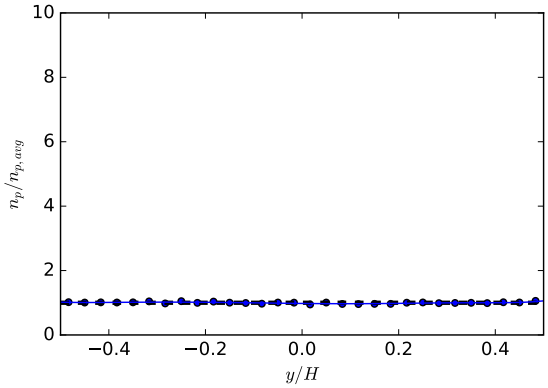

(c)

Figure 5.3: (a) Mean velocity profile; (b) turbulent kinetic energy profile; (c) particle concentration profile when $St = 0.001$, $m_p/m_f = 9.31 \times 10^{-6}$, and $d_p/\eta_k = 0.2$ (Case 1). The symbols in (c) represent the concentration in each slice and the curve is a fit through these symbols.

Next, consider the case where $St = 0.5$ and particle mass loading is 4.12×10^{-3}. Figure 5.4a compares the mean velocity in the cross-section of the channel with and without particles. There is no significant influence of the particles on the mean velocity. At this mass loading, the momentum is primarily with the carrier phase. Figure 5.4b shows the normalized turbulent kinetic energy (TKE). As expected, the effect of the particles is negligible. As turbulence statistics are derived from the instantaneous and mean velocity profiles, these results also implicitly suggest that there is negligible effect on the instantaneous velocity flow field from the presence of the particles. Figure 5.4c shows the particle concentration profile in a transverse cross-section of the channel. While the mean fluid velocity and TKE are not noticeably affected by the particles, the particle transport is significantly affected by the turbulence, i.e. one-way coupling is important. The particles concentrate near the walls. The normalized concentration at the wall is about a factor of seven greater than the average and consequently in the core of the channel, it is about 50% lower.

The increased concentration of particles near the wall can be explained by the phenomenon of turbophoresis. Turbophoresis is the process by which particles are transported down gradients of TKE. In a region of high gradient in TKE, particles with lower inertia, i.e. particles with lower St, are transported by the high energy eddies preferentially from a region of high TKE to low TKE. The greater the inertia of the particle, the lesser this tendency. Figure 5.4b shows the highest TKE is at a $y^+ \approx 18$. The TKE decreases sharply to zero at the wall. Hence, particles in the region of $y^+ \approx 18$ are transported to the wall where they concentrate because the low energy eddies near the wall do not transport them away from the wall fast enough. The gradient toward the center of the channel is noticeably lower than toward the wall. Hence particle transport toward the center is less impacted.

Figures 5.5 and 5.6 show results for $St = 2$ (Case 3) and $St = 10$ (Case 4) respectively. From Figs. 5.5a and 5.6a, it can be seen that the mean velocity profile is not affected significantly at either of these St. This is expected since the mass loading in both these cases is small, i.e. $m_p/m_f < 0.1$. Figures C.9 and 5.6b show that TKE

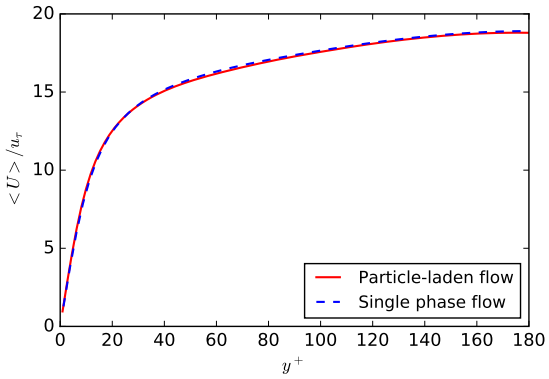

(a)

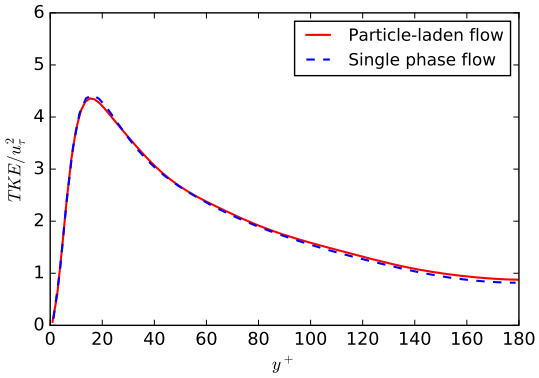

(b)

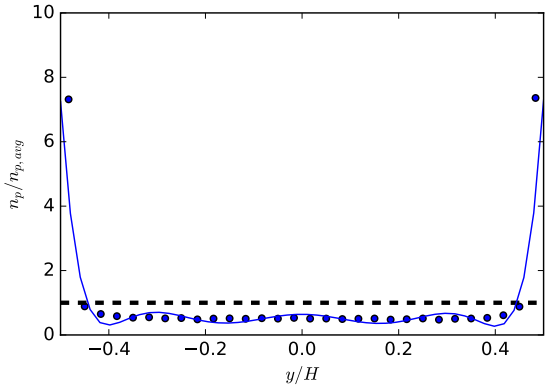

(c)

Figure 5.4: (a) Mean velocity profile; (b) turbulent kinetic energy profile; (c) particle concentration profile when $St = 0.5$, $m_p/m_f = 4.12 \times 10^{-3}$, and $d_p/\eta_k = 0.2$ (Case 2). The symbols in (c) represent the concentration in each slice and the curve is a fit through these symbols.

profile is close to the single-phase results, although the differences in Fig. 5.6b are noticeable, probably because of the greater mass loading. Figure 5.5c shows that the particle concentration near the wall is about 5 times higher than the bulk average concentration for $St = 2$, i.e. it decreases from a factor of 7 when the St was lower in Case 2. As the St is increased to 10, i.e. Case 4, the near wall concentration is about a factor 2 higher than the bulk average concentration. In the core of the channel, i.e. $-0.4 < y/H < 0.4$, the concentration is nearly uniform in both cases. Turbophoresis causes the large concentration of particles near the wall. The concentration near the wall decreases as St increases since particle inertia increases with St. Increasing particle inertia increases the response time of the particles to the turbophoretic force.

Figures 5.7 and 5.9 show results for $St = 40$ (Case 5) and $St = 100$ (Case 6), respectively. For Case 5, the particle mass loading, m_p/m_f, is 0.335. The effect of the increased mass loading on the mean velocity profile is apparent in Fig. 5.7a. The mean velocity is now lower than its single-phase counterpart. In the case of a single-phase flow, the maximum mean velocity normalized by the friction velocity, u_τ, is about 19, whereas it is roughly 17 in Case 5. The reduction in mean velocity occurs because the momentum is shared between the carrier and dispersed phases. The TKE shown in Fig. 5.7b is lower than the single-phase results as well. The peak normalized TKE decreases from 4.5 to 3.5. A decrease is observed throughout the channel. The decrease in TKE is expected because of the reduction in mean velocity. Note that u_τ which is employed for the normalization does not change across the cases considered. If the normalization is carried out using mean velocities for the single-phase flow and the particle-laden flow respectively, the TKE profiles overlap more closely as shown in Fig. 5.8 confirming that the reduction in TKE is on account of the reduction in mean velocity. Figure 5.7c shows the concentration profile of particles in the channel. At this St, the particles are almost uniformly concentrated in the channel. So as $St \to 0$, e.g. Case 1, and at higher St, e.g. Case 5, the particle distribution is relatively uniform, in one case because the particles have negligible

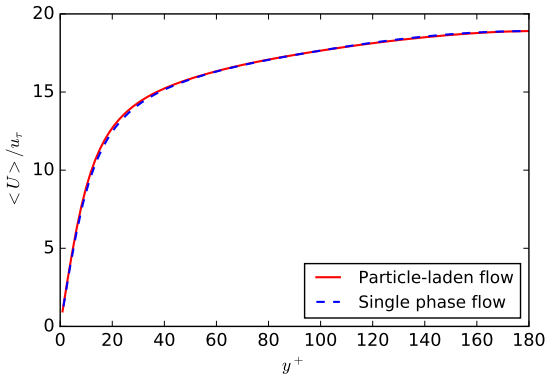

(a)

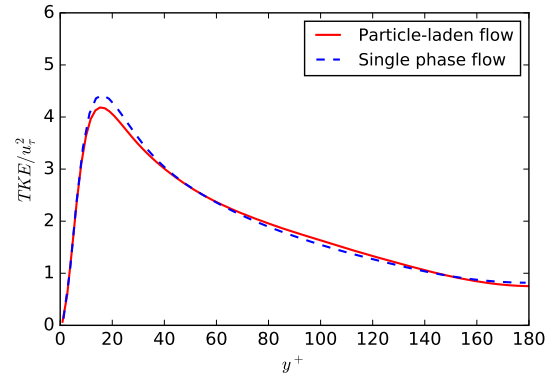

(b)

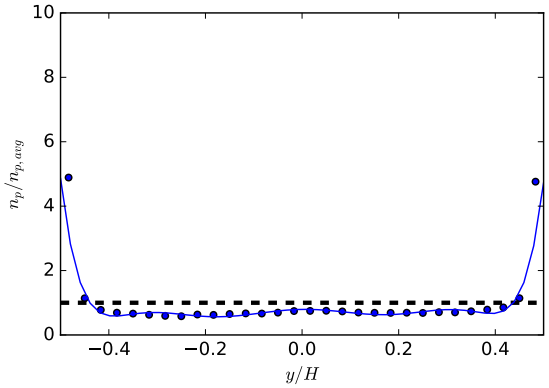

(c)

Figure 5.5: (a) Mean velocity profile; (b) turbulent kinetic energy profile; (c) particle concentration profile when $St = 2$, $m_p/m_f = 1.67 \times 10^{-2}$, and $d_p/\eta_k = 0.2$ (Case 3). The symbols in (c) represent the concentration in each slice and the curve is a fit through these symbols.

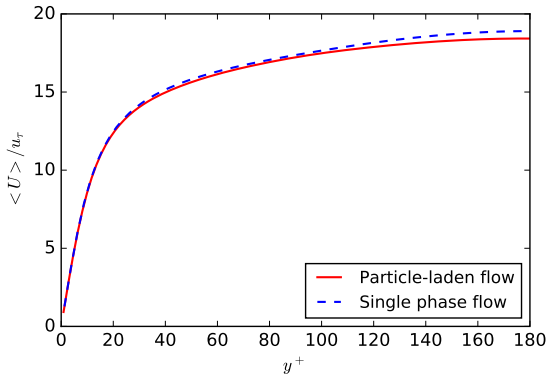

(a)

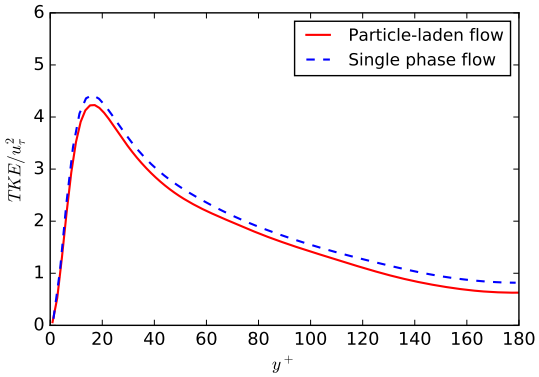

(b)

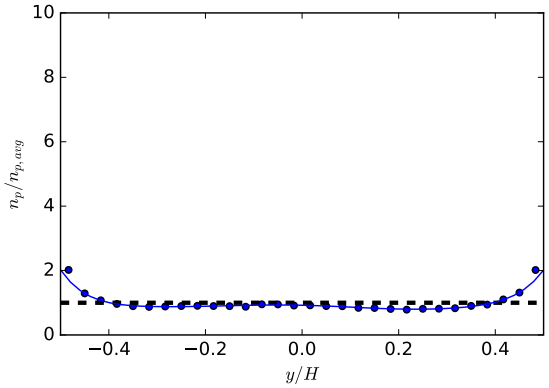

(c)

Figure 5.6: (a) Mean velocity profile; (b) turbulent kinetic energy profile; (c) particle concentration profile when $St = 10$, $m_p/m_f = 8.38 \times 10^{-2}$, and $d_p/\eta_k = 0.2$ (Case 4). The symbols in (c) represent the concentration in each slice and the curve is a fit through these symbols.

inertia and respond instantaneously to the turbulence and in the other case because the particles have too high an inertia to respond to the turbulence.

For Case 6 with $St = 100$, the mas loading is even higher at 0.837 and hence the deviation from the single-phase results is even more noticeable. From Fig. 5.9a, notice that the normalized maximum mean velocity has now dropped to 15, compared to 17 for Case 5 and 19 for the single-phase flow. Notice in Fig. 5.9b, notice that the peak TKE has dropped to about 2.5, compared to 3.5 for the case where the mass loading was 0.335 (Case 5) and 4.5 for the single-phase flow. Moreover, the location of the peak TKE has moved away from the wall, from $y^+ \approx 15$ for the single-phase flow to $y^+ \approx 20$. It is known that the location of peak TKE moves closer to the wall as Reynolds number, Re, increases [133]. Since the mean velocity decreases in this case, the Re decreases and this could be the reason why the location of peak TKE moves away from the wall. When the TKE profile is normalized by the mean kinetic energy as shown in Fig. 5.10, the particle-laden flow and the single phase flow profile are similar to each other suggesting that the change in TKE is account of the reduction in mean velocity.

Figure 5.9c shows particle concentration profile when the mass loading is 0.837 and St is 100. Interestingly, a distinct peak near the center is now evident. As discussed earlier, the center is a region of minimum TKE. The effect of turbophoretic force at the center becomes important as the St increases. This is consistent with what was observed in the experimental work of Lau and Nathan [11]. It is possible that at higher St, the longer response time of the particles restrains the particles from lateral movement. In the cases where there was a distinct rise of concentration of particles near the wall, which, in turn, resulted in a uniform, but lower, concentration in the core of the channel, e.g. Case 2, the tendency of particles to concentrate at the walls dominated the distribution of the particles. In the absence of this tendency, local gradients in TKE can act to concentrate particles locally, e.g. at the center.

Next the effect of the mass loading on the mean velocity, TKE and concentration profiles when keeping St constant are assessed. Case 7 has the same St as Case 2 and

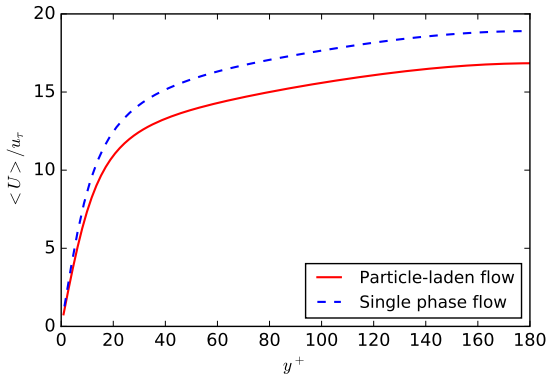

(a)

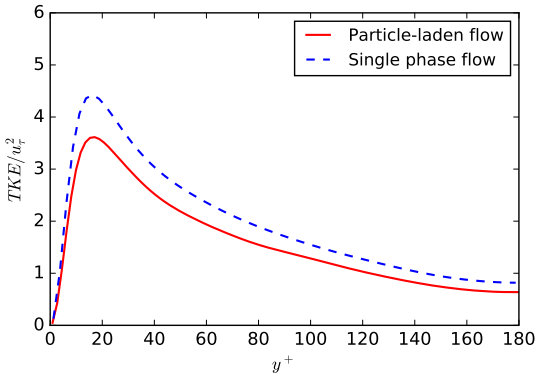

(b)

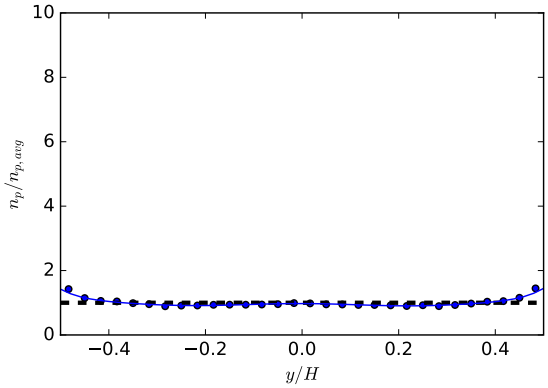

(c)

Figure 5.7: (a) Mean velocity profile; (b) turbulent kinetic energy profile; (c) particle concentration profile when $St = 40$, $m_p/m_f = 3.35 \times 10^{-1}$, and $d_p/\eta_k = 0.2$ (Case 5). The symbols in (c) represent the concentration in each slice and the curve is a fit through these symbols.

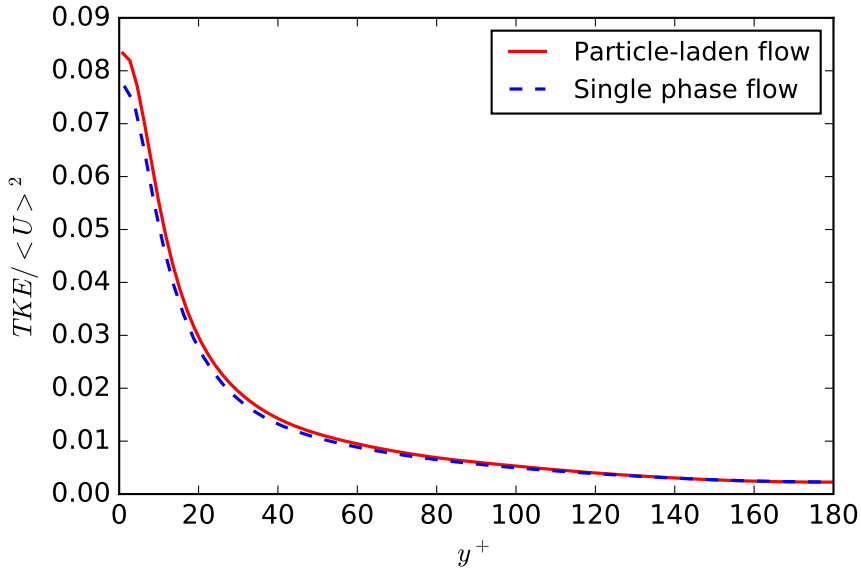

Figure 5.8: Turbulent kinetic energy normalized by the square of the mean velocity for Case 5.

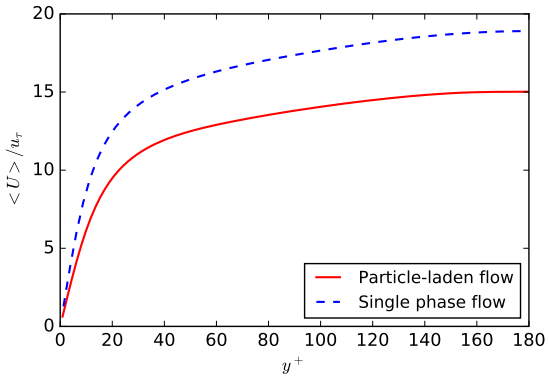

(a)

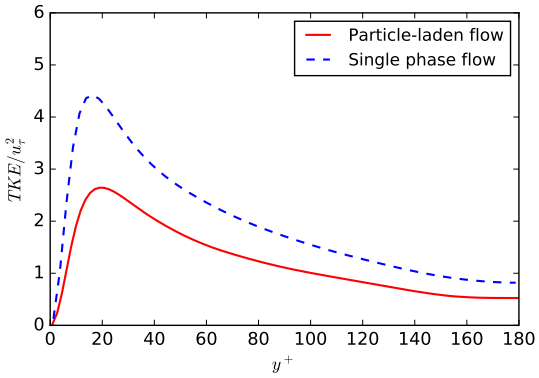

(b)

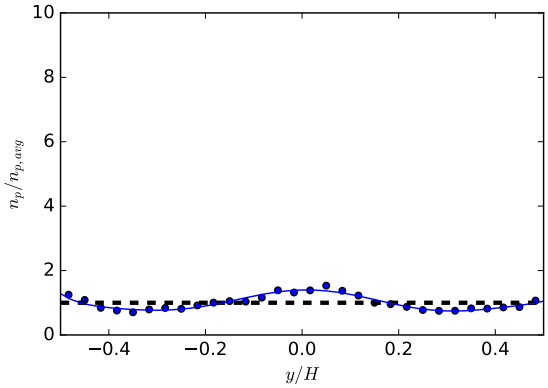

(c)

Figure 5.9: (a) Mean velocity profile; (b) turbulent kinetic energy profile; (c) particle concentration profile when $St = 100$, $m_p/m_f = 8.37 \times 10^{-1}$, and $d_p/\eta_k = 0.2$ (Case 6). The symbols in (c) represent the concentration in each slice and the curve is a fit through these symbols.

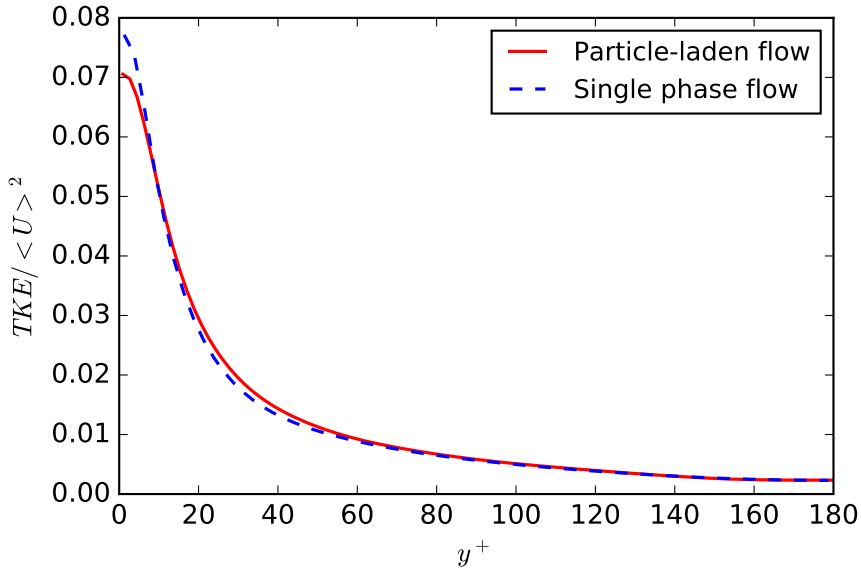

Figure 5.10: Turbulent kinetic energy normalized by the square of the mean velocity for Case 6.

Case 8 the same St as Case 6, but the mass loading is doubled. The density of the particle is adjusted to get the same St. The mass loading remains relatively small at 8.38×10^{-3} for Case 7, but the mass loading when $St = 100$ in Case 8 is large at 1.676.

Figures 5.11a and 5.11b show the mean velocity and TKE profile respectively for $St = 0.5$ and mass loading 0.00838 (Case 7). The effect of the presence of the particles is noticeable, but the differences are within 5%. This is on account of the higher mass loading of 8.38×10^{-3} in Case 7 relative to Case 2. The effect of the flow on the particles is evident in Fig. 5.11c. The concentration profile shows a peak near the walls as was seen for Case 2. The mass loading, m_p/m_f, in this case is small ($m_p/m_f = 0.00838$) and hence a one-way coupling is predominant. Comparing with Case 2, we see that even though the St is same for both the cases, the particle concentration near the wall is reduced. The reduction is because the increased mass loading for fixed St is achieved by increasing particle diameter. A larger particle would have a smaller drag per unit mass since the surface area per unit mass decreases. Thus the influence of the turbulent eddies on the particle motion decreases and hence the effect of turbophoresis decreases.

Figure 5.12a shows the mean velocity profiles for $St = 100$ and mass loading of 1.676 (Case 8). In this case, the mass loading is relatively large ($m_p/m_f = 1.676$). In fact, this is the case with the largest mass loading. Hence, a significant decrease in the mean velocity is observed. From Fig. 5.12a, we can see that the normalized maximum mean velocity is about 12.5, whereas it is roughly 19 in the single-phase flow. Figure 5.12b shows the TKE profile. Again, the effect of the particles is clearly seen. The peak normalized TKE decreases from 4.5 for the single-phase flow to 1.5 for the current case. It is seen that the near the wall ($y^+ < 20$), the shape of the TKE profile looks similar to that of the single-phase profile. However, as we move farther from the wall, the TKE keeps increasing and reaches a peak value of about 1.5 at $y^+ \approx 70$. It then decreases and the decrease is similar to the single-phase flow. Figure 5.13 shows the TKE profile normalized by the mean velocity square. It is seen

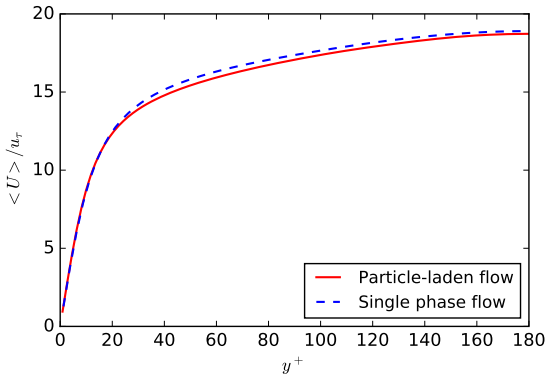

(a)

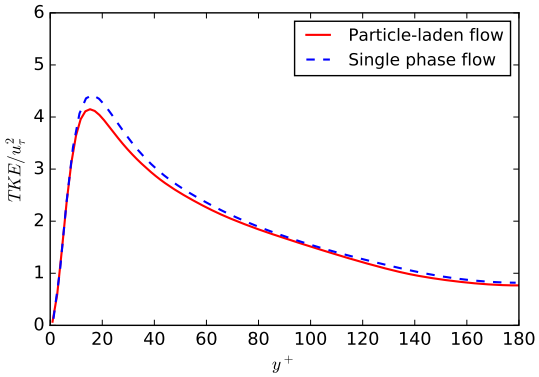

(b)

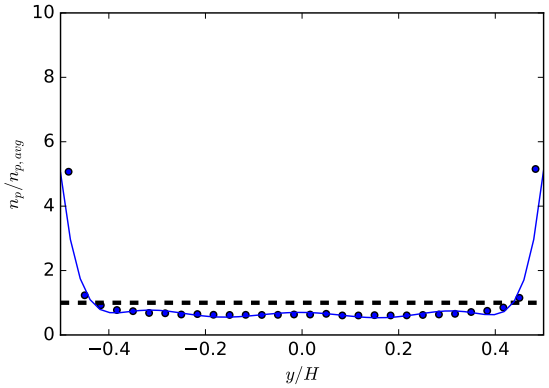

(c)

Figure 5.11: (a) Mean velocity profile; (b) turbulent kinetic energy profile; (c) particle concentration profile when $St = 0.5$, $m_p/m_f = 8.38 \times 10^{-3}$, and $d_p/\eta_k = 0.4$ (Case 7). The symbols in (c) represent the concentration in each slice and the curve is a fit through these symbols.

that this profile differs considerably from the single-phase flow. The Re based on the maximum mean velocity and the channel height is 4500 for this case, which lies in the laminar-turbulence transition regime. This might explain the difference in shape of the TKE profile seen in Fig. 5.12b and Fig. 5.13. Metzger and Klewicki [148] suggest that at low Re, the fluctuations in the buffer layer do not grow accordingly with the fluctuations outside the buffer layer which might cause a dramatic shift in the location of peak TKE away from the wall. The particle concentration profile is shown in Fig. 5.12c. A similar high concentration near the center is observed as was seen when the mass loading and the particle diameter were a factor of two lower, and the St was 100 (Case 6).

5.4 Summary and Conclusions

The lattice-Boltzmann method is employed to carry out direct numerical simulations of particle-laden turbulent flows in a channel under the approximation that the particle diameter is smaller than the Kolmogorov length scale and it can be approximated as a point particle. Two-way coupling is implemented through the drag coefficient and an external force term in the discretized Boltzmann equation. The simulations show that the Stokes number, St, mass loading of particles, i.e. ratio of mass of dispersed to carried phase, m_p/m_f, and particle diameter, d_p, are important parameters that determine the distribution of the particles and the impact of the particles on the fluid velocity flow field.

At relatively low mass loading, typically less than 0.1, the impact on the mean velocity flow field and the turbulent kinetic energy is not significant. But, under these conditions, the preferential motion of particles in the lateral direction is impacted by the fluid motion. The impact depends on the St. When the St is infinitesimally small, the particles are uniformly distributed across the cross-section of the channel. As St is increased, the particle concentration near the wall initially increases and then decreases. At even higher St, the particle concentration near the center

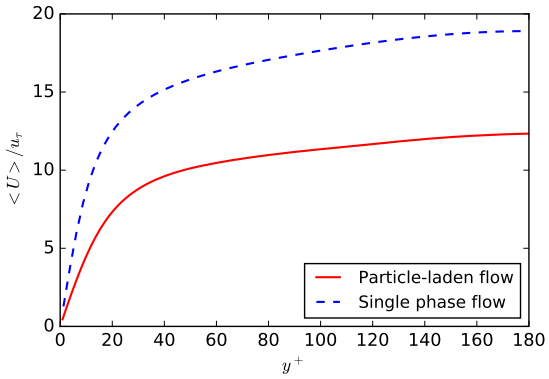

(a)

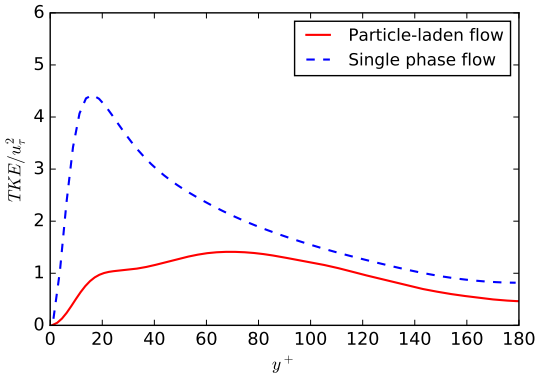

(b)

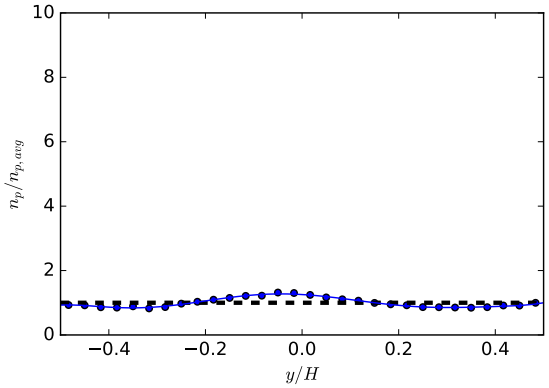

(c)

Figure 5.12: (a) Mean velocity profile; (b) turbulent kinetic energy profile; (c) particle concentration profile when $St = 100$, $m_p/m_f = 1.676$, and $d_p/\eta_k = 0.4$ (Case 8). The symbols in (c) represent the concentration in each slice and the curve is a fit through these symbols.

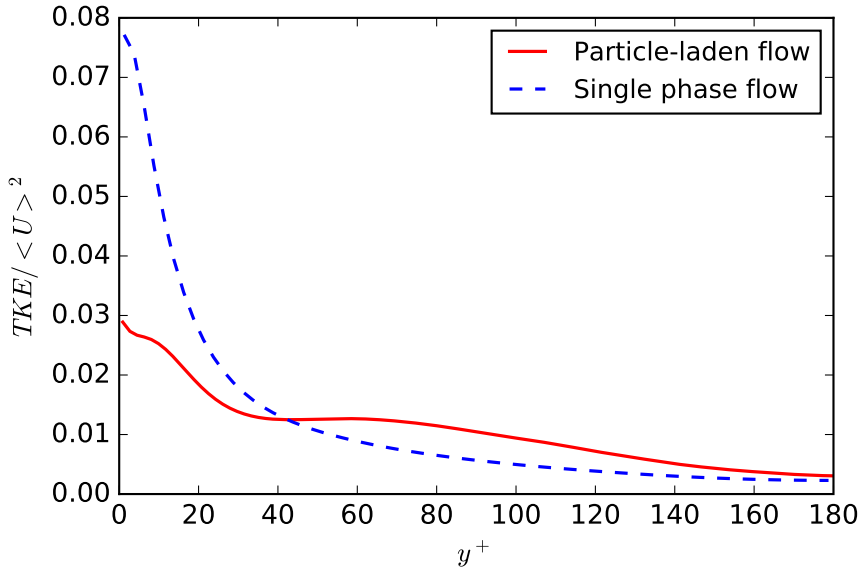

Figure 5.13: Turbulent kinetic energy normalized by the square of the mean velocity for Case 8.

of the channel increases slightly. This preferential motion, and resulting concentration, is attributed to turbophoresis as that is the only mechanism that can result in preferential lateral movement of particles within the framework of these simulations where point particles are considered. Turbophoresis results in preferential motion when the tendency for turbulent eddies to move particles is opposed by their inertia. In fact, larger diameter particles with the same St as smaller diameter particles, are less impacted by turbophoresis because the larger particle would have a smaller drag per unit mass. As particle mass loading increases, the fluid flow field is increasingly affected, with the mean velocity decreasing relative to the single phase flow mean velocity. The turbulent kinetic energy also decreases as a result of the decrease in the mean velocity. In summary, preferential movement and distribution of particles is affected by St and particle diameter whereas the impact on the mean velocity is primarily affected by the mass loading.

6. EFFECT OF STOKES NUMBER ON PARTICLE TRAJECTORIES IN A LAMINAR CHANNEL FLOW

6.1 Introduction

The last chapter presented point-particle simulations results for particle-laden flow in a channel. In this chapter, particle-resolved simulations of laminar channel flow are discussed. The effect of Stokes number on the migration of a particle in a laminar channel flow is studied. Part of this work was recently published in *Computers and Fluids* (*A. S. Jebakumar, K. N. Premnath, and J. Abraham, Lattice Boltzmann method simulations of Stokes number effects on particle trajectories in a wall-bounded flow, Computers and Fluids, available online, July 31, 2015.*) [149].

6.2 Stokes Number

The Stokes number (St) is the ratio of particle response time to the flow response time. A particle with a low St adjusts itself to the flow almost instantaneously whereas a particle with a high St takes a long time to accommodate to the flow. The St of a particle is an important parameter that determines its behavior in several flows of interest. The response time τ_p for a spherical particle at low Reynolds number is given by [10] as

$$\tau_p = \frac{(2\rho_p + \rho_f)d_p^2}{36\mu}, \tag{6.1}$$

where ρ_p is the density of the particle, ρ_f is the density of the fluid, d_p is the diameter of the particle and μ is the viscosity of the fluid. If the particle density is much higher than the fluid density, this reduces to

$$\tau_p = \frac{\rho_p d_p^2}{18\mu}. \tag{6.2}$$

This can be expressed alternatively as

$$\tau_p = \frac{d_p^2}{18\nu}\left(\frac{\rho_p}{\rho_f}\right), \tag{6.3}$$

where ν is the kinematic viscosity of the fluid. This expression brings in a ratio of the particle density to the fluid density. The flow response time can be obtained from a characteristic length scale L_c and velocity scale U_c of the bulk flow as

$$\tau_f = \frac{L_c}{U_c}. \tag{6.4}$$

For a channel flow, the characteristic velocity U_c can be taken as the maximum velocity U_{max} and the channel height H can be taken as the characteristic length scale L_c. This gives an expression for St as

$$St = \frac{\rho_p d_p^2 U_{max}}{18\mu H}. \tag{6.5}$$

The aim of this work is to understand the effect of St on the migration trajectories of particles in a laminar channel flow by carrying out Direct Numerical Simulations (DNS) with the particle itself being numerically resolved.

6.3 Segré - Silberberg Effect

Segré-Silberberg effect refers to the phenomenon of neutrally buoyant particles settling at a position between the wall and center-line in a pipe flow. In Section 4.6.2, computations of a neutrally buoyant particle in a channel flow were presented. The migration trajectories are redrawn again in Fig. 6.1. The mechanism of this particle migration is explained by Feng *et al.* [38] in terms of the forces acting on the particle viz. the Saffman lift, the Magnus lift and the wall repulsion. A brief description of the mechanism will now be provided.

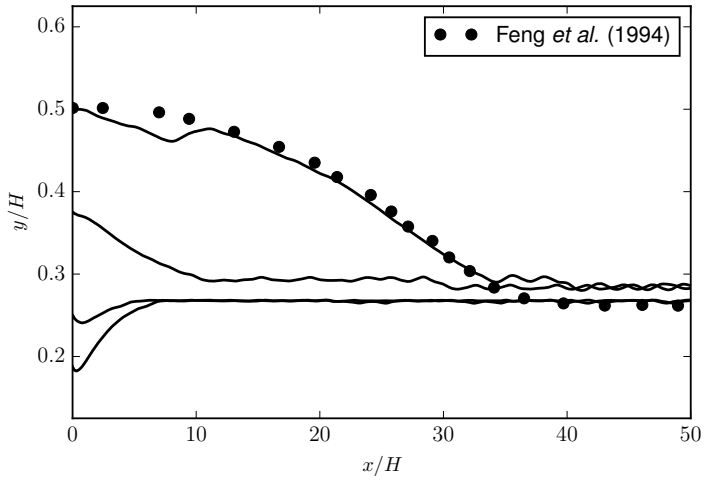

Figure 6.1: Comparison of the particle migration trajectories for a neutrally buoyant particle in a channel flow at $Re_p = 0.875$.

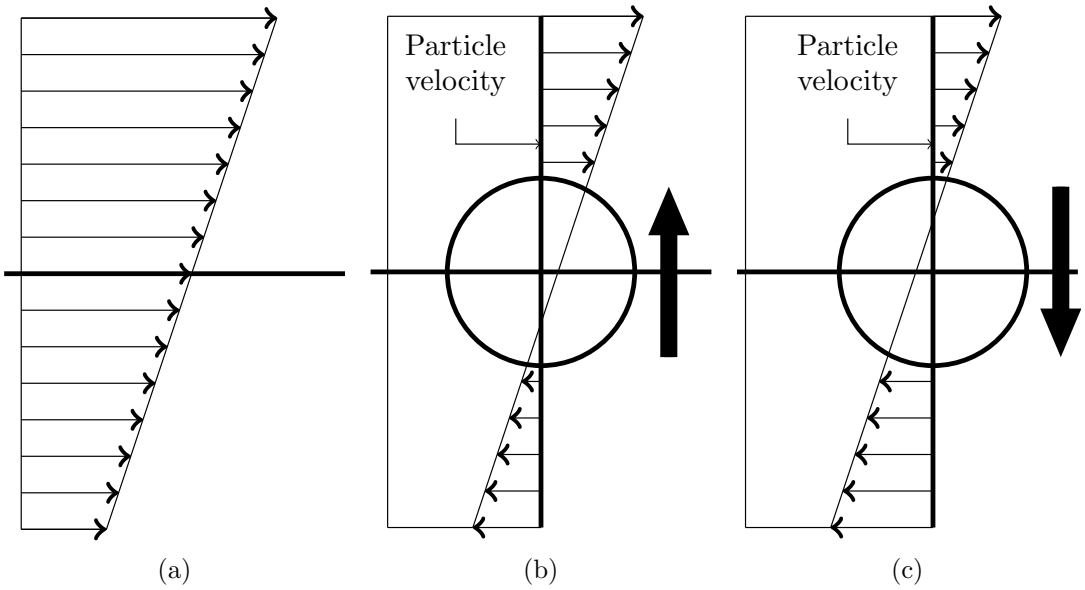

Figure 6.2: Schematic of a particle in a uniform shear flow; (a) linear velocity profile, (b) relative velocity of fluid when particle is lagging fluid, (c) relative velocity of fluid when particle is leading fluid.

The Saffman lift force is a lateral force that tends to move a particle that either leads or lags the fluid velocity. In a linear velocity profile, the Saffman lift would push a particle that leads the fluid toward the region with low velocity and vice versa. Figure 6.2a shows a particle in a uniform shear flow. If the particle lags the fluid velocity, then the relative velocity (see Fig. 6.2b) on top of the particle would be higher than that on its bottom. This develops a high pressure beneath the particle pushing it upwards. Similarly, if the particle leads the fluid velocity, then the relative velocity (see Fig. 6.2c) will be higher beneath the particle which develops a high pressure on top of the particle pushing it downward.

However, in the case of a particle in a channel flow, the curvature in the velocity profile of the undisturbed flow tends to reverse this trend. Figure 6.3 shows the relative velocity of the fluid with respect to the particle for two possible cases: one with a large slip velocity where the particle lags the fluid in all regions and another with a small slip velocity where the particle velocity lags the fluid. It should be noted

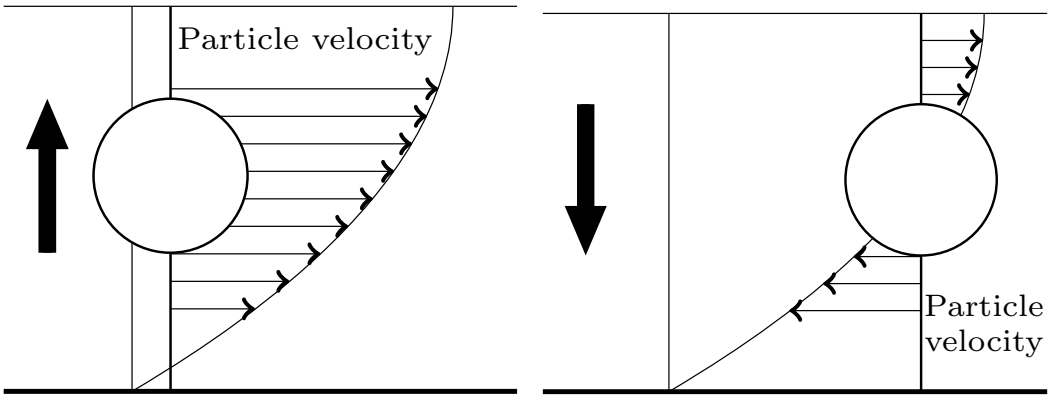

Figure 6.3: Schematic illustration of the relative velocity of a particle in a parabolic velocity profile; a) large slip velocity b) small slip velocity.

that since the particle is released with zero velocity, the particle would lag behind the fluid most of the time. However, it is possible that when a particle is pushed from a streamline with a higher velocity to one with lower velocity, it may lead the fluid for a short time. When the slip velocity is large, the relative velocity of fluid on the free stream side of the particle would be higher than that on its wall side. This would cause a high pressure buildup beneath the particle pushing it away from the wall. When the slip velocity is small, the behavior is different. Consider the sketch in Fig. 6.3b. It is seen that the magnitude of relative velocity is higher on its wall side than on its free stream side. This causes a high pressure buildup on top of the particle which pushes it toward the wall. Hence, in this case, for most part of the particle motion (except the initial transient time interval), the Saffman lift pushes the particle toward the wall. The direction of Saffman lift is the same even if the particle leads the fluid with a small slip velocity. The center will be an equilibrium position where there would be no effect of Saffman lift on the particle.

Figure 6.4 shows the velocity contour of the fluid during one of the simulations in which the particle is moving. The particle position at the time when the velocity contour plot is taken is also shown. The undisturbed velocity profile is a parabolic

profile. It can be seen that the presence of the particle alters the velocity distribution in its vicinity. Figure 6.5 shows the relative velocity magnitude of the flow with respect to the particle. It is evident from this figure that the velocity between the particle and the bottom wall is higher than the velocity on the other side. This causes a high pressure buildup on top of the particle which pushes it toward the wall.

The movement of the particle toward the wall is opposed by wall repulsion [37,38]. This is a force that arises when there is a relative motion between the wall and the particle. During this relative motion, a thin layer of fluid is squeezed in the gap between the particle and the wall, increasing the pressure which pushes the particle away from the wall. This force is similar in nature to lubrication force. If only wall repulsion force existed, the equilibrium position would be where wall repulsion from the top and bottom wall are equal and opposite each other. This would correspond to the centerline of the channel.

The Magnus lift force arises on account of the rotation of the particle. When a particle rotates in a uniform flow, it would push fluid in the direction of motion on one side and against the direction of motion in the opposite side. This would cause a velocity gradient, which in turn causes a pressure gradient pushing the particle toward the low pressure region. At the centerline of the channel, the particle would not rotate since the undisturbed velocity profile is symmetric about the center line and hence the center would be an equilibrium position. Thus, if a particle is released from the centerline, it would not experience the Magnus lift force. Now, if the particle is displaced slightly from the center, Saffman lift pushes the particle toward the wall and it keeps moving until Saffman lift, Magnus lift and wall repulsion are in balance. This would be a stable equilibrium for the particle and it would be at a location between the wall and the centerline. The centerline is not a stable equilibrium. It will be shown later in this work that the Magnus lift force also acts in the same direction as the Saffman lift.

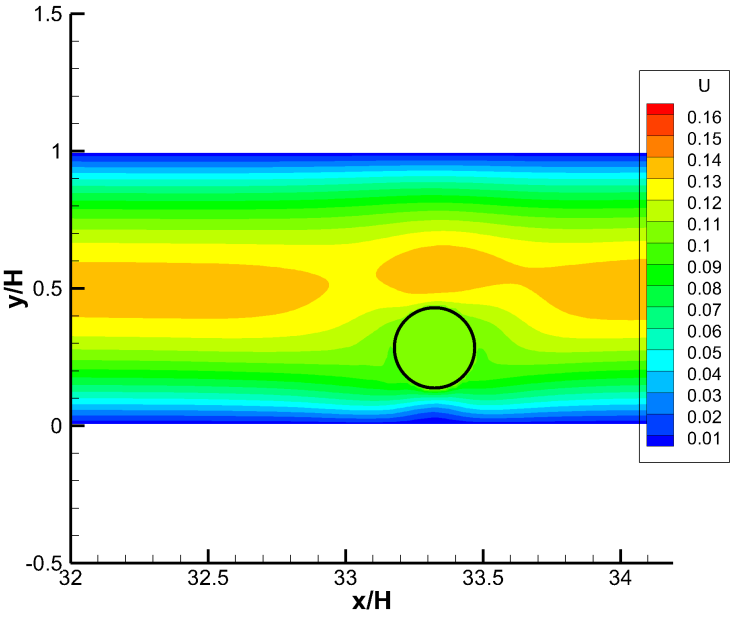

Figure 6.4: Velocity contour plot

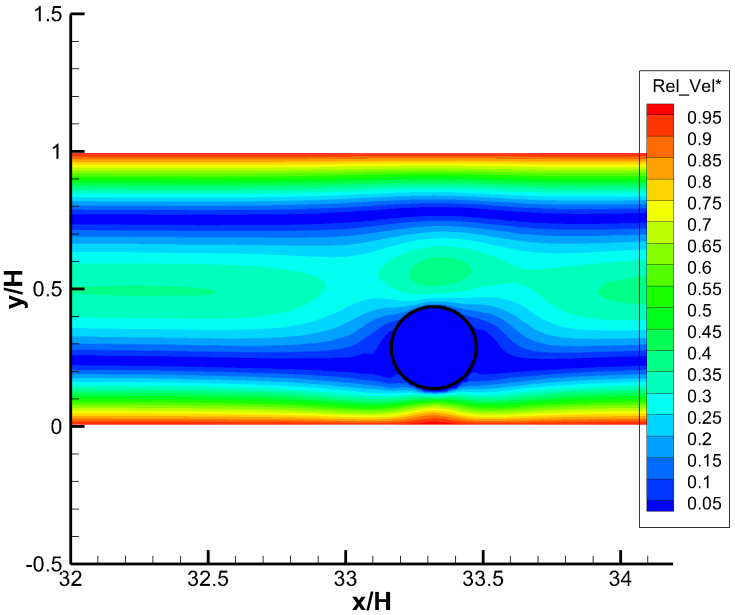

Figure 6.5: Relative velocity magnitude of the fluid with respect to the particle

Table 6.1: A list of cases examined in this study.

Case	ρ_p	ρ_f	U_{max}	St
1	0.72	1.0	0.16	0.5
2	3.36	1.0	0.16	1.6
3	26.88	1.0	0.16	11.4
4	33.60	1.0	0.16	14.2
5	96.00	1.0	0.16	40
6	120.00	1.0	0.16	50
7	168.00	1.0	0.16	70
8	240.00	1.0	0.16	100

6.4 Results and Discussion

Table 6.1 shows a list of cases that are examined in this work. The particle time constant for cases 1-4 are calculated using Eq. (6.1) while that for the other cases are calculated using Eq. (6.2).

Figure 6.6 shows the trajectory of the particle in the channel for four different St (0.5, 1.6, 11.4 and 14.2). The St is varied by changing the density of the particle. The particle is released from a location $y/H = 0.25$. The channel height is 4 times the particle diameter. It can be seen that for $St = 0.5$, the particle behaves as a neutrally buoyant particle in a channel flow exhibiting the Segré-Silberberg effect (See Fig. 6.1 and related discussion). When $St = 1.6$, the particle behavior is not very different from $St = 0.5$, but minor oscillations about the equilibrium position is evident. When $St = 11.4$, the particle moves all the way to the center of the channel and farther towards the top wall and settles in its equilibrium position close to the top wall. The initial motion of the particle toward the top wall is just a transient effect. It should be noted that the channel flow has two equilibrium positions, one near the top wall and one near the bottom wall on account of its symmetry about the center line. For clarity, 1-y/H is plotted against x/H for this case. It is seen that the

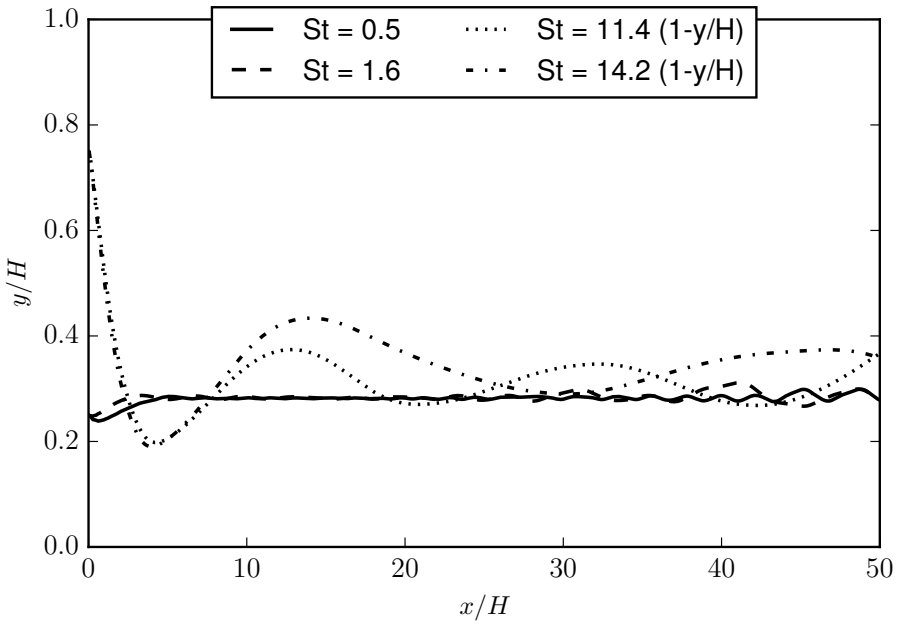

Figure 6.6: Particle migration trajectories for different St numbers. (For $St = 11.4$ and $St = 14.2$, 1-y/H is plotted against x/H).

particle oscillation about the equilibrium position has now become noticeable. Similar behavior is observed for $St = 14.2$, but the mean is more close to the centerline.

For the lower St cases, the behavior of particles settling at a location between the wall and the axis is similar to that of a neutrally buoyant particle and has been explained by Feng *et al.* [38] in terms of Saffman lift, Magnus lift, curvature of the undisturbed velocity profile and wall repulsion.

It is of interest to understand why the particle with the larger St oscillates about this equilibrium position rather than remain at the position. A particle with a larger St has a longer response time which implies that it has a higher inertia than a particle with a lower St. The particle is released from $y/H = 0.25$. During the initial transient time, Saffman lift pushes the particle away from the wall owing to the large slip velocity. Hence the particle moves toward the center. As it comes closer to the center, the particle's velocity in the axial direction increases and so its slip velocity decreases. As a result of inertia, the particle moves beyond the center line and moves

closer to the equilibrium position near the top wall. Since the slip velocity is now small, Saffman lift acts to push the particle toward the wall and the particle moves upwards. As it approaches the equilibrium position, the sum of the Saffman lift, Magnus lift and wall repulsion force decreases. But, due to its inertia, it continues to move further toward the wall until the wall repulsion overcomes the inertial effects. At this position, the wall repulsion is higher than the Saffman and Magnus lift and this unbalanced force causes the particle to move back toward its equilibrium position. Again, due to inertia it will overshoot a short distance and then move back toward the wall and this oscillation continues. Mortazavi and Tryggvason [39] have reported similar oscillations of drops in a channel flow at high Re number. Further studies should be conducted to see if the oscillations are just transient effects.

In order to determine how the particle behaves when the St is increased further, four more cases are considered with St of 40, 50, 70 and 100. The trajectories for these particles are shown in Fig. 6.7. Increasing the St appears to increase the amplitude although changes are small for the range considered. Compared to the result for St of 11.4 shown in Fig. 6.6, the frequency of the oscillation for St of 50 in Fig. 6.7 is about a factor of four lower. The larger amplitude and the lower frequency are consistent with larger inertia particles adjusting slower to changes in the forces.

Simulations are carried out to determine if the initial position at which the particle is released from has an effect on its equilibrium position. Figure 6.8 shows the migration trajectories for particles released from varying y/H distance. It can be seen that the particle migrates to the same position irrespective of the location from which it is released. Also, it should be noted that when the particle is released from the center it travels a longer distance before reaching its equilibrium position. This is because, as mentioned earlier, the centerline is also an equilibrium position but not a stable one. However, depending on the initial location there seems to be a minor difference in the amplitude of the oscillations. Particles released closer to the equilibrium position have smaller amplitude of oscillations than those released farther away.

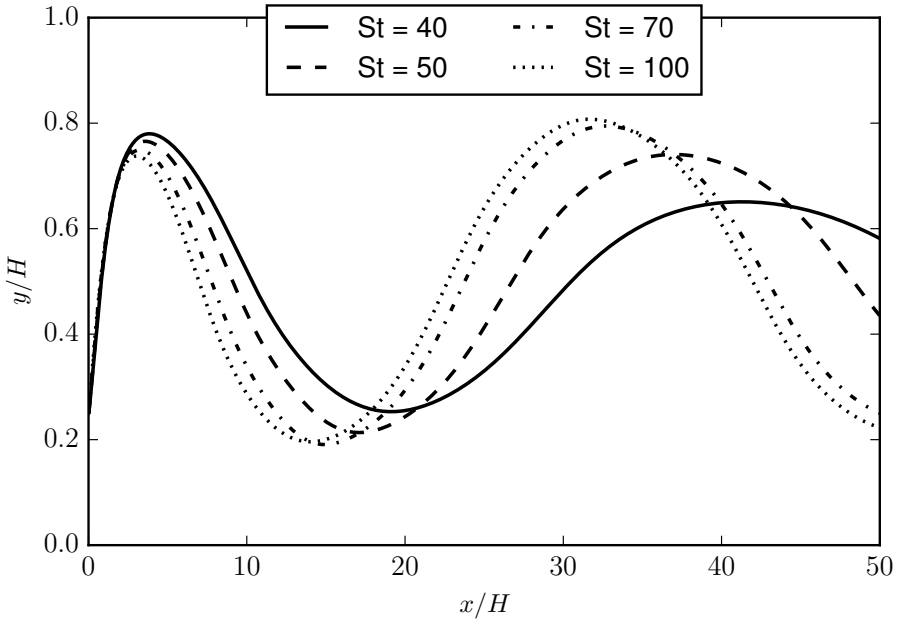

Figure 6.7: Particle migration trajectories for high St numbers.

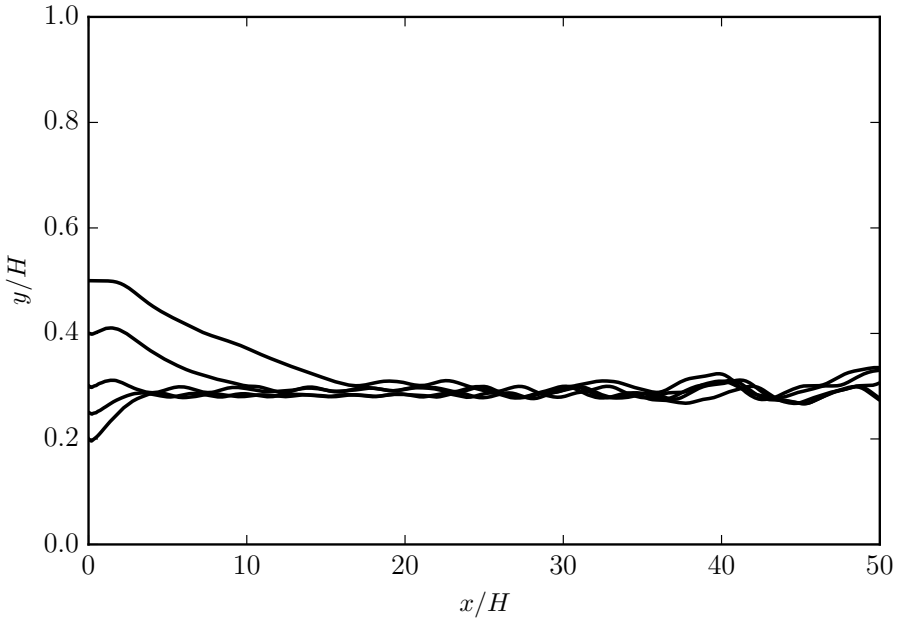

Figure 6.8: Effect of initial position on the particle migration trajectories ($St = 1.6$).

Next, the effect of particle size relative to the channel width, i.e. H/d, for a given St is studied. Figure 6.9 shows the particle migration trajectories for 3 different H/d ratios. The velocity of the fluid and density of the particle are changed so that the St remains the same in all cases. As the H/d ratio becomes larger, the particle moves closer to the wall. This is because as the relative size of the particle decreases, the wall repulsion force decreases, allowing the Saffman and Magnus lift to push the particle closer to the wall. It is also seen that at higher H/d ratios, the particle begins to exhibit oscillations. This can be explained by understanding the role of the Magnus lift in more detail. Feng *et al.* [37] report that the presence of a wall near the particle tends to suppress the rotation of the particle and thereby reduce the Magnus lift force acting on the particle. Figure 6.10 shows the particle migration trajectories for the low St cases with and without the Magnus force. It is evident from this figure that the equilibrium position of the particle shifts toward the centerline, from y/H value of about 0.28 to about 0.4. Furthermore, the oscillations that are seen for the St = 11.4 and St = 14.2 cases are not seen when Magnus lift force is absent. Figure 6.11 shows similar results for the high St cases. For this range of St, it can be seen that the oscillation persists but its amplitude is reduced because the wall repulsion has to overcome only the Saffman lift and hence the particle is pushed away from the wall to a greater distance than in the case with the Magnus lift force The implication is that the Magnus force adds to the Saffman force to move the particle toward the wall. The absence of the Magnus force does not remove the oscillations. It just changes the St for which the oscillation sets in. Increasing the H/d ratio increases the effective distance between the wall and the particle. Hence the Magnus lift force acting on the particle increases and the St at which the oscillations appear decreases.

6.5 Conclusions

The lattice-Boltzmann method (LBM) is employed to carry out simulations of particle motion in a channel for various Stokes (St) numbers. It is shown that the St

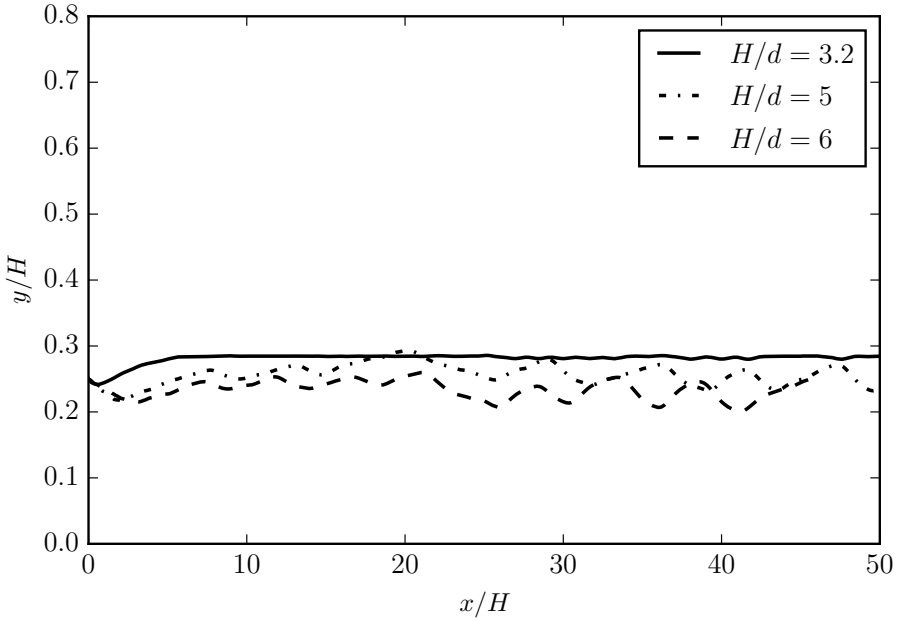

Figure 6.9: Particle migration trajectories for different H/d ratios ($St = 0.5$).

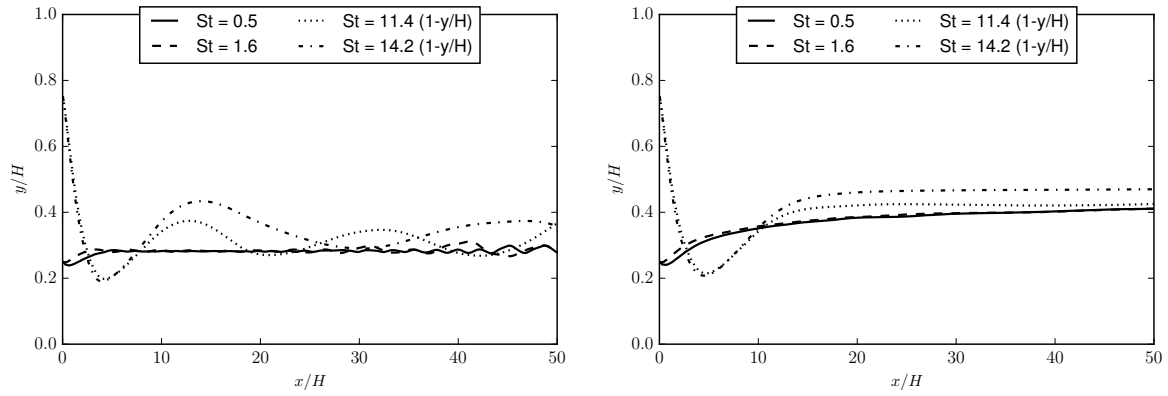

Figure 6.10: Particle migration trajectories for particles a) with rotation and b) without rotation, i.e. no Magnus force.

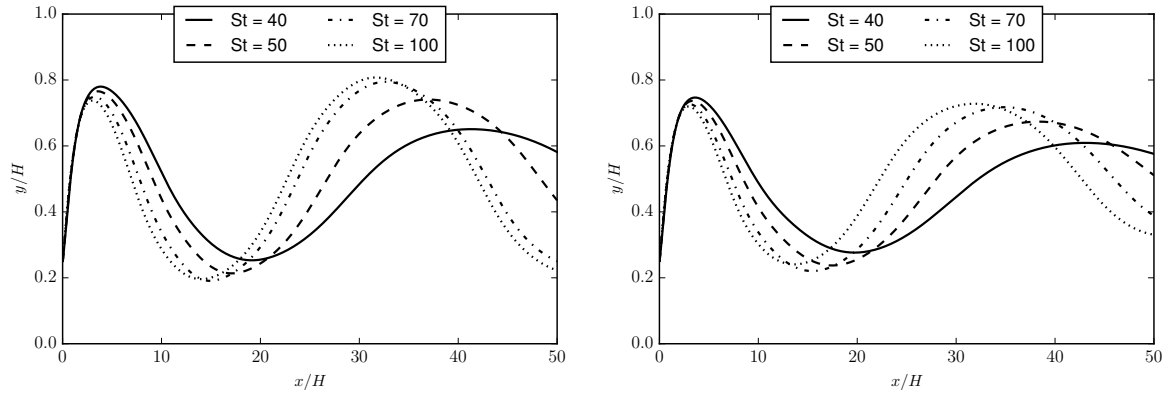

Figure 6.11: Particle migration trajectories for higher St cases a) with rotation b) without rotation.

influences the motion. Particles with low St behave similar to a neutrally buoyant particle in a channel flow exhibiting the Segré-Silberberg effect. They move to an equilibrium position that is between the wall and the axis. This lateral migration of the particle arises as a result of three different forces acting on the particle namely: the Saffman lift, the Magnus lift and wall repulsion. Except for an initial transient time, the Saffman and Magnus lift forces act in the same direction and push the particle toward the wall while the wall repulsion acts to push the particle away from the wall. The particle settles at an equilibrium location where these three forces balance. As the St is increased, the particle exhibits an oscillatory behavior about its equilibrium position. The oscillation amplitude and time period increases with increasing St. The oscillations arise from the increasing importance of inertial effects. Increasing the ratio of the channel width to the particle diameter for a given St reduces the effect of wall repulsion due to which the particle moves closer to the wall. Increasing the H/d ratio decreases the St at which the oscillations begin to occur.

7. SIMULATIONS OF FLOW MODULATION IN A CHANNEL WITH STATIONARY PARTICLES

7.1 Introduction

In the last chapter, particle-resolved direct numerical simulations of a laminar channel flow was presented. In this chapter, particle-resolved direct numerical simulations of a turbulent channel flow is considered. As a first step, the effect of stationary particles in a turbulent channel flow on the flow field is examined. Part of this work has been submitted for publication in *International Journal of Computational Fluid Dynamics*.

Bagchi and Balachander [150] have numerically studied the flow in the wake of a stationary particle in an isotropic turbulent flow. They report that the length of the wake is shorter than that in a laminar flow. They also report that vortex shedding in the wake of the particle is different from that in a laminar flow. As turbulence intensity is increased, vortex shedding is suppressed and the oscillation frequency of the wake increases. Streamwise fluctuation is always enhanced; cross-stream fluctuations are enhanced at lower intensities and damped at higher intensities.

Merle et al. [151] have performed PR-DNS of a stationary, non-deforming spherical bubble situated at the axis of a turbulent pipe flow and have compared the computed lift and drag forces to predictions from correlations available in the literature. They found that the lift force experiences much larger fluctuations than the drag force. Zeng et al. [152] have studied the interaction of a stationary particle with wall turbulence. They have examined the flow field around the particle and its effect on the drag on the particle. They found that high and low speed streaks near the wall cause a low frequency fluctuation of the drag force while the vortex shedding from the particle causes a high frequency component.

Wang et al. [153] carried out PR-DNS of a turbulent channel flow with neutrally buoyant particles. They found that the mean flow velocity decreases with addition of the particles indicating the flow becomes effectively more viscous. Luo et al. [154] have carried out PR-DNS of fluidized beds and have studied the relationship of the pressure drop across the fluidized bed to the local porosity and mobility of particles. They noted that PR-DNS has a better predictive capability than conventional discrete element models.

Burton and Eaton [42] have numerically studied the interaction of a stationary particle with decaying homogeneous isotropic turbulence. They found that the particle modifies the turbulent kinetic energy and its dissipation locally. Attenuation of turbulence and enhancement of dissipation rate is significant within 1.5 diameters of the particle surface. Beyond 5 diameters, turbulence modification is negligible.

Of specific interest to this work is the distance to which the modification of the flow field by a fixed particle extends in a turbulent flow. This information is useful when modeling particle-laden flows and determining if the flows are dilute or dense. Regime maps for various levels of interaction have been developed and presented in the literature [12], but they have not been assessed at a fundamental level. PR-DNS are carried out for flow past single particles and multiple particles. The Reynolds number, Re, based on the mean velocity and the height of the channel is fixed. This implies that the pressure gradient is increased when particles are present to overcome the pressure loss due to the presence of the particles. The multiple particle simulations provide insight into the effect of particle-particle interactions on the distance to which the flow field is affected. Detailed analysis of the flow field downstream of the particle is carried out to understand how the flow field is modified. It is expected that the flow field will recover to the single-phase flow field some distance from the particle. An interesting questions relates to potential differences in recovery distances for the mean turbulence parameters and mean velocity.

The next section of the chapter presents the lattice-Boltzmann computational method adopted in this work for the PR-DNS. The computational conditions are

then discussed. Results and discussion follow, first for the single-particle simulations and then for the multiple particle simulations. The chapter ends with summary and conclusions.

7.2 Computational Model

The lattice-Boltzmann method (LBM) is employed to carry out the particle-resolved direct numerical simulations. The Boltzmann equation describes the evolution of the distribution function of single molecule velocity within the framework of kinetic theory. The lattice-Boltzmann equation (LBE) can be derived from the Boltzmann Equation by discretizing the velocity space with finite velocities. It is shown in Chapter 3 that by performing a Taylor-series expansion in time and space and by using the Chapman-Enskog expansion, the Navier-Stokes equations can be recovered from the LBE. In the computations presented in this work, the multiple relaxation time (MRT) collision operator [115,116,155] is used to model the effect of intermolecular collisions. The MRT collision operator is stable and allows for simulations with lower viscosities than the Bhatnagar-Gross-Krook (BGK) collision operator. Simulations of high Reynolds number (Re) flows require lower viscosities and hence the MRT collision operator is employed. An interpolation supplemented half-way bounce back scheme is used to represent the particle boundary [124].

7.3 Computational Conditions

Figures 7.1-7.2 show the computational setup for the single particle and multiple particle simulations. The flow is in the X-direction, the walls are normal to the Y-axis and the Z-direction is periodic. Table 7.1 shows the parameters of the 9 PR-DNS cases that are studied in this work. In Table 7.1, the Reynolds number based on friction velocity, Re_τ, is defined as

$$Re_\tau = \frac{u_\tau \delta}{\nu}, \tag{7.1}$$

where u_τ is the friction velocity, δ is the channel half-width and ν is the kinematic viscosity. The particle diameter, d_p, and the distance between the particle and the wall, δ_h, are normalized by the viscous length scale as follows:

$$d_p^+ = \frac{d_p}{l_v}, \tag{7.2}$$

$$\delta_h^+ = \frac{\delta_h}{l_v}, \tag{7.3}$$

where the viscous length scale, l_v, is obtained from u_τ and ν as

$$l_v = \frac{\nu}{u_\tau}. \tag{7.4}$$

Cases 1-6 have a single particle in the channel. The distance from the center of the channel to the wall in viscous units is 180. In Case 1, the distance between the particle surface and the wall, δ_h^+, is 10.8, i.e. the particle is positioned close to the wall. The particle is at the center of the channel for Case 2. Cases 1 and 3 and 2 and 4, respectively, provide insight into the effect of particle size and Cases 1 and 5 and 2 and 6, respectively, examine the effect of the Reynolds number, Re_τ. Cases 7 to 9 are multiple particle simulations. The particles are arranged in one plane. The arrangements are shown in Fig. 7.2. Case 7 has 6 particles of the same size as the particles of Case 1. Case 8 has the same area reduction ratio as Case 7, but the particle diameters are halved and hence there are 24 particles. Cases 9 has six particles and a similar arrangement to Case 7, but the particle diameter is halved.

7.4 Results and Discussion

7.4.1 Single Particle Simulations

To begin with, the mean flow and turbulent kinetic energy (TKE) profiles in the channel for $Re_\tau = 180$, when particles are not present will be discussed. This would

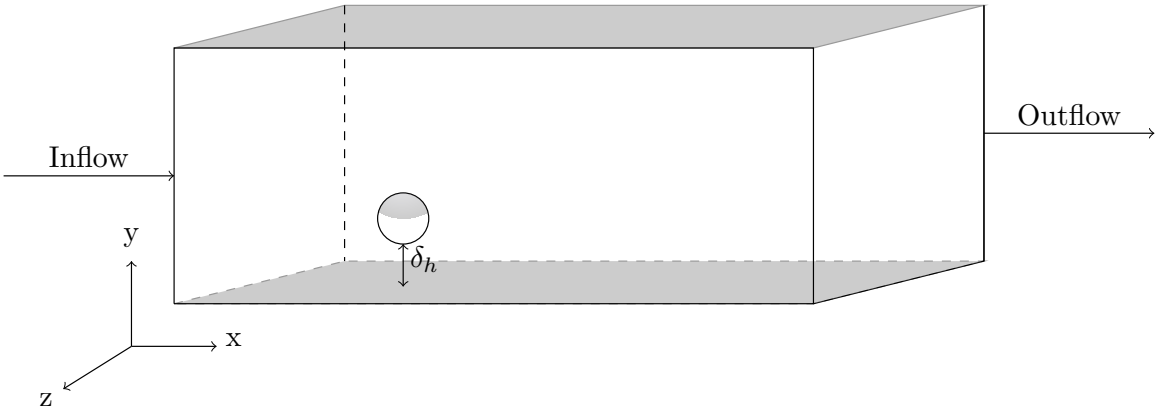

Figure 7.1: Schematic of the computational domain showing a single particle near the wall.

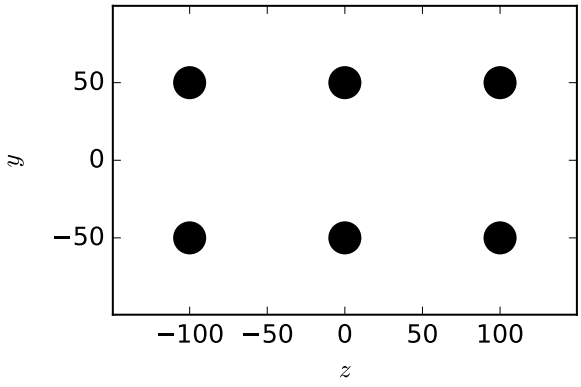

(a)

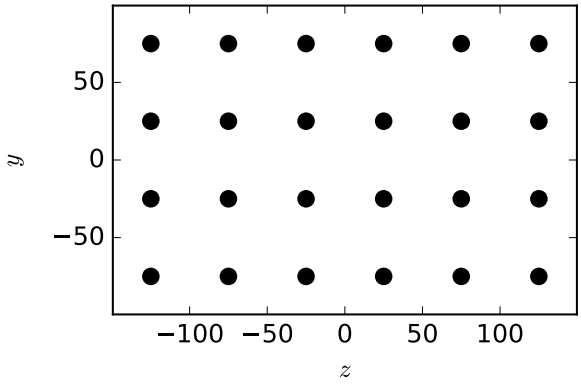

(b)

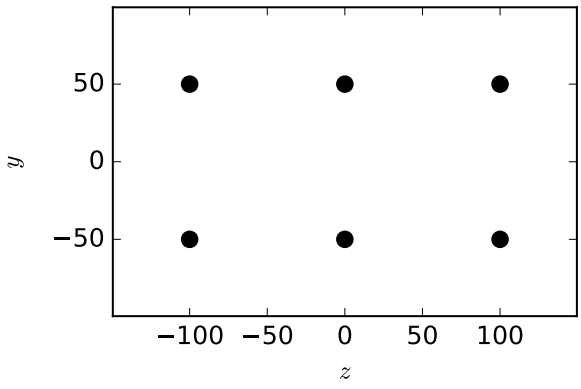

(c)

Figure 7.2: Particle arrangement for the multi-particle simulations: (a) Case 7; (b) Case 8; (c) Case 9.

Table 7.1: Parameters employed for simulations.

Case	Reynolds number (Re_τ)	Particle diameter (d_p^+)	Particle position (δh^+)	Number of particles (n_p)	Area fraction of particles ($A_p/A_{tot}(\%)$)
1	180	36	10.8	1	0.3926
2	180	36	Center	1	0.3926
3	180	18	10.8	1	0.0981
4	180	18	Center	1	0.0981
5	270	36	10.8	1	0.2873
6	270	36	Center	1	0.2873
7	180	36	-	6	3.14
8	180	18	-	24	3.14
9	180	18	-	6	0.786

correspond to a Reynolds number of about 6000 based on the channel height and the maximum mean velocity.

Figure 7.3 shows the mean velocity profile in the channel when no particles are present. In this case, when the flow is fully developed, the mean velocity profile is dependent on only the Y-coordinate (i.e. distance from the wall). The velocity is normalized by the friction velocity ($u^+ =< U > /u_\tau$) and the distance by the viscous length scale ($y^+ = y/l_v$). The mean velocity profile in a turbulent channel flow is well known [133, 137]. Figure 7.3 also shows that profile [133]. The agreement between the results from this work and those in the literature are within 5%. Note that from $y^+ = 40$ to $y^+ = 180$, the fluid velocity increases from $u^+ \approx 15$ to $u^+ \approx 19$.Turbulent mixing ensures the fluid velocity is nearly uniform throughout the interior core. For $y^+ < 20$, there is a sharp decrease in the velocity in the turbulent boundary layer. In the first set of simulations with a single particle, the effect of a particle on the flow field near the wall where the velocity gradient is large and another particle in the center of the channel, where the velocity gradient is small, will be assessed.

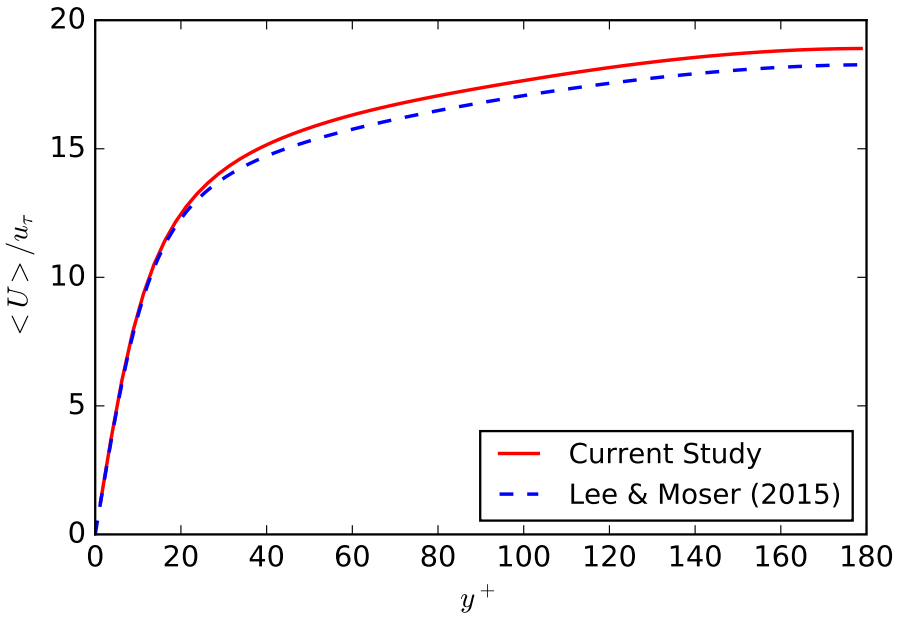

Figure 7.3: Mean velocity profile in a single phase flow.

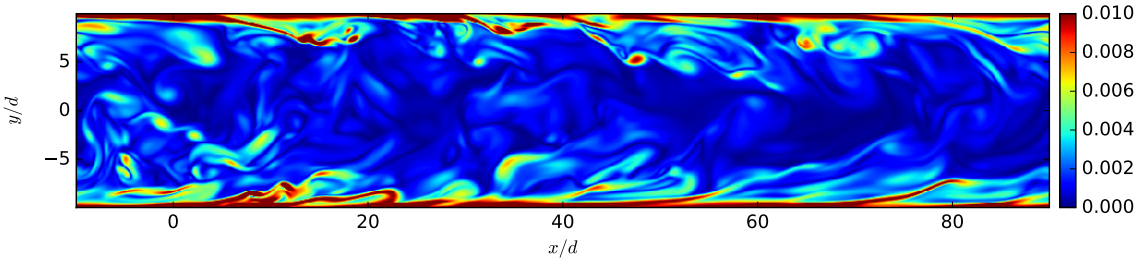

Figure 7.4: Instantaneous vorticity magnitude in a single phase flow. Color scale is in lattice units.

Figure 7.4 shows the magnitude of instantaneous vorticity in the middle Z-plane when there are no particles. Near the wall, maximum vorticity is observed since the velocity gradient is high in that region. Moreover, although this is not evident in the figure, the vortices in this wall have a smaller length scale. Away from the wall, the magnitude of vorticity is smaller and the length scales are larger. Figure 7.5 shows the TKE profile in the channel. TKE is maximum in regions of high shear where the production of TKE is high. Consequently, at a relatively short distance from the wall ($y^+ \approx 15$), the TKE reaches a maximum. Toward the center, the TKE decreases since the production of TKE due to shear decreases. From $y^+ = 15$ to the wall, there is a sharp decrease in TKE. The TKE profiles is also well documented in the literature [133] and that profile is also shown in Fig. 7.5 for comparison. The agreement between the results from this work and those in the literature are within 5% in terms of the peak value of TKE and its location from the wall.

Results will now be presented when a single particle is located near the wall at $\delta_h^+ = 10.8$, i.e. Case 1 in Table 7.1. Figure 7.6a shows the normalized mean U-velocity in the Y-direction, i.e. normal to the flow direction at various downstream distances from the particle. $x/d = 0$ corresponds to a plane passing through the center of the particle. $x/d = 1$, corresponds to a plane which is located one radius from the surface of the particle. The presence of the particle eliminates homogeneity in the X and Z direction and hence statistics are obtained by averaging in time only. By examining

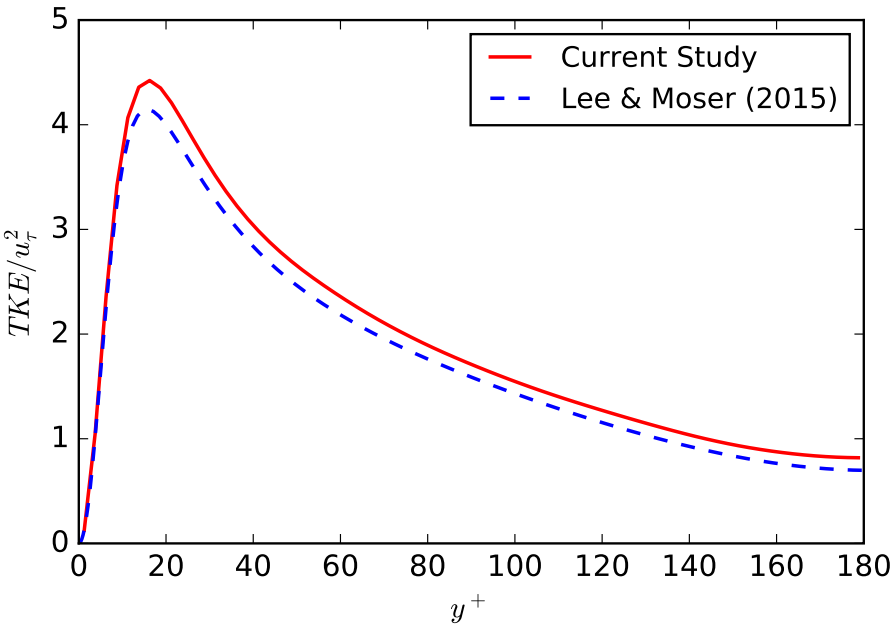

Figure 7.5: Turbulent kinetic energy (TKE) profile in a single phase flow.

the velocity profile in Fig. 7.6a and the velocity vectors in Fig. 7.6b, a high speed streak of fluid in the gap between the particle and the wall is evident in the plane passing through the center of the particle. Figure 7.6a shows a u^+ value of 14 at y^+ of about 5 between the particle surface and the wall. This is about a factor three greater than the velocity of the single-phase at the same location. Similar high speed streaks have been observed in the case of turbulent flow over a particle located at a distance from a flat plate [156, 157]. Interestingly, such high speed streaks have not been observed in laminar flow around a particle in a channel [158]. A possible reason for this is that in the case of a turbulent flow, the inertia of the flow is higher such that the fluid is forced into the gap whereas in a laminar flow, viscous effects dominate and viscous forces oppose the flow in the gap between the particle and the wall. The consequence of the high fluid velocity between the particle and wall is that it induces a vortex in the wake, rotating counter-clockwise downstream of the particle as evident in Fig. 7.6b. The wake shifts away from the wall. The wake region extends to an x/d of about 2. At $x/d = 1$, there is a negative velocity which arises due to the recirculation region in the wake of the particle.

Figure 7.6c shows the TKE profiles as a function of the distance from the wall, y^+, at various x locations from the particle center. At $x/d = 2$, there is a spike in the TKE downstream of the particle on the side of the wake away from the wall. This is due to the interaction of the vortices that are shed in the wake of the particle with the free stream turbulence. On the wall side however, there is no observable spike since the high speed fluid in the gap pushes the vortices shed from the particle away from the wall. The peak TKE occurs at an $x/d \approx 2$ the maximum X-distance where the influence of the recirculation bubble is evident on Fig. 7.6b. The high turbulence observed is the effect of continuing generation of turbulence and convection of turbulent vortices from upstream. The modulation in the TKE decreases in its effect with increasing distance from the particle. At $x/d = 20$, the mean velocity profile shown in Fig. 7.6a and the TKE profile shown in Fig. 7.6c show negligible differences compared to the profiles in a channel where the Re_τ is the same, but

without any particle i.e., the distance of influence is less than 20 particle diameters. That the mean velocity profile and the TKE profile recover to these values is not surprising since those profiles are dependent only on the Re_τ.

When the particle is at the center, i.e. Case 2, Fig. 7.7a shows a small spike in the velocity of the fluid close to the particle surface. This increase is, however, less than 20% of the fluid velocity at that location without a particle. At $x/d = 1$, there is a negative velocity which arises due to the recirculation region in the wake of the particle. The recirculation region is evident in Fig. 7.7b which shows the mean flow velocity vectors and color contours. This is similar to what is seen in Fig. 7.6a. The mean flow is symmetric about the centerline and two vortices induced in the wake are consistent with well documented findings [159]. Figure 7.7c shows the TKE along the Y-direction in a X-plane passing through the center of the particle and several planes downstream of the particle. There is no noticeable effect on the TKE in the fluid region in the plane passing through the center of the particle. However, a large increase in TKE is observed at $x/d = 1$, i.e. in the shear region at the interface between the recirculation bubble and the free stream, which increases further and is noticeable throughout the bubble by $x/d = 2$. The peak value in TKE is greater than the value at the same location when there is no particle by a factor of about 16. This TKE subsequently decays. At $x/d = 6$, the highest value of TKE is only a factor of about 4 greater than the value at the same location when there is no particle. Comparing the results with the earlier case where the particle is close to the wall, the peak TKE in this case, like the earlier case, is at $x/d \approx 2$ which is the axial dimension of the recirculation bubble. One difference is that the peak TKE is about 16 times higher than the undisturbed TKE at the particle center whereas it was about 4 times higher when the particle was close to the wall. This is likely because of a viscous damping effect near the wall. An important conclusion is that by $x/d \approx 20$, the single-phase results are recovered in mean velocity and TKE.

Figures 7.8 and 7.9 show the results when the particle diameter is halved and the particle is located close to the wall (Case 3) and at the centerline (Case 4),

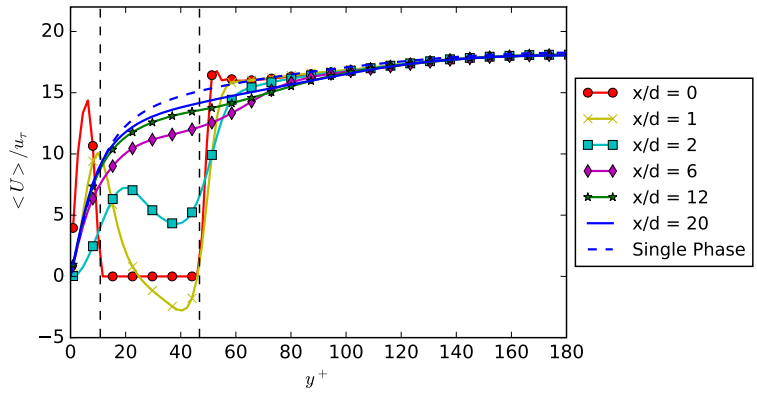

(a)

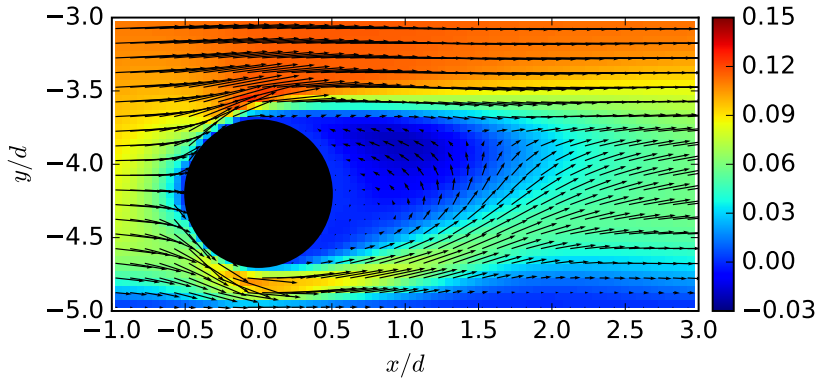

(b)

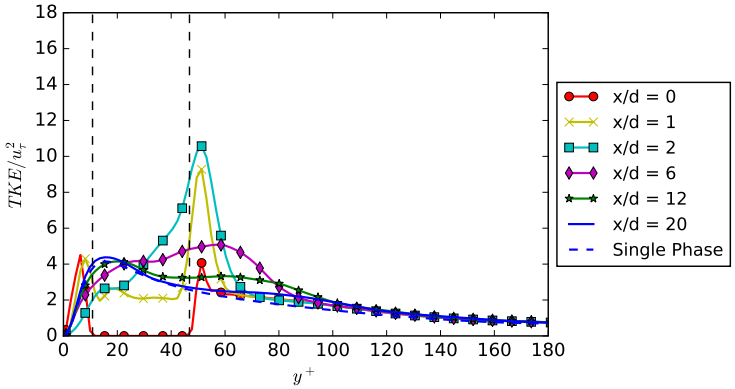

(c)

Figure 7.6: Flow field results when particle is close to wall and $Re_\tau = 180$, $d_p^+ = 36$ (Case 1): (a) Mean velocity in the X-direction as a function of y^+ at various x/d; (b) Mean velocity vectors. Color contours, with scale in lattice units, are indicative of the velocity magnitude; and (c) Turbulent kinetic energy (TKE) profile as a function of y^+ at various x/d.

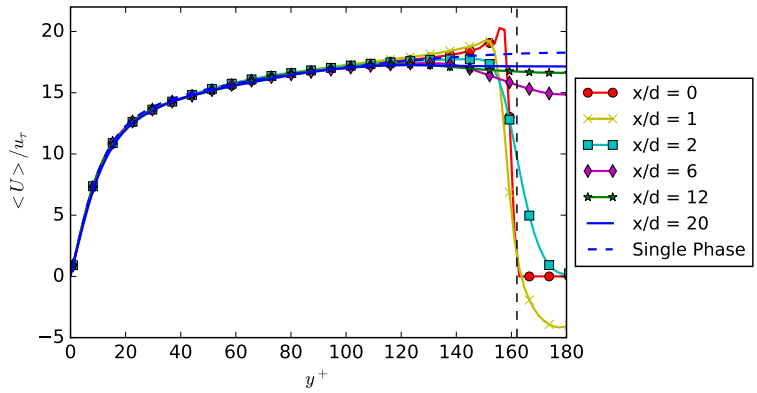

(a)

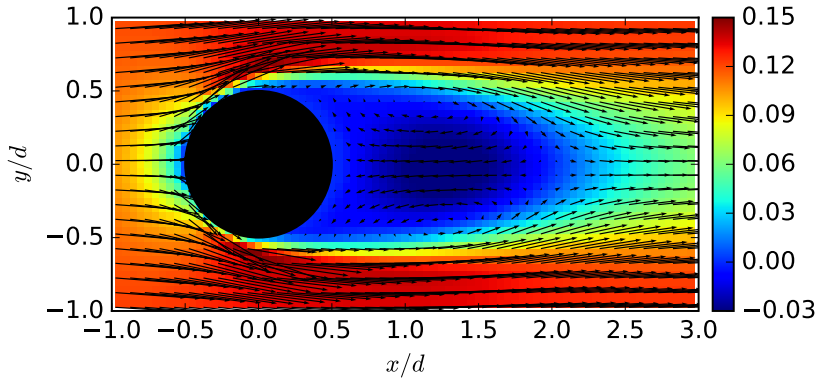

(b)

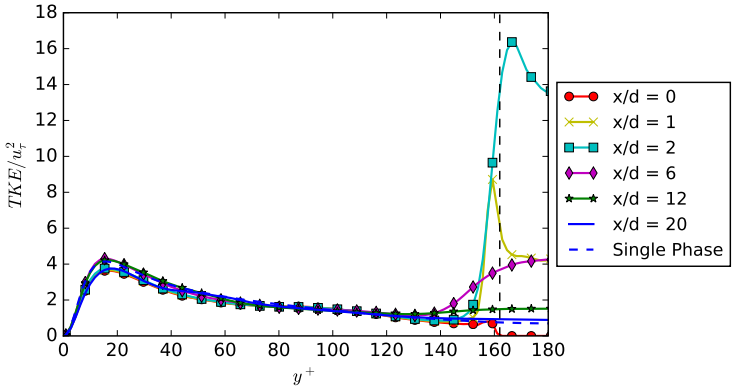

(c)

Figure 7.7: Flow field results when particle is at the center and $Re_\tau = 180$, $d_p^+ = 36$ (Case 2): (a) Mean velocity in the X-direction as a function of y^+ at various x/d; (b) Mean velocity vectors. Color contours, with scale in lattice units, are indicative of the velocity magnitude; and (c) Turbulent kinetic energy (TKE) profile as a function of y^+ at various x/d.

respectively. Note that results for Case 3 should be compared with those for Case 1 and Case 4 with Case 2. Figures 7.8a and 7.9a show the mean velocity in various X-planes, 7.8b and 7.9b show the velocity vectors and color contours, and 7.8c and 7.9c the TKE profiles in various X-planes. From Fig. 7.8a, we observe that the increase in velocity between the particle surface and wall is now smaller compared to Case 1. In both cases, the spacing between the particle and the wall is held constant, but in Case 3, the obstacle is smaller, and hence less fluid is forced into the gap. Comparing Figs. 7.8b and 7.6b, we see that the length of the recirculation bubble is shorter. In the earlier case, it was about 1.5 to 2 diameters whereas in Case 3 it is about 1 to 1.5 diameters.

Comparing the TKE profiles shown in Figs. 7.6c and 7.8c, there is increase in TKE on either side of the particle in both cases. However, for Case 3, there is a higher peak value of TKE in the gap between the particle and the wall. It is possible that this may reflect lower rate of decay of the TKE near the wall from its value upstream where the particle effect was not felt, i.e. the TKE profile corresponds to that shown in Fig. 7.5. The increase in TKE on the side away from the wall is, however, lower than in Fig. 7.6c. The single-phase flow results are recovered within 5% by $x/d = 20$ although the physical distance corresponding to $x/d = 20$ is shorter for the smaller diameter particle.

Comparing the results in Fig. 7.9 with those in Fig. 7.7, i.e. when the particle is at the center of the channel, the results are similar. Since the results presented are non-dimensional, the expectation is that the they would be close if not identical. The mean velocity profiles of Figs. 7.9a and 7.7a are, in fact, very close. Visually, the results of Figs. 7.9b and 7.7b are very close. However, there are noticeable differences between the results of Figs. 7.9c and 7.7c. One obvious difference is that the increase in TKE appears to be primarily concentrated in the shear layer between the recirculation bubble and the free stream in all x/d planes. This TKE generated in the shear layer is not convected into the center of the bubble. This may arise from the fact that the actual physical distance corresponding to a certain x/d is shorter in

Fig. 7.9c compared to Fig. 7.7c. Correspondingly the residence time of the fluid is also shorter. In both cases, the TKE decays approximately to the values that exist when there is no particle by $x/d = 20$.

Figures 7.10 (Case 5) and 7.11 (Case 6) show the results when the Reynolds number, Re_τ is increased by 50%, i.e. $Re_\tau = 270$. The results of Figs. 7.10 and 7.11 should be compared with those of Figs. 7.6 and 7.7, respectively. Figure 7.10a shows that when the particle is close to the wall, there is an increase in velocity in the gap. This increase is about a factor 3 greater than the single-phase results, and is similar to what was observed in Case 1. Comparing Figs. 7.10b with 7.6b and 7.10c with 7.6c, it can be seen that the velocity flow field and the TKE behavior are very similar. In both cases, the flow field is not affected for more than about 20 diameters downstream. When the particle is at the center, Fig. 7.11a shows that the velocity increase is less than 20%. Again, this is similar to what was observed in Fig. 7.7a for Case 2. The mean velocity vectors and TKE profiles are also similar. Figure 7.11c shows the TKE profile as a function of y/d at various downstream distance from the particle for Case 6 where $Re_\tau = 270$. Comparing with Case 2, where $Re_\tau = 180$, it can be seen that the peak TKE is similar in magnitude and occurs at $x/d = 2$. At $x/d > 6$, increasing the Reynolds number by 50% does not appear to have a significant effect. As pointed when comparing Cases 2 and 4 where Case 4 has a smaller diameter particle, when comparing Cases 2 and 6, the TKE in Case 6 is concentrated in the shear layer between the wake and the free stream and does not increase in the center of the recirculation bubble. As pointed out earlier, this maybe related to the shorter residence time of the fluid at higher Re_τ.

7.4.2 Multiple Particle Simulations

The effect of multiple particles in a plane normal to the flow direction on the flow downstream will now be considered (Cases 7-9). In Cases 7, the particle size is the same as was in Cases 1 and 2 of the single particle study. In Case 7, there are 6

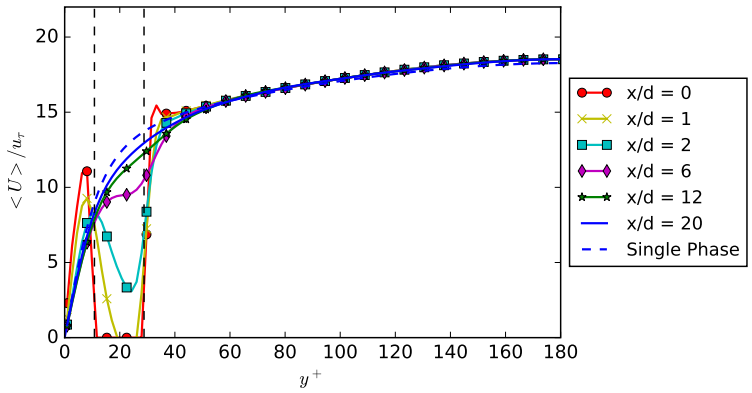

(a)

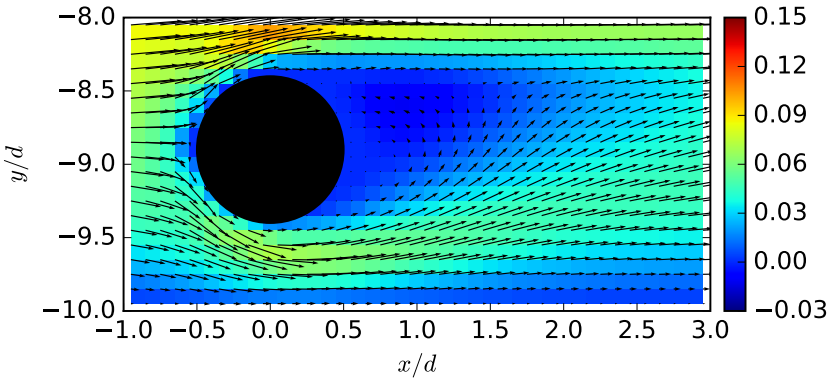

(b)

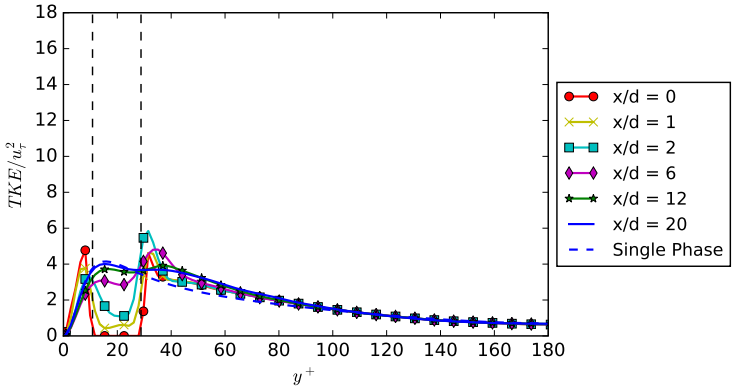

(c)

Figure 7.8: Flow field results when particle is close to wall and $Re_\tau = 180$, $d_p^+ = 18$ (Case 3): (a) Mean velocity in the X-direction as a function of y^+ at various x/d; (b) Mean velocity vectors. Color contours, with scale in lattice units, are indicative of the velocity magnitude; and (c) Turbulent kinetic energy (TKE) profile as a function of y^+ at various x/d.

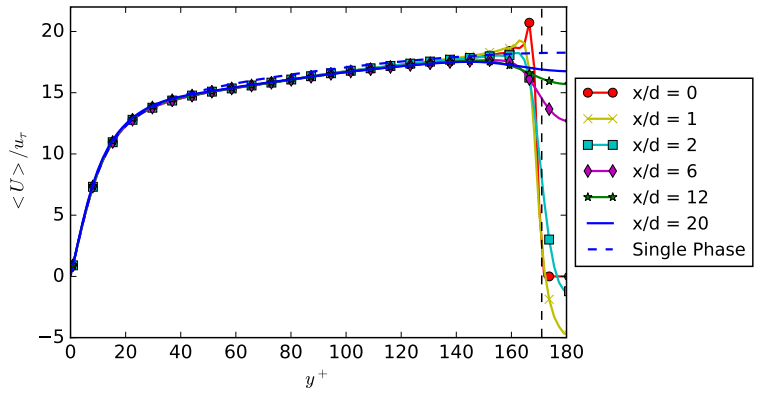

(a)

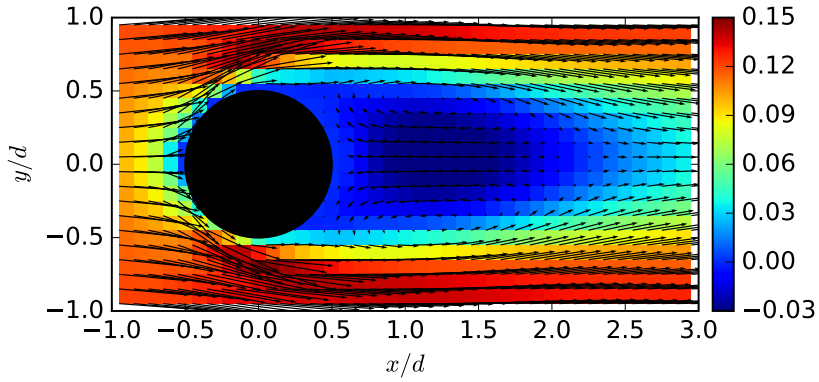

(b)

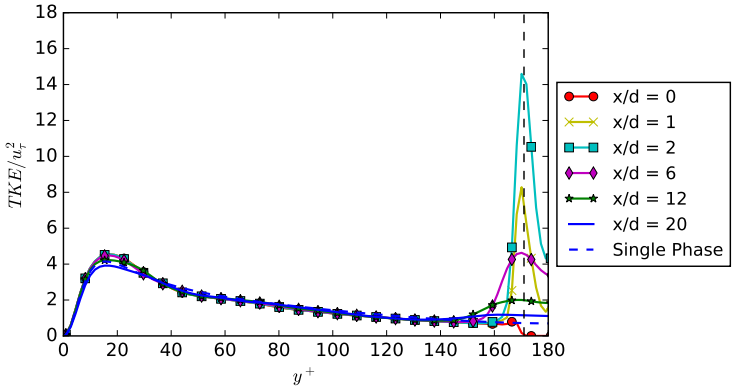

(c)

Figure 7.9: Flow field results when particle is at the center and $Re_\tau = 180$, $d_p^+ = 18$ (Case 4): (a) Mean velocity in the X-direction as a function of y^+ at various x/d; (b) Mean velocity vectors. Color contours, with scale in lattice units, are indicative of the velocity magnitude; and (c) Turbulent kinetic energy (TKE) profile as a function of y^+ at various x/d.

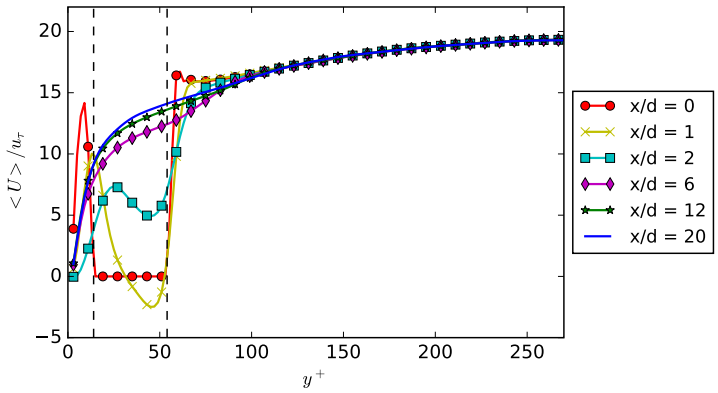

(a)

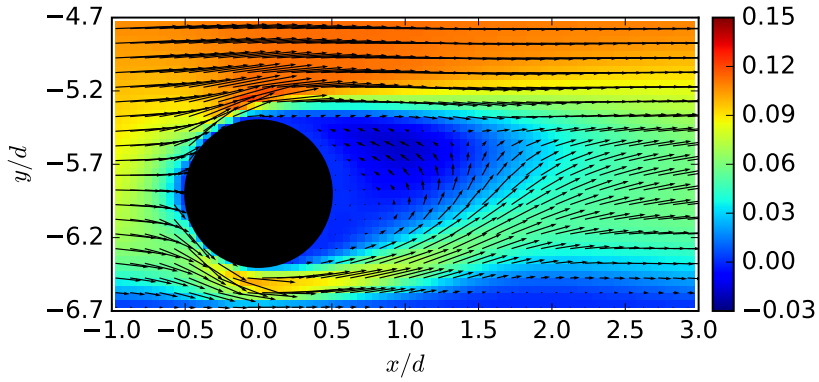

(b)

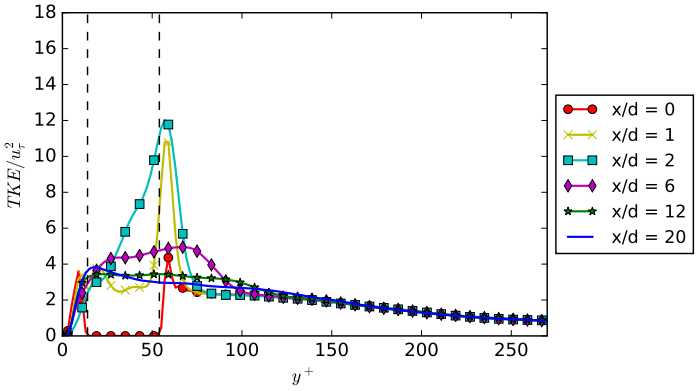

(c)

Figure 7.10: Flow field results when particle is close to wall and $Re_\tau = 270$, $d_p^+ = 36$ (Case 5): (a) Mean velocity in the X-direction as a function of y^+ at various x/d; (b) Mean velocity vectors. Color contours, with scale in lattice units, are indicative of the velocity magnitude; and (c) Turbulent kinetic energy (TKE) profile as a function of y^+ at various x/d.

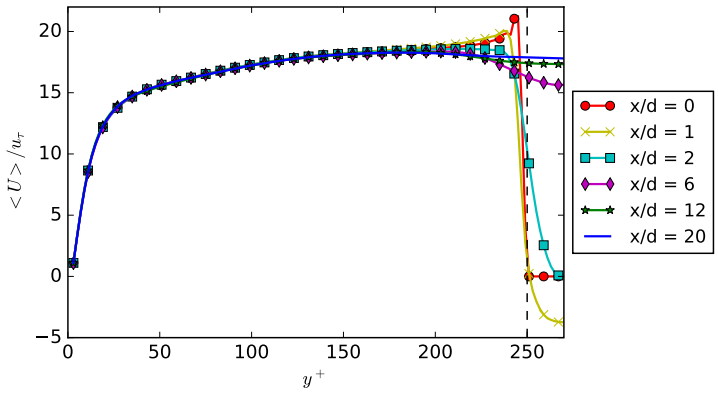

(a)

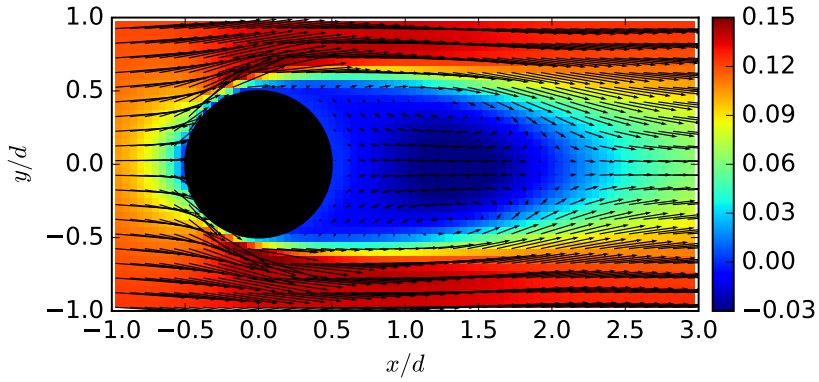

(b)

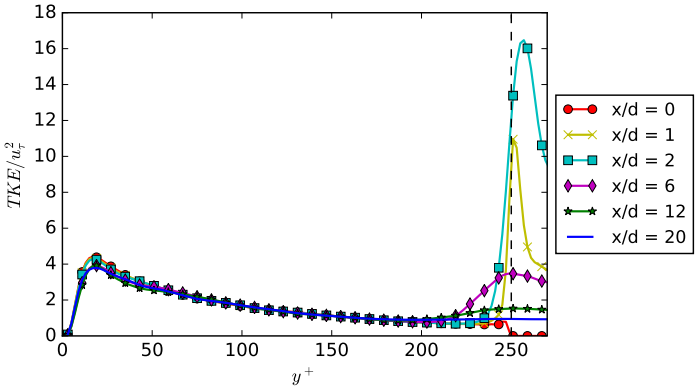

(c)

Figure 7.11: Flow field results when particle is at the center and $Re_\tau = 270$, $d_p^+ = 36$ (Case 6): (a) Mean velocity in the X-direction as a function of y^+ at various x/d; (b) Mean velocity vectors. Color contours, with scale in lattice units, are indicative of the velocity magnitude; and (c) Turbulent kinetic energy (TKE) profile as a function of y^+ at various x/d.

particles. Cases 8 and 9 have the same particle size as that of Cases 3 and 4 in the single particle study. Case 8 has 24 particles and the same area fraction of particles as Case 7, while Case 9 has 6 particles. Figure 7.2 shows the arrangement of particles for all the three cases. In the case of multiple particles, averaging is done in both the Z direction and time unlike the single-particle cases where averaging was done only in time. This was done to account for the effect of all the particles on the flow field as opposed to just one.

Figure 7.12 shows results for Case 7 where there are 6 particles in a single plane normal to the flow direction, with three particle on either side of the mid-plane of the channel. Other conditions, listed in Table 7.1, include non-dimensional particle diameter of 36. This may be compared to a non-dimensional channel width of 360. The cross-sectional area of the plane in which the particles are centered is reduced by 3.14% relative to the rest of the channel. Figure 7.12a shows the mean velocity profile in several x/d planes downstream from the plane that passes through the center of the particles. Results are shown only in the lower half of the channel. The averaging in the Z-plane reduces the observed impact of the particles on the flow field. It is known from the single particle simulations earlier that this impact is more significant than revealed in Fig. 7.12a. This impact is also clearly evident in Fig. 7.12b which shows the instantaneous vorticity contours in a Z-plane passing through two particles. Comparing the results of Fig. 7.12b with those of Fig. 7.4 without any particles, it is evident that the effect of the particles extends to an x/d of about 30. Recall that since $d = 36$, x corresponds to 1080 for x/d of 30. Although Fig. 7.4 shows results only until x of about 400, the high concentration of vorticity that is evident in Fig. 7.12b at x/d of 30 is not evident at $x = 400$ in Fig. 7.4. The mean velocity in Fig. 7.12a suggests, however, that the mean velocity profile upstream of the particles is recovered downstream by x/d of about 6, although it is known from the single particle simulations earlier that it took until an x/d of about 20 for the mean velocity downstream of individual particles to recover. This apparent discrepancy is just on account of the averaging in the Z plane for the multi-particle simulations. While

the mean velocity recovers by x/d of about 6, Fig. 7.12c shows that the turbulent kinetic energy (TKE) recovers to the single-phase values within 10% by an x/d of 20 and within 5% by an x/d of 40. In other words, the TKE takes a longer distance to recover even when averaged in the Z-plane. This conclusion is consistent with the instantaneous vorticity contours shown in Fig. 7.12b where the effect of the particles on the vorticity is evident until x/d of about 30 and beyond. The interaction between wakes of multiple particles is likely responsible for this longer distance compared to the distance when only one particle is present, see Case 1.

The impact of this interaction between particles is further examined by increasing the number of particles in Case 8 while keeping the reduction of the cross-sectional area to 3.14%. The diameter of an individual particle is reduced by 50% thereby making it possible to increase the number of particles in the cross-sectional plane to 24, i.e. with 12 particles arranged in two rows of 6 each, on either side of the mid-plane of the channel as shown in Fig. 7.2b. The mean velocity is shown in Fig. 7.13a. Although the area reduction in Cases 7 and 8 is the same, it can be seen from Fig. 7.13a that it takes a longer x/d, of about 20, for the mean velocity to recover to the single-phase value. It is, however, important to note that the x/d of 20 in Fig. 7.13a corresponds to an x/d of 10 in Fig. 7.12a because the particle diameter in Case 8 is 50% of that in Case 7. In other words, the actual physical distances are not that different. Nevertheless, the 50% increase in distance suggest that interaction between the wakes of larger number of particles can have greater impact on the mean velocity. Figure 7.13b shows the vorticity contours. Compared to Fig. 7.4 which shows the vorticity contours for a simulation without particles, the impact of the particles can be seen in Fig. 7.13b until an x/d of about 80 well beyond the maximum value of x for which results are shown in Fig. 7.4. Fig. 7.13c shows the TKE. The TKE recovers to its single phase value within 10% by an x/d of 20 and within 5% by x/d of 40. It is possible that higher order turbulent statistics may take longer to recover. The effect of increasing number of particles appears to be to increase the interactions between particle wakes and lengthen the distance of such interactions in the mean

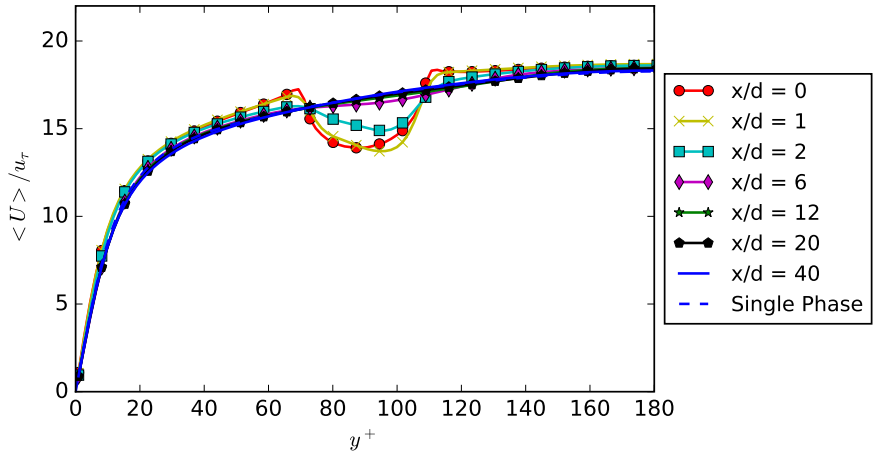

(a)

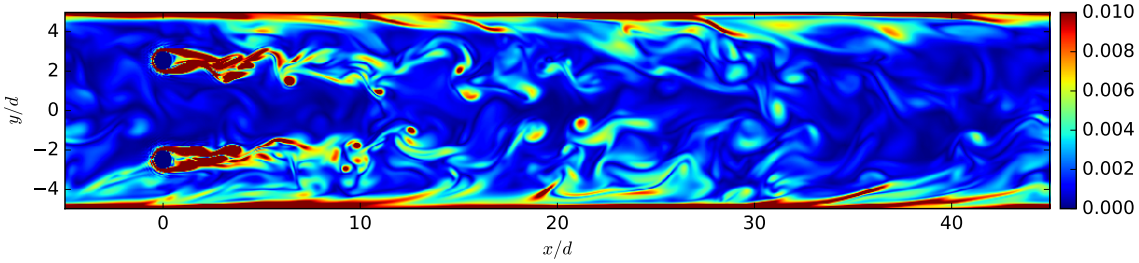

(b)

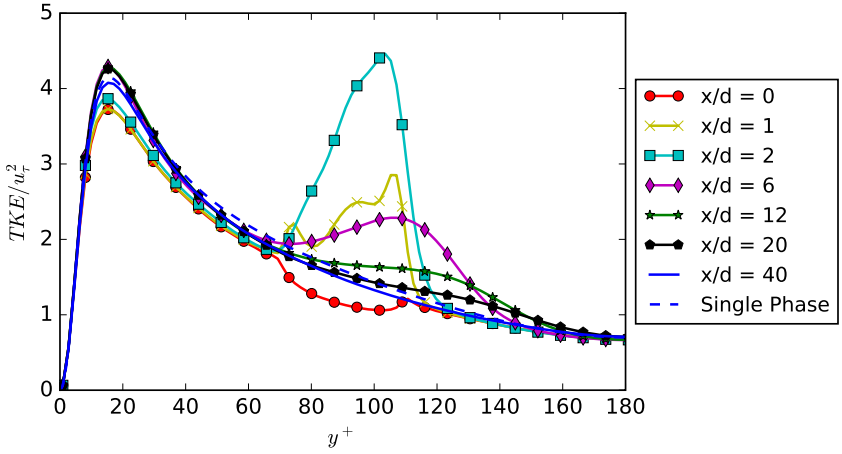

(c)

Figure 7.12: Flow field results when $d_p^+ = 36$ and $n_p = 6$ (Case 7): (a) Mean velocity in the X-direction as a function of y^+ at various x/d; (b) Instantaneous vorticity magnitude in the wake of the particles. Color scale is in lattice units; and (c) Turbulent kinetic energy (TKE) profile as a function of y^+ at various x/d.

flow direction. Since both diameter of particle and number of particles are changed in Case 8 relative to Case 7, it is interesting to consider a simulation where only particle diameter is changed.

Figure 7.14 shows results from a simulation (Case 9) where there are 6 particles with the identical arrangement to Case 7 earlier, but with each particle diameter reduced by 50%. It is interesting to first examine the vorticity contours shown in Fig. 7.14b. The impact of the particles on the vorticity is evident until an x/d of about 60 which for the simulation with the larger particle diameter corresponds to an x/d of about 30. Recall that in that simulation the impact was evident until an x/d of about 30. In other words, the physical distance of influence is about the same. This can suggest that the turbulent eddy turnover time scales, which relate to the dissipation of the vorticity, are not very different between the two simulations. The results of mean velocity in Fig. 7.14a and TKE in Fig. 7.14c show less impact of the particle relative to Fig. 7.12a and 7.12c, respectively, because of the averaging in the Z-plane.

An interesting observation in the vorticity contours of all three simulations is that there appears to be relatively strong interaction of the vorticity field of the particle closest to the wall with the vorticity field generated by the wall.

7.5 Summary and Conclusions

The lattice-Boltzmann method is employed to carry out direct numerical simulations (DNS) of flow past a spherical particle, fixed either at the center or close to the wall of a channel, and multiple spherical particles fixed in a plane normal to the flow direction in a channel. The particle boundary layer is fully resolved by adopting a method that accounts for the curved boundary. The focus of the study is on the distance of influence of the particle on the flow field in the direction of the flow. It is shown that for the single particle simulations, this distance extends to a non-dimensional distance x/d of about 20. In the case of the multiple parti-

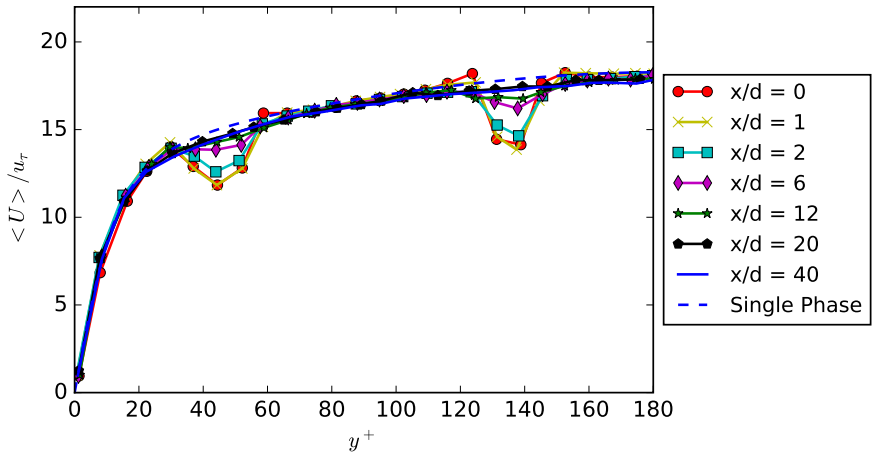

(a)

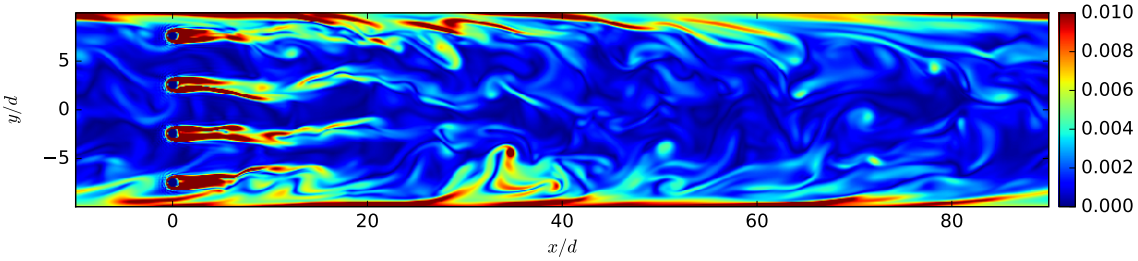

(b)

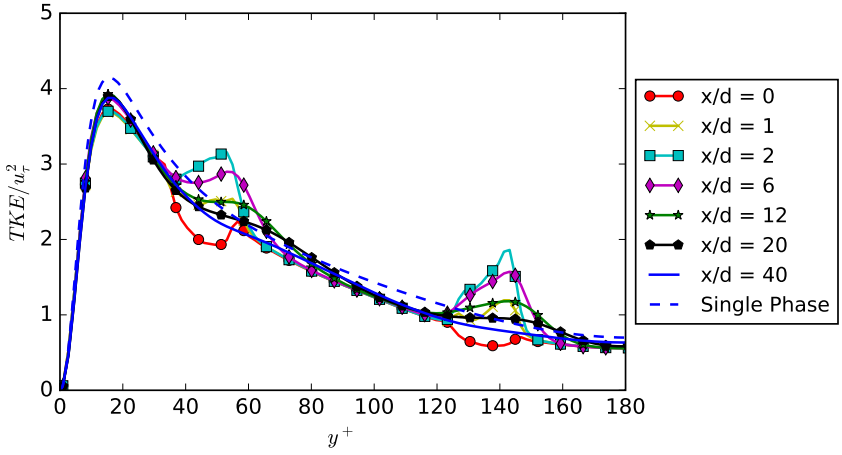

(c)

Figure 7.13: Flow field results when $d_p^+ = 18$ and $n_p = 24$ (Case 8): (a) Mean velocity in the X-direction as a function of y^+ at various x/d; (b) Instantaneous vorticity magnitude in the wake of the particles. Color scale is in lattice units; and (c) Turbulent kinetic energy (TKE) profile as a function of y^+ at various x/d.

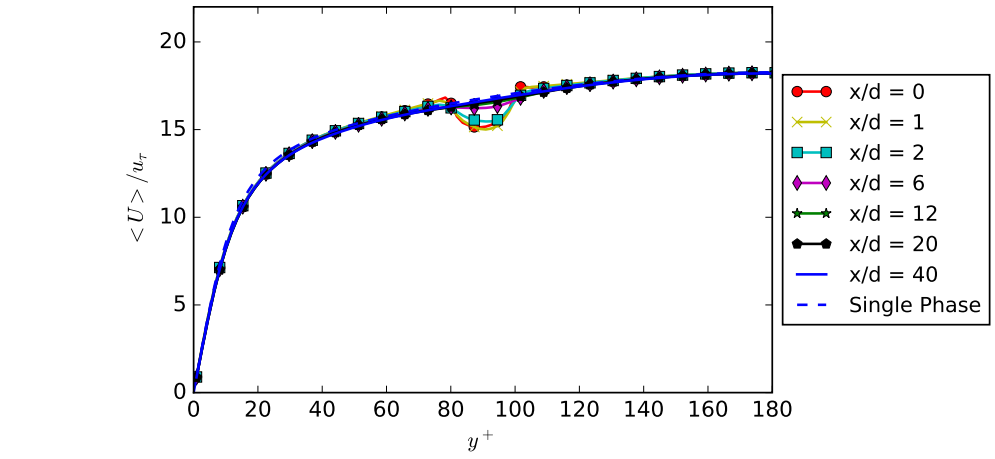

(a)

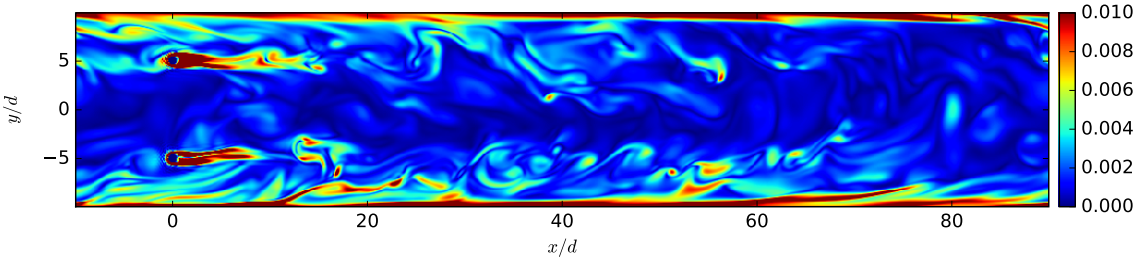

(b)

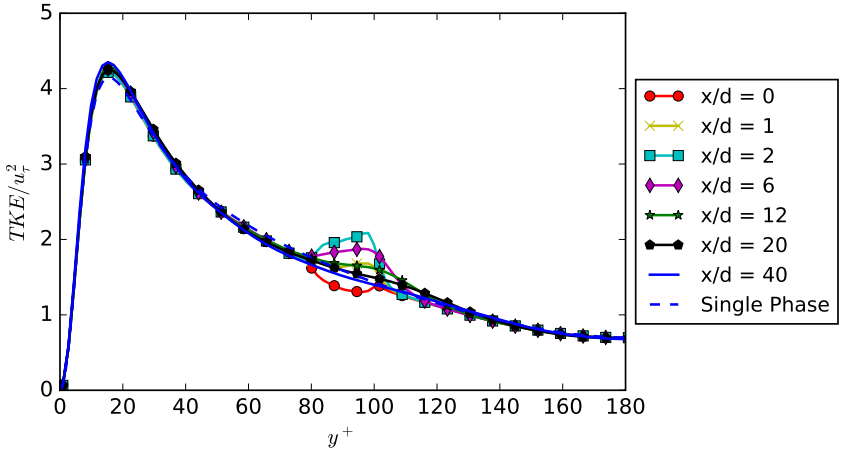

(c)

Figure 7.14: Flow field results when $d_p^+ = 18$ and $n_p = 6$ (Case 9): (a) Mean velocity in the X-direction as a function of y^+ at various x/d; (b) Instantaneous vorticity magnitude in the wake of the particles. Color scale is in lattice units; and (c) Turbulent kinetic energy (TKE) profile as a function of y^+ at various x/d.

cles, the distance extends to an x/d distance of about 40. Increasing the number of particles increases the distance of influence. This suggests that in a particle-laden flow, if particles are separated by a distance greater than x/d of about 40 on average, inter-particle interactions can be neglected. At shorter distances, such interactions are important, possibly becoming increasingly important as distances are reduced. There is also evidence that the presence of particles close to the wall results in strong interactions of the vorticity flow fields generated by the particle and the wall. This needs further study. In this work, only mean velocity and turbulent kinetic energy have been used as measurable variables to assess the influence of the particles. It will be interesting to consider higher-order turbulent statistics in future work.

8. FULLY-RESOLVED DIRECT NUMERICAL SIMULATIONS OF PARTICLE MOTION IN A TURBULENT CHANNEL FLOW

8.1 Introduction

In the last chapter, particle-resolved direct numerical simulations of stationary particles in a turbulent channel flow was considered. The effect of moving particles in a turbulent channel flow is presented in this chapter. The effect of Stokes number, St, and the particle size, d_p on the concentration of particles in a turbulent channel flow is examined to see if particles exhibit preferential motion. The work employs the same code that was used to carry out the particle-laden flow study in Section 4.8 and the turbulent flow studies in Section 4.9. Part of this work has been submitted for publication in *Computers and Fluids*.

8.2 Preferential Particle Movement

Preferential particle movement has been studied by several researchers in the past [3–5, 5–10, 36]. At first instance, one would expect particles in a turbulent flow to be distributed uniformly on account of enhanced mixing. This, however, is not the case in most flows. Even in an homogeneous isotropic turbulent flow, the particle concentration can be highly non-uniform [3].

Consider the experimental study by Lau and Nathan [11] of particle-laden turbulent pipe flow described in Chapter 2. In this work, particles were introduced into a turbulent pipe flow and were transported by the flow. The length of the pipe was sufficiently long to achieve a fully developed flow. In their experiment, the particles were larger than the Kolmogorov length scale or about the same. They noticed that

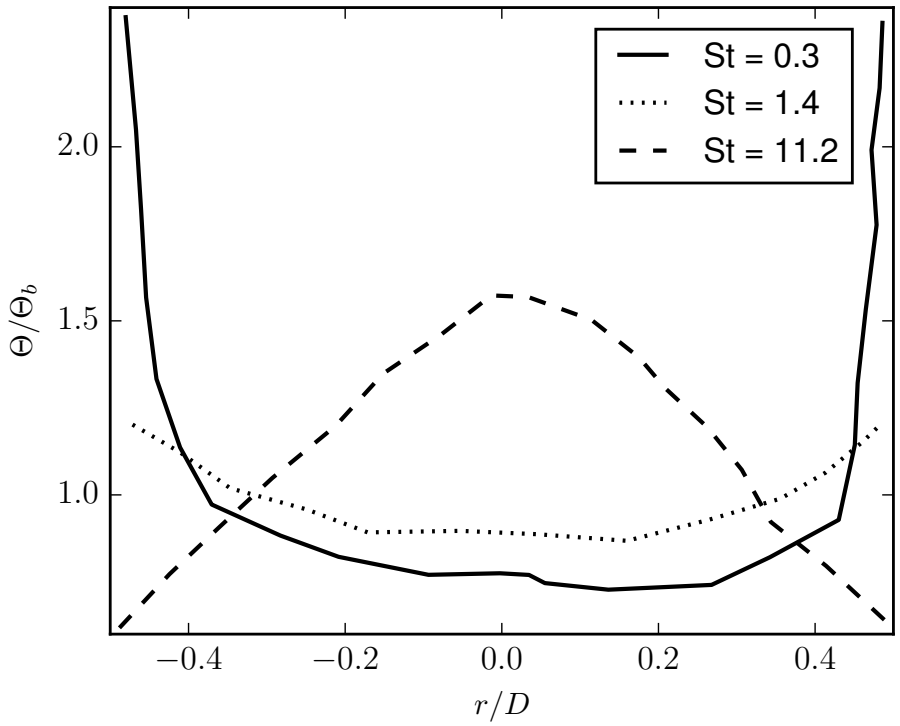

Figure 8.1: Concentration profile of particles at the exit of a turbulent pipe flow (Adapted from Lau and Nathan [11]).

the particle concentration at the exit of the pipe was not uniform. The particles preferentially concentrated near the axis or the wall depending on their St. Figure 2.2 shows the concentration profile of particles across the cross section of the pipe normalized by the bulk concentration at the exit. At a relatively low St of 0.3, the particle concentration near the wall is about 2.5 times the bulk concentration. For a higher St of 11.2, the particle concentration is high near the axis of the pipe. Particles with a St of 1.4 are distributed almost uniformly. Thus, as the St increases from 0.3 to 11.2, the radial concentration profile changes from a 'U-shape' to a '$\wedge$-shape'. Turbophoresis has been suggested as the cause of this behavior.

Prior DNS numerical studies have generally considered the limit where particles are small with respect to the Kolmogorov length scale, i.e. $d_p << \eta_k$, and hence the point-particle approach can be employed. If d_p is of the order of Kolmogorov length scale or larger, the point particle assumption cannot be made and the particle

boundary has to be numerically resolved to compute the interaction of the turbulent eddies with the particle [160]. In other words, particle-resolved direct numerical simulations (PR-DNS) are necessary. These simulations are computationally very expensive. They often involve a limited number of particles, far less than what one would encounter practically. The advantage of the particle-resolved method, however, is that the force acting on the particle is computed directly from the viscous stresses acting on the particle and no model is used. Moreover, as the flow field around every particle is resolved, the dissipation of turbulent kinetic energy at the surface is resolved and need not be modeled [45].

There are several particle-resolved studies in laminar flows. One of the earliest works is that of Feng *et al.* [37, 38] who performed *two-dimensional* numerical simulations of cylindrical "particles" settling in a channel with no mean flow, and transported in a channel by fluid moving in the laminar flow regime. They were able to observe the Segré-Silberberg effect [22, 23]. They also identified Saffman lift [19], Magnus lift [141], and wall repulsion [142, 143] to be the dominant forces that cause the particle movement in the cross-flow direction. They reported the dependence of the particle trajectories on parameters such as the particle based Reynolds number, Re_p , the ratio of channel height to the particle diameter, H/d_p, and the ratio of the particle to the fluid density, ρ_p/ρ_f. Mortazavi and Tryggvason [39] performed similar simulations with deformable drops in a channel flow. They observed that at high Re_p, the drops began to oscillate about the center of the channel.

Nourbakhsh *et al.* [41] have carried out three-dimensional simulations of drops in a Poiseuille flow and studied the effect of capillary number, Ca, the Re and the volume fraction of the drop phase on the drop movement. They found that drops with small deformation migrate to an equilibrium position half-way between the wall and the center i.e., Segre-Silberberg effect [22, 23], while highly deformable drops migrate to the center of the channel.

Chapter 6 presented studies involving the inertial migration of resolved particles in a laminar flow. It was found that at low St, the particles exhibited the Segre-

Silberberg effect [22, 23] while at high St, the particles oscillate about the channel center. As an extension of this work, Zhang et al. [161] studied the regime of transition St where particles move from near the wall and start oscillating about the center. They found that oscillations arise when the Saffman lift and inertial forces are comparable.

The studies listed so far have been for laminar flow. There are few studies available for PR-DNS of turbulent flows. Zeng et al. [152] have studied the interaction of a stationary particle with wall turbulence through PR-DNS. They examined the flow field around the particle and how it affects the drag on the particle. They found that high and low speed streaks near the wall cause a low frequency fluctuation of the drag force on the particle while the vortex shedding from the particle causes a high frequency component. Wang et al. [153] carried out PR-DNS of a turbulent channel flow with neutrally buoyant particles. They found that the mean flow velocity decreases with addition of the particles indicating the flow becomes effectively more viscous.

Shao et al. [162] carried out PR-DNS of particle-laden turbulent channel flow. They studied the effect of particles on turbulent intensities. They found that particle sedimentation on the walls can increase turbulent intensity from vortex shedding. If sedimentation effect is negligible, particles decrease streamwise fluctuations. Kidanemariam et al. [163] carried out resolved simulations of particles in an open turbulent channel flow. They found that particles lag the fluid velocity and tend to reside in low-speed streaks.

While there have been a few PR-DNS studies on turbulence modulation by particles in a turbulent channel, there have been none on preferential movement of particles. In this chapter, particle-resolved DNS are carried out to provide insight into the preferential cross-flow movement of particles in a turbulent channel flow. A wide range of St, 0.5-100, is considered. The results are analyzed to understand the relative importance of various forces at different St. The lattice-Boltzmann method (LBM) is employed for the simulations. The method has been employed for particle-laden

flows in the past [51–54]. The next section discusses the LBM adopted in this study. Results and discussion follow. The chapter ends with summary and conclusions.

8.3 The Computational Method

In this work, the lattice-Boltzmann Method (LBM) is employed to carry out the PR-DNS. The LBM solves the Boltzmann equation with discrete velocity directions. The local and explicit nature of the method makes the resulting numerical code highly parallelizable. The LBM is a kinetic solver derived from the Boltzmann Equation by discretizing the velocity space with finite velocities. It is shown in Chapter 3 that by performing a Taylor-series expansion in time and space and by using the Chapman-Enskog expansion, the Navier-Stokes equations can be recovered from the lattice-Boltzmann equations. In this work, the multiple relaxation time (MRT) collision operator [115,116,155] is used to represent the effect of collisions. The MRT collision operator has been used because it has been shown to have superior numerical stability and is thus suited to simulate high Reynolds number (Re) flows [155].

The particles are treated as moving walls within the fluid domain. In the LBM, a no-slip boundary condition can be achieved by placing a wall halfway between the last fluid node and an imaginary boundary node and allowing the fluid particles to bounce on the wall and return to its initial node with a velocity in the opposite direction. He *et al.* [121] have shown that a bounce-back scheme with the wall placed halfway between the last fluid node and an imaginary boundary node gives second-order accurate results. However, the curved surface of the particle cuts the lattices at varying distances and not halfway as can be seen from Fig. 8.2. Hence, the halfway bounce-back scheme cannot be used as originally proposed. Bouzidi *et al.* [123] as well as Lallemand and Luo [124] have proposed a technique to account for curved boundaries. Consider the one-dimensional situation in Fig. 8.3. Fluid node at $\boldsymbol{r}_j$ is the last node near the wall while $\boldsymbol{r}_s$ is the first node in the solid region. The intersection of the wall and the boundary link is represented as $\boldsymbol{r}_w$. The distance of

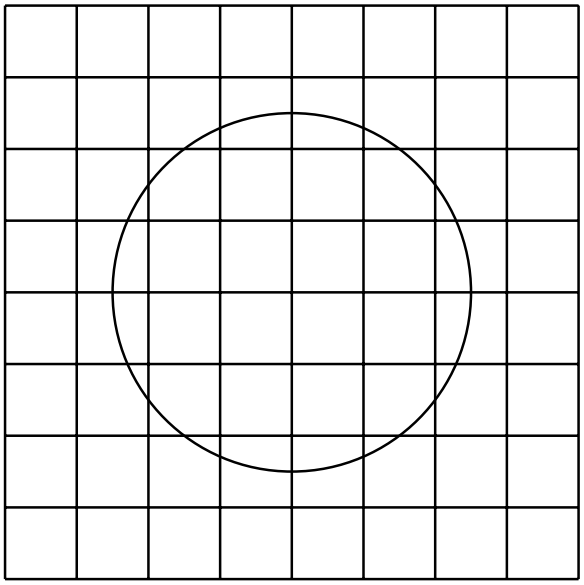

Figure 8.2: Schematic of a particle on a lattice.

the wall from the last fluid node is given as $q\delta_x = |\boldsymbol{r}_j - \boldsymbol{r}_w|$. If $q = 1/2$, the wall is located midway between the last fluid node and the first solid node and a half way bounce-back can be applied (Fig. 8.3a). However, if $q < 1/2$, the particle would reach position $\boldsymbol{r}_i$ between $\boldsymbol{r}_j$ and $\boldsymbol{r}_{j'}$ (Fig. 8.3b). Similarly, if $q > 1/2$, the particle would reach position $\boldsymbol{r}_i$ between $\boldsymbol{r}_j$ and $\boldsymbol{r}_{j'}$ (Fig. 8.3c).

The following procedure is adopted to preserve the boundary representation of the particle: when $q < 1/2$ (Fig. 8.3b), the distribution function at $\boldsymbol{r}_i$ is computed from the post collision distribution functions at $\boldsymbol{r}_{j''}$,$\boldsymbol{r}_{j'}$ and $\boldsymbol{r}_j$ through interpolation. This distribution function is then streamed so that it arrives at $\boldsymbol{r}_j$. When $q > 1/2$ (Fig. 8.3c), the distribution function at $\boldsymbol{r}_j$ is streamed to $\boldsymbol{r}_i$. Then the post streaming distribution functions at $\boldsymbol{r}_{j''}$,$\boldsymbol{r}_{j'}$ and $\boldsymbol{r}_i$ is used to evaluate the distribution function at $\boldsymbol{r}_j$. One can use either a linear or a quadratic interpolation. A quadratic interpolation is employed in this work.

In order to determine the force acting on the particle due to fluid drag, a momentum exchange technique, similar to that employed by Mei *et al.* [125], is used. In this method, the momentum transferred by the "LBM-particles" to the solid particle as

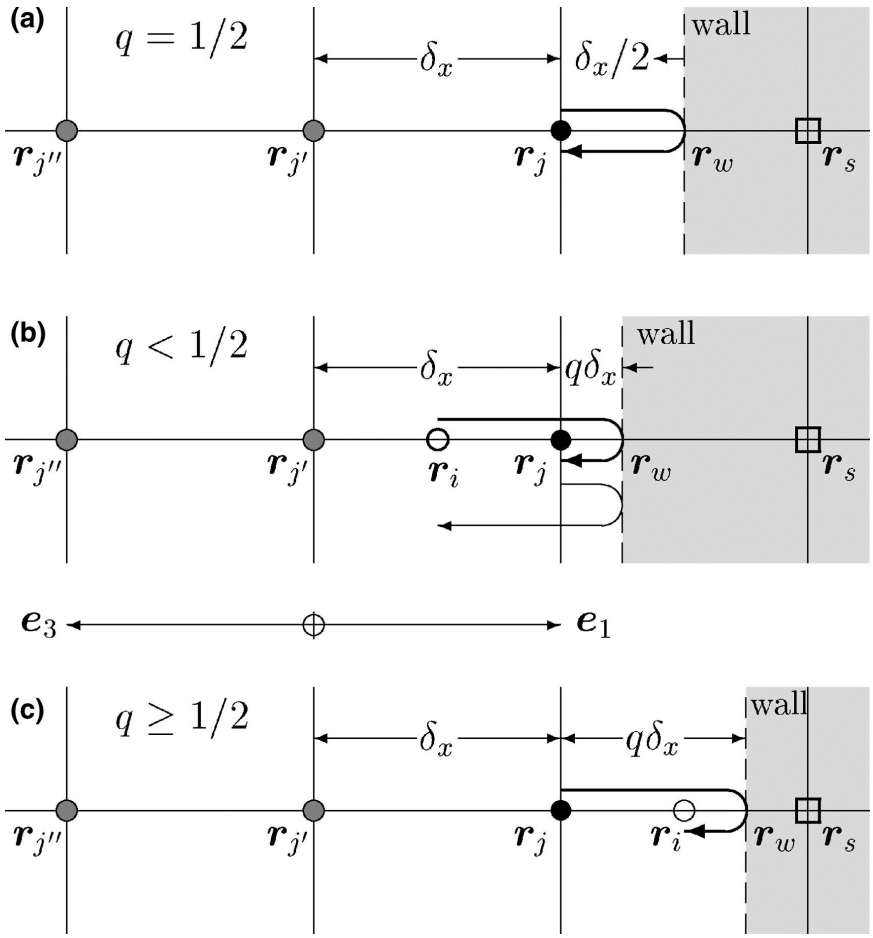

Figure 8.3: Schematic to illustrate boundary condition for a curved wall (Adapted from Ref. [124]).

it bounces from the surface of the particle is summed up to get the total momentum transferred to the particle in a time step. When the particle moves in the computational domain, some of the fluid nodes are uncovered and some covered. In such cases, the density at the newly appeared fluid node is obtained as the average density of all the neighboring fluid nodes. The velocity of the uncovered node is equal to the sum of the velocity of the particle and the angular velocity times the position vector joining the lattice node and the particle center. From this velocity and density, the equilibrium distribution functions are calculated and are assigned as the distribution functions of this node. This newly created fluid node gains some momentum. The particle momentum should therefore decrease by the same amount to ensure momentum conservation. Similarly, when a particle covers a fluid node, it gains the momentum of the fluid node at that instant. These forces due to particle covering and uncovering a fluid node are added to the force found by the momentum exchange method and used to update the velocity and position of the particle. Ref. [53] may be consulted for a detailed explanation of the implementation. The code has been tested for its accuracy in simulating particle-laden flows in Chapter 4.

8.4 Results and Discussion

Table 8.1 lists the computational conditions of seven PR-DNS cases considered in this work. The Reynolds number based on the friction velocity, Re_τ, is 180. There are 400 lattice points in the wall-normal direction, 600 in the span-wise direction and 1200 in the stream-wise direction. The grid size, Δ, is about 0.5 times the Kolmogorov length scale, η_k. The DNS of single-phase turbulent channel flow at this Re_τ does not require this many grid points, but the relatively large number of points was required because the inclusion of particles necessitated that the Mach number be less than 0.1 for stability considerations. There are 120 particles considered in this simulation.

In the first five cases, the effect of Stokes number, St, on particle movement is studied. The particle size d_p/η_k is held constant for these cases. For Cases 6 and 7,

Table 8.1: Parameters for the PR-DNS cases studied in this work.

Case	St	ρ_p/ρ_f	d_p/η_k
1	0.5625	1.2	11.1
2	2.3438	5	11.1
3	9.3752	20	11.1
4	37.5	80	11.1
5	93.75	200	11.1
6	0.432	3	5.92
7	10.368	72	5.92

the particle diameter is reduced by about a factor 2 while keeping the St comparable to Cases 1 and 3, respectively, to assess the effect of particle size on the motion.

It has been suggested in the literature that Saffman lift and turbophoresis affect the particle motion in the cross-flow direction [11]. Saffman lift is a force that acts on a particle in a shear flow when it either leads or lags the fluid velocity [19]. It was first identified by Saffman for a spherical particle in an unbounded uniform shear flow. Saffman showed that this lateral force acts to force the particle toward the faster moving fluid when it lags the fluid velocity and toward the slower moving fluid when it leads the fluid velocity. The magnitude of this force depends on the velocity gradient across the particle, and the slip velocity, i.e. relative velocity magnitude between the particle and the fluid.

Consider the non-dimensional mean velocity profile, u^+, as a function of non-dimensional normal distance from the wall, y^+, shown in Fig. 4.19. u^+ is obtained as

$$u^+ = \frac{< U >}{u_\tau}, \tag{8.1}$$

where $< U >$ is the mean velocity and u_τ is the friction velocity. u_τ is obtained from the wall shear stress, τ_w and fluid density, ρ, as

$$u_\tau = \sqrt{\frac{\tau_w}{\rho}}. \tag{8.2}$$

y^+ is obtained as,

$$y^+ = \frac{y}{l_v}, \tag{8.3}$$

where y is the normal distance from the wall and l_v is the viscous length scale. This mean velocity was obtained in a separate single-phase flow simulation of a turbulent channel flow. The averaging was done in both time and X and Z directions. Figure 8.4a shows the mean velocity as a function of normal distance from the wall whereas Fig. 8.4b shows the same profile plotted on a semi-log scale. The profiles are in agreement with well-known profiles in turbulent channel flows [137, 164]. It can be seen that near the wall there is a large gradient in the velocity whereas near the center the velocity change is small. The velocity increases from 0 at the wall ($y^+ = 0$) to about 13 at $y^+ = 25$, whereas from $y^+ = 100$ to $y^+ = 150$, it increases from 17.5 to 18. Enhanced mixing in the core of the channel by turbulent eddies reduces the gradients. Figure 8.5 shows the gradient of the mean velocity. Notice that it starts from 1 at $y^+ = 0$, since near the wall the velocity profile varies as $u^+ = y^+$. The gradient is large near the wall ($y^+ < 50$) and smaller away from the wall ($y^+ > 50$).

When a particle moves from the core of the channel toward the wall, it has a higher streamwise velocity than the fluid velocity because the fluid velocity decreases abruptly near the wall. The particle requires a longer time to adjust to the change in velocity because of inertia. While this is not applicable for tracer particles, it is indeed the case for finite-sized particles with inertia. Consider the schematic in Fig. 8.6a. The particle along with the mean flow velocity profile and the relative velocity vectors near the particle are shown. In the sketch, the relative velocity of the fluid on the wall side of the particle is higher than on the other side. This results in a lower pressure on the wall side which forces the particle to move toward the wall. This is Saffman

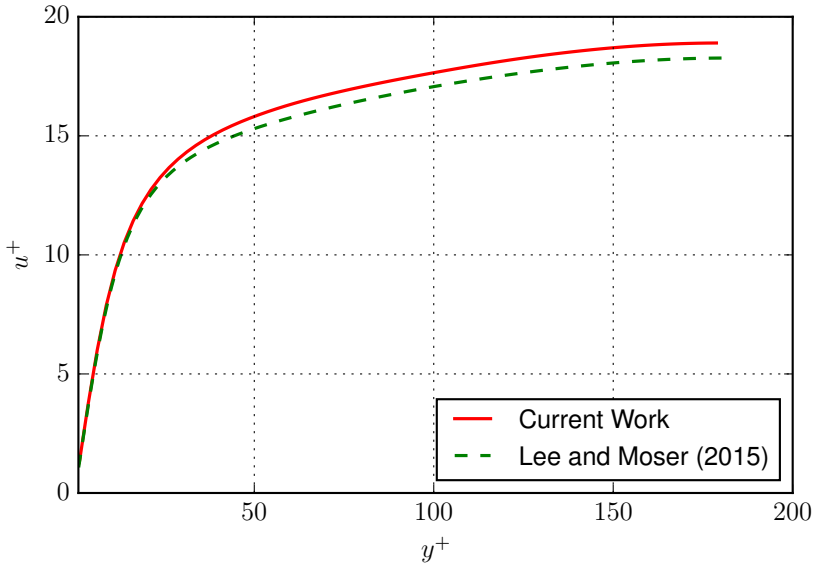

(a)

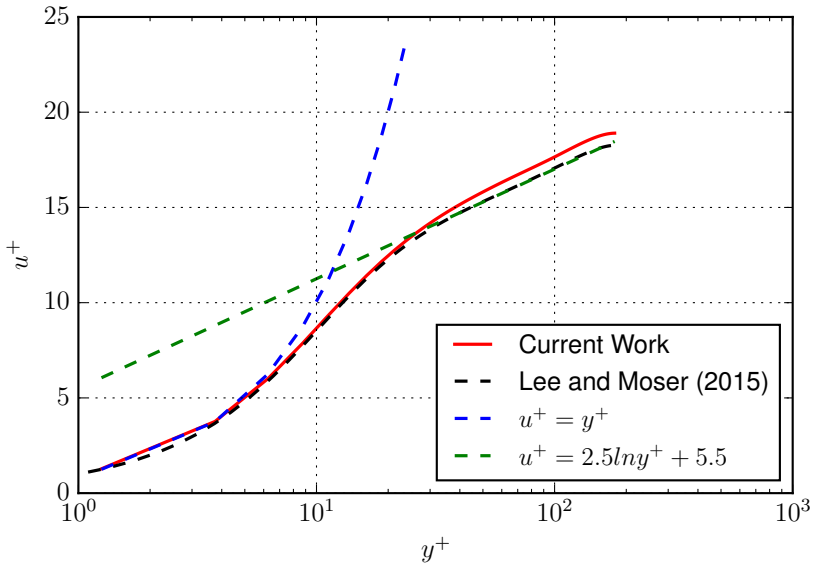

(b)

Figure 8.4: (a) Mean velocity profile in the cross-flow direction in a turbulent channel flow; (b) Mean velocity profile on a semi-log axis.

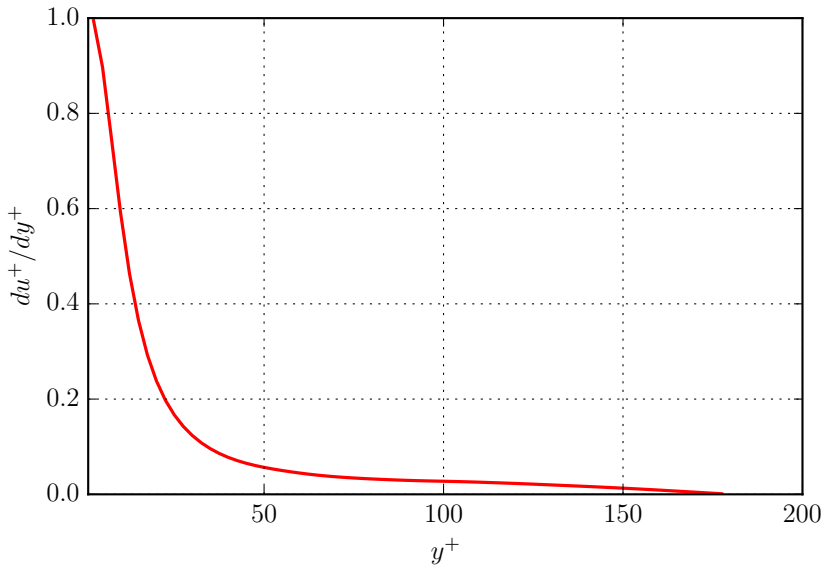

Figure 8.5: Gradient of the mean velocity profile in a fully developed turbulent channel flow.

lift. Additionally, the gradient in velocity across the particle is large near the wall and hence Saffman lift is large. Now, consider a case when the particle moves toward the center. In this case, the particle velocity would lag the fluid velocity. Figure 8.6b schematically shows a particle near the center and the relative velocity vectors. The relative velocity on the side close to the center is higher than the other side. This causes a lower pressure on the center side thereby forcing the particle towards the center. Since the gradient in the core of the channel is small, the magnitude of this force is small. Thus, Saffman lift forces the particle toward the wall with a larger force when it is close to the wall and toward the center with a smaller force when it is in the core of the channel.

Turbophoresis refers to the force acting on the particles when there is a gradient in turbulent kinetic energy (TKE) [165]. There are two mechanisms for turbophoresis: "global" turbophoresis and "local" turbophoresis. When the particle diameter, d_p, is larger than the Kolmogorov length scale, η_k, such that it encounters a gradient in TKE across it, it experiences a net force in the direction of lower TKE. This is analogous to thermophoresis. The turbulent fluctuations on one side transfer momentum to the particle at a higher rate than the other side which results in a net force on the particle in the direction of decreasing TKE. In this work, this effect is referred to as "local" turbophoresis. The magnitude of this force depends on the gradient of the TKE across the particle and on the size of the particle. Consider the variation of TKE with normal distance from the wall in a single phase turbulent channel flow shown in Fig. 8.7. These results are obtained from the single-phase flow simulation and they agree well with results from a spectral element code reported in the literature and shown in the figure [164]. It can be seen that the peak TKE occurs at about $y^+ \approx 15$ where the production of TKE is maximum. As the wall is approached, the TKE decreases sharply to zero as expected. There is a slower decrease in TKE toward the center of the channel. Figure 8.8 shows the gradient of the TKE as a function of y^+. Notice that near the wall ($y^+ < 20$), the magnitude of this gradient is large. As we move away from the wall ($y^+ > 20$), the gradient is smaller and approaches zero as

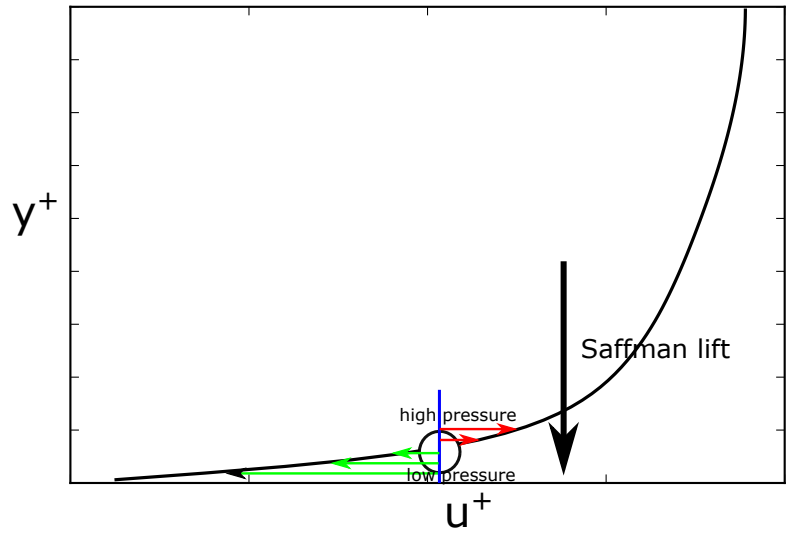

(a)

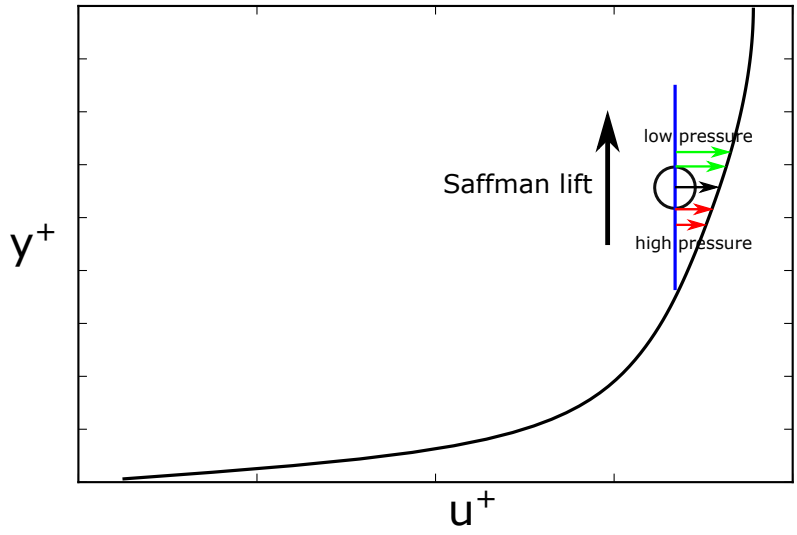

(b)

Figure 8.6: Schematic to illustrate Saffman lift force: (a) particle near the wall; (b) particle near center of channel. Velocity profile shown is in a cross-section.

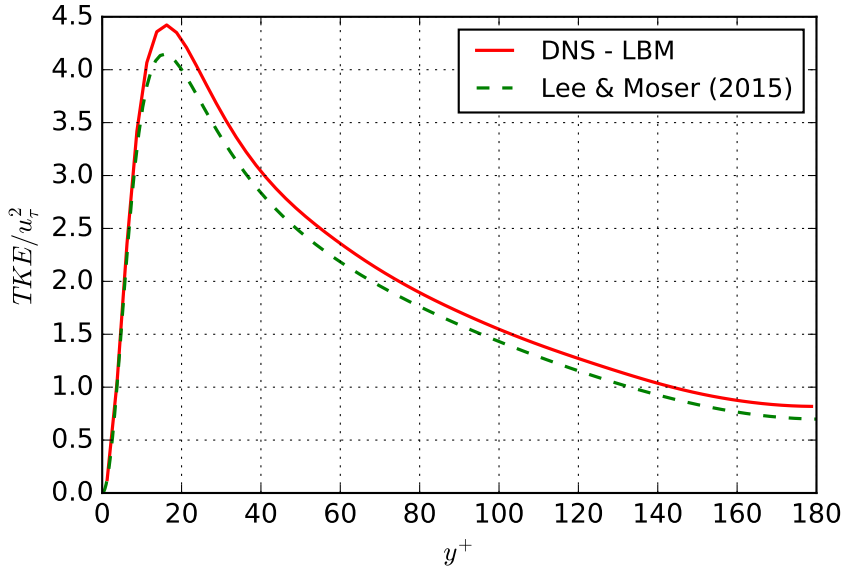

Figure 8.7: Turbulent kinetic energy profile in a channel flow without particles.

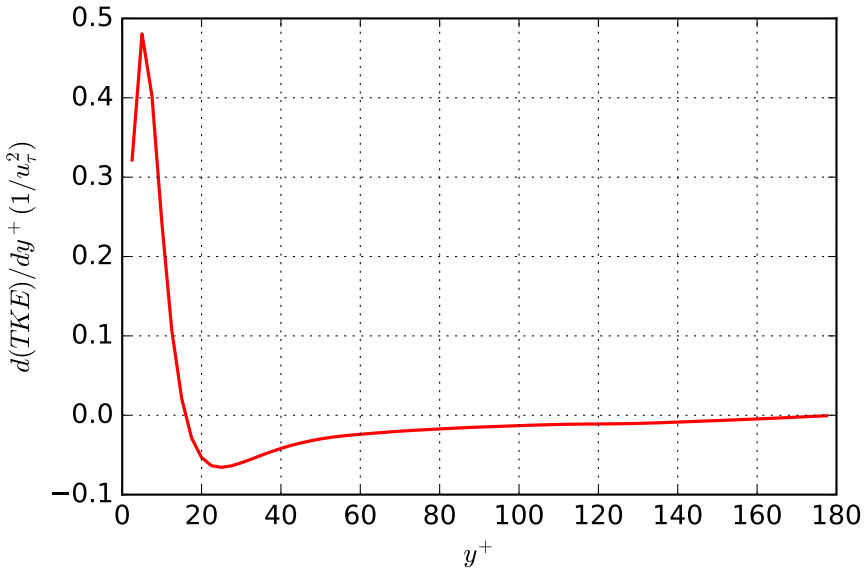

Figure 8.8: Gradient of turbulent kinetic energy in the channel.

we move toward the center. Thus, near the wall, turbophoresis is strong and forces the particle toward the wall. Away from the wall, turbophoresis is weak and forces the particle toward the center.

There is another way in which turbophoresis can act even when particles are not resolved. This will be referred to as "global" turbophoresis in this work. In a turbulent flow, particles are randomly dispersed by the turbulent eddies. If a particle has no inertia, i.e. $St = 0$ (tracer particles), then turbulence will ensure homogeneous particle concentration. However, if the particles have finite inertia, then the turbulent eddies have to overcome inertia to move the particle. Regions where TKE is higher would more easily disperse particles while regions with low TKE would have slower dispersion. This can concentrate particles in regions of low turbulence. This causes particles to concentrate near the wall and near the center. The random motion of turbulence will continually transport particles to the wall region or the center where they will concentrate. "Global" turbophoresis is much more dominant for particles with moderate St ($\sim O(1)$) since they respond more readily to turbulent fluctuations. As $St \to 0$ or $St \to \infty$, the effect of "global" turbophoresis vanishes. If the particles are larger than the integral length scale, l_e, i.e. $d_p > l_e$, only "local" turbophoresis would be relevant.

Figures 8.9-8.13 show the particle concentration profiles for Cases 1-5, respectively. The concentration profiles are obtained by separating the domain into slices in the Y-direction (i.e. normal to the walls) and then counting the number of particles in each slice. This is then normalized by the number of particles that should be in the slice if the particles are uniformly distributed. Thus each symbol represents a non-dimensional concentration of particles in that slice. Since the slices are discrete, the non-dimensional concentration shows some fluctuations. These fluctuations would decrease if we increase the number of particles or average over a long time.

Figure 8.9 shows the non-dimensional concentration profile for Case 1 where the St is 0.5625. The most significant trend is the high concentration near the wall, where the concentration is about 6 times higher than the bulk average concentration, while it is nearly uniform in the core of the channel ($-0.4 < y/H < 0.4$). This can be explained in terms of Saffman lift and turbophoresis. As discussed above, turbophoresis causes particles to concentrate near the wall or center. Saffman lift also forces the particle

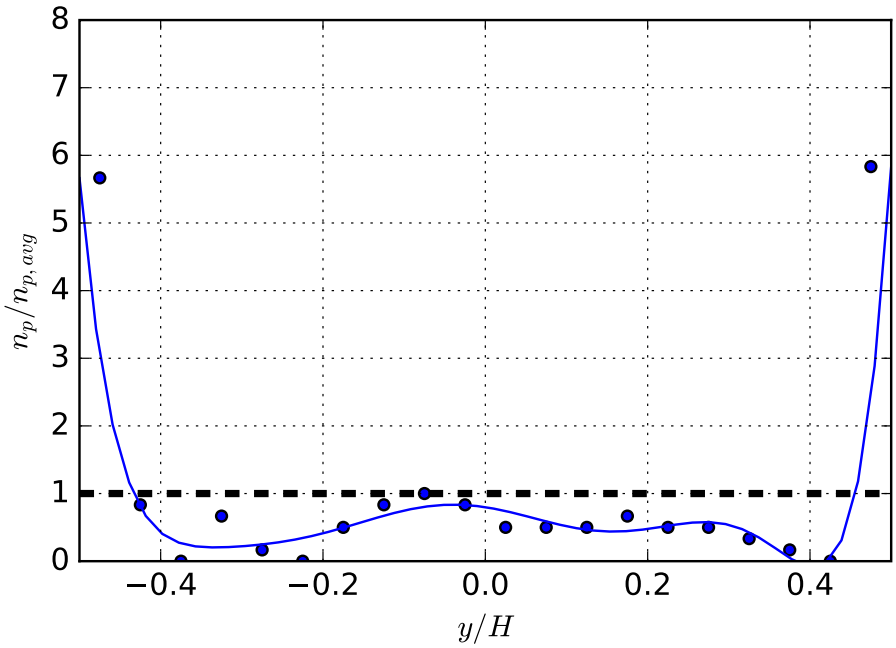

Figure 8.9: Non-dimensional particle concentration along the cross-section of the channel for Case 1. The symbols represent the concentration in each slice and the curve is a fit through these symbols.

toward the wall. As the particle moves toward the wall, lubrication forces act against that movement. The lubrication forces are not strong to cause the particle to escape from the wall region completely and so it accumulates. It should be noted that if the particle has no inertia (i.e. tracer particles), then global turbophoresis would have no effect. Saffman lift would also be absent since the particle would adjust to the fluid instantly and thus would not lag/lead the fluid velocity. "Local" turbophoresis can, however, still impact the particle motion. In fact, it is this "local" turbophoresis that may be more important for the low inertia, i.e. low St particles.

As the St is increased to 2.3438 (Case 2), we notice from Fig. 8.10 that the particle concentration near the wall is now about 7 times larger than the bulk average concentration. This is higher than what was seen for Case 1. One reason for this may be that since the inertia is higher, "global" turbophoresis also becomes important. Furthermore, once the particle comes close to the wall, the Saffman lift is larger than

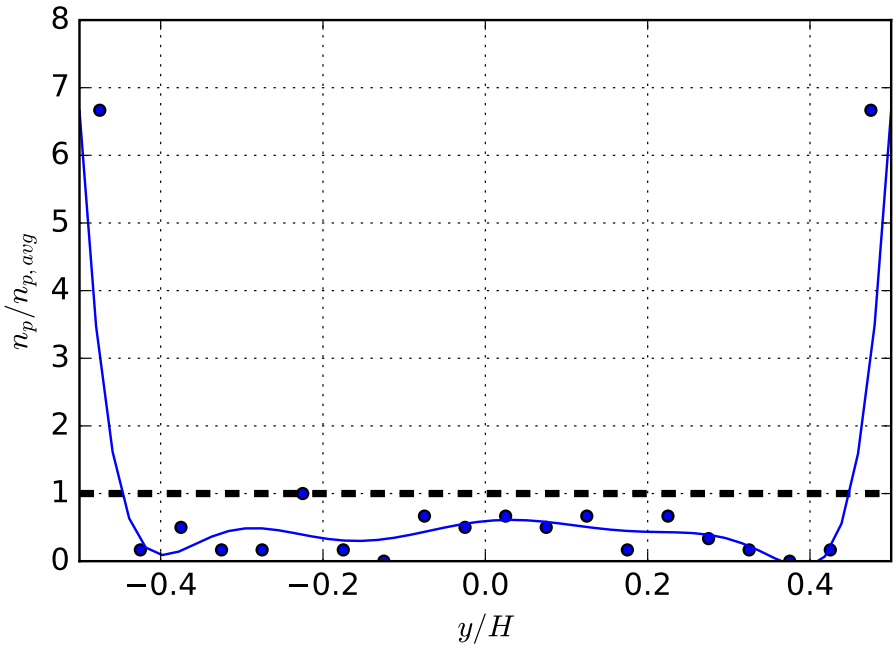

Figure 8.10: Non-dimensional particle concentration along the cross-section of the channel for Case 2. The symbols represent the concentration in each slice and the curve is a fit through these symbols.

what particles in Case 1 experienced because of the higher slip velocity magnitude. Since the particle size is same, the "local" turbophoretic force is same, though higher particle inertia reduces its effect on the particle motion. The increase in "global" turbophoresis and the Saffman lift is higher than the decrease in "local" turbophoresis so that the net effect of these forces result in a higher concentration near the wall than Case 1.

When the St is increased further to 9.3752, we observe that the particle concentration near the wall is about 5 times the bulk average concentration (See Fig. 8.11). As the particle inertia increases, the effect of both "local" and "global" turbophoresis decreases since the larger energy containing eddies have lesser impact on the particle. Thus the likelihood of particles approaching the wall decreases. Once a particle does come close to the wall, the slip velocity is much larger compared to the previous two cases and there is a strong Saffman lift toward the wall.

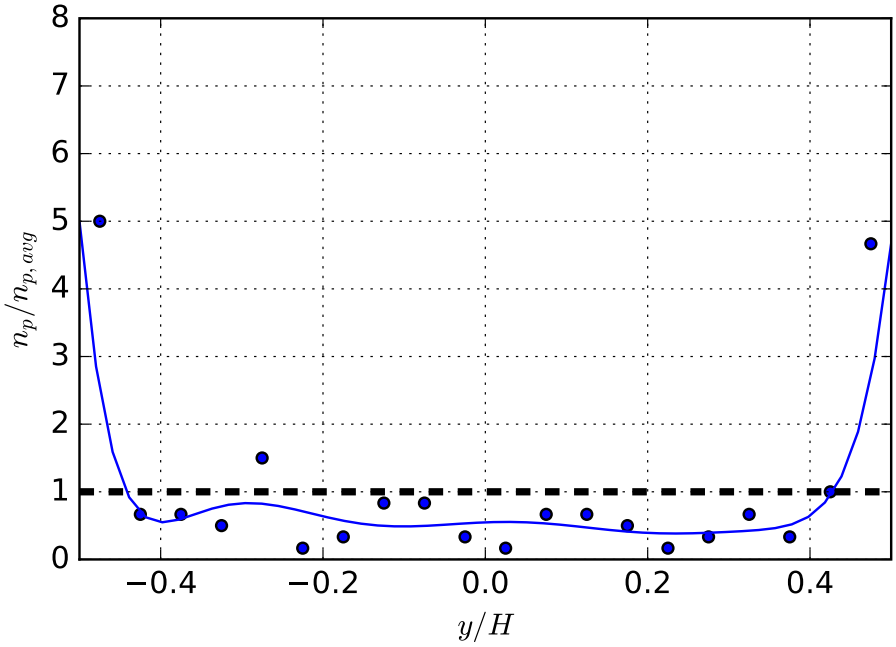

Figure 8.11: Non-dimensional particle concentration along the cross-section of the channel for Case 3. The symbols represent the concentration in each slice and the curve is a fit through these symbols.

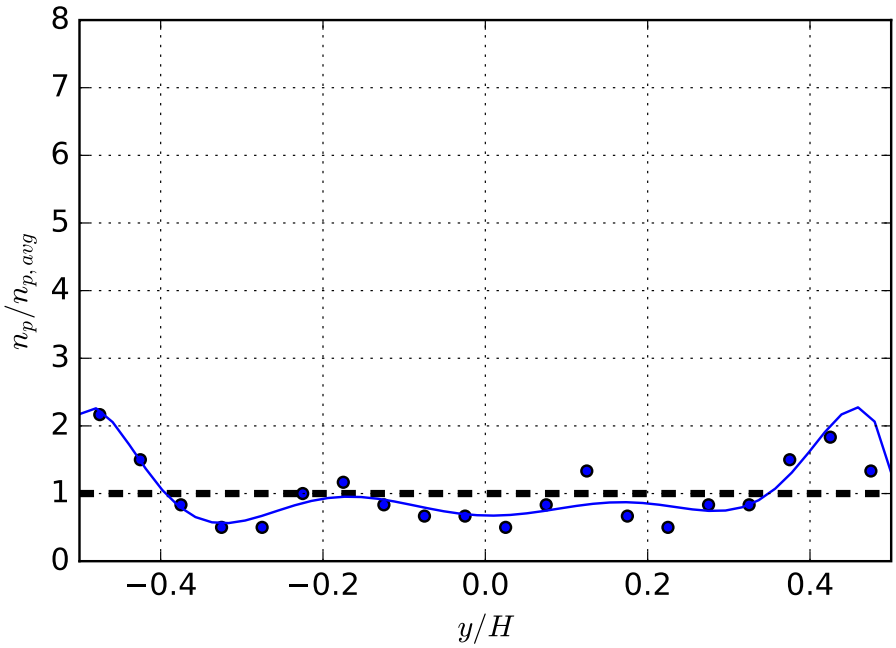

Figure 8.12: Non-dimensional particle concentration along the cross-section of the channel for Case 4. The symbols represent the concentration in each slice and the curve is a fit through these symbols.

For Case 4, when the St is 37.5, the non-dimensional near wall concentration decreases further to about 2. This decrease is again due to the decreasing influence of turbophoresis while the Saffman lift increases only slightly. As the St is increased to 93.75, the concentration profiles become almost uniform. Since the inertia is large, turbophoresis has negligible effect on particle movement. It is interesting to note that for particles with infinitesimally small and infinitely large inertia, turbophoresis has no effect, but becomes relevant only when the particle inertia is finite.

Consider now the effect of particle size on the preferential concentration profiles. Figure 8.14 shows particle concentration profiles for a study where the particle diameter is approximately halved compared to the earlier cases, but the St is 0.432, i.e., comparable to Case 1. Notice that the particle concentration near the wall is about 5 times larger than the bulk average concentration. Since the particle St is the same as Case 1, the global turbophoretic effect would be similar and transports

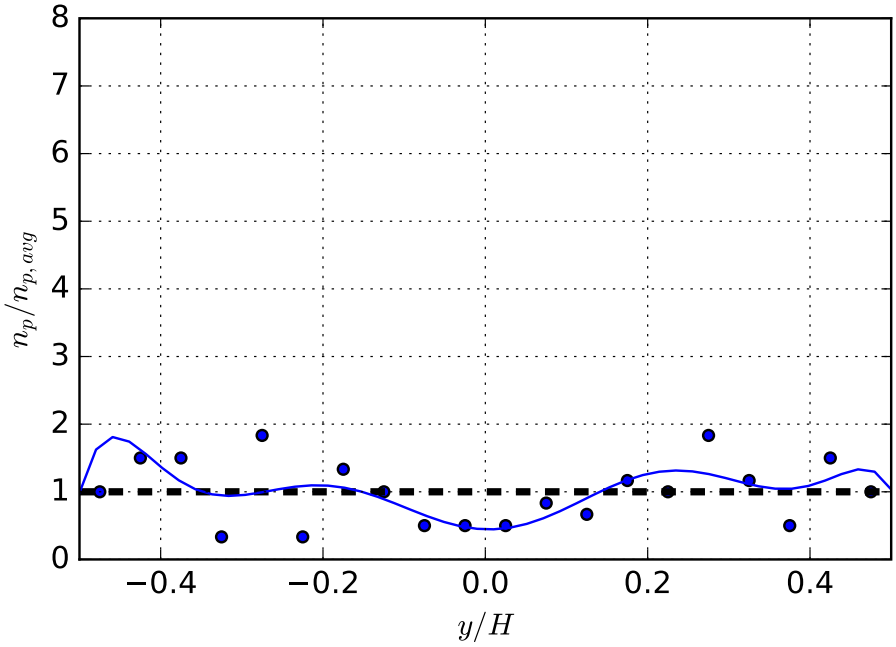

Figure 8.13: Non-dimensional particle concentration along the cross-section of the channel for Case 5. The symbols represent the concentration in each slice and the curve is a fit through these symbols.

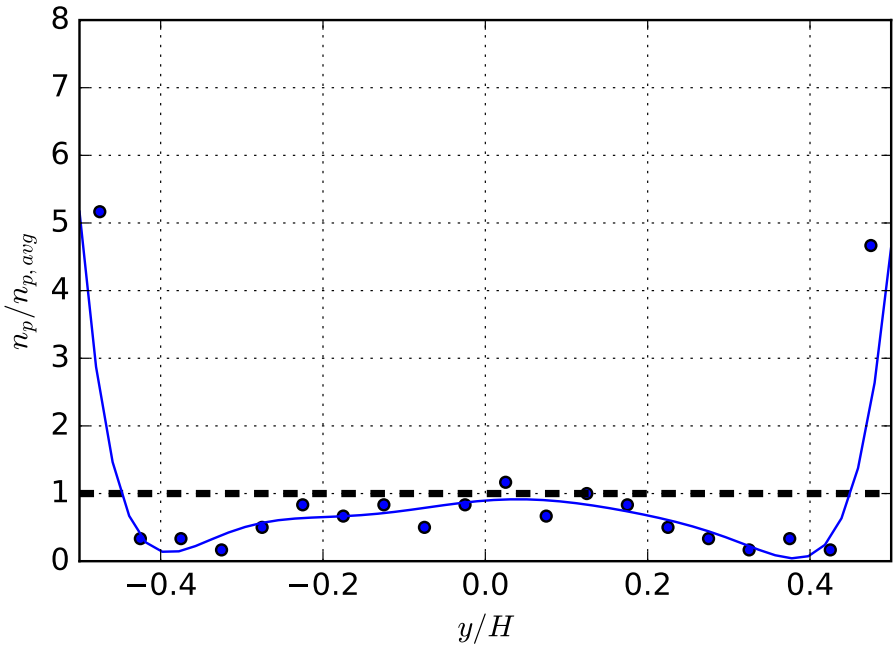

Figure 8.14: Non-dimensional particle concentration along the cross-section of the channel for Case 6. The symbols represent the concentration in each slice and the curve is a fit through these symbols.

the particle toward regions of low TKE. However, since the particle is smaller, the gradient across the particle would be smaller and hence both Saffman lift and "local" turbophoresis are weaker. This can explain the decrease in near wall concentration compared to Case 1. Interestingly, a local maxima in the concentration profile near the center is observed. This is because the center is a region of local TKE minima and hence global turbophoresis would transport particles to the center as well. Since the Saffman lift and local turbophoresis near the wall were much stronger in Case 1, the particles were immediately transported toward the wall and hence a high center-line concentration was not observed.

For Case 7, the St is 10.368, which is comparable to that of Case 3, but the diameter is reduced by a factor of about 2. The particle concentration shows a small peak near the walls where the concentration is roughly 2.5 times the bulk average concentration, but it is nearly uniform in the core of the channel. At this St, the

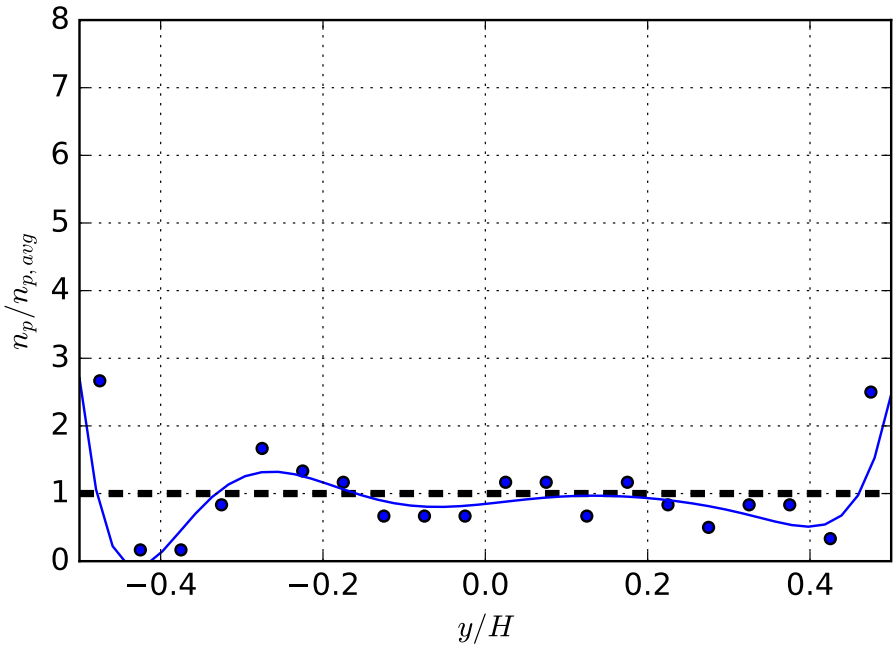

Figure 8.15: Non-dimensional particle concentration along the cross-section of the channel for Case 7. The symbols represent the concentration in each slice and the curve is a fit through these symbols.

Saffman lift and "global" turbophoresis seem to be almost negligible. It is interesting that when $d_p/\eta_k = 11.1$, the concentration becomes uniform at $St = 93.75$ while when $d_p/\eta_k = 5.92$, the concentration becomes uniform at $St = 10.368$. Thus, we see that decreasing the size of the particle decreases the St at which the uniform concentration is achieved. This is possibly because decreasing the particle size reduces the effect of both Saffman lift and "local" turbophoresis both of which cause particles to concentrate preferentially.

8.5 Summary and Conclusions

The lattice-Boltzmann method is employed to carry out direct numerical simulations of particle-laden turbulent flows in a channel. The method adopted resolves the boundary of individual particles by employing a technique developed to represent

curved boundaries. The momentum exchange between the solid and fluid phases is computed through a discrete method that tracks the state of the lattice nodes. Prior studies with particles in a laminar flow have shown that the method is numerically accurate. Stokes number and particle diameter are varied to study the effect of particle inertia and diameter on particle distribution across the channel cross-section. The studies are carried out under the condition where the particle diameter is an order of magnitude larger than the Kolmogorov length scale. In these conditions, the dominant forces that impact particle motion are Saffman lift and turbophoresis. Turbophoresis can act in a local sense whereby the more intense exchange of momentum of eddies on the side of the particle with higher turbulent kinetic energy relative to the opposite side move the particle toward the lower turbulent kinetic region or in a global sense whereby even when the particles do not directly feel the effect of eddies, particles tend to diffuse down gradients. If the particles were larger than the integral length scale, only local turbophoresis effect will be relevant.

It is seen that at lower Stokes number, the particles tend to accumulate near the walls because of Saffman lift and turbophoresis forces. The distribution of particles in the core of the channel is relatively uniform. As Stokes number is increased, the tendency of the particles to concentrate near the wall decreases and distribution of the particles approaches uniform throughout the channel cross-section. As particle size is increased, the Stokes number at which the uniform distribution is reached increases. The likely reason is that the effect of local turbophoresis and Saffman lift increase for larger particles and these forces tend to concentrate particles near the wall. Higher Stokes number, i.e. higher inertia, is needed to resist this tendency.

9. CONCLUSIONS AND FUTURE WORK

9.1 Introduction

Particle-laden flows are of interest in many engineering devices. The ability to simulate such flows accurately can accelerate the development of these devices. The work in this thesis has been motivated by the need to accurately simulate particle-laden flows in confined walls. In particular, the mechanisms that cause preferential particle motion in a channel flow are examined. In the next Section, the work carried out will be summarized and some conclusions drawn. Section 9.3 will discuss proposed future work.

9.2 Summary and Conclusions

The contributions of this work are now now summarized and conclusions are drawn. In Chapter 1, several examples of particle-laden flows are presented, where the understanding of particle-turbulence interactions are critical to the performance of the devices. Understanding of particle-wall and particle-turbulence interactions are important to aid in the development of these engineering devices. Accurate models will significantly accelerate the design and optimization of these devices.

In Chapter 2, the work that has been done to improve understanding of various interactions in particle-laden flows and model such flows are summarized. Relevant non-dimensional parameters that characterize these interactions are examined. Of particular importance are the Stokes number (St), the volume loading ratio (Φ_v) and the mass loading ratio (Φ_m). While the St determines how fast particles respond to the flow, Φ_v and Φ_m determine the coupling between the dispersed and carrier phases. Based on these paramters, three regimes are reported in the literature:

1. One way coupling: The particles are influenced by the turbulence but the turbulence itself is similar to its single phase counterpart. This regime is characterized by low Φ_v and Φ_m.

2. Two way coupling: The particles are affected by the turbulence vice versa. The turbulence can be either augmented or attenuated depending on other parameters such as the St. This is referred to as turbulence modulation. This happens when $\Phi_v << 1$ and $\Phi_m \sim 1$.

3. Four way coupling: In addition to the coupling between turbulence and particles, the particles themselves interact with each other. This regime is characterized by Φ_v and Φ_m of the order unity. In this study, attention will be focused on the first two regimes.

The literature review then presents some analytical studies of particle-laden flows. Despite their limited range of application, they provide useful insight into the behavior of particle-fluid interaction. Then we report experimental works on particle-laden flows. This section shows several interesting features that occur in turbulent particle-laden flows such as dispersion, clustering and deposition among others. This is followed by a review of computational studies that seek to elucidate the physics behind many such phenomena. Then, models that are used to simulate particle-laden flows of practical interest are presented. Several interesting features of the flow that are not clearly understood are summarized in this Chapter and this sets the motivation for our work. These features are:

1. Preferential concentration of particles in a pipe-flow.

2. Turbulence modulation by the particles.

Fundamental insight into these features are provided by employing direct numerical simulations. The lattice-Boltzmann method (LBM) is used to carry out the simulations. The explicit and local nature of the LBM makes it amenable to large scale parallelization.Furthermore, the implementation of a moving particle is easier

in the LBM framework than in a conventional Navier-Stokes solver. In Chapter 3, the LBM is formally introduced and it is shown that in the continuum limit, the Navier-Stokes equations are recovered from the lattice-Boltzmann equations. Various boundary conditions that are relevant to simulations of particle-laden flows are discussed in detail. The particle surface and the boundary layer are resolved in this study. The particles are treated as moving walls in the domain with the momentum augmented half-way bounce back condition with interpolation. For the point-particle simulations, the particle tracking algorithm is parallelized by storing the particles as a doubly linked list in each processor.

In Chapter 4, the LBM code that is developed to perform the particle-resolved simulations is assessed for accuracy by simulating increasing complex problems and comparing the solutions with analytical solutions and prior computational results. These problems start from the decaying Taylor vortex with periodic boundary conditions to a turbulent flow case. Across the range of configurations simulated, it is shown that the LBM code is able to reproduce existing results. A turbulent channel flow is simulated and the mean flow and the turbulent intensities are compared with results of Lee and Moser [133]. The results agree well with differences less than 5%.

Having developed the LBM code and assessed its accuracy, it is employed to carry out direct numerical simulations of particle-laden flows. Particle motion in a channel flow where the particles are smaller than the Kolmogorov length scale is examined. Under this condition, the point-particle approach can be used. Two-way coupling is implemented through the drag coefficient and an external force term in the discretized Boltzmann equation. Results are presented in Chapter 5. *The simulations show that the Stokes number, St, mass loading of particles, i.e. ratio of mass of dispersed to carried phase, m_p/m_f, and particle diameter, d_p, are important parameters that determine the distribution of the particles and the impact of the particles on the fluid velocity flow field. At relatively low mass loading, typically less than 0.1, the impact on the mean velocity flow field and the turbulent kinetic energy is not significant. But,*

under these conditions, the preferential motion of particles in the lateral direction is impacted by the fluid motion. The impact depends on the St.

When the St is infinitesimally small, the particles are uniformly distributed across the cross-section of the channel. As St is increased, the particle concentration near the wall increases. At even higher St, the particle concentration near the wall decreases, but it increases at the center of the channel. This preferential motion, and resulting concentration, is attributed to turbophoresis as that is the only mechanism that can result in preferential lateral movement of particles within the framework of these simulations where point particles are considered. Turbophoresis results in preferential motion when the tendency for turbulent eddies to move particles is opposed by their inertia. In fact, larger diameter particles with the same St as smaller diameter particles, are less impacted by turbophoresis because the larger particle would have a smaller drag per unit mass. As particle mass loading increases, the fluid flow field is increasingly affected, with the mean velocity decreasing relative to the single phase flow mean velocity. The turbulent kinetic energy also decreases as a result of the decrease in the mean velocity. In summary, preferential movement and distribution of particles is affected by St and particle diameter whereas the impact on the mean velocity is primarily affected by the mass loading.

Next particle-resolved simulations are carried out. As a first step, simulations are carried out for laminar flow in a channel. The results of these computations are presented in Chapter 6. The influence of St on the behavior of particle motion is examined. The particle migration is explained in terms of the forces acting on the particle in the lateral direction. Saffman lift, Magnus lift and wall repulsion were found to affect the particle migration trajectories. The Saffman lift and Magnus lift act toward the wall while wall repulsion is directed away from the wall. At low St, the particles come to an equilibrium position that is between the wall and the centerline where the forces balance. At high St, the particles oscillate about the centerline due to its inertia.

Particle-resolved simulations of moving particles in turbulent flows are challenging. So, the effect of stationary particles on the turbulent flow field is presented in Chapter 7. Direct numerical simulations (DNS) of turbulent flow past stationary particles in a channel are carried out. The simulations provide information about particle-flow interactions when the particle is near the wall and at the center. Multiple particles fixed in a cross-sectional plane are also considered. The position of the particles in the channel, the particle size, the Reynolds number and the number of particles are varied. The details of the flow field are analyzed to provide insight into the factors that control the distance of influence of the fixed particles on the flow field. With a single particle, the effect of the particle is felt for about 20 diameters downstream. With multiple particles, the interaction of vortices shed by the particles increases this distance to about 40 diameters. These results suggest that if the particles are separated by an average distance greater than 40 diameters, then the effect of particle-fluid-particle interactions can be ignored.

Particle-resolved simulations are then carried out for particle-laden turbulent flow, the results of which are described in Chapter 8. One of the challenges in these simulations was that the Mach number was required to be less than 0.1 for stability considerations which required a large number of grid points. In a turbulent flow, the turbophoretic force plays an important role in lateral particle motion in addition to the other forces described. Turbophoresis forces the particle in the direction of decreasing turbulent kinetic energy. Turbophoresis can act in a local sense whereby the more intense exchange of momentum of eddies on the side of the particle with higher turbulent kinetic energy relative to the opposite side move the particle toward the lower turbulent kinetic region or in a global sense whereby even when the particles do not directly feel the effect of eddies, particles tend to diffuse down gradients. If the particles were larger than the integral length scale, only local turbophoresis effect will be relevant. It is seen that at lower St, the particles tend to accumulate near the walls because of Saffman lift and turbophoresis forces. The distribution of particles in the core of the channel is relatively uniform. As St is increased, the tendency of

the particles to concentrate near the wall decreases and distribution of the particles approaches uniform throughout the channel cross-section. The effect of particle size on its lateral motion is also studied. As particle size is increased, the St at which the uniform distribution is reached increases. The likely reason is that the effect of local turbophoresis and Saffman lift increase for larger particles and these forces tend to concentrate particles near the wall. Higher Stokes number, i.e. higher inertia, is needed to resist this tendency.

9.3 Future Work

In this work, particle-laden flows were simulated using the lattice-Boltzmann method (LBM) in channel flows to study preferential particle motion. The work involved both particle-resolved and point-particle direct numerical simulations (DNS).

While most of the direct numerical simulations reported in this work are at a Reynolds number of about 6500, the Reynolds number in devices of engineering interest are much higher. Direct numerical simulations with higher Reynolds number can be performed to assess particle motion under these conditions. One interesting aspect is that at higher Reynolds number, the location of peak turbulent kinetic energy shifts closer to the wall [133]. DNS studies can be carried out to see how this affects turbophoretic effects and the particle concentration profiles. At higher Reynolds number, DNS computations have certain challenges that need to be addressed:

- In the LBM framework, higher Reynolds number simulations require lower viscosities and hence lower values of the relaxation parameter, τ. It is known that as τ approaches 0.5, the lattice-Boltzmann method becomes unstable. The multiple relaxation time (MRT) collision operator has been employed in this work to overcome this. However, lower values of τ require formulation of more sophisticated collision operators.

- For particle-resolved DNS studies, it was found in this work that the Mach number, Ma, be less than 0.1 for stability considerations. The likely reason for

this instability is the particle motion in the domain which requires filling new fluid nodes that appear and removal of old fluid nodes that have been occupied by the particle when the particle moves. Improved particle motion techniques are required to ease this Ma constraint.

- In addition to stability, DNS studies require resolution of the Kolmogorov length scale, which can be computationally extremely expensive. The computational time scales with Reynolds number as Re^3. While the number of processors available in modern supercomputers is on the rise, code optimization is essential to make sure that the computational time scales with the number of processors. Minimizing communication time between processors and ensuring a balanced load among all processors is critical to achieve reasonable run times. Load-balancing issues pose a major challenge, especially with particle-laden flows. While the fluid domain can be easily distributed evenly among processors, particles may not be evenly distributed in the fluid domain, giving rise to load-balancing issues that need to be dealt with. One possible approach might be to consider dynamic load balancing with a partitioned global address space (PGAS) programming model.

Another aspect of the lattice-Boltzmann method that makes it challenging for higher Re DNS computations is the coupling of lattice spacing and time step, which prevents the use of stretched grids commonly employed in Navier-Stokes solvers. While interpolation-supplemented LBM has shown to help with decoupling the lattice spacing and time step, it is known to affect the accuracy of computations [166]. One way to overcome this restriction is to use multi-block grids in regions where finer grids are required. This is especially important for confined flows where fine grids are required near the wall to resolve the boundary layer. Some initial studies using local grid refinement is presented in Appendix C and it is shown to save computational time significantly. This work could be extended to include adaptive mesh refinement (AMR) which would bring additional savings in computational time, especially for

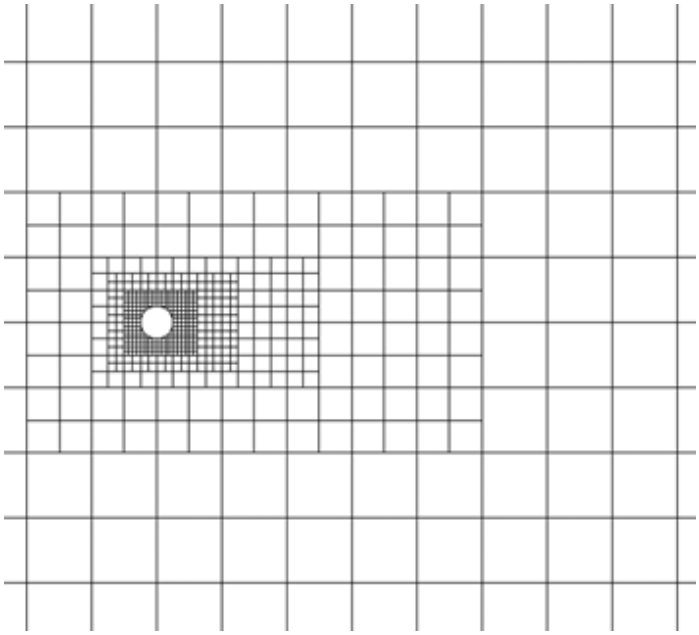

Figure 9.1: Adaptive mesh refinement around a particle. Figure adapted from [167].

particle-resolved simulations where the particle size is of the order of Kolmogorov length scale.

Figure 9.1 shows adaptive mesh refinement around a particle [167]. Typically these are developed using tree data structures instead of arrays. In a tree, each node has some data (in this case, it would be the distribution functions and hydrodynamic variables) and pointers to its child nodes, as well as information about its neighbors. For example, in a typical 3 dimension simulation, each node would have eight children (oct-tree) for each refinement level. Employing a tree data structure offers flexibility when it comes to collapsing a set of fine grids into a coarse grid or splitting a coarse grid into finer ones. However, neighboring data is no longer stored contiguously and hence cache hit ratio might decrease potentially increasing computational time. This is a challenge that should be addressed.

The computations carried out in this work are for mono-disperse spherical particles. This could be extended to include polydisperse particles. Moreover, objects with non-spherical shapes can also be considered. Implementation of AMR as discussed

earlier might make this easier and computationally feasible. Such particle shapes are of special interest in pharmaceutical applications where cylindrical particles are common. These introduce additional parameters to consider such as aspect ratio, and size distribution of particles. It would be interesting to see the effect of these parameters on particle concentration profiles. The major challenge in this study would be the implementation of efficient algorithms for contact and collision detection. Accounting for rotation of non-spherical particles is another area where additional effort would be required. Motion of deformable particles can also be considered. Potential applications for these include study of deposition of blood cells on arteries and bacterial migration in the atmosphere. In this case, the challenge would be a technique to store the boundary information of each particle.

The information gained from the direct numerical simulation (DNS) studies presented in this thesis can be used to develop models for particle-laden flows. Large eddy simulations (LES) is an area where efforts can be focused. In LES, most of the energy containing eddies are resolved while smaller eddies are modeled. Appendix D presents some initial results of particle-laden flows in a turbulent channel using large eddy simulations (LES). These results showed that a model to account for the effect of sub-grid scale eddies on the particle motion is required to accurately predict particle concentration profiles. Other aspects to consider include modeling of sub-grid stress, accounting for turbulence modulation by the particles, and implementation of Saffman lift.

Similar model development work can also be carried out for Reynolds averaged Navier-Stokes (RANS) techniques. With RANS, a greater modeling effort is required. Since only the mean flow velocity is being solved, models are required to account for dispersion of particles by turbulent eddies. It is shown in Chapter 5 that even with point-particles, turbulence can cause preferential motion of particles through turbophoresis. Moreover, when the particles are larger, there is an additional Saffman lift force and "local" turbophoresis effect as discussed in Chapter 8. These effects can

be modeled within a RANS framework to get accurate particle concentration profiles. The effect of particles on the turbulence can also be modeled in RANS framework.

With both the RANS and the LES framework, modeling of turbulence modulation is required to get accurate results. Point-particle simulations in Chapter 5 showed that the effect of particles on the flow field becomes important as the mass-loading of the particles increases. Additionally, it was shown in Chapter 7 that when inter-particle distances are less than 40 diameters, particle-fluid-particle interactions become important indicating that the effect of particles on the fluid cannot be neglected. In such cases, depending on the particle size, particles can either augment or attenuate turbulent kinetic energy. These effects can be modeled in a Reynolds averaged Navier-Stokes (RANS) or large eddy simulation (LES) framework.

In many engineering applications, particles in a pipe flow are often injected as a jet. Initial computations of particle-laden jets using RANS and a discussion of various models currently employed and its effect on the predictions of jet spreading are presented in the Appendix E. Some areas requiring work are turbulence modulation modeling and particle dispersion modeling.

REFERENCES

REFERENCES

[1] S. Balachandar and John K. Eaton. Turbulent Dispersed Multiphase Flow. *Annual Review of Fluid Mechanics*, 42(1):111–133, 2010.

[2] A. Z'Graggen, P. Haueter, G. Maag, A. Vidal, M. Romero, and A. Steinfeld. Hydrogen production by steam-gasification of petroleum coke using concentrated solar power-III. Reactor experimentation with slurry feeding. *International Journal of Hydrogen Energy*, 32(8):992–996, 2007.

[3] A. M. Wood, W. Hwang, and J. K. Eaton. Preferential concentration of particles in homogeneous and isotropic turbulence. *International Journal of Multiphase Flow*, 31(10-11):1220–1230, 2005.

[4] M. R. Maxey. The gravitational settling of aerosol particles in homogeneous turbulence and random flow fields. *Journal of Fluid Mechanics*, 174:441–465, 1987.

[5] Kyle D. Squires and John K. Eaton. Preferential concentration of particles by turbulence. *Physics of Fluids*, pages 1169–1178, 1991.

[6] S. Elghobashi and G. C. Truesdell. Direct simulation of particle dispersion in a decaying isotropic turbulence. *Journal of Fluid Mechanics*, 242:655–700, 1992.

[7] M I Yudine. Physical considerations on heavy-particle diffusion. *Adv. Geophys*, 6(185):41–71, 1959.

[8] G. T. Csanady. Turbulent diffusion of heavy particles in the atmosphere. *Journal of the Atmospheric Sciences*, 20(3):201–208, 1963.

[9] M R Wells and D E Stock. The effects of crossing trajectories on the dispersion of particles in a turbulent flow. *Journal of fluid mechanics*, 136:31–62, 1983.

[10] J K Eaton and J R Fessler. Preferential Concentration of Particles by Turbulence. *International Journal of Multiphase Flow*, 20(94):169–209, 1994.

[11] Timothy C.W. Lau and Graham J. Nathan. Influence of Stokes number on the velocity and concentration distributions in particle-laden jets. *Journal of Fluid Mechanics*, 757:432–457, 2014.

[12] S. Elghobashi. On predicting particle-laden turbulent flows. *Applied Scientific Research*, 52:309–329, 1994.

[13] G. G. Stokes. For creeping flow around an object of arbitray shape. *Trans. Cambridge Philos. Soc*, 9(8), 1851.

[14] A. B. Basset. A treatise on hydrodynamics vol I. Deighton, Bell and Co, London George Bell and sons, 1888.

[15] J. Boussinesq. Sur la résistance qu'oppose un liquide indéfini en repos. *CR Acad. Sci. Paris*, 100:935–937, 1885.

[16] C. W. Oseen. Hydrodynamic, 1927.

[17] M. Parmar, a. Haselbacher, and S. Balachandar. Generalized Basset-Boussinesq-Oseen Equation for Unsteady Forces on a Sphere in a Compressible Flow. *Physical Review Letters*, 106(8):084501, 2011.

[18] F. P. Bretherton. The motion of rigid particles in a shear flow at low Reynolds number. *Journal of Fluid Mechanics*, pages 284–304, 1962.

[19] P. G. Saffman. The lift on a small sphere in a slow shear flow. *Journal of Fluid Mechanics*, 22:385–400, mar 1965.

[20] J. B. McLaughlin. The lift on a small sphere in wall-bounded linear shear flows. *Journal of Fluid Mechanics*, 246:249–265, apr 1993.

[21] G. Segre and A. Silberberg. Radial Particle Displacements in Poiseuille Flow of Suspensions. *Nature*, 189(209-210), 1961.

[22] G. Segre and Silberberg A. Behaviour of macroscopic rigid spheres in Poiseuille flow Part 1. Determination of local concentration by statistical analysis of particle passages through crossed light beams. *Journal of Fluid Mechanics*, pages 115–135, 1962.

[23] G. Segre and A Silberberg. Behaviour of macroscopic rigid spheres in Poiseuille flow Part 2. Experimental results and interpretation. *Journal of Fluid Mechanics*, pages 136–157, 1962.

[24] D. R. Oliver. Influence of Particle Rotation on Radial Migration in the Poiseuille Flow of Suspension. *Nature*, 194:1269–1271, 1962.

[25] R. C. Jeffrey and J. R. Pearson. Particle motion in laminar vertical tube flow. *Journal of Fluid Mechanics*, 22(04):721, 1965.

[26] Y. Tsuji, Y. Morikawa, T. Tanaka, K. Karimine, and S. Nishida. Measurement of an axisymmetric jet laden with coarse particles. *International Journal of Multiphase Flow*, 14(5):565–574, 1988.

[27] C B Rogers and J K Eaton. The Effect of Small Particles on Fluid Turbulence in a Flat-plate, Turbulent Boundary Layer in Air. *Physics of Fluids A: Fluid Dynamics*, 3(5):928–937, 1991.

[28] J. D. Kulick, J. R. Fessler, and J. K. Eaton. Particle response and turbulence modification in fully developed channel flow. *Journal of Fluid Mechanics*, 277:109–134, 1994.

[29] Yohei Sato, Koichi Hishida, and Masanobu Maeda. Effect of Dispersed Phase on Modification of Turbulent Flow in a Wall Jet. *Journal of Fluids Engineering*, 118(2):307, 1996.

[30] M. Muste, V. C. Patel, and R. N. Parthasarathy. Discriminator laser Doppler velocimetry for measurement of liquid and particle velocities in sediment-laden flows. *Experiments in Fluids*, 22(1):45–56, 1996.

[31] Tomohiko Tanaka and John K. Eaton. Sub-Kolmogorov resolution partical image velocimetry measurements of particle-laden forced turbulence. *Journal of Fluid Mechanics*, 643:177, 2010.

[32] A Karnis, H L Goldsmith, and S G Mason. Axial Migration of Particles in Poiseuille Flow. *Nature*, 200(4902):159–160, oct 1963.

[33] R. V. Repetti and E. F. Leonard. Segre-Silberberg Annulus Formation : A Possible Explanation. *Nature*, 203(4952):1346–1348, sep 1964.

[34] Yuji Suzuki, Motofumi Ikenoya, and Nobuhide Kasagi. Simultaneous measurement of fluid and dispersed phases in a particle-laden turbulent channel flow with the aid of 3-D PTV. *Experiments in fluids*, 29(1):S185–S193, 2000.

[35] K. D. Squires and J. K. Eaton. Particle response and turbulence modification in isotropic turbulence. *Physics of Fluids*, pages 1191–1203, 1990.

[36] A. Ferrante and S. Elghobashi. On the physical mechanisms of two-way coupling in particle-laden isotropic turbulence. *Physics of Fluids*, 15(2):315–329, 2003.

[37] J Feng, H H Hu, and D D Joseph. Direct simulation of initial value problems for the motion of solid bodies in a Newtonian fluid Part 1. Sedimentation. *Journal of Fluid Mechanics*, 261:95–134, 1994.

[38] J. Feng, H. H. Hu, and D. D. Joseph. Direct simulation of initial value problems for the motion of solid bodies in a Newtonian fluid. Part 2. Couette and Poiseuille flows. *Journal of Fluid Mechanics*, 277:271–301, apr 1994.

[39] Saeed Mortazavi and Grétar Tryggvason. A numerical study of the motion of drops in Poiseuille flow. Part 1. Lateral migration of one drop. *Journal of Fluid Mechanics*, 411:325–350, 2000.

[40] Lanying Zeng, S. Balachandar, and Paul Fischer. Wall-induced forces on a rigid sphere at finite Reynolds number. *Journal of Fluid Mechanics*, 536:1–25, jul 2005.

[41] Amireh Nourbakhsh, Saeed Mortazavi, and Yaser Afshar. Three-dimensional numerical simulation of drops suspended in Poiseuille flow at non-zero Reynolds numbers. *Physics of Fluids*, 23(12):123303, 2011.

[42] Tristan M. Burton and John K. Eaton. Fully resolved simulations of particle-turbulence interaction. *Journal of Fluid Mechanics*, 545:67–111, 2005.

[43] P. Bagchi and S. Balachandar. Effect of turbulence on the drag and lift of a particle. *Physics of Fluids*, 15(11):3496, 2003.

[44] Prosenjit Bagchi and S. Balachandar. Response of the wake of an isolated particle to an isotropic turbulent flow. *Journal of Fluid Mechanics*, 518:95–123, 2004.

[45] Sudheer Tenneti and Shankar Subramaniam. Particle-Resolved Direct Numerical Simulation for Gas-Solid Flow Model Development. *Annual Review of Fluid Mechanics*, 46(1):199–230, 2014.

[46] Amrita R. Wadhwa, John Abraham, and Vinicio Magi. Hybrid Compressible-Incompressible Numerical Method for Transient Drop-Gas Flows. *AIAA Journal*, 43(9):1974–1983, 2005.

[47] Amrita R. Wadhwa, Vinicio Magi, and John Abraham. Transient deformation and drag of decelerating drops in axisymmetric flows. *Physics of Fluids*, 19(11):113301, 2007.

[48] Kunihiko Taira and Tim Colonius. The immersed boundary method: A projection approach. *Journal of Computational Physics*, 225(2):2118–2137, 2007.

[49] Sourabh V. Apte, Mathieu Martin, and Neelesh a. Patankar. A numerical method for fully resolved simulation (FRS) of rigid particle-flow interactions in complex flows. *Journal of Computational Physics*, 228(8):2712–2738, 2009.

[50] Francesco Lucci, Antonino Ferrante, and Said Elghobashi. Modulation of isotropic turbulence by particles of Taylor length-scale size. *Journal of Fluid Mechanics*, 650:5, 2010.

[51] A J C Ladd. Numerical simulations of particulate suspensions via a discretized Boltzmann equation. Part 2. Numerical results. *Journal of Fluid Mechanics*, 271:311–339, 1994.

[52] A. J. C. Ladd. Numerical simulations of particulate suspensions via a discretized Boltzmann equation. Part 2. Numerical results. *Journal of Fluid Mechanics*, 271:311–339, 1994.

[53] Cyrus K. Aidun, Yannan Lu, and E.-Jiang Ding. Direct analysis of particulate suspensions with inertia using the discrete Boltzmann equation. *Journal of Fluid Mechanics*, 373:287–311, 1998.

[54] Dewei Qi. Lattice-Boltzmann simulations of particles in non-zero-Reynolds-number flows. *Journal of Fluid Mechanics*, 385:41–62, 1999.

[55] Hui Gao, Hui Li, and Lian-Ping Wang. Lattice Boltzmann simulation of turbulent flow laden with finite-size particles. *Computers & Mathematics with Applications*, 65:194–210, 2013.

[56] Lian Ping Wang, Orlando Ayala, Hui Gao, Charles Andersen, and Kevin L. Mathews. Study of forced turbulence and its modulation by finite-size solid particles using the lattice Boltzmann approach. *Computers and Mathematics with Applications*, 67(2):363–380, 2014.

[57] Howard H. Hu, N.A. Patankar, and M.Y. Zhu. Direct Numerical Simulations of FluidSolid Systems Using the Arbitrary LagrangianEulerian Technique. *Journal of Computational Physics*, 169(2):427–462, 2001.

[58] A J C Ladd and R Verberg. Lattice-Boltzmann Simulations of Particle-Fluid Suspensions. *Journal of Statistical Physics*, 104(September):1191–1251, 2001.

[59] C. T. Crowe. ReviewNumerical Models for Dilute Gas-Particle Flows. *Journal of Fluids Engineering*, 104(3):297, 1982.

[60] E. Loth. Numerical approaches for motion of dispersed particles, droplets and bubbles. *Progress in Energy and Combustion Science*, 26(3):161–223, 2000.

[61] S. Balachandar and a. Prosperetti. Report on a symposium on "computational approaches to disperse multiphase flow". *International Journal of Multiphase Flow*, 31(12):1337–1341, 2005.

[62] Andrea Prosperetti and Grétar Tryggvason. *Computational methods for multiphase flow*. Cambridge university press, 2007.

[63] D Brian Spalding. A general purpose computer program for multi-dimensional one-and two-phase flow. *Mathematics and computers in simulation*, 23(3):267–276, 1981.

[64] C T Crowe, T R Troutt, and J N Chung. Numerical models for two-phase turbulent flows. *Annual Review of Fluid Mechanics*, 28(1):11–43, 1996.

[65] S. E. Elghobashi and T. W. Abou-Arab. A two-equation turbulence model for two-phase flows. *Physics of Fluids*, 26(4):931, 1983.

[66] M A Rizk and S E Elghobashi. A two-equation turbulence model for dispersed dilute confined two-phase flows. *International Journal of Multiphase Flow*, 15(1):119–133, 1989.

[67] Alain Picart, Alain Berlemont, and Gérard Gouesbet. Modelling and predicting turbulence fields and the dispersion of discrete particles transported by turbulent flows. *International journal of multiphase flow*, 12(2):237–261, 1986.

[68] Myung Kyoon Chung, Hyung Jin Sung, and Kye Bock Lee. Computational study of turbulent gas-particle flow in a venturi. *Journal of fluids engineering*, 108(2):248–253, 1986.

[69] Jianmin Ding, Robert W Lyczkowski, T Sha William, Stephen A Altobelli, and Eiichi Fukushima. Numerical analysis of liquidsolids suspension velocities and concentrations obtained by NMR imaging. *Powder technology*, 77(3):301–312, 1993.

[70] Clayton T. Crowe, M. P. Sharma, and David E. Stock. The particle-source-in cell (PSI-CELL) model for gas-droplet flows. *Journal of Fluids Engineering*, 99(2):325–332, 1977.

[71] Martin R Maxey and James J Riley. Equation of motion for a small rigid sphere in a nonuniform flow. *Physics of Fluids (1958-1988)*, 26(4):883–889, 1983.

[72] Roland Clift, John R Grace, and Martin E Weber. *Bubbles, drops, and particles*. Courier Corporation, 2005.

[73] Shinichi Yuu, Naoto Yasukouchi, Yasuo Hirosawa, and Tomosada Jotaki. Particle turbulent diffusion in a dust laden round jet. *AIChE Journal*, 24(3):509–519, 1978.

[74] John K Dukowicz. A particle-fluid numerical model for liquid sprays. *Journal of Computational Physics*, 35:229–253, 1980.

[75] A. D. Gosman and E. Ioannides. Aspects of computer simulation of liquid-fueled combustors. *Journal of Energy*, 7(6):482–490, 1983.

[76] Amsden A. A., P. J. O'Rourke, and T. D. Butler. KIVA-II: A Computer Program for Chemically Reactive Flows with Sprays. Technical report, Los Alamos National Laboratory, Los Alamos, New Mexico., 1989.

[77] Qunzhen Wang and Kyle D. Squires. Large eddy simulation of incompressible turbulent channel flow. *Physics of Fluids*, (May):1207–1223, 1996.

[78] Y Yamamoto, M Potthoff, T Tanaka, T Kajishima, and Y Tsuji. Large-eddy simulation of turbulent gas-particle flow in a vertical channel: effect of considering inter-particle collisions. *Journal of Fluid Mechanics*, 442:303–334, 2001.

[79] S.V. Apte, K. Mahesh, P. Moin, and J.C. Oefelein. Large-eddy simulation of swirling particle-laden flows in a coaxial-jet combustor. *International Journal of Multiphase Flow*, 29(8):1311–1331, 2003.

[80] M Sommerfeld and H-H Qiu. Detailed measurements in a swirling particulate two-phase flow by a phase-Doppler anemometer. *International Journal of Heat and Fluid Flow*, 12(1):20–28, 1991.

[81] M. Sommerfeld, A. Ando, and D. Wennerberg. Swirling, particle-laden flows through a pipe expansion. *Journal of fluids engineering*, 114(4):648–656, 1992.

[82] P. Moin and S. Apte. Large-eddy simulation of realistic gas turbine combustors. *AIAA Journal*, 44(4):698–708, 2006.

[83] J. G. M. Kuerten and A. W. Vreman. Can turbophoresis be predicted by large-eddy simulation? *Physics of Fluids*, 17(1):011701, 2005.

[84] Babak Shotorban and Farzad Mashayek. A stochastic model for particle motion in large-eddy simulation. *Journal of Turbulence*, 7(October):N18, 2006.

[85] M. Bini and W. P. Jones. Large-eddy simulation of particle-laden turbulent flows. *Journal of Fluid Mechanics*, 614:207, 2008.

[86] B. J. Lazaro and J. C. Lasheras. Particle dispersion in a turbulent, plane, free shear layer. *Physics of Fluids A: Fluid Dynamics (1989-)*, 1(6):1035–1044, 1989.

[87] B J Lazaro and J C Lasheras. Particle dispersion in the developing free shear layer. Part 1. Unforced flow. *Journal of Fluid Mechanics*, 235:143–178, 1992.

[88] B J Lazaro and J C Lasheras. Particle dispersion in the developing free shear layer. Part 2. Forced flow. *Journal of Fluid Mechanics*, 235:179–221, 1992.

[89] M.J. Cernick, S.W. Tullis, and M.F. Lightstone. Particle subgrid scale modelling in large-eddy simulations of particle-laden turbulence. *Journal of Turbulence*, 16(2):101–135, 2014.

[90] K. Fukagata, S. Zahrai, and F.H. Bark. Dynamics of Brownian particles in a turbulent channel flow. *Heat and Mass Transfer*, 40(9):715–726, 2004.

[91] a. S. Berrouk, D. Laurence, J. J. Riley, and D. E. Stock. Stochastic modelling of inertial particle dispersion by subgrid motion for LES of high Reynolds number pipe flow. *Journal of Turbulence*, 8(October):N50, 2007.

[92] Rodney O. Fox. Large-Eddy-Simulation Tools for Multiphase Flows. *Annual Review of Fluid Mechanics*, 44(1):47–76, 2012.

[93] Leo P Kadanoff. On two levels. *Physics today*, 39:7, 1986.

[94] Uriel Frisch, Brosl Hasslacher, and Yves Pomeau. Lattice-Gas Automata for the Navier-Stokes Equation. *Physical Review Letters*, 56:1505–1508, 1986.

[95] Stephen Wolfram. Cellular Automaton Fluids 1: Basic Theory. *Journal of Statistical Physics*, 45:471–526, 1986.

[96] Guy R. McNamara and Gianluigi Zanetti. Use of the Boltzmann equation to simulate lattice gas automata. *Physical review letters*, 61(20):2332–2335, 1988.

[97] F. J Higuera and J Jiménez. Boltzmann Approach to Lattice Gas Simulations. *Europhysics Letters (EPL)*, 9(7):663–668, 1989.

[98] F. J Higuera, S Succi, and R Benzi. Lattice Gas Dynamics with Enhanced Collisions. *Europhysics Letters (EPL)*, 9(4):345–349, 1989.

[99] P. L. Bhatnagar, E. P. Gross, and M. Krook. A Model for Collision Processes in Gases. I. Small Amplitude Processes in Charged and Neutral One-Component Systems. *Physical Review*, 94(3):511–525, 1954.

[100] Shiyi Chen, Hudong Chen, Daniel Martinez, and William Matthaeus. Lattice Boltzmann Model for Simulation of Magnetohydrodynamics. *Physical Review Letters*, 67(27):3776–3780, 1991.

[101] Y H Qian, D D'Humières, and P Lallemand. Lattice BGK Models for Navier-Stokes Equation. *EPL (Europhysics Letters)*, 17:479–484, 1992.

[102] Xiaoyi He and Li-Shi Luo. Theory of the lattice Boltzmann method: From the Boltzmann equation to the lattice Boltzmann equation. *Physical Review E*, 56(6):6811–6817, 1997.

[103] Xiaoyi He and Li-shi Luo. A priori derivation of the lattice Boltzmann equation. *Physical Review E*, 55(6):6333–6336, 1997.

[104] R. Benzi, S. Succi, and M. Vergassola. The lattice Boltzmann equation: theory and applications. *Physics Reports*, 222(3):145–197, 1992.

[105] Shiyi Chen and Gary D.' Doolen. Lattice Boltzmann Method for Fluid Flows. Annual Review of Fluid Mechanics. *Annual Review of Fluid Mechanics*, pages 329–364, 1998.

[106] Sauro Succi. *The Lattice Boltzmann Equation for Fluid Dynamics and Beyond*. Oxford Science Publications, 2001.

[107] R.R. Nourgaliev, T.N. Dinh, T.G. Theofanous, and D. Joseph. The lattice Boltzmann equation method: theoretical interpretation, numerics and implications. *International Journal of Multiphase Flow*, 29(1):117–169, 2003.

[108] Dazhi Yu, Renwei Mei, Li-Shi Luo, and Wei Shyy. Viscous flow computations with the method of lattice Boltzmann equation. *Progress in Aerospace Sciences*, 39(5):329–367, 2003.

[109] Cyrus K. Aidun and Jonathan R. Clausen. Lattice-Boltzmann Method for Complex Flows. *Annual Review of Fluid Mechanics*, 42(1):439–472, jan 2010.

[110] Philip J Davis and Philip Rabinowitz. *Methods of numerical integration*. Courier Corporation, 2007.

[111] Dieter A Wolf-Gladrow. *Lattice-gas cellular automata and lattice Boltzmann models: An Introduction*. Number 1725. Springer Science & Business Media, 2000.

[112] Uriel Frisch, D D'Humières, Brosl Hasslacher, Pierre Lallemand, Yves Pomeau, and Jean-Pierre Rivet. Lattice Gas Hydrodynamics in Two and Three Dimensions. *Complex Systems*, 1:649–707, 1987.

[113] Uriel Frisch. *Turbulence: the legacy of AN Kolmogorov*. Cambridge university press, 1995.

[114] Shuling Hou, Qisu Zou, Shiyi Chen, Gary D. Doolen, and Allen C. Cogley. Simulation of Cavity Flow by the Lattice Boltzmann Method. *Journal of Computational Physics*, 118:329–347, 1995.

[115] Kannan N. Premnath and John Abraham. Three-dimensional multi-relaxation time (MRT) lattice-Boltzmann models for multiphase flow. *Journal of Computational Physics*, 224:539–559, jun 2007.

[116] Michael McCracken and John Abraham. Multiple-relaxation-time lattice-Boltzmann model for multiphase flow. *Physical Review E*, 71(3):036701, mar 2005.

[117] Paul Lavallée, Jean Pierre Boon, and Alain Noullez. Boundaries in lattice gas flows. *Physica D: Nonlinear Phenomena*, 47(1):233–240, 1991.

[118] Rémi Cornubert, Dominique D'Humières, and David Levermore. A Knudsen layer theory for lattice gases. *Physica D: Nonlinear Phenomena*, 47(1):241–259, 1991.

[119] Donald P Ziegler. Boundary conditions for lattice Boltzmann simulations. *Journal of Statistical Physics*, 71(5-6):1171–1177, 1993.

[120] I Ginzbourg and P M Adler. Boundary flow condition analysis for the three-dimensional lattice Boltzmann model. *Journal de Physique II*, 4(2):191–214, 1994.

[121] Xiaoyi He, Qisu Zou, Li-shi Luo, and Micah Dembo. Analytic Solutions of Simple Flows and Analysis of Nonslip Boundary Conditions for the Lattice Boltzmann BGK Model. *Journal of Statistical Physics*, 87:115–136, 1997.

[122] Shiyi Chen, Daniel Martínez, and Renwei Mei. On boundary conditions in lattice Boltzmann methods. *Physics of Fluids*, 8(9):2527–2536, sep 1996.

[123] M'hamed Bouzidi, Mouaouia Firdaouss, and Pierre Lallemand. Momentum transfer of a Boltzmann-lattice fluid with boundaries. *Physics of Fluids*, 13(11):3452, 2001.

[124] Pierre Lallemand and Li-Shi Luo. Lattice Boltzmann method for moving boundaries. *Journal of Computational Physics*, 184(2):406–421, 2003.

[125] Renwei Mei, Dazhi Yu, Wei Shyy, and Li-Shi Luo. Force evaluation in the lattice Boltzmann method involving curved geometry. *Physical Review E*, 65(4):41203, apr 2002.

[126] Dewei Qi. Lattice-Boltzmann simulations of fluidization of rectangular particles. *International Journal of Multiphase Flow*, 26:421–433, 2000.

[127] Dewei Qi. Simulations of fluidization of cylindrical multiparticles in a three-dimensional space. *International Journal of Multiphase Flow*, 27:107–118, 2001.

[128] Dewei Qi, Lishi Luo, Raja Aravamuthan, and William Strieder. Lateral migration and orientation of elliptical particles in Poiseuille flows. *Journal of Statistical Physics*, 107(1-2):101–120, 2002.

[129] Lian-Ping Wang, Cheng Peng, Zhaoli Guo, and Zhaosheng Yu. Lattice Boltzmann Simulation of Particle-Laden Turbulent Channel Flow. *Computers & Fluids*, 000:1–11, 2015.

[130] Jonathan R. Clausen, Daniel A. Reasor, and Cyrus K. Aidun. Parallel performance of a lattice-Boltzmann/finite element cellular blood flow solver on the IBM Blue Gene/P architecture. *Computer Physics Communications*, 181(6):1013–1020, 2010.

[131] Kannan Nandha Premnath. Lattice Boltzmann models for simulations of drop-drop collisions. 2004.

[132] Michael E. McCracken. Development and evaluation of lattice Boltzmann models for investigations of liquid break-up. 2004.

[133] Myoungkyu Lee and Robert D. Moser. Direct numerical simulation of turbulent channel flow up to Reτ=590. *Journal of Fluid Mechanics*, 774:395–415, 2015.

[134] G. I. Taylor. LXXV. On the decay of vortices in a viscous fluid. *The London, Edinburgh, and Dublin Philosophical Magazine and Journal of Science*, 46(274):671–674, 1923.

[135] U Ghia, K.N Ghia, and C.T Shin. High-Re solutions for incompressible flow using the Navier-Stokes equations and a multigrid method. *Journal of Computational Physics*, 48:387–411, 1982.

[136] A. Miyamura, S. Iwasaki, and T. Ishi. Experimental Wall Correction Factors of Single Solid Spheres in Triangular and Square Cylinders , and Parallel Plates. *International Journal of Multiphase Flow*, 7:41–46, 1981.

[137] J Kim, P Moin, and R Moser. Turbulence statistics in fully developed channel flow at low Reynolds number. *J. Fluid Mech.*, 177:133–166, 1987.

[138] P. Lammers, K. N. Beronov, R. Volkert, G. Brenner, and F. Durst. Lattice BGK direct numerical simulation of fully developed turbulence in incompressible plane channel flow. *Computers and Fluids*, 35(10):1137–1153, 2006.

[139] Kannan N. Premnath, Martin J. Pattison, and Sanjoy Banerjee. Generalized lattice Boltzmann equation with forcing term for computation of wall-bounded turbulent flows. *Physical Review E - Statistical, Nonlinear, and Soft Matter Physics*, 79(2):1–19, 2009.

[140] Christopher E Brennen. *Fundamentals of multiphase flow*. Cambridge university press, 2005.

[141] S I Rubinow and Joseph B Keller. The transverse force on a spinning sphere moving in a viscous fluid. *Journal of Fluid Mechanics*, 11(3):447–459, 1961.

[142] Arthur Joseph Goldman, Raymond G Cox, and Howard Brenner. Slow viscous motion of a sphere parallel to a plane wallI Motion through a quiescent fluid. *Chemical engineering science*, 22(4):637–651, 1967.

[143] A. J. Goldman, R. G. Cox, and H. Brenner. Slow viscous motion of a sphere parallel to a plane wallII Couette flow. *Chemical engineering science*, 22(4):653–660, 1967.

[144] Xueming Shao, Tenghu Wu, and Zhaosheng Yu. Fully resolved numerical simulation of particle-laden turbulent flow in a horizontal channel at a low Reynolds number. pages 319–344, 2012.

[145] Aman G. Kidanemariam, Clemens Chan-braun, and Todor Doychev. Direct numerical simulation of horizontal open channel flow with finite-size , heavy particles at low solid volume fraction. *New Journal of Physics*, 2013.

[146] Yiming Li and J. B. Mclaughlin. Numerical simulation of particle-laden turbulent channel flow. *Physics of Fluids*, 13(10), 2001.

[147] C. Marchioli, A. Soldati, J. G. M. Kuerten, B. Arcen, A. Taniere, G. Goldensoph, K. D. Squires, M. F. Cargnelutti, and L. M. Portela. Statistics of particle dispersion in direct numerical simulations of wall-bounded turbulence: results of an international collaborative benchmark test. *International Journal of Multiphase Flow*, 34(9):879–893, 2008.

[148] M. M. Metzger and J. C. Klewicki. A comparative study of near-wall turbulence in high and low Reynolds number boundary layers. *Physics of Fluids*, 13(3):692–701, 2001.

[149] Anand Samuel Jebakumar, Kannan N. Premnath, and John Abraham. Lattice Boltzmann method simulations of Stokes number effects on particle trajectories in a wall-bounded flow. *Computers and Fluids*, 124:208–219, 2016.

[150] Prosenjit Bagchi and S. Balachandar. Response of the wake of an isolated particle to an isotropic turbulent flow. *Journal of Fluid Mechanics*, 518(2004):95–123, 2004.

[151] A. Merle, D. Legendre, and J. Magnaudet. Forces on a high-Reynolds-number spherical bubble in a turbulent flow. *Journal of Fluid Mechanics*, 532(2005):53–62, 2005.

[152] Lanying Zeng, S. Balachandar, Paul Fischer, and Fady Najjar. Interactions of a stationary finite-sized particle with wall turbulence. *Journal of Fluid Mechanics*, 594(2008):271–305, 2008.

[153] Lian-ping Wang, Cheng Peng, Zhaoli Guo, and Zhaosheng Yu. Lattice Boltzmann simulation of particle-laden turbulent channel flow. *Computers and Fluids*, 124:226–236, 2016.

[154] Kun Luo, Junhua Tan, Zeli Wang, and Jianren Fan. Particle-Resolved Direct Numerical Simulation of Gas Solid Dynamics in Experimental Fluidized Beds. 62(6), 2016.

[155] Dominique D'Humières, Irina Ginzburg, Manfred Krafczyk, Pierre Lallemand, and Li-Shi Luo. Multiple-relaxation-time lattice Boltzmann models in three dimensions. *Philosophical Transactions of the Royal Society of London A*, pages 437–451, 2002.

[156] Hui Zhao, Anyang Wei, Kun Luo, and Jianren Fan. Numerical Study of Turbulent Boundary-Layer Flow Induced by a Sphere Above a Flat Plate. *Simulation and Modeling Methodologies, Technologies and Applications, Advances in Intelligent Systems and Computing 256*, 256:239–252, 2014.

[157] Hui Zhao, Xiaofei Liu, Dong Li, Anyang Wei, Kun Luo, and Jianren Fan. Vortex dynamics of a sphere wake in proximity to a wall. *International Journal of Multiphase Flow*, 79:88–106, 2016.

[158] Lanying Zeng, S. Balachandar, and Fady M. Najjar. Wake response of a stationary finite-sized particle in a turbulent channel flow. *International Journal of Multiphase Flow*, 36(5):406–422, 2010.

[159] Ivette Rodriguez, Ricard Borell, Oriol Lehmkuhl, Carlos D. Perez Segarra, and Assensi Oliva. Direct numerical simulation of the flow over a sphere at Re = 3700. *Journal of Fluid Mechanics*, 679(2011):263–287, 2011.

[160] J. K. Eaton. Two-way coupled turbulence simulations of gas-particle flows using point-particle tracking. *International Journal of Multiphase Flow*, 35:792–800, 2009.

[161] Lenan Zhang, Anand Samuel Jebakumar, and John Abraham. Lattice Boltzmann method simulations of Stokes number effects on particle motion in a channel flow. *Physics of Fluids*, 28(6), 2016.

[162] Xueming Shao, Tenghu Wu, and Zhaosheng Yu. Fully resolved numerical simulation of particle-laden turbulent flow in a horizontal channel at a low Reynolds number. *Journal of Fluid Mechanics*, 693:319–344, 2012.

[163] Aman G Kidanemariam, Clemens Chan-Braun, Todor Doychev, and Markus Uhlmann. Direct numerical simulation of horizontal open channel flow with finite-size, heavy particles at low solid volume fraction. *New Journal of Physics*, 15(2):25031, 2013.

[164] Myoungkyu Lee and Robert D Moser. Direct numerical simulation of turbulent channel flow up to Re_tau approx 5200. *Journal of Fluid Mechanics*, 774:395–415, 2015.

[165] M. W. Reeks. The transport of discrete particles in inhomogeneous turbulence. *Journal of Aerosol Science*, 14(6):729–739, 1983.

[166] Pierre Lallemand and Li-shi Luo. Theory of the lattice Boltzmann method: Dispersion, dissipation, isotropy, Galilean invariance, and stability. 61(6):6546–6562, 2000.

[167] Marcos Vanella, Antonio Posa, and Elias Balaras. Adaptive mesh refinement for immersed boundary methods. *Journal of Fluids Engineering*, 136(4):40909, 2014.

[168] Arie Kaufman, Zhe Fan, and Kaloian Petkov. Implementing the lattice Boltzmann model on commodity graphics hardware. *Journal of Statistical Mechanics: Theory and Experiment*, 2009:P06016, 2009.

[169] Frédéric Kuznik, Christian Obrecht, Gilles Rusaouen, and Jean-Jacques Roux. LBM based flow simulation using GPU computing processor. *Computers & Mathematics with Applications*, 59(7):2380–2392, 2010.

[170] C. Obrecht, F. Kuznik, B. Tourancheau, and J. J. Roux. A new approach to the lattice Boltzmann method for graphics processing units. *Computers & Mathematics with Applications*, 61(12):3628–3638, 2011.

[171] Xiaoyi He, Li-Shi Luo, and Micah Dembo. Some progress in lattice Boltzmann method. Part I. Nonuniform mesh grids. *Journal of computational Physics*, 129(2):357–363, 1996.

[172] A G Kravchenko, P Moin, and R Moser. Zonal embedded grids for numerical simulations of wall-bounded turbulent flows. *Journal of Computational Physics*, 127(2):412–423, 1996.

[173] H. Chen, O. Filippova, J. Hoch, K. Molvig, R. Shock, C. Teixeira, and R. Zhang. Grid refinement in lattice Boltzmann methods based on volumetric formulation. 362:158–167, 2006.

[174] M. Rohde, D. Kandhai, J. J. Derksen, and H. E. A. Van Den Akker. A generic , mass conservative local grid refinement technique for lattice-Boltzmann schemes. (September 2005):439–468, 2006.

[175] Massimo Germano, Ugo Piomelli, Parviz Moin, William H Cabot, Massimo Germane, Ugo Piomelli, and William H Cabot. A dynamic subgrid-scale eddy viscosity model A dynamic subgrid-scale eddy viscosity model. *Physics of Fluids A: Fluid Dynamics*, 1760, 1991.

[176] S Stolz, N A Adams, L Kleiser, S Stolz, N A Adams, and L Kleiser. An approximate deconvolution model for large-eddy simulation with application to incompressible wall-bounded flows An approximate deconvolution model for large-eddy simulation with application to incompressible wall-bounded flows. *Physics of Fluids*, 997(2001), 2001.

[177] Thomas J R Hughes, Assad A Oberai, Luca Mazzei, Thomas J R Hughes, Assad A Oberai, and Luca Mazzei. Large eddy simulation of turbulent channel flows by the variational multiscale method Large eddy simulation of turbulent channel flows by the variational multiscale method. *Physics of Fluids (1958-1988)*, 1784(2001), 2001.

[178] A W Vreman. The filtering analog of the variational multiscale method in large-eddy simulation The filtering analog of the variational multiscale method in large-eddy simulation. *Physics of Fluids*, 61(2003), 2003.

[179] B J Geurts. Regularization modeling for large-eddy simulation of homogeneous isotropic decaying turbulence Regularization modeling for large-eddy simulation of. 2008.

[180] W. S. J. Uijttewaal and R. V. A. Oliemans. Particle dispersion and deposition in direct numerical and large eddy simulations of vertical pipe flows Particle dispersion and deposition in direct numerical and large eddy simulations of vertical pipe flows. *Physics of Fluids*, 2590(1996), 1996.

[181] Cristian Marchioli and Alfredo Soldati. Mechanisms for particle transfer and segregation in a turbulent boundary layer. *Journal of Fluid Mechanics*, 468:283–315, 2002.

[182] Cristian Marchioli, Andrea Giusti, Maria Vittoria, and Alfredo Soldati. Direct numerical simulation of particle wall transfer and deposition in upward turbulent pipe flow. *International Journal of Multiphase Flow*, 29:1017–1038, 2003.

[183] Fungee Yeh and U Lei. On the motion of small particles in a homogeneous isotropic turbulent flow. *Physics of Fluids A: Fluid Dynamics*, 2571(1991), 1991.

[184] Vincenzo Armenio, Ugo Piomelli, Virgilio Fiorotto, and Vincenzo Armenio. Effect of the subgrid scales on particle motion Effect of the subgrid scales on particle motion. *Physics of Fluids*, 3030, 1999.

[185] Shuling Hou, J Sterling, Shiyi Chen, and G D Doolen. A lattice Boltzmann subgrid model for high Reynolds number flows. *arXiv preprint comp-gas/9401004*, 1994.

[186] Jack G M Eggels. Direct and large-eddy simulation of turbulent fluid flow using the lattice-Boltzmann scheme. *International journal of heat and fluid flow*, 17(3):307–323, 1996.

[187] Jos Derksen and Harry E. A. Van den Akker. Large eddy simulations on the flow driven by a Rushton turbine. *AIChE Journal*, 45(2):209–221, 1999.

[188] Zhenyu Lu, Ying Liao, Dongying Qian, J B McLaughlin, J J Derksen, and K Kontomaris. Large eddy simulations of a stirred tank using the lattice Boltzmann method on a nonuniform grid. *Journal of Computational Physics*, 181(2):675–704, 2002.

[189] Manfred Krafczyk, Jonas Tölke, and Li-Shi Luo. Large-eddy simulations with a multiple-relaxation-time LBE model. *International Journal of Modern Physics B*, 17(01n02):33–39, 2003.

[190] Huidan Yu, Sharath S Girimaji, and Li-Shi Luo. DNS and LES of decaying isotropic turbulence with and without frame rotation using lattice Boltzmann method. *Journal of Computational Physics*, 209(2):599–616, 2005.

[191] Huidan Yu, Li-Shi Luo, and Sharath S Girimaji. LES of turbulent square jet flow using an MRT lattice Boltzmann model. *Computers & Fluids*, 35(8-9):957–965, 2006.

[192] E R Van Driest. On turbulent flow near a wall. *Journal of the Aeronautical Sciences*, 23(11):1007–1011, 1956.

[193] R. A. Antonia and R. W. Bilger. An experimental investigation of an axisymmetric jet in a co-flowing air stream. *Journal of Fluid Mechanics*, 61:805–822, 1973.

[194] L. Boguslawski and Cz. O. Popiel. Flow structure of the free round turbulent jet in the initial region. *Journal of Fluid Mechanics*, 90:531–539, 1979.

[195] S. B. Pope. An explanation of the turbulent round-jet/plane-jet anomaly. *AIAA Journal*, 16(March):279–281, 1978.

[196] John Abraham. Entrainment Characteristics of Transient Gas Jets. *Numerical Heat Transfer, Part A: Applications*, 30:347–364, 1996.

[197] John Abraham and Vinicio Magi. Computations of transient jets: RNG k-ϵ model versus standard k-ϵ model. *SAE paper 970885*, 1997.

[198] J.-S. Shuen, A. S. P. Solomon, Q-F. Zhang, and G. M. Faeth. Structure of Particle-Laden Jets - Measurements and Predictions. *AIAA Journal*, 23(3):396–404, 1985.

[199] D. Modarress, H. Tan, and S. Elghobashi. Two-component LDA measurement in a two-phase turbulent jet. *AIAA Journal*, 22(5):624–630, 1984.

[200] D. Fleckhaus, K. Hishida, and M. Maeda. Effect of laden solid particles on the turbulent flow structure of a round free jet. *Experiments in Fluids*, 5:323–333, 1987.

[201] A. A. Mostafa, H. C. Mongia, V. G. McDonell, and G. S. Samuelsen. Evolution of particle-laden jet flows - A theoretical and experimental study. *AIAA Journal*, 27(2):167–183, 1989.

[202] Y. Hardalupas, Taylor A. M. K. P., and J. H. Whitelaw. Velocity and particle-flux characteristics of turbulent particle-laden jets. *Proceedings of the Royal Society of London A*, 426:31–78, 1989.

[203] H.J. Sheen, B.H. Jou, and Y.T. Lee. Effect of particle size on a two-phase turbulent jet. *Experimental Thermal and Fluid Science*, 8:315–327, 1994.

[204] F. Prevost, J. Boree, H. J. Nuglisch, and G. Charnay. Measurements of Fluid/Particle correlated motion in the far field of an axisymmetric jet. *International Journal of Multiphase Flow*, 22(4):685–701, 1996.

[205] Jianren Fan, Xinyu Zhang, Lihua Chen, and Kefa Cen. New stochastic particle dispersion modeling of a turbulent particle-laden round jet. *Chemical Engineering Journal*, 66:207–215, 1997.

[206] G. J. Nathan, P. A. M. Kalt, Z. T. Alwahabi, B. B. Dally, P. R. Medwell, and Q. N. Chan. Recent advances in the measurement of strongly radiating, turbulent reacting flows. *Progress in Energy and Combustion Science*, 38:41–61, 2012.

[207] Vinicio Magi. REC-87: A new 3D code for flows, sprays and combustion in reciprocating and rotary engines. Technical report, Department of Mechanical and Aerospace Engineering, Princeton University, Princeton, New Jersey., 1987.

[208] Vinicio Magi, Venkatraman Iyer, and John Abraham. The k- ϵ model and computed spreading rates in round and plane jets. *Numerical Heat Transfer , Part A : Applications*, 40:317–334, 2001.

[209] Venkatraman Iyer and John Abraham. An Evaluation of a Two-Fluid Eulerian-Liquid Eulerian-Gas Model for Diesel Sprays. *Journal of Fluids Engineering*, 125(July):660–669, 2003.

[210] John Abraham. What is adequate resolution in the numerical computations of transient jets? *SAE paper 970051*, pages 81–95, 1997.

[211] Venkatraman Iyer and John Abraham. Penetration and Dispersion of Transient Gas Jets and Sprays. *Combustion Science and Technology*, 130:315–334, 1997.

[212] Chetan Bajaj, John Abraham, and Lyle M. Pickett. Vaporization effects on transient diesel spray structure. *Atomization and Sprays*, 21(5):411–426, 2011.

[213] J. G. M. Eggels, F. Unger, M. H. Weiss, J. Westerweel, R. J. Adrian, R. Friedrich, and F. T. M. Nieuwstadt. Fully developed turbulent pipe flow: a comparison between direct numerical simulation and experiment. *Journal of Fluid Mechanics*, 268:175–209, 1994.

[214] J-S. Shuen, A. S. P. Solomon, Q-F. Zhang, and G. M. Faeth. A theoritical and experimental study of turbulent particle-laden jets. Technical report, NASA Contractor Report 168293, 1983.

[215] David C. Wilcox. *Turbulence-Modeling-for-CFD*. 1993.

[216] Z. Yuan and E. E. Michaelides. Turbulence modulation in particulate flowsa theoretical approach. *International Journal of Multiphase Flow*, 18(5):779–785, 1992.

[217] L P Yarin and G Hetsroni. Turbulence intensity in dilute two-phase flows3 The particles-turbulence interaction in dilute two-phase flow. *International Journal of Multiphase Flow*, 20(1):27–44, 1994.

APPENDICES

A. MULTIPLE RELAXATION TIME IMPLEMENTATION

The components of various elements in the moments are given following Ref. [155]:

$$\widehat{f_0} = \rho \tag{A.1}$$

$$\widehat{f_1} = e \tag{A.2}$$

$$\widehat{f_2} = e^2 \tag{A.3}$$

$$\widehat{f_3} = j_x \tag{A.4}$$

$$\widehat{f_4} = q_x \tag{A.5}$$

$$\widehat{f_5} = j_y \tag{A.6}$$

$$\widehat{f_6} = q_y \tag{A.7}$$

$$\widehat{f_7} = j_z \tag{A.8}$$

$$\widehat{f_8} = q_z \tag{A.9}$$

$$\widehat{f_9} = 3p_{xx} \tag{A.10}$$

$$\widehat{f_{10}} = 3\pi_{xx} \tag{A.11}$$

$$\widehat{f_{11}} = p_{ww} \tag{A.12}$$

$$\widehat{f_{12}} = \pi_{ww} \tag{A.13}$$

$$\widehat{f_{13}} = p_{xy} \tag{A.14}$$

$$\widehat{f_{14}} = p_{yz} \tag{A.15}$$

$$\widehat{f_{15}} = p_{xz} \tag{A.16}$$

$$\widehat{f_{16}} = m_x \tag{A.17}$$

$$\widehat{f_{17}} = m_y \tag{A.18}$$

$$\widehat{f_{18}} = m_z \tag{A.19}$$

Here, ρ is the density, e and e^2 represent kinetic energy of the molecules and the square of the kinetic energy respectively; j_x, j_y and j_z are the components of momentum, i.e. $j_x = \rho u_x$, $j_y = \rho u_y$ and $j_z = \rho u_z$; q_x, q_y and q_z are the components of the energy flux; p_{xx}, p_{xy}, p_{yz} and p_{xz} are the components of the symmetric traceless viscous stress tensor. The other normal components p_{yy} and p_{zz} can be found from p_{ww} and p_{xx} where $p_{ww} = p_{yy} - p_{zz}$. Other moments include π_{xx}, π_{ww}, m_x, m_y and m_z. The first two of these moments have the same symmetry as the diagonal part of the traceless viscous tensor p_{ij}, while the last three vectors are parts of a third rank tensor, with the symmetry of $j_k p_{mn}$.

The transformation matrix for the D3Q19 lattice is given as (Ref. [155]): $T =$

$$
\begin{bmatrix}
1 & 1 & 1 & 1 & 1 & 1 & 1 & 1 & 1 & 1 & 1 & 1 & 1 & 1 & 1 & 1 & 1 & 1 & 1 \\
-30 & -11 & -11 & -11 & -11 & -11 & -11 & 8 & 8 & 8 & 8 & 8 & 8 & 8 & 8 & 8 & 8 & 8 & 8 \\
12 & -4 & -4 & -4 & -4 & -4 & -4 & 1 & 1 & 1 & 1 & 1 & 1 & 1 & 1 & 1 & 1 & 1 & 1 \\
0 & 1 & -1 & 0 & 0 & 0 & 0 & 1 & -1 & 1 & -1 & 1 & -1 & 1 & -1 & 0 & 0 & 0 & 0 \\
0 & -4 & 4 & 0 & 0 & 0 & 0 & 1 & -1 & 1 & -1 & 1 & -1 & 1 & -1 & 0 & 0 & 0 & 0 \\
0 & 0 & 0 & 1 & -1 & 0 & 0 & 1 & 1 & -1 & -1 & 0 & 0 & 0 & 0 & 1 & -1 & 1 & -1 \\
0 & 0 & 0 & -4 & 4 & 0 & 0 & 1 & 1 & -1 & -1 & 0 & 0 & 0 & 0 & 1 & -1 & 1 & -1 \\
0 & 0 & 0 & 0 & 0 & 1 & -1 & 0 & 0 & 0 & 0 & 1 & 1 & -1 & -1 & 1 & 1 & -1 & -1 \\
0 & 0 & 0 & 0 & 0 & -4 & 4 & 0 & 0 & 0 & 0 & 1 & 1 & -1 & -1 & 1 & 1 & -1 & -1 \\
0 & 2 & 2 & -1 & -1 & -1 & -1 & 1 & 1 & 1 & 1 & 1 & 1 & 1 & 1 & -2 & -2 & -2 & -2 \\
0 & -4 & -4 & 2 & 2 & 2 & 2 & 1 & 1 & 1 & 1 & 1 & 1 & 1 & 1 & -2 & -2 & -2 & -2 \\
0 & 0 & 0 & 1 & 1 & -1 & -1 & 1 & 1 & 1 & 1 & -1 & -1 & -1 & -1 & 0 & 0 & 0 & 0 \\
0 & 0 & 0 & -2 & -2 & 2 & 2 & 1 & 1 & 1 & 1 & -1 & -1 & -1 & -1 & 0 & 0 & 0 & 0 \\
0 & 0 & 0 & 0 & 0 & 0 & 0 & 1 & -1 & -1 & 1 & 0 & 0 & 0 & 0 & 0 & 0 & 0 & 0 \\
0 & 0 & 0 & 0 & 0 & 0 & 0 & 0 & 0 & 0 & 0 & 0 & 0 & 0 & 0 & 1 & -1 & -1 & 1 \\
0 & 0 & 0 & 0 & 0 & 0 & 0 & 0 & 0 & 0 & 0 & 1 & -1 & -1 & 1 & 0 & 0 & 0 & 0 \\
0 & 0 & 0 & 0 & 0 & 0 & 0 & 1 & -1 & 1 & -1 & -1 & 1 & -1 & 1 & 0 & 0 & 0 & 0 \\
0 & 0 & 0 & 0 & 0 & 0 & 0 & -1 & -1 & 1 & 1 & 0 & 0 & 0 & 0 & 1 & -1 & 1 & -1 \\
0 & 0 & 0 & 0 & 0 & 0 & 0 & 0 & 0 & 0 & 0 & 1 & 1 & -1 & -1 & -1 & -1 & 1 & 1
\end{bmatrix}
$$

Components of equilibrium moments for the D3Q19 lattice are as follows [155]:

$$\widehat{f}_0^{eq} = \rho \tag{A.20}$$

$$\widehat{f}_1^{eq} = e^{eq} = -11\rho + 19\frac{\boldsymbol{j}\cdot\boldsymbol{j}}{\rho} \tag{A.21}$$

$$\widehat{f}_2^{eq} = e^{2,eq} = 3\rho - \frac{11}{2}\frac{\boldsymbol{j}\cdot\boldsymbol{j}}{\rho} \tag{A.22}$$

$$\widehat{f}_3^{eq} = j_x \tag{A.23}$$

$$\widehat{f}_4^{eq} = q_x^{eq} = -\frac{2}{3}j_x \tag{A.24}$$

$$\widehat{f}_5^{eq} = j_y \tag{A.25}$$

$$\widehat{f}_6^{eq} = q_y^{eq} = -\frac{2}{3}j_y \tag{A.26}$$

$$\widehat{f}_7^{eq} = j_z \tag{A.27}$$

$$\widehat{f}_8^{eq} = q_z^{eq} = -\frac{2}{3}j_z \tag{A.28}$$

$$\widehat{f}_9^{eq} = 3p_{xx}^{eq} = \frac{\left(3j_x^2 - \dfrac{\boldsymbol{j}\cdot\boldsymbol{j}}{\rho}\right)}{\rho} \tag{A.29}$$

$$\widehat{f}_{10}^{eq} = 3\pi_{xx}^{eq} = 3\left(-\frac{1}{2}p_{xx}^{eq}\right) \tag{A.30}$$

$$\widehat{f}_{11}^{eq} = p_{ww}^{eq} = \frac{\left(j_y^2 - j_z^2\right)}{\rho} \tag{A.31}$$

$$\widehat{f}_{12}^{eq} = \pi_{ww}^{eq} = -\frac{1}{2}p_{ww}^{eq} \tag{A.32}$$

$$\widehat{f}_{13}^{eq} = p_{xy}^{eq} = \frac{j_x j_y}{\rho} \tag{A.33}$$

$$\widehat{f}_{14}^{eq} = p_{yz}^{eq} = \frac{j_y j_z}{\rho} \tag{A.34}$$

$$\widehat{f}_{15}^{eq} = p_{xz}^{eq} = \frac{j_x j_z}{\rho} \tag{A.35}$$

$$\widehat{f}_{16}^{eq} = 0 \tag{A.36}$$

$$\widehat{f}_{17}^{eq} = 0 \tag{A.37}$$

$$\widehat{f}_{18}^{eq} = 0 \tag{A.38}$$

Source terms in moment space are given as follows [139]:

$$\widehat{S}_0 = 0 \tag{A.39}$$

$$\widehat{S}_1 = 38\left(F_x u_x + F_y u_y + F_z u_z\right) \tag{A.40}$$

$$\widehat{S}_2 = -11\left(F_x u_x + F_y u_y + F_z u_z\right) \tag{A.41}$$

$$\widehat{S}_3 = F_x \tag{A.42}$$

$$\widehat{S}_4 = -\frac{2}{3}F_x \tag{A.43}$$

$$\widehat{S}_5 = F_y \tag{A.44}$$

$$\widehat{S}_6 = -\frac{2}{3}F_y \tag{A.45}$$

$$\widehat{S}_7 = F_z \tag{A.46}$$

$$\widehat{S}_8 = -\frac{2}{3}F_z \tag{A.47}$$

$$\widehat{S}_9 = 2\left(2F_x u_x - F_y u_y - F_z u_z\right) \tag{A.48}$$

$$\widehat{S}_{10} = -\left(2F_x u_x - F_y u_y - F_z u_z\right) \tag{A.49}$$

$$\widehat{S}_{11} = 2\left(F_y u_y - F_z u_z\right) \tag{A.50}$$

$$\widehat{S}_{12} = -\left(F_y u_y - F_z u_z\right) \tag{A.51}$$

$$\widehat{S}_{13} = \left(F_x u_y + F_y u_x\right) \tag{A.52}$$

$$\widehat{S}_{14} = \left(F_y u_z + F_z u_y\right) \tag{A.53}$$

$$\widehat{S}_{15} = \left(F_x u_z + F_z u_x\right) \tag{A.54}$$

$$\widehat{S}_{16} = 0 \tag{A.55}$$

$$\widehat{S}_{17} = 0 \tag{A.56}$$

$$\widehat{S}_{18} = 0 \tag{A.57}$$

$$\tag{A.58}$$

B. GPU COMPUTING

It is a well known fact that Direct Numerical Simulations (DNS) in general incur a huge computational cost. Particle Resolved - DNS (PR-DNS) computations are even more expensive than DNS of single-phase flows. Especially, if the particle size is of the order of Kolmogorov length scale, then a sub-Kolmogorov resolution is required to resolve the particle surface correctly. Thus the codes developed need to be highly optimized and fully parallelized to ensure that accurate results are obtained in a reasonable amount of time. During the initial code development, some studies on parallelizing the LBM code using Graphics Processing Units (GPUs) were carried out.

Modern GPUs can be employed to perform high performance computations in addition to their intended specialized graphics operations. Due to the highly parallel nature of graphics processing, the GPU has evolved into a coprocessor that can be used in applications involving high data parallelism. As explained in Chapter 3, the operations in LBM are local and explicit unlike the conventional Navier-Stokes solvers which have to solve a Poisson type equation for pressure. This makes the LBM suited to be run on a GPU.

There are relatively fewer works that have reported LBM computations on a GPU. They are listed in Ref. [168–170]. The main idea is that the GPU has several threads each of which can perform arithmetic or logical operations simultaneously. A typical GPU has thousands of threads operating on separate pieces of data. Each thread can be assigned to perform computations on one grid point. Individual operations on a GPU are slower than those on CPU. However, the large number of threads render a large throughput (total number of operations per unit time) than the CPU.

The code development in a GPU environment differs considerably from usual distributed memory systems (i.e. MPI codes). In a GPU, there are various levels of

memory hierarchies. The register is obviously the fastest. Then there is also a shared memory which has speeds comparable to a cache. This memory is shared by a group of threads referred to as a block. Finally, there is the global memory which is common to all threads and blocks. The data access is fastest in the following order: registers $>$ shared memory $>>$ global memory. Any data transfer between the GPU and the CPU is slower than all these data access and should therefore be kept to a minimum. Much of the effort is thus spent on ensuring efficient memory access patterns. This is critical in the stream operation of the LBM.

As a part of this work, a two-dimensional LBM code was developed to solve flow in a plane channel with the SRT collision operator. We ran our codes on an NVIDIA Tesla M2090 GPU. With just one GPU, speedup of over 100 times than a single CPU (Intel Xeon L5640) was achieved. The cost of the GPU that was used is less than a \$1000. Thus the computation/cost ratio is very high for a GPU.

However, there were some limitations. Firstly, the code development time to obtain an efficient code is very high. Secondly, even the latest GPUs have a RAM of about 6GB. This necessitates the use of multiple GPUs for PR-DNS computations which requires some sort of CPU-CPU communication routines (MPI for instance). This adds further complexity to the code. Finally, current GPU resources were not as much as the conventional CPU cores available. Hence the work in this thesis was carried out on distributed memory systems using the MPI.

C. LOCAL GRID REFINEMENT

As originally proposed, the lattice-Boltzmann method employs uniform grids since space and time are coupled for a lattice with a discrete velocity set. For example, in a D3Q19 lattice, where D3 refers to three dimensions and Q19 to 18 velocity directions and a null velocity, a "fluid particle" moving in any of the 18 directions has to land exactly at another grid point. This requires that the grid employed be uniform. Figure C.1 illustrates a D3Q19 lattice commonly employed in the LBM computations. It is clearly evident that having a lattice points at each locations marked 1-18 would give rise to a uniform grid.

However, in the computation of turbulent wall-bounded flows such as a channel flow, the length scale of eddies near the wall are much smaller compared to those in the core of the channel. Figure C.2a shows the Kolmogorov length scale normalized by the viscous length scale as a function of the distance from the wall (results are from Ref. [133]). This is at a friction Reynolds number, Re_τ, of 180, which corresponds to a bulk Reynolds number of about 6500. It can be seen from Fig. C.2a that near

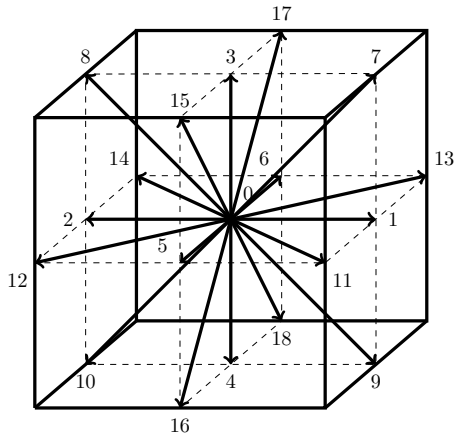

Figure C.1: A D3Q19 lattice showing the requirement for a uniform arrangement of lattice points.

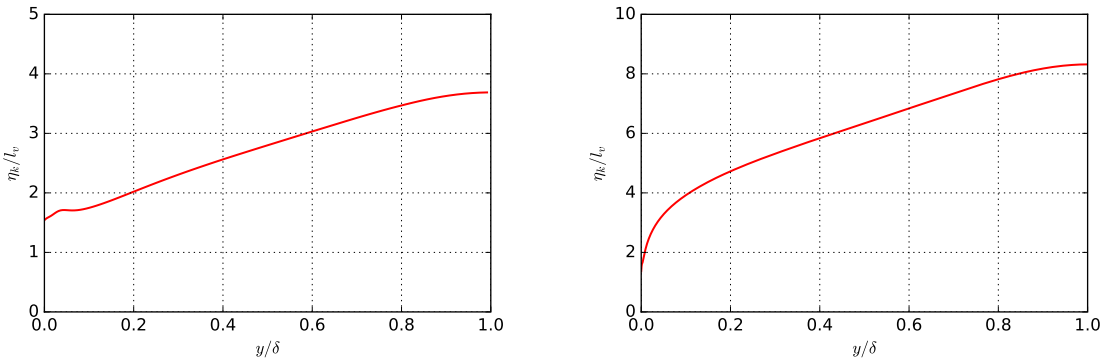

(a) (b)

Figure C.2: Variation of Kolmogorov length scale normalized by the viscous length scale as a function of distance from the wall for (a) $Re_\tau = 180$ and (b) $Re_\tau = 5200$.

the wall, the normalized Kolmogorov length scale is about 1.5 while it is about 3.7 near the wall, i.e. length scale of eddies near the wall are about 2.5 times smaller than that at the core of the channel. At higher Re, this factor increases. From Fig. C.2b, it is seen that at $Re_\tau = 5200$ which corresponds to a bulk Reynolds number of 125000, this factor is roughly 6. Having uniform grids throughout the channel for such a case would increase the computational time enormously. This can be avoided if grids of variable sizes are employed in the domain.

One approach is to employ continuously varying grid resolution using an interpolation supplemented LBM that decouples particle velocity space and the computational grid [171]. However, interpolation is known to introduce numerical dissipation [166], which affects the accuracy of computations, especially for turbulent flows. A preferred alternate approach would be to employ local grid refinement techniques. Such techniques are commonly employed in Navier-Stokes solvers where variable grid size is required [172]. Chen et al. [173] and Rhode et al. [174] have proposed a method for local grid refinement in the LBM framework with a conservative approach that ensures mass and momentum is conserved across the transition from coarse to fine grids. A brief explanation of the method is provided here.

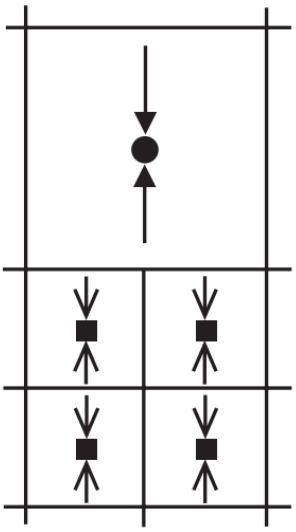

Figure C.3: A schematic of a coarse-fine transition layer.

Consider an interface where there is a transition from fine to coarse grid. The transition is such that each coarse grid will have some integer "n" number of fine grids. This refinement factor is 2 in the present work. Thus at the interface, for each coarse grid, there are two neighboring fine grids. The lattice points themselves are staggered to ensure conservation of mass and momentum. Figure C.3 shows a schematic of a transition layer. The dot indicates a lattice point in the coarse layer and the solid squares lattice points in the fine layer. The squares represent a voxel, analogous to a cell in the finite-volume formulation. The arrangement is such that coarse and fine voxels are aligned with each other as shown in Fig. C.3.

In the fine layer, two iterations are carried out for every iteration in the coarse cell. During each streaming operation, information has to be transmitted between the coarse and fine cells. To transfer information from the coarse layer to the fine layer, the distributions functions have to be distributed to the fine voxels. In the current work, this is distributed equally. This process is referred to as the "explode" step. To transfer information from the fine layer to the coarse layer, the distribution

functions are to be gathered together by summing them up. This is referred to as the "coalesce" step. The complete algorithm is specified below:

1. Explode from coarse voxels into fine voxels.
2. Stream fine voxels.
3. Collide fine voxels.
4. Stream fine voxels.
5. Collide fine voxels.
6. Stream coarse voxels.
7. Coalesce from fine voxels to coarse voxels.
8. Collide coarse voxels.
9. Continue again from Step 1.

The implementation of this algorithm is done in C++ using an object oriented programming methodology with MPI for parallelization. First the code is assessed for its accuracy in simulating a laminar channel flow. The grid employed for this simulation is shown in Fig. C.4. The grid refinement is in the Y-direction, i.e. normal to the walls. The flow is in the X-direction. Z-direction is periodic. There are three layers of refinement. Near the wall, four cells are employed. In the next layer, four cells with a refinement factor 2 is used. The third layer has 7 cells with size four times larger than the cells near the wall. The idea behind this refinement is that near the walls, the velocity gradient is large and hence more cells are required while near the center, the gradient is small and fewer cells are sufficient. The flow is driven by a body force and is similar to the laminar channel arrangement presented in Chapter 4.

Figure C.5 shows the velocity profile obtained from the simulations. The results agree well with the analytical profile. Figure C.6 shows the contour plot of streamwise velocity along with the computational grid with refinement.

Next, the accuracy of this technique for a turbulent channel flow will be demonstrated. The Re_τ considered here is 180. The simulation parameters are identical to

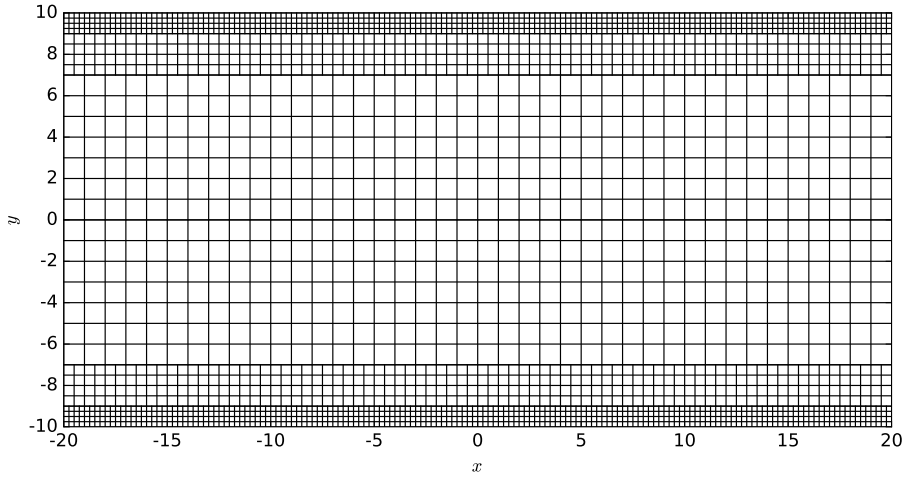

Figure C.4: Grid employed for the laminar channel flow simulation.

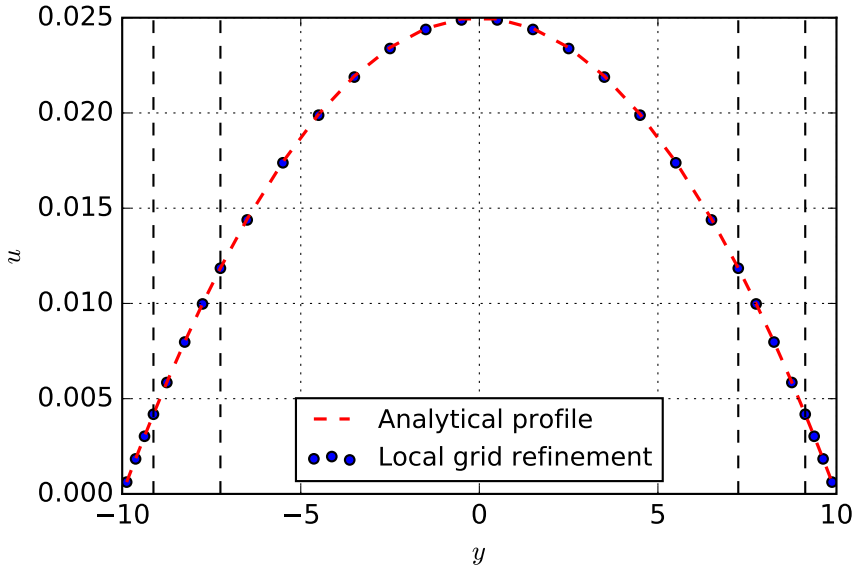

Figure C.5: Velocity profile as a function of distance from the wall.

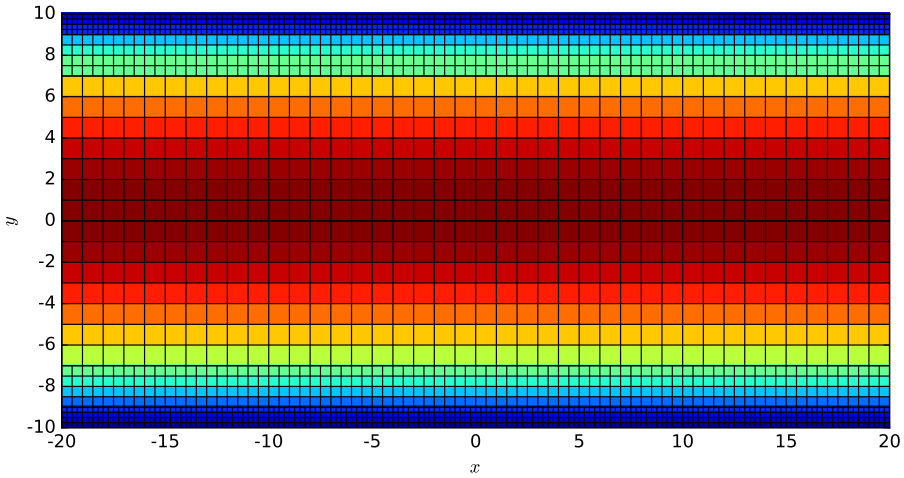

Figure C.6: Contour plot of streamwise velocity. Computational grid is also shown.

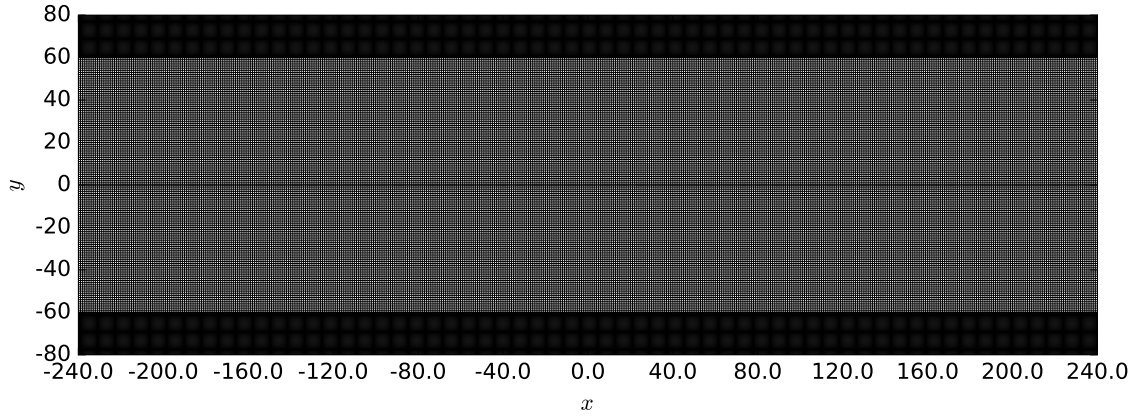

Figure C.7: Grid employed for the turbulent channel flow simulation.

the turbulent channel flow simulations described in Chapter 4. Figure C.7 shows the grid employed for this computation. There are two levels of refinement. Near the wall, at $y^+ < 40$, the grid size is about $1l_v$, where l_v is the viscous length scale. At $y^+ > 40$, the grid size is about $2l_v$. The ratio of grid size to Kolmogorov length scale is about 1 throughout the channel.

The mean velocity profile is shown in Fig. C.8. It is seen that the profile almost lies on top of the profile obtained by Lee & Moser [133] using a spectral element solver. Figure C.9 shows the turbulent kinetic energy profile. The agreement is reasonable with the differences being less than 5% at all locations. The number of grid points employed in this simulation is 50.688 million whereas if the fine cell was uniformly used, 147.45 million cells would be required. Thus savings in computational time achieved is about a factor 3.

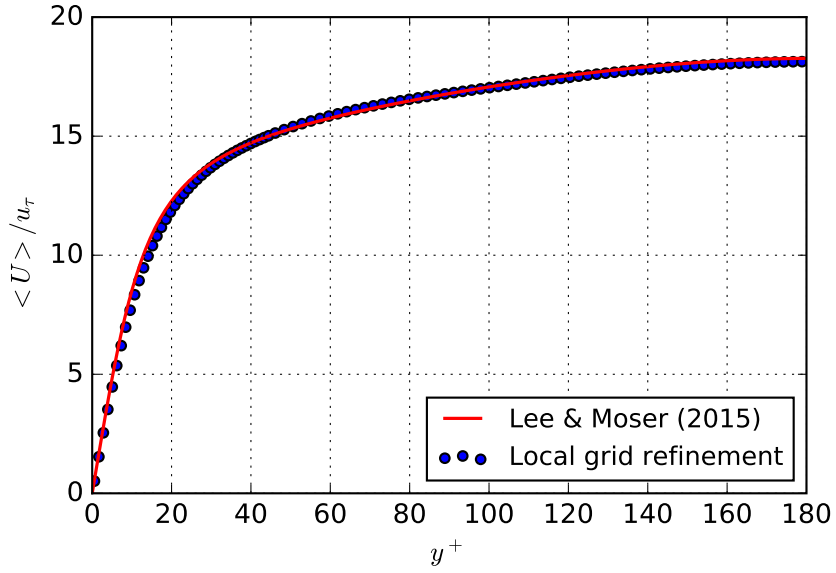

Figure C.8: Mean velocity profile as a function of distance from the wall.

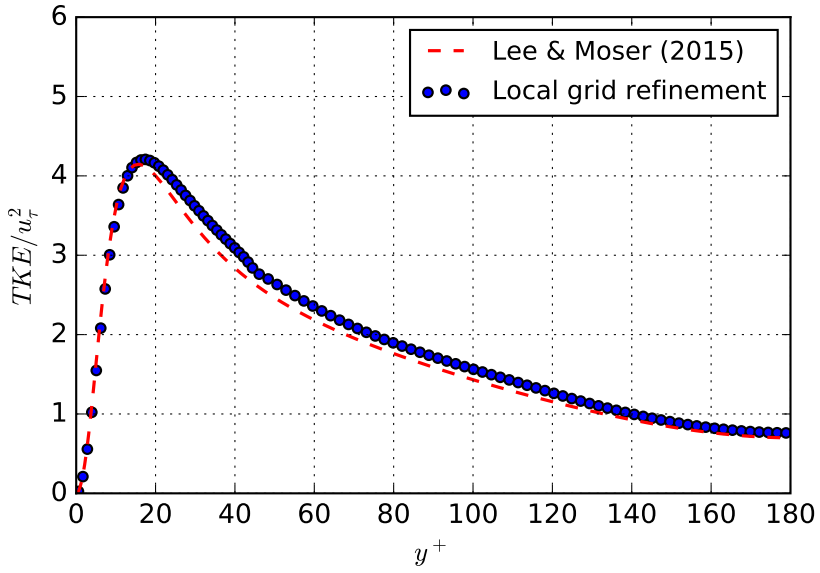

Figure C.9: Turbulent kinetic energy (TKE) profile as a function of distance from the wall.

D. LARGE EDDY SIMULATIONS USING THE LBM

Large eddy simulation (LES) refers to a simulation technique for turbulent flows where the larger energy containing eddies are resolved numerically, while the smaller eddies are modeled. The effects of the smaller eddies are taken into account with an eddy viscosity approximation. While this technique is computationally more expensive than Reynolds averaged Navier-Stokes (RANS) solvers, it is more accurate in its representation of turbulence. With increasing computational power, LES is becoming frequently employed, even for simulations of practical interest. In this section, some preliminary results for LES of particle-laden flows using the lattice-Boltzmann method (LBM) are presented.

While LES has been used extensively to simulate single-phase flows [175–179], it has recently been used for particle-laden flows [180]. If the particle size is small compared to the Kolmogorov length scale, a point-particle approximation can be used [181, 182]. While some works employ the filtered LES velocity directly in the particle equation of motion [77,183], this can lead to inaccurate prediction of particle-dispersion [83, 184]. Initial studies of LES using the lattice-Boltzmann method of particle-laden flows are presented in this section to assess the accuracy of sub grid models and its effect on the particle motion. This is the first work to report LES of particle-laden flows using the LBM.

LES for single-phase flows using the LBM was initially proposed by Hou et al. [185] and Eggels et al. [186]. In later works, it has been employed to study flows with different configurations [187–190]. While these studies used the single relaxation time (SRT) collision operator, Yu et al. [191] extended this work to carry out LES using the multiple relaxation time (MRT) collision operator. Premnath et al. [139] have performed LES of channel flow using MRT schemes with a body force to drive the

flow. A similar approach has been employed in this work to carry out simulations of particle-laden turbulent channel flow.

To model the effect of sub-grid scale (SGS) eddies, a Smagorinsky model is employed. The eddy viscosity, ν_t, can be computed from the strain rate as

$$\nu_t = (C_s\Delta)^2\bar{S}, \tag{D.1}$$

where C_s is a constant, Δ is the cutoff length and $\bar{S}$ is the magnitude of strain rate tensor. The magnitude of strain rate tensor is given as

$$\bar{S} = \sqrt{2S_{ij}S_{ij}}, \tag{D.2}$$

where S_{ij} is the strain rate tensor. In the LBM framework, the magnitude of strain rate tensor can be calculated directly from the non-equilibrium moments [191] eliminating the need for calculation of velocity derivatives. In order to account for viscous damping near the wall, the cutoff length, Δ, includes the van Driest damping function [192],

$$\Delta = \delta_x \left[1 - exp\left(\frac{-y^+}{25}\right)\right], \tag{D.3}$$

where δ_x is the grid size, and y^+ is the normalized distance from the wall. The results for a single-phase flow using the LES code is now presented.

For the LES computation, the local grid refinement technique described in Appendix C is employed. Two layers of refinement are used with 15 cells in each layer in the wall-normal direction. The mesh employed is shown in Fig. D.1. The grid size is roughly 2.5 times the Kolmogorov length scale. Figure D.2 shows the mean velocity profile as a function of y^+. It is seen that the profile agrees with the DNS results from literature [133] with differences being less than 5%. The TKE profile is shown in Fig. D.3. The profile agrees reasonably well with the DNS results. Figure D.4 shows the contour plot of instantaneous streamwise velocity.

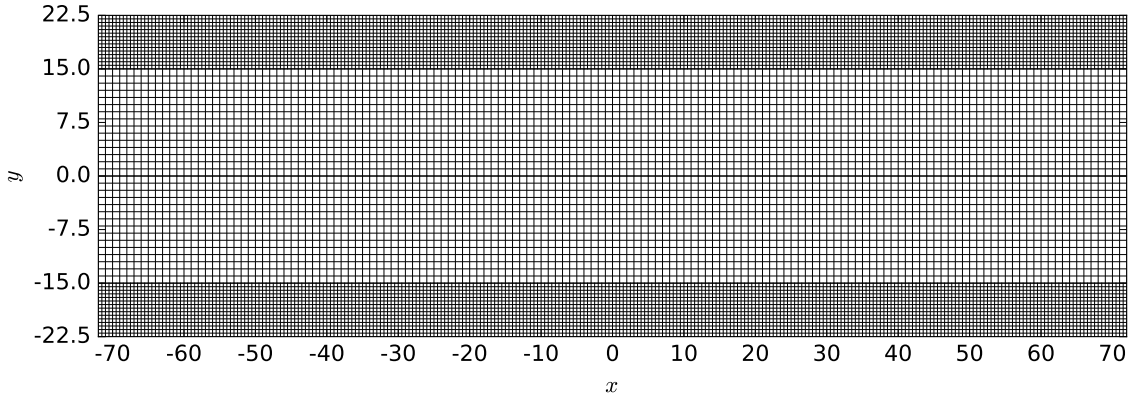

Figure D.1: Grid employed for the LES of turbulent channel flow.

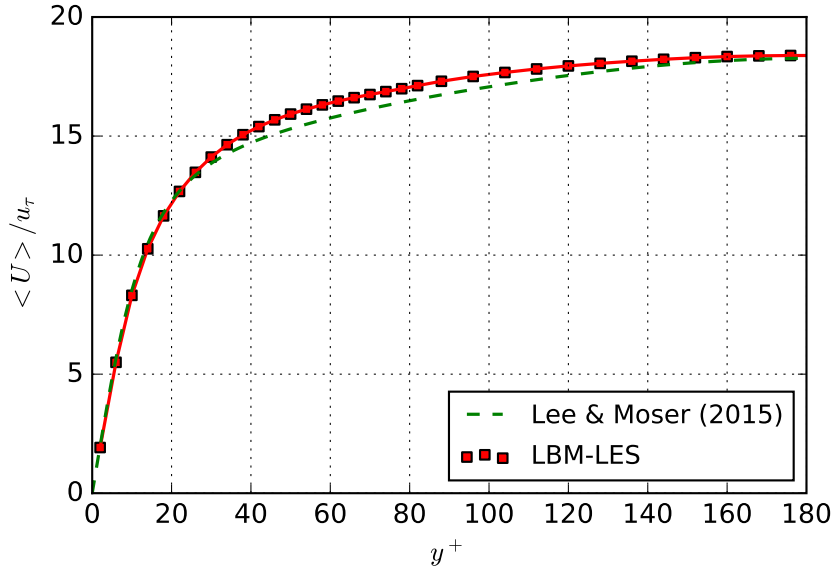

Figure D.2: Mean velocity profile as a function of distance from the wall.

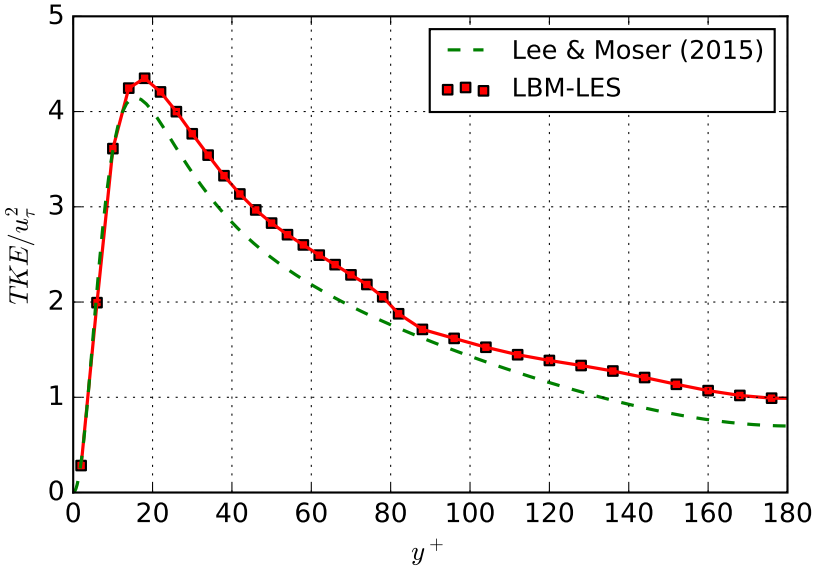

Figure D.3: Turbulent kinetic energy (TKE) profile as a function of distance from the wall.

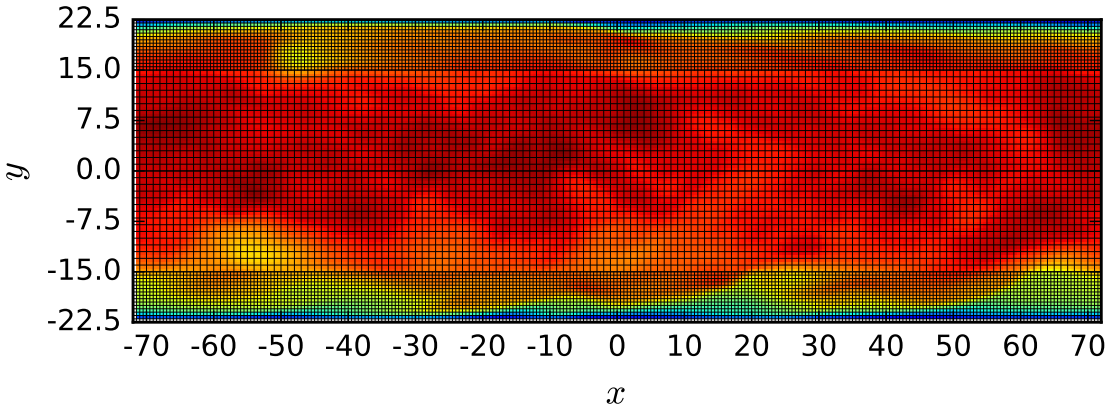

Figure D.4: Contour plot of instantaneous streamwise velocity. Computational grid is also shown.

Table D.1: Parameters employed for the LES study.

Case	St	ρ_p/ρ_f	d_p/H
1	0.5	450	2×10^{-3}
2	2	1800	2×10^{-3}
3	10	9000	2×10^{-3}
4	40	36000	2×10^{-3}
5	100	90000	2×10^{-3}

The parameters employed for simulation is shown in Table D.1. 1000 particles are employed in the simulation. The St is varied from 0.5 to 100 by changing the particle density. The particle size is kept constant throughout and is smaller than the Kolmogorov length scale. The mass loading is small in all cases and hence only one-way coupling is considered. Results for particle concentration are shown in Figs. D.5-D.9.

Figure D.5 shows particle concentration profile for Case 1 ($St = 0.5$). While the peak concentration near the wall is about 8 times the average value in the DNS, it is about 9 times the average value in the LES. As the St is increased to 2 (Case 2), Fig. D.6 shows significant differences between the DNS and the LES. The magnitude of near wall concentration is 3 times the average value for the DNS while it is about 9 times the average value. This increase might be due to the absence of smaller isotropic eddies near the wall. These eddies increase particle dispersion. For Case 3 ($St = 10$), Fig. D.7 shows that the LES prediction of particle concentration near the wall is still higher than the DNS value. However, for Case 4 ($St = 40$) and Case 5 ($St = 100$), the LES and DNS predictions are reasonably close. This is likely because the St in these cases are high that the smaller eddies have negligible impact on the

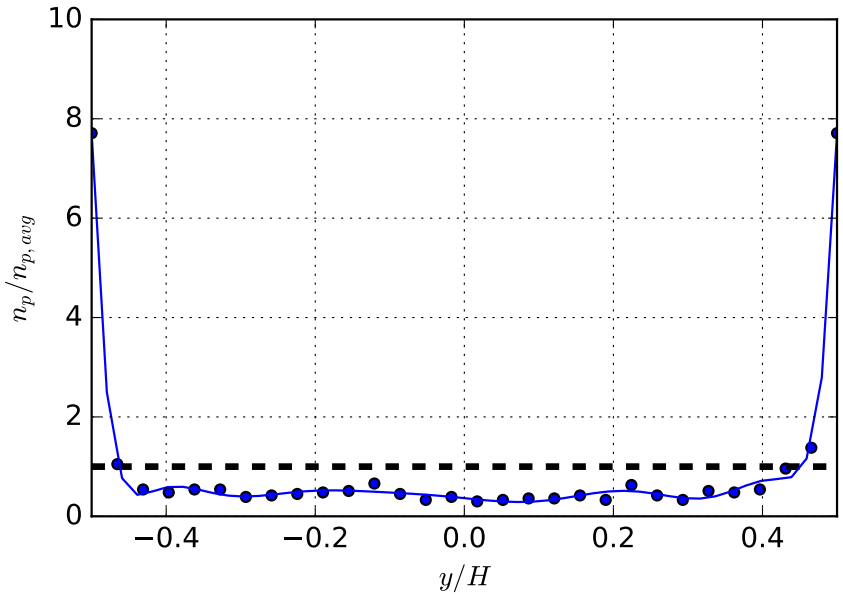

(a)

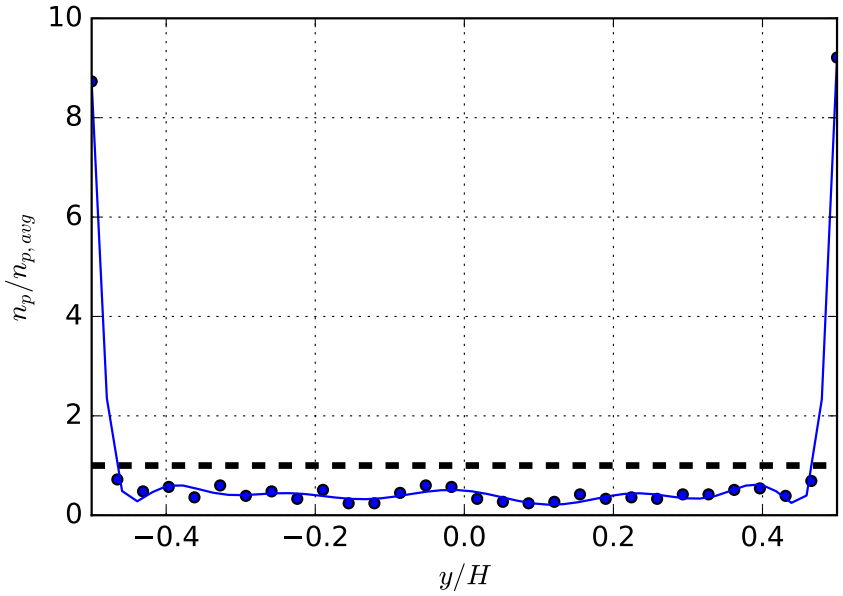

(b)

Figure D.5: Particle concentration profile normalized by the average concentration for Case 1: (a) DNS and (b) LES.

particle motion. Thus initial results seem to indicate that a model for the effect of smaller eddies on the particle is required, especially for the low St cases.

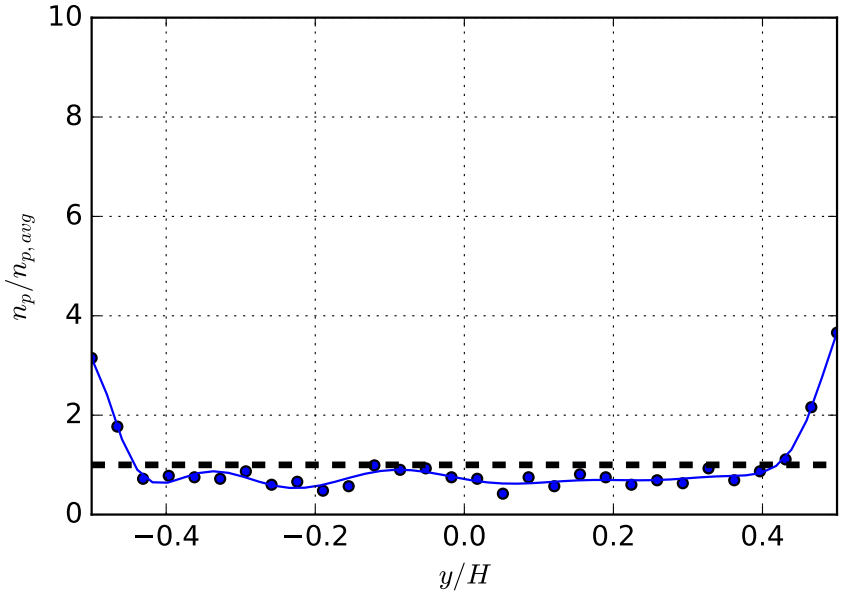

(a)

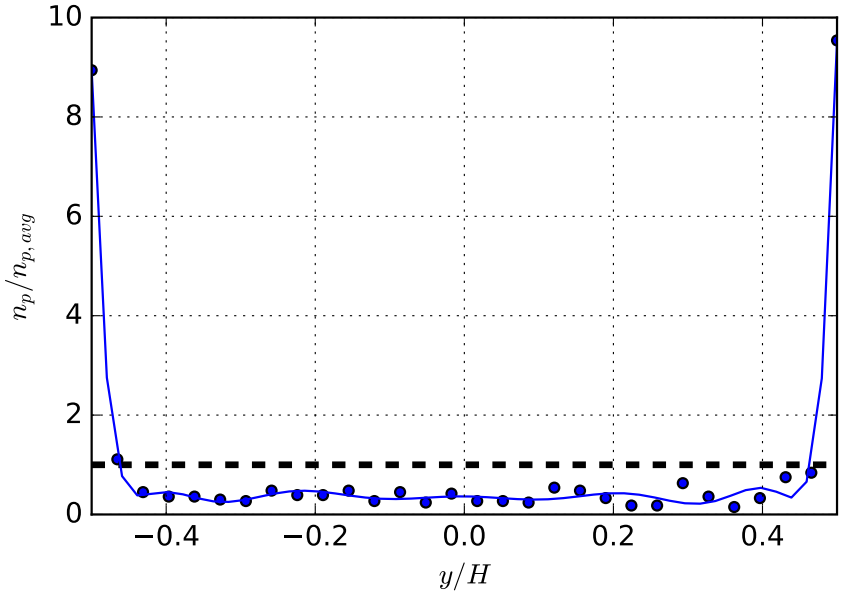

(b)

Figure D.6: Particle concentration profile normalized by the average concentration for Case 2: (a) DNS and (b) LES.

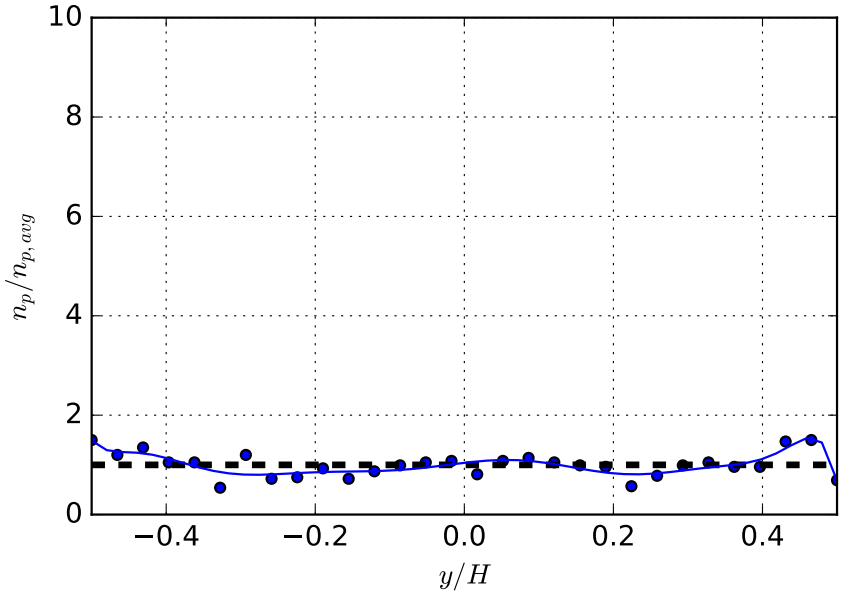

(a)

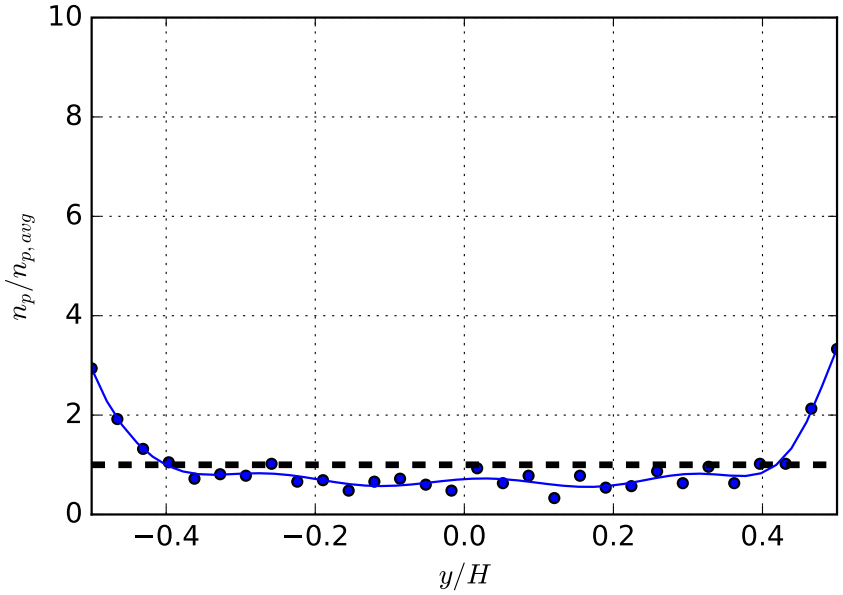

(b)

Figure D.7: Particle concentration profile normalized by the average concentration for Case 3: (a) DNS and (b) LES.

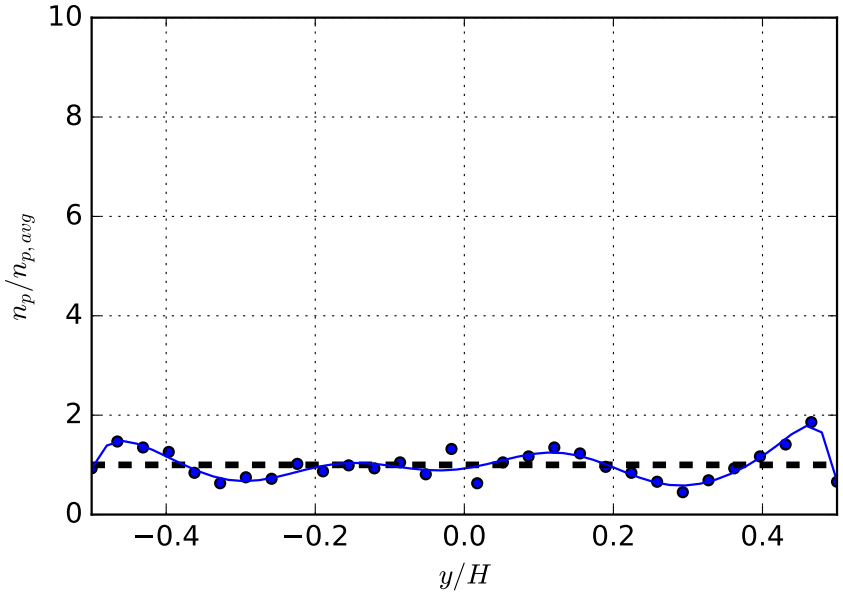

(a)

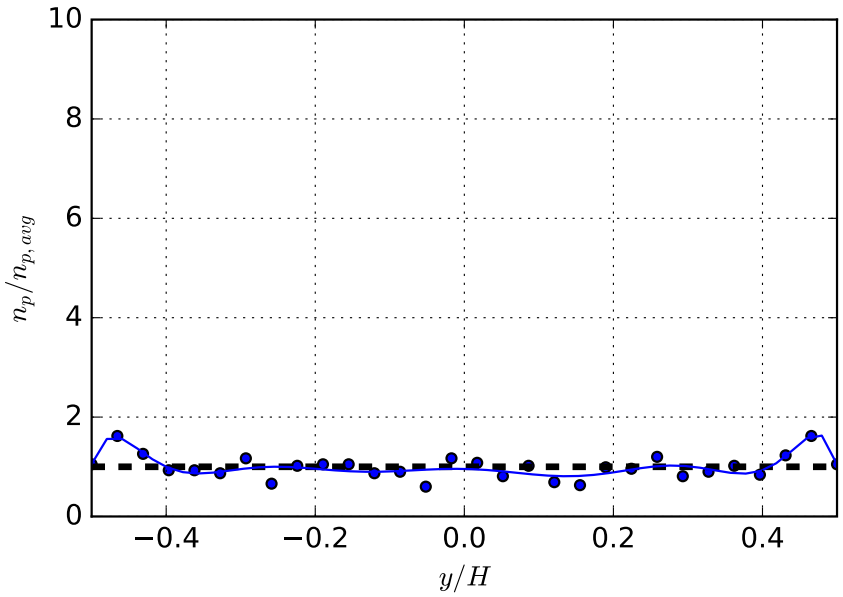

(b)

Figure D.8: Particle concentration profile normalized by the average concentration for Case 4: (a) DNS and (b) LES.

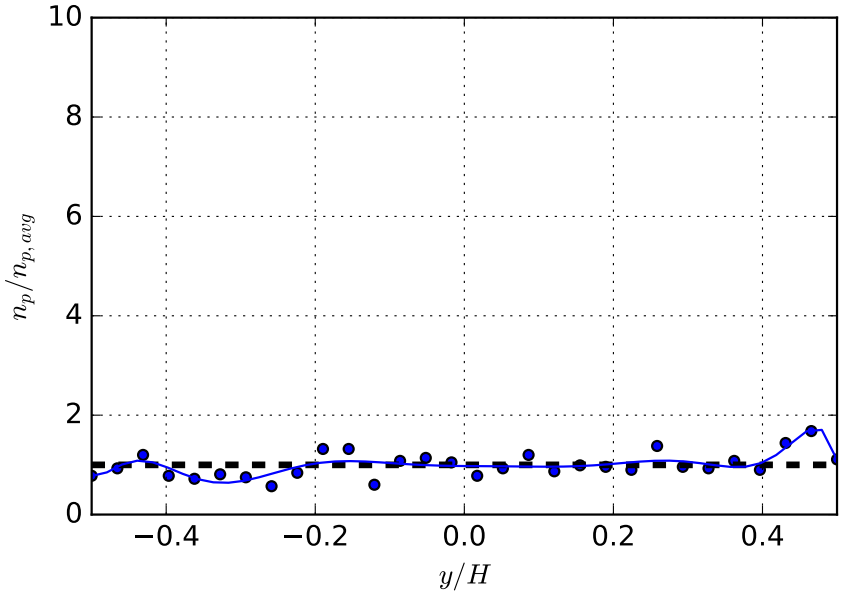

(a)

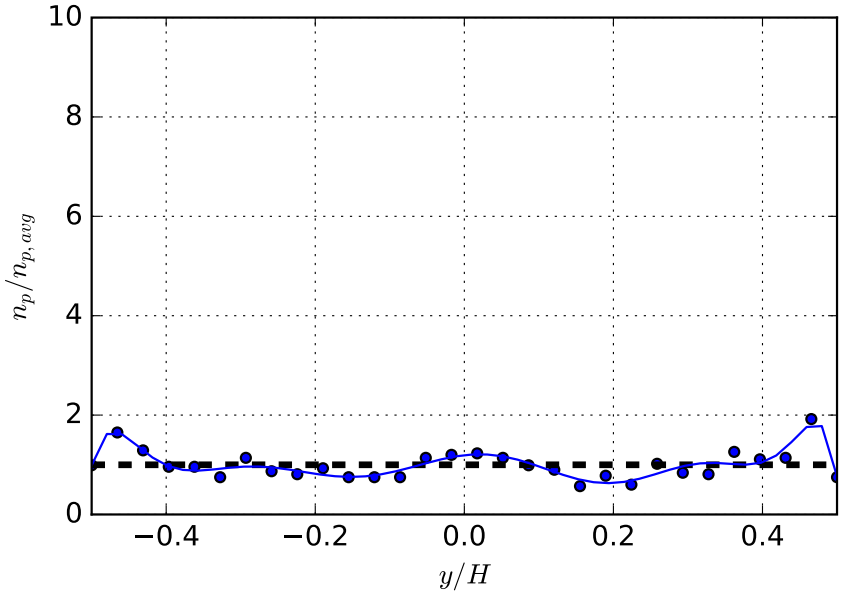

(b)

Figure D.9: Particle concentration profile normalized by the average concentration for Case 5: (a) DNS and (b) LES.

E. RANS COMPUTATIONS OF PARTICLE-LADEN JETS

E.1 Introduction

An in-house Reynolds Averaged Navier Stokes (RANS) code is employed to simulate particle-laden jets for which experimental measurements are available. The objective of the study is to understand the limitations of current RANS models in simulating particle-laden flows.

E.2 Background

Turbulent jets are common in several devices like engines, combustors and gasifiers. These jets have been studied in detail by several researchers in the past [193–197]. As a result, the behavior of turbulent jets is well understood. However, in most of these devices, the flow often includes a dispersed phase as well. For instance, internal combustion engines and gas turbines have turbulent drop-laden jets, while a gasifier often has a solid particle-laden turbulent jet. Addition of a dispersed phase significantly increases the complexity of the flow.

In a particle-laden turbulent flow, there can be different regimes of particle-turbulence interaction [12] (See Section 2.3.2 and related discussion):

- One-way coupling regime: The particles are affected by the turbulence but not vice-versa.
- Two-way coupling regime: Both the particles and the turbulence influenced each other.
- Four-way coupling regime: Particle-particle interactions become important in addition to the particle-turbulence interaction.

In this work, particle-laden jets that are in the two-way coupling regime will be studied.

For particle-laden turbulent flow, the particle Stokes number (St) at the jet exit is an important parameter. The St is defined as the ratio the particle response time, τ_p to the flow response time τ_f, i.e.

$$St = \frac{\tau_p}{\tau_f}. \tag{E.1}$$

For a spherical particle, the particle response time can be taken as the time constant of the particle in Stokes flow, i.e.

$$\tau_p = \frac{\rho_p d_p^2}{18\mu}, \tag{E.2}$$

where ρ_p is the particle density, d_p is the particle diameter and μ is the viscosity of the carrier fluid. The flow response time can be obtained from a characteristic length scale and a velocity scale of the flow. For example, in the case of a pipe flow, the pipe diameter D provides a characteristic length scale and the bulk velocity provides a characteristic velocity scale. The flow response time can then be expressed as

$$\tau_f = \frac{D}{U_b}. \tag{E.3}$$

Thus the St at the jet exit is given by

$$St = \frac{\rho_p d_p^2 U_b}{18\mu D}. \tag{E.4}$$

If the St is small, the particles would adjust quickly to any changes in the flow. If the St is large, the particles would take a longer time to adjust to the flow. In a two-way coupling regime, the particle St at the jet exit would influence the structure of the jet.

Several researchers have studied turbulent particle-laden jets through both experimental and computational techniques. Shuen *et al.* [198] have reported measurements and computations of particle laden jets. They have measured the mean velocities of the carrier and the dispersed phase using Laser Doppler Anemometry (LDA). In their work, they compare the effect of particle diameter d_p, the mass loading ratio Φ_m and the Reynolds number Re. However, no explicit discussions are made about the development of the jet at different St. From their experimental conditions, the St is calculated to be between $100 \sim 500$.

Particle-laden jet measurements of Modarress *et al.* [199] indicate that the fluctuations of the carrier phase decreases with increase in Φ_m. These measurements however are for $St > 10$. It is known that particles can either augment or attenuate turbulence depending on the St [12]. Fleckhaus *et al.* [200] report similar findings, but their St is about 70. Moreover, the standard deviation in the particle size is not mentioned in the work of Modarress *et al.* [199]. In the study of Fleckhaus *et al.* [200], the standard deviation is about 25%. Owing to the squared dependence of the St on the d_p, the effect of St might be masked in these measurements due to the polydispersity of the dispersed phase. Mostafa *et al.* [201] report measurements of particle-laden jets with the standard deviation of the particles being about 5%. This can be considered monodisperse. However, the St investigated in this study is of the order 10. Ref. [26, 202–205] are other measurements on particle-laden jets. However, none of them report the behavior of the jet when St is of the order unity and lower. Moreover, the measurements are not for truly monodisperse particles (standard deviation $< 5\%$).

Eaton and Fessler [10] report that particle behavior can be significantly different depending on the St. They report that St of the order unity, in particular, shows a strong tendency to concentrate preferentially, while no such effects are observed for higher St. This necessitates the need to study the accuracy of particle-turbulence models under a large range of St to determine the validity of the model. There might be applications where the St is of the order unity. The predictive capabilities of the

particle-turbulence model should be studied before they are used in the design of such devices. For instance, in typical industrial furnaces, the St is of the order 1 [206]. Recently, Lau and Nathan [11] have reported detailed measurements of the velocity and concentration of the dispersed phase in particle-laden jets for St of the order unity and lower. This gives us an experimental benchmark to test existing models and identify their shortcomings if any.

In this work, the structure of a turbulent particle-laden jet is studied for a wide range of St numbers ranging from 0.3 to ~ 500 through computations and the computed results are compared with the measurements available. The sensitivity of the structure of the jet to parameters such as the turbulence intensity of the gas phase at the jet exit and the particle velocity fluctuations at the jet exit is examined. The effect of Pope's correction [195], turbulence modulation and the dispersion model employed is also studied.

E.3 Computational Method and Conditions of Study

The computations are done with an in-house numerical code [207] that solves the Reynolds Averaged Navier Stokes (RANS) equations with a $k - \epsilon$ model for turbulence. This code has been widely employed in our earlier works for spray and jet computations [196, 197, 208–212]. Axi-symmetry of the jet is assumed in the current study. The particles are solved in a Lagrangian framework employing the Lagrangian-Drop Eulerian-Fluid (LDEF) approach of Dukowicz [74]. The coupling between the carrier and dispersed phase is modeled using a drag coefficient with a high-Reynolds number correction [76]. Particle-turbulence interactions are modeled using a random-walk dispersion model as proposed by Gosman and Ioannides [75]. The void fraction in all cases is less than 1%. The correction proposed by Pope [195] to account for vortex stretching in a round jet is included.

The axisymmetric domain has dimensions 100 (axial) x 30 (radial) cm and the domain is resolved by a 196 x 98 stretched grid. The orifice has 6 cells radially. The

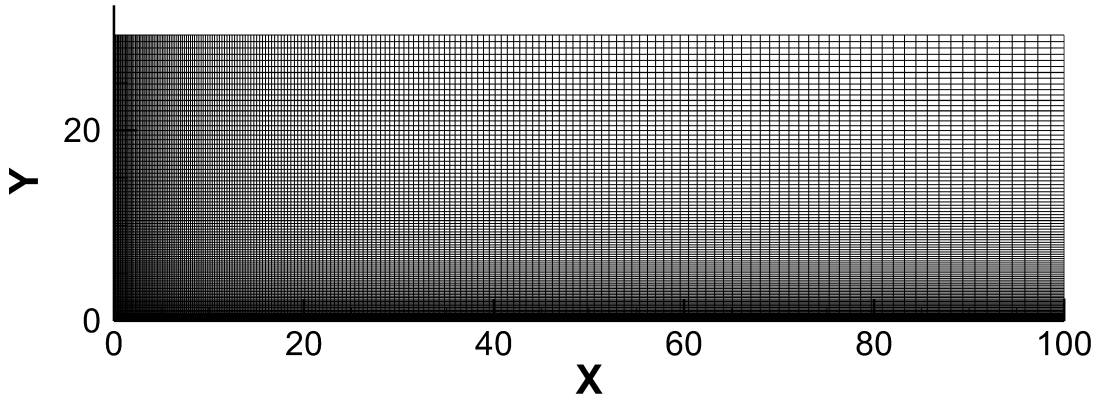

Figure E.1: The axisymmetric computational grid.

grid employed for our computations is shown in Fig. E.1 Increasing the resolution was found to have no significant effect on the results. Figures E.2 and E.3 show the non-dimensional centerline velocity decay of the particles for two different grid resolutions. It can be seen that both the centerline velocity curves are close to each other. We have used the 196 x 98 grid for all our computations. Further the high and the low St cases show certain differences in their decay. This will be discussed in detail in the next section. Table E.1 shows the conditions at the jet exit. The range of St studied varies from 0.3 to 533.8. The St is varied by changing the particle diameter, d_p, particle density, ρ_p and/or the bulk jet exit velocity U_b. The first three cases are compared with the measurements of Lau and Nathan [11], while the other cases are compared with the measurements and computations of Shuen *et al.* [198].

E.4 Results and Discussion

Figures E.4-E.10 show the centerline velocity of the particles u, non-dimensionalized by the mean centerline velocity at the exit $U_{c,e}$, as a function of the non-dimensional axial distance x/D for various St. The computations are compared with the measurements of Lau and Nathan [11] for $St = 0.3$, 1.4 and 11.2 and with the measurements and computations of Shuen *et al.* [198] for $St = 101.3$, 208.8, 230.8 and 533.8.

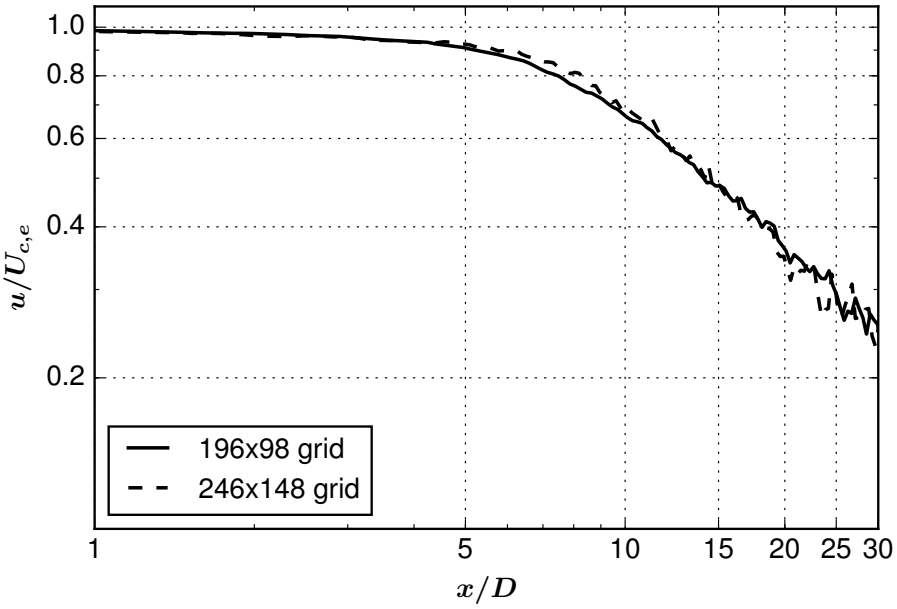

Figure E.2: Centerline velocity decay for $St = 0.3$.

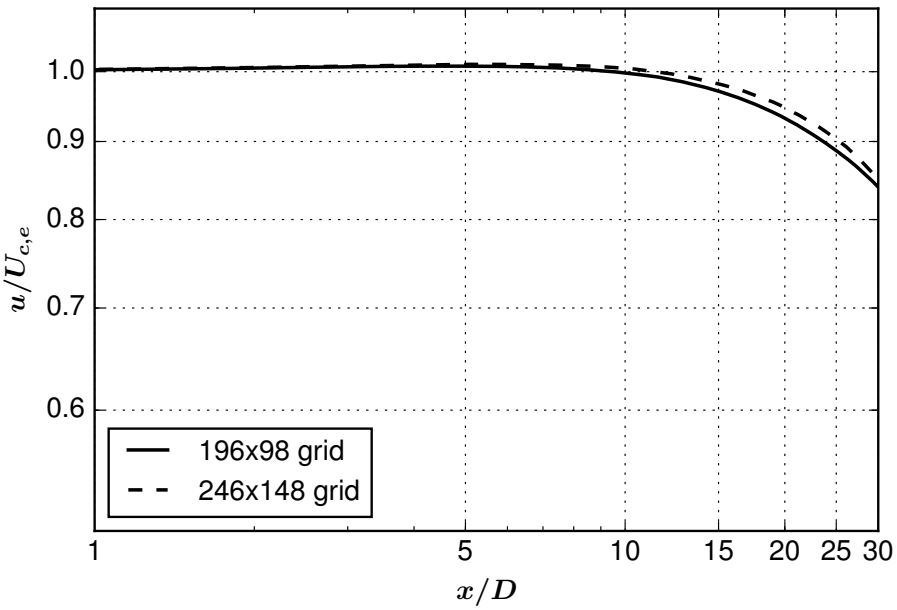

Figure E.3: Centerline velocity decay for $St = 533.8$.

Table E.1: Boundary conditions at the jet exit.

St	$d_p(\mu m)$	Φ_m	$U_b(m/s)$	$\rho_p(kg/m^3)$
0.3	10	0.4	12	1200
1.4	20	0.4	12	1200
11.2	40	0.4	24	1200
101.3	79	0.2	24.1	2620
208.8	119	0.66	21.9	2620
230.8	119	0.2	24.2	2620
533.8	207	0.66	18.5	2620

It is seen from Figs. E.4 and E.5 that for lower St ($St = 0.3$ and 1.4), the computed results match closely with that of the experimental results. For these St, the coupling is one-way in that the particles do not influence the gas-phase turbulence and act as "tracer particles". This is not to suggest that the particles have no influence on the jet structure because the particle loading ratio is about 0.4 and the net momentum of the jet is the sum of that of the carrier and dispersed phases, but the jet behaves like one that has higher density.

Looking at the measurements, the centerline decay for $St = 0.3$ and $St = 1.4$ are similar. For instance, in Fig. E.4, at $x/D = 30$, the $u/U_{c,e}$ is about 0.25. Looking at Fig. E.5, $u/U_{c,e}$ is about the same value at this location. However, for $St = 11.2$, $u/U_{c,e} = 0.3$ at the same location (Fig E.6). Thus at this St, the centerline velocity decays slower. We can see from Fig. E.6 that the computations capture this trend. However, the predicted centerline velocity decays faster than the measured decay. One reason for this could be that the computations overestimate the turbulence levels of the gas phase and increased turbulence causes increased spreading.

Figure E.7 shows the centerline decay for $St = 101.3$. Again we can see that the measured centerline velocity decay is smaller than for $St = 11.2$. But in this case, the computed centerline velocity decays slower than the measured value. The reason for this discrepancy is unknown, but could likely be with the way particles interact

with turbulence. Since the mass loading for this case is lower than the earlier cases, the turbulence level predictions might be underestimated giving a lower spread. At St = 208.8 (Fig. E.8), the computations seem to overpredict the spread. For St = 230.8 (Fig. E.9), the agreement is better than the earlier cases. At St = 533.8 (Fig. E.10), the computations underpredict the spread. These results indicate that existing models might not work well over a wide range of St. This might be because the model lacks some information that represents the physics of particle-turbulence interaction at different St.

Next, the sensitivity of the spreading rate of the jet on various parameters such as the turbulence intensity of the gas phase at the jet exit, velocity fluctuations of the particles at the jet exit is examined. The effects of Pope's correction [195], turbulence modulation and the dispersion model employed are also studied.

E.4.1 Effect of Gas Phase Turbulence Intensity at the Jet Exit

In a fully developed turbulent pipe flow, it has been shown through both measurements and Direct Numerical Simulation (DNS) studies that the fluctuating component of velocity in the axial direction is significantly higher than the other two components [213]. This is because of two reasons: the mean flow in the axial direction tends to increase fluctuations in that direction; the presence of walls in the wall-normal direction dampens the fluctuations in that direction. With the addition of particles however, it is not known whether this anisotropy would decrease or increase. It is possible that this anisotropy may depend on the St. Squires and Eaton [5, 35] report that particles exhibit preferential concentration even in isotropic turbulence depending on their St. This might introduce anisotropy in the flow if the preferential concentration is large. On the other hand, particles with high St might actually tend to decrease this anisotropy since they are more uniformly distributed. This is currently not known and further DNS or highly resolved measurements are required to address this issue. Lau and Nathan [11] report the fluctuating component

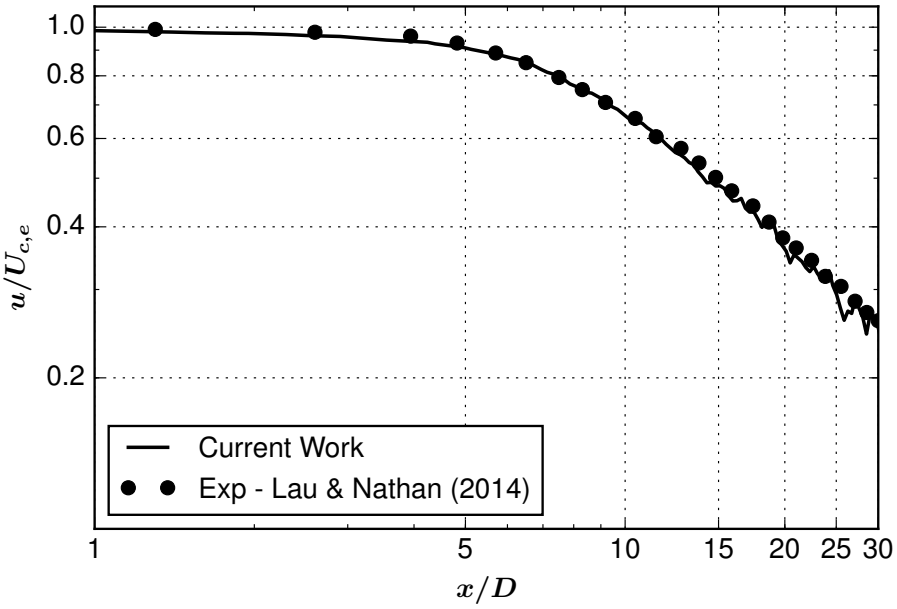

Figure E.4: Particle centerline velocity decay for $St = 0.3$.

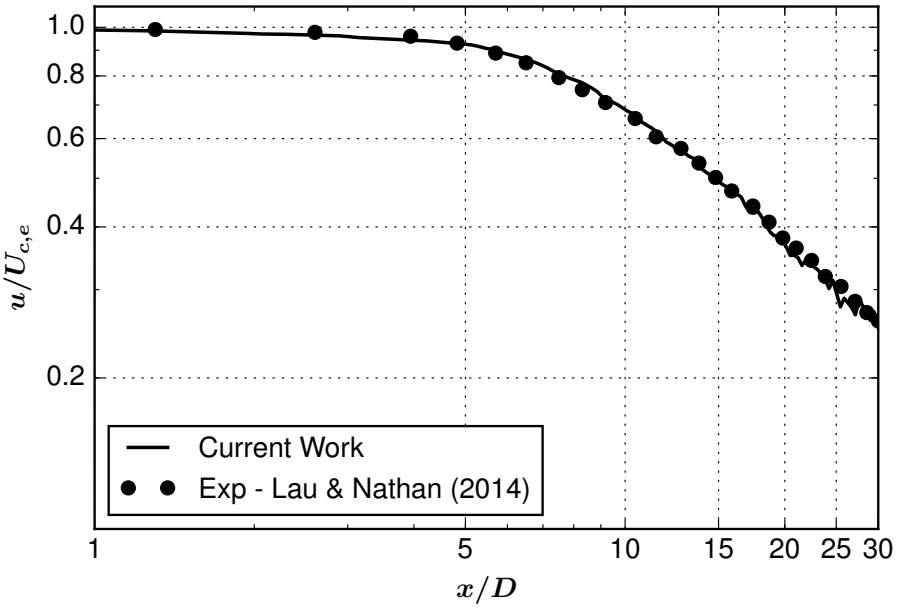

Figure E.5: Particle centerline velocity decay for $St = 1.4$.

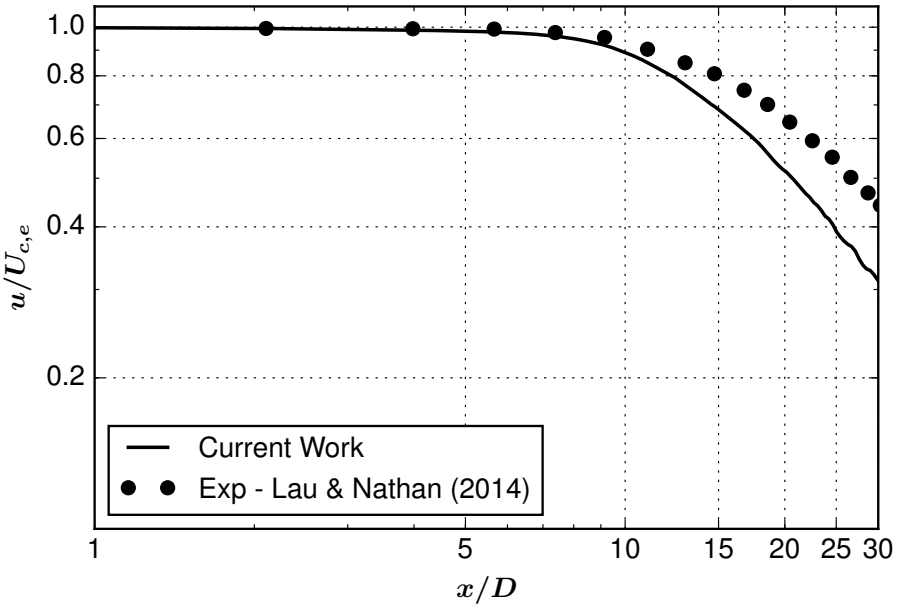

Figure E.6: Particle centerline velocity decay for $St = 11.2$.

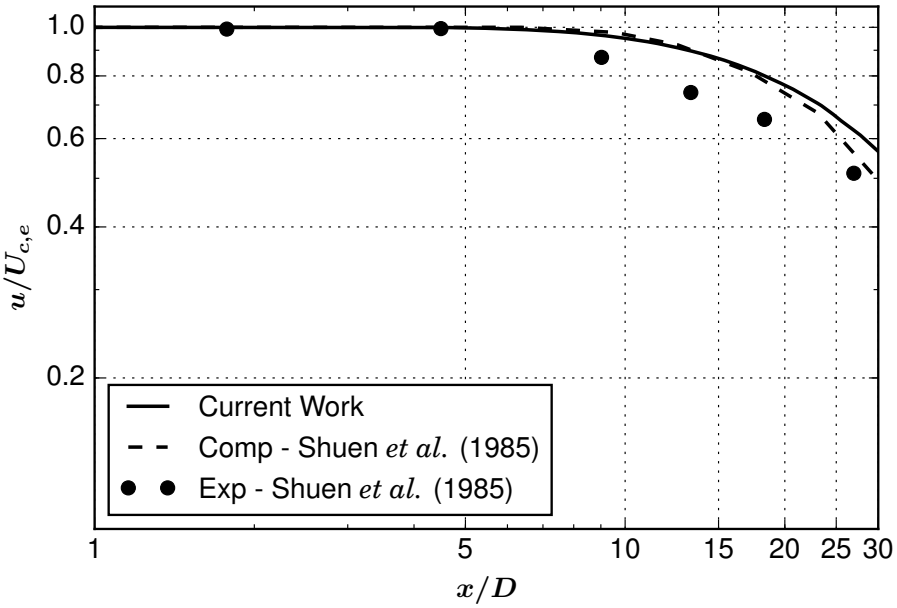

Figure E.7: Particle centerline velocity decay for $St = 101.3$.

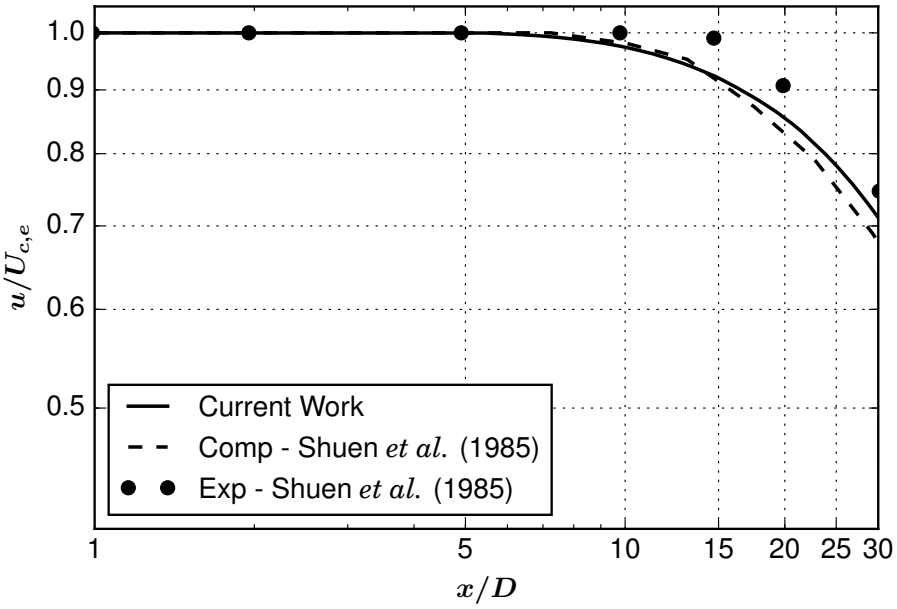

Figure E.8: Particle centerline velocity decay for $St = 208.8$.

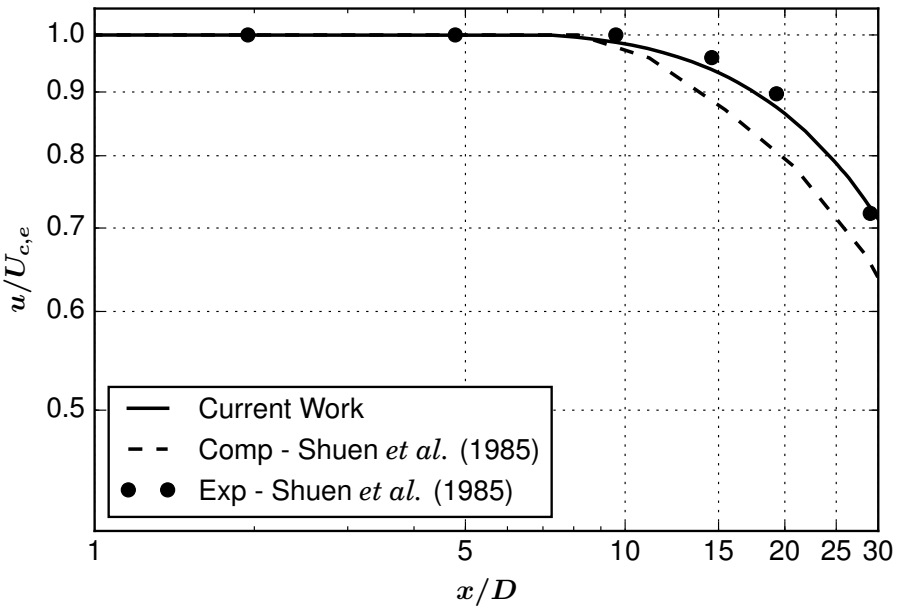

Figure E.9: Particle centerline velocity decay for $St = 230.8$.

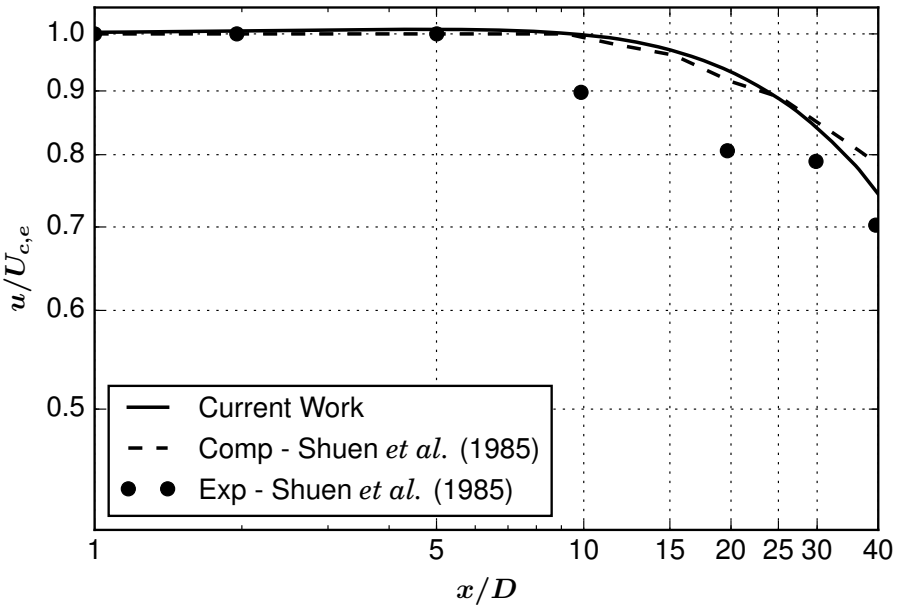

Figure E.10: Particle centerline velocity decay for $St = 533.8$.

of the axial velocity. No data however is provided for the other two velocity components. In the work of Shuen et al. [214], the axial and the lateral velocity components are reported. From their data, no conclusive trends in relationship can be established between the axial and lateral fluctuating velocity component based on the St. Since the turbulent kinetic energy k and the dissipation rate ϵ of the gas phase are to be specified as a boundary condition in the computations, there exists an element of uncertainty. In order to study the effect of k and ϵ at the jet exit on the structure of the jet, computations with different k and ϵ for the lowest and highest St (0.3 and 533.8) have been carried out.

Figure E.11 shows the non-dimensional centerline velocity decay of the particles as a function of the non-dimensional axial distance for $St = 0.3$. The turbulence intensity of the gas phase at the jet exit is decreased by a factor of two. From Fig. E.11, it is evident that for $St = 0.3$, the jet spreads slower as a result of which the centerline velocity decays slower. This is not surprising since the spreading of the jet is caused by turbulence. The "potential core" (region where the axial velocity does not decrease with axial distance) in the baseline case is about $4D$ whereas in the case with lower turbulent intensity, it is about $6D$. The axial velocity $u/U_{c,e}$ at $x/D = 10$ is about 0.65 for the baseline case while it is 0.72 for the case with reduced turbulent intensity, which corresponds to a difference of more than 10%.

Figure E.12 shows the results when the turbulence is increased and decreased by a factor of two for a particle for $St = 533.8$. The structure of the jet does not change significantly with change in the gas phase turbulence intensity at the jet exit as seen from Fig. E.12. For instance, consider an axial distance of $x/D = 20$. The axial velocity $u/U_{c,e}$ of the baseline case is about 0.93, while that of the case with higher turbulence intensity is 0.9 and that of the case with lower turbulence intensity is 0.95. In both cases, the difference is less than 3.5%. This is due to the fact that at high St, the particles take a longer time to respond to the changes in the gas phase and hence, the spreading of the dispersed phase is not affected much.

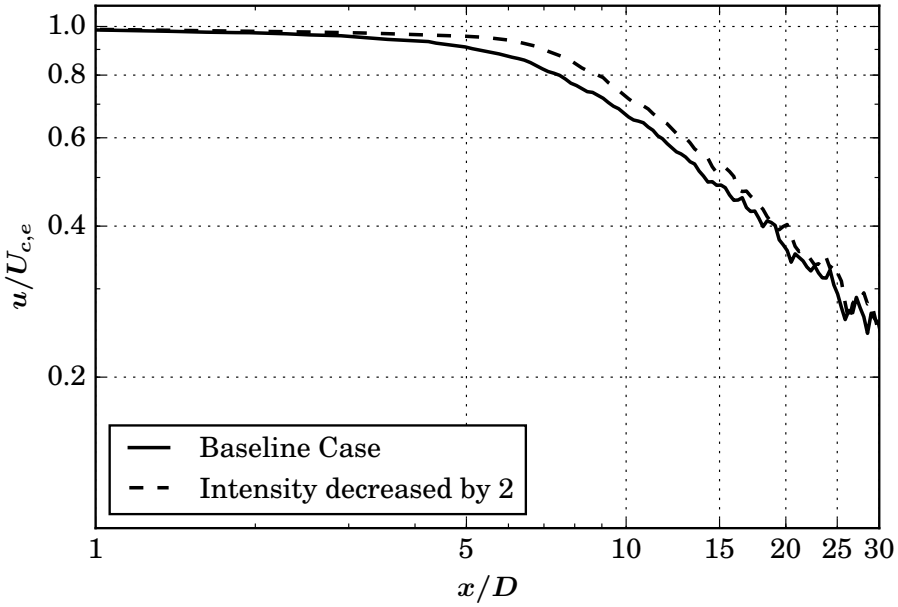

Figure E.11: Particle centerline velocity decay for $St = 0.3$ for different values of gas phase turbulence intensity at the jet exit.

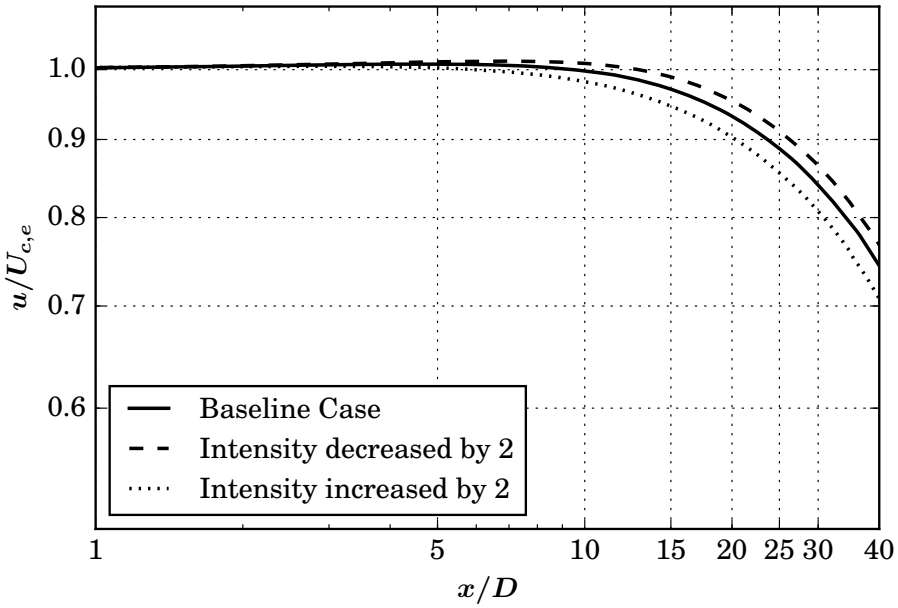

Figure E.12: Particle centerline velocity decay for $St = 533.8$ for different values of gas phase turbulence intensity at the jet exit.

E.4.2 Effect of Velocity Fluctuations of the Particle at the Jet Exit

In a turbulent flow, the fluid has a mean and fluctuating velocity component. The fluctuating component induces a fluctuating motion on the particle. Such motion would not exist in a laminar flow. This fluctuating velocity of the dispersed phase implies that it has a turbulent kinetic energy of its own in addition to that of the carrier phase. In order to see if the fluctuating velocity component of the particles is important when boundary conditions are specified, computations are done in which the particles are injected with a fluctuating velocity (varying in time) component in addition to its mean velocity. These are chosen from a Gaussian distribution with zero mean and variance related to the turbulent kinetic energy of the carrier phase. This study is done on cases with the highest and lowest St.

Figures E.13 shows the non-dimensional centerline velocity decay for $St = 0.3$ with and without particle velocity fluctuations at the boundary. For this case, the addition of fluctuations does not seem to make any noticeable difference. Since the St is low, the particle quickly adapts to the flow and memories of its initial fluctuating velocity (at the boundary) are lost. Figure E.14 shows the particle centerline velocity decay for $St = 533.8$. For this case, the particle center line velocity shows fluctuations when the fluctuating velocity component is added to the particles at the jet exit. Moreover, it seems that near the jet exit ($x/D < 20$), the centerline velocity decays somewhat faster (indicating greater spread). One possible explanation for this is that at high St, the particles take a longer time to respond to the flow. Thus they retain their fluctuating component for a longer time and hence spread more. As they move further downstream, the decay rate comes closer to the case without fluctuations.

From the discussion in the previous section and the current one, it seems that at low St the particles are sensitive to the turbulence in the carrier phase while the turbulence (or fluctuations) in the dispersed phase makes little difference. For high St, the particles show little effect to changes in the carrier phase turbulence but are sensitive to the fluctuations in the dispersed phase. This needs further examination.

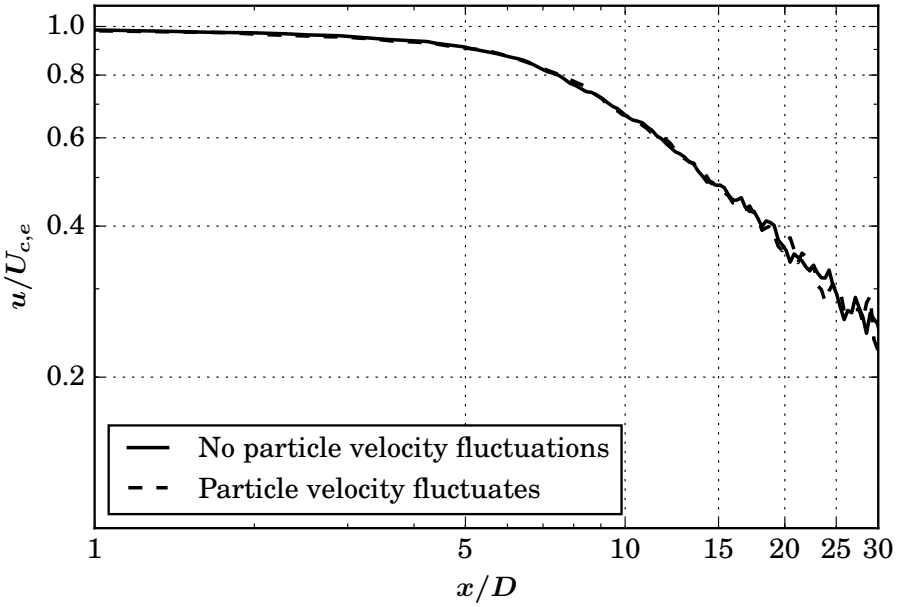

Figure E.13: Particle centerline velocity decay for $St = 0.3$ with and without particle velocity fluctuations at the jet exit.

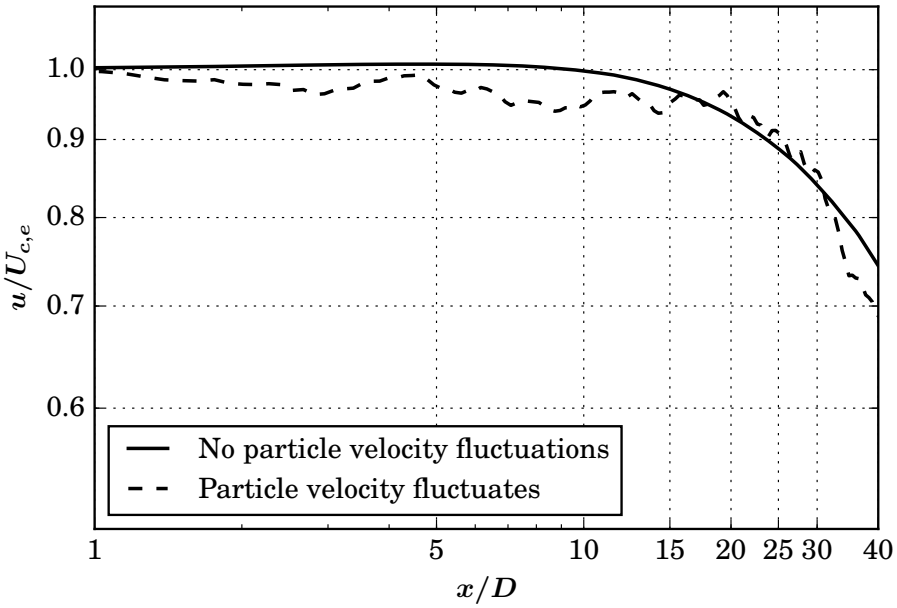

Figure E.14: Particle centerline velocity decay for $St = 533.8$ with and without particle velocity fluctuations at the jet exit.

E.4.3 Effect of Pope's Correction

It has been reported that when the $k-\epsilon$ model is used for turbulence, the spreading of a round jet is over predicted by about 30% [195, 208, 215]. Pope [195] suggested that this could be due to the fact that in a round jet, as the jet spreads, the vortex rings expand due to which the vortex will increase in frequency to conserve angular momentum. This enhances dissipation of turbulent kinetic energy as a result of which the turbulent kinetic energy decreases. This in turn decreases the spreading of the jet. This effect however is not accounted for in the standard $k-\epsilon$ model. The non-dimensional measure of vortex stretching χ is given by

$$\chi = \omega_{ij}\omega_{jk}S_{ki}, \tag{E.5}$$

where

$$S_{ij} = \frac{1}{2}\frac{k}{\epsilon}\left(\frac{\partial U_i}{\partial x_j} + \frac{\partial U_j}{\partial x_i}\right) \tag{E.6}$$

and

$$\omega_{ij} = \frac{1}{2}\frac{k}{\epsilon}\left(\frac{\partial U_i}{\partial x_j} - \frac{\partial U_j}{\partial x_i}\right) \tag{E.7}$$

U_i being the velocity along the direction x_i. From the arguments above, the dissipation should increase with the vortex stretching. Pope [195] has considered the rate of change of dissipation to be a linear function of the vortex stretching χ. The ϵ equation thus has a source term $S_{\epsilon 3}$ given by

$$S_{\epsilon 3} = C_{\epsilon 3}\frac{\epsilon^2}{k}\chi, \tag{E.8}$$

where $C_{\epsilon 3}$ is an empirical constant that needs to be determined. Based on the measured spreading rate of a single phase gas jet, this constant is chosen to be 0.79 [195]. With the addition of particles however, it is not known how the vortex stretching of the jet will change. In order to see the effect of this empirical constant on the

spreading rate of the jet, computations are carried out with different values of this constant for the smallest and largest St cases that are examined in this study.

Figures E.15 and E.16 show the non-dimensional centerline velocity decay of the particles for $St = 0.3$ and $St = 533.8$ for three different $C_{\epsilon 3}$. It is seen that the effect of this empirical constant is minimal on the structure of the jet for both the St for the range of the constants considered. This seems surprising and contrary to what one would expect. It could be that the range of constants selected for this study did not make a significant difference to the decay of the centerline velocity. This needs further investigation.

E.4.4 Effect of Turbulence Modulation

In a two-way coupling regime, the particles are influenced by the turbulence and the particles influence the turbulence. As a result, the turbulent kinetic energy (TKE) of the jet can either decrease or increase. Turbulent dispersion of the particles decreases the TKE. This can be understood by considering the fact that if a particle is injected in a quiescent fluid without the jet, it would not move in the lateral direction. The lateral motion (i.e. dispersion) of the particle is caused by the spreading of the gas phase component of the jet. As the turbulent eddies move the particles laterally, the turbulence energy would decrease. There are other mechanisms that might augment the TKE. For instance, vortex shedding effects in the particle wake can increase the TKE. This change in the TKE due to the dispersed phase is referred to as turbulence modulation. A change in the TKE might bring about a change in the dissipation of TKE as well.

There are different methods to incorporate the effect of turbulence modulation. Yuan and Michaelides [216] proposed a model in which the velocity defect in the wake of the particle is responsible for the augmentation of turbulence and the work associated with the motion of particulate phase is responsible for its attenuation. Yarin and Hetsroni [217] proposed a similar idea but they use a more detailed description of

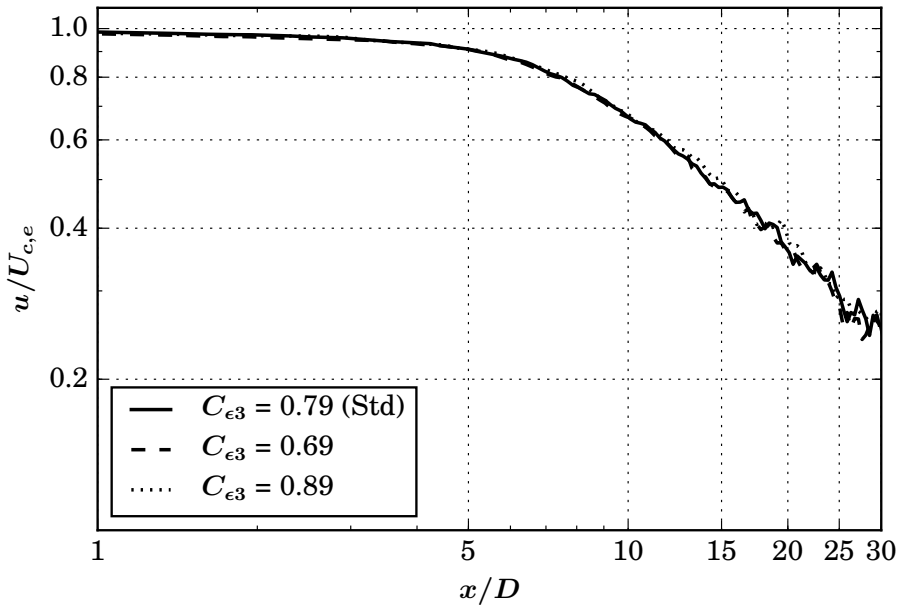

Figure E.15: Particle centerline velocity decay for $St = 0.3$ for different values of constant $C_{\epsilon 3}$.

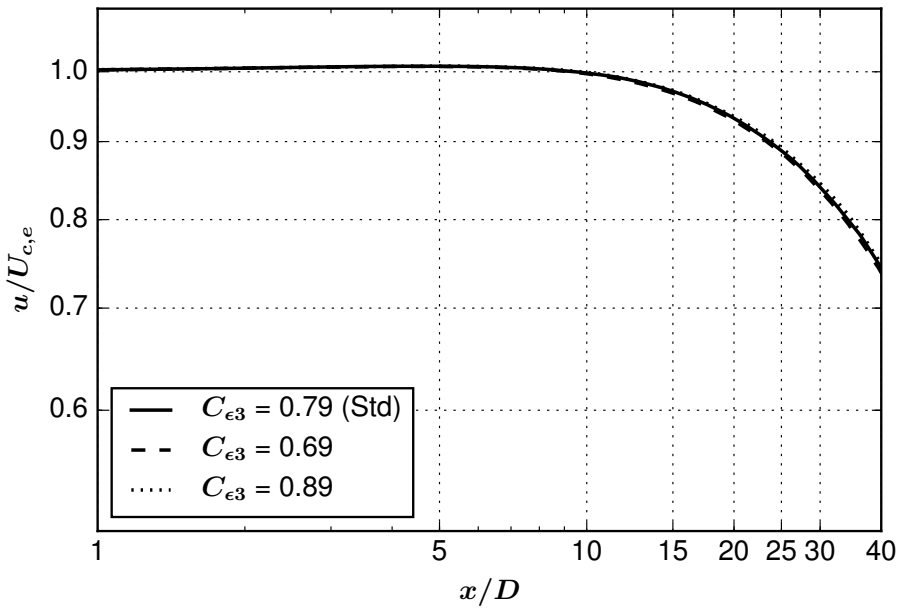

Figure E.16: Particle centerline velocity decay for $St = 533.8$ for different values of constant $C_{\epsilon 3}$.

the wake. In general, in order to include turbulence modulation in the computations, an extra source term needs to be included in the k and ϵ equation. The source term in the k equation can be related to the drag force on the particle and the fluctuating component of the gas phase velocity [76]. The drag co-efficient for a particle in Stokes flow is given by

$$C_d = \frac{24}{Re}. \tag{E.9}$$

A high Reynolds number correction is incorporated into this expression to determine drag force acting on particles in turbulent flows. This modified drag co-efficient is [76]

$$C_d = \frac{24}{Re}\left(1 + \frac{Re^{2/3}}{6}\right). \tag{E.10}$$

Now, the source term for inclusion of turbulence modulation in the k equation is given by the following expression [76]

$$S_k = \sum \boldsymbol{F_d} \cdot \boldsymbol{u'}, \tag{E.11}$$

where $\boldsymbol{F_d}$ is the drag force per unit volume and $\boldsymbol{u'}$ is the fluctuating component of the gas phase velocity which is chosen from a Gaussian distribution based on the k and ϵ values. The summation is done over all the particles in the computational cell. The source term in the ϵ equation is given by [76]

$$S_{\epsilon 4} = C_{\epsilon 4} S_k \frac{\epsilon}{k}, \tag{E.12}$$

where $C_{\epsilon 4}$ is an empirical constant.

Inclusion of turbulence modulation introduces an empirical constant $C_{\epsilon 4}$ that needs to be determined. Shuen et al. [198] report that the turbulence modulation does not influence the centerline velocity decay significantly, even when the empirical constant is varied by a large extent. We test the effect of this constant for the lowest and highest St. Figure E.17 shows the particle centerline velocity decay for $St = 0.3$ for two different $C_{\epsilon 4}$. It can be seen that the constant has a significant effect on

the velocity decay. Figure E.18 shows the particle centerline decay for $St = 533.8$ at different $C_{\epsilon 4}$. Changing the constant does not seem to make any significant difference to the centerline velocity decay for this high St.

Possible reasons why the modulation has a significant effect for the low St while there is no observable effect on the high St is examined. In the model, the source term due to turbulence modulation in the k equation is specified as the dot product of the drag force times the fluctuating velocity summed over all the particles in the computational cell. Now, for the same mass loading ratio, the smaller particles will have higher drag than the larger particles due to the larger total surface area for smaller particles. Smaller particles will thus have a larger source term in the k equation than larger particles. The case for $St = 533.8$ has larger particles and hence the model does not give rise to any noticeable difference.

In the case of the lower St, the turbulence modulation can either increase or decrease the TKE. The additional terms in the k and ϵ equations to account for the turbulence modulation actually acts as a sink terms [76]. The constant $C_{\epsilon 4}$ decides the decrease of ϵ over the decrease of k. If $C_{\epsilon 4} = 1.5$, the decrease in TKE dominates the decrease in the dissipation of TKE and hence there is a net decrease in TKE. This causes the jet to spread less than the case with no turbulence modulation. Now for $C_{\epsilon 4} = 2.0$, the decrease in dissipation of TKE dominates the decrease in TKE and hence there is an increase in the TKE. This causes the jet to spread more. This however is not what happens physically. Better models should be developed that addresses this issue.

E.4.5 Effect of the Dispersion Model Employed

The particles that are injected along with the jet are dispersed due to the turbulent motion of the eddies. In a RANS solver, since only the mean quantities are solved for, a dispersion model has to be used to account for the dispersion of the particles by the turbulent flow field. Gosman and Ioannides [75] proposed a stochastic formulation to

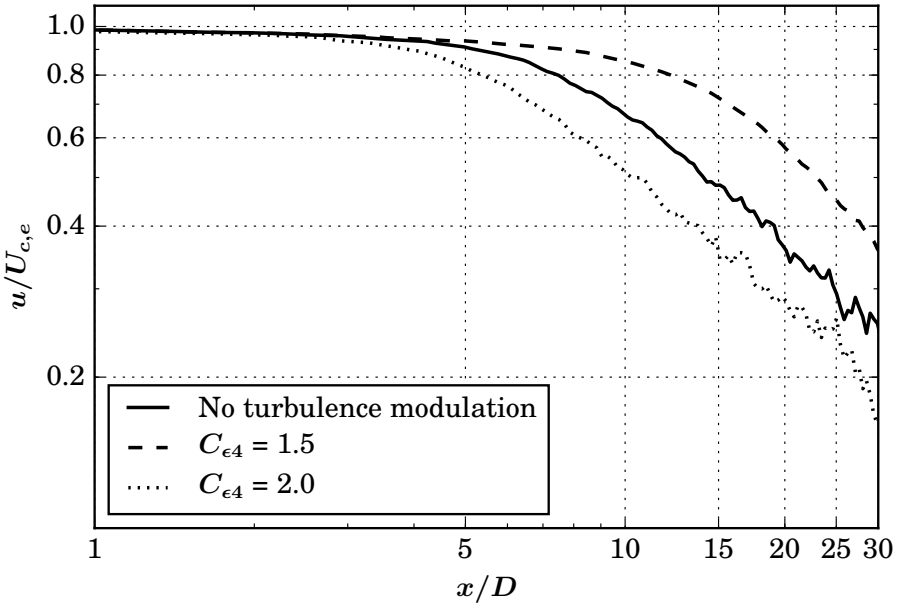

Figure E.17: Particle centerline velocity decay for $St = 0.3$ for different values of constant $C_{\epsilon 4}$ in the ϵ equation for turbulence modulation.

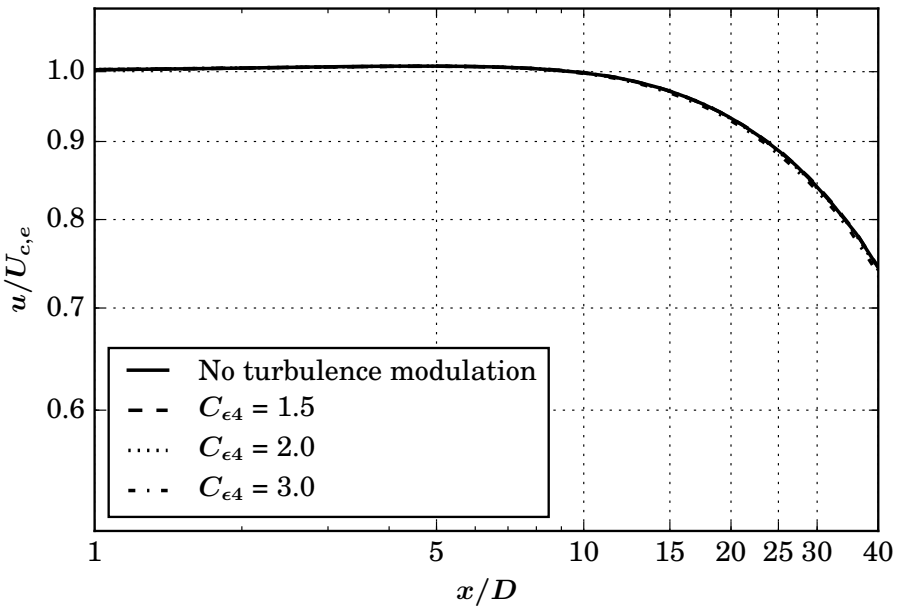

Figure E.18: Particle centerline velocity decay for $St = 533.8$ for different values of constant $C_{\epsilon 4}$ in the ϵ equation for turbulence modulation.

account for the dispersion of particles in a turbulent flow. A brief overview of their method is presented below for completeness.

The particle dispersion model involves calculating the drag force acting on the particle from the relative velocity of the particle with respect to the instantaneous velocity of the gas. In order to determine the instantaneous gas phase velocity, a fluctuating velocity component is required. This fluctuating component is found from a Gaussian distribution with mean zero and standard deviation σ given by

$$\sigma = (2k/\epsilon)^{2/3}, \tag{E.13}$$

where k is the turbulent kinetic energy. Now the instantaneous velocity can be obtained and the drag force is computed. This drag force is used to update the position and velocity of the particle. Now a suitable time scale should be selected for which the particle will interact with the randomly selected velocity field. A length scale and velocity scale of the eddy are determined from the k and ϵ from which a time scale is calculated. Once a particle moves a distance greater than the length scale of the eddy or interacts with a random velocity field for a time greater than the time scale of the eddy, a new random velocity component is chosen. The reasoning behind this is that a particle would experience a fluctuating velocity component as long as it remains inside the eddy or for one eddy turnover time whichever is shorter.

In order to see the effect of this method, computations where the eddy turnover time is modified by a factor of two are carried out. Figures E.19 shows the non-dimensional centerline-velocity decay of the particle for $St = 0.3$. The centerline velocity has no noticeable difference from the original case. Figure E.20 shows the particle centerline velocity decay for $St = 533.8$. Again, no significant differences are observed when this time scale is changed. One possible reason could be that for high St, the time the particle remains inside the eddy depends more on the time taken by the particle to traverse distances comparable to the length scale of the eddy since the

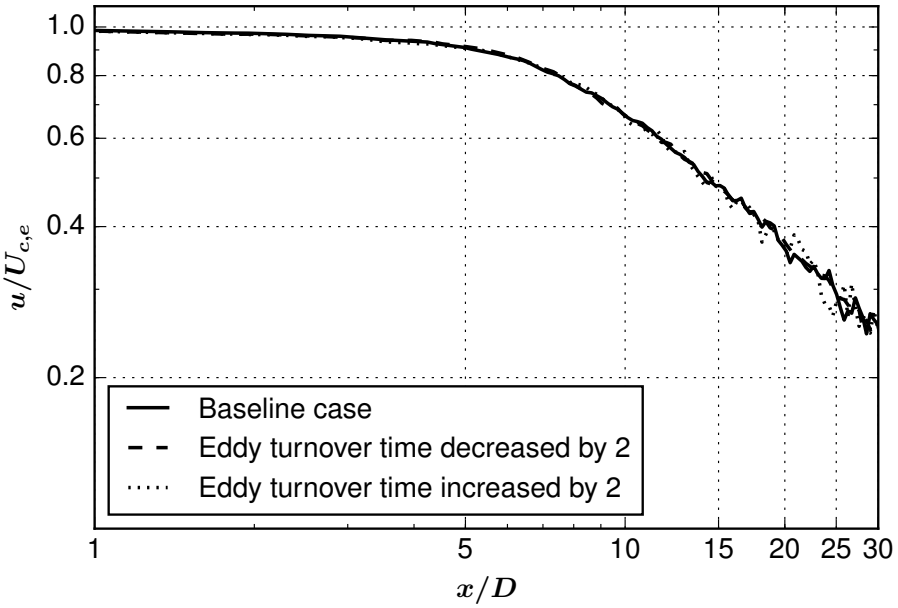

Figure E.19: Particle centerline velocity decay for $St = 0.3$ as the particle residence time in an eddy is changed.

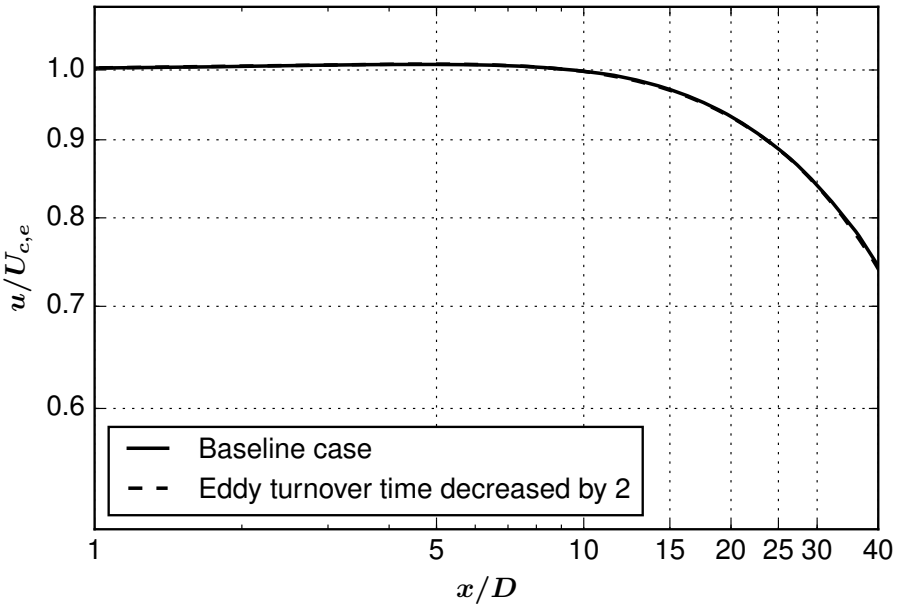

Figure E.20: Particle centerline velocity decay for $St = 533.8$ as the particle residence time in an eddy is changed.

particle responds slowly to the eddy. However, the reason for the low St exhibiting similar is not known and needs further investigation.

E.5 Conclusions

A comparison of the structure of computed and measured particle-laden jets is presented for a wide range of Stokes (St) numbers. For St of the order unity and lower, the computations agree very well with the measurements. For higher St considered, the agreement is within 20%. Several studies are also presented to study the sensitivity of the structure of the jet on parameters such as the inlet gas phase turbulence intensity and the velocity fluctuations of the particle at the jet exit. Further, the effect of Pope's correction, turbulence modulation and the dispersion model are studied. It is found that the gas phase turbulence intensity at the jet exit has a significant effect on the centerline velocity decay especially for lower St. It seems that this sensitivity decreases as the St increases. The particle velocity fluctuation at the jet exit does not affect the centerline velocity decay significantly for lower St. However, at higher St, the centerline velocity decay shows considerable difference when the particle velocity fluctuations at the jet exit are included. The effect of employing Pope's correction for a particle-laden jet is discussed. It appears that the results are not too sensitive with the empirical constant in the Pope's correction expression. The influence of turbulence modulation terms on the structure of the jet is also examined. It is found that for high St, the turbulence modulation does not influence the centerline velocity significantly, while for low St, the effect is significant and is extremely sensitive on the model constant employed. This behavior needs further study. Changing the eddy turnover time (for the dispersion model) by a factor of two does not seem to affect the structure of the jet significantly.

VITA

VITA

Anand Samuel Jebakumar received his Bachelor of Engineering in Mechanical Engineering with highest honors from College of Engineering, Guindy in May 2013. As an undergraduate student, he was the recipient of the University Gold Medal, the best outgoing student in Mechanical Engineering and Sir Arthur Hope Scholarship. During his undergraduate program, he did a research internship at the Indian Institute of Technology (IIT) - Madras during which he investigated the acoustic lock-on phenomena in segmented solid-rocket motors using numerical simulations. He joined the Graduate School at Purdue University in August 2013 to pursue his PhD in Professor Abraham's research group in the School of Mechanical Engineering. His current research focuses on modeling of particle-laden flows. His work has resulted in three journal papers accepted, and three more submitted for publication, as well as four international conference presentations. As a graduate student, he has been a recipient of the Ross Doctoral Fellowship and the Burton Morgan Fellowship. He has served as a mentor for the Summer Undergraduate Research Fellowship (SURF). He is also a member of the Computational Science and Engineering (CSE) program.

PUBLICATIONS

Refereed Journal Publications

A. S. Jebakumar, K. N. Premnath, and J. Abraham, "Lattice Boltzmann method simulations of Stokes number effects on particle trajectories in a wall-bounded flow", Computers and Fluids 124 (2016): 208-219.

A. S. Jebakumar, and J. Abraham, "Comparison of the structure of computed and measured particle-laden jets for a wide range of Stokes numbers", International Journal of Heat and Mass Transfer 97 (2016): 779-786.

L. Zhang, A. S. Jebakumar, and J. Abraham, "Lattice Boltzmann method simulations of Stokes number effects on particle motion in a channel flow", Physics of Fluids 28.6 (2016): 063306.

A. S. Jebakumar, V. Magi, and J. Abraham, "Lattice-Boltzmann simulations of flow modulation in a channel with stationary particles", submitted to International Journal of Computational Fluid Dynamics, April 2018.

A. S. Jebakumar, K. N. Premnath, V. Magi, and J. Abraham, "Fully-resolved direct numerical simulations of particle motion in a turbulent channel flow with the lattice-Boltzmann method", submitted to Computers and Fluids, April 2018.

A. S. Jebakumar, V. Magi, and J. Abraham, "Lattice-Boltzmann simulations of particle transport in a turbulent channel flow", submitted to International Journal for Numerical Methods in Fluids, April 2018.

Conference Presentations

A. S. Jebakumar, K. N. Premnath, and J. Abraham, "Lattice Boltzmann method simulations of Stokes number effects on particle trajectories in a wall-bounded flow", presented at the 11th International Conference for Mesoscopic Methods in Engineering and Science (ICMMES), New York, 2014.

A. S. Jebakumar, K. N. Premnath, and J. Abraham, "Direct numerical simulations of particle-flow interactions in a channel", presented at the American Physical Society (APS) March Meeting, New Orleans, 2017.

A. S. Jebakumar, K. N. Premnath, and J. Abraham, "Lattice Boltzmann simulations of turbulence modulation in a particle-laden channel flow", presented at the 14th International Conference for Mesoscopic Methods in Engineering and Science (ICMMES), Nantes, France, 2017.

A. S. Jebakumar, K. N. Premnath, and J. Abraham, "Direct numerical simulations of particle-laden turbulent channel flow", presented at the 70th American Physical Society (APS) - Division of Fluid Dynamics (DFD) Annual Meeting, Denver, 2017.